AGH UNIVERSITY OF SCIENCE AND TECHNOLOGY
Faculty of Physics and Applied Computer Science

Doctoral thesis

Łukasz Fulek

Charged particle production in diffractive proton-proton scattering at the RHIC and LHC energies

Supervisor: **prof. dr hab. inż. Mariusz Przybycień**
Auxiliary Supervisor: **dr inż. Leszek Adamczyk**

Cracow, April 2020

Declaration of the author of this dissertation:

Aware of legal responsibility for making untrue statements I hereby declare that I have written this dissertation myself and all the contents of the dissertation have been obtained by legal means.

Declaration of the thesis Supervisor:

This dissertation is ready to be reviewed.

Streszczenie

W rozprawie doktorskiej zaprezentowano pomiary produkcji cząstek naładowanych w oddziaływaniach dyfrakcyjnych z użyciem danych zebranych przez eksperymenty STAR na akceleratorze RHIC i ATLAS na akceleratorze LHC w roku 2015. Oddziaływania dyfrakcyjne stanowią istotny wkład do całkowitego przekroju czynnego w zderzeniach proton-proton. Jedną z cech takich oddziaływań jest obecność w stanie końcowym zderzających się protonów, które są rozproszone pod małymi kątami, tzw. protony do przodu.

Znakomita większość cząstek produkowanych w zderzeniach proton-proton jest wynikiem procesów miękkich. Zazwyczaj do ich opisu stosuje się modele fenomenologiczne, których parametry muszą być ustalone na podstawie dostępnych danych eksperymentalnych. Pomiary rozkładów cząstek naładowanych w zderzeniach hadronów przy różnych energiach w układzie środka masy są prowadzone od wielu dekad. Niestety, większość badań jest dedykowana produkcji cząstek w oddziaływaniach nieelastycznych bez podziału na dyfrakcyjne i niedyfrakcyjne. Z tego powodu istnieje wielka potrzeba wykonania podobnych pomiarów w oddziaływaniach dyfrakcyjnych w celu walidacji dostępnych modeli fenomenologicznych.

Dane zebrane przez eksperymenty STAR i ATLAS pochodzą ze zderzeń protonów przy energiach w układzie środka masy równych odpowiednio 200 GeV i 13 TeV. Ich scałkowana świetlność wynosi, odpowiednio, 16 nb^{-1} i 723 nb^{-1}. W rozprawie zbadano rozkłady cząstek naładowanych w procesach z jednym protonem do przodu, rejestrowanym przez układy STAR RP i ATLAS ALFA. Względna strata energii protonu i kwadrat przekazu czteropędu wynoszą odpowiednio $0.02 < \xi < 0.2$, $0.04 < -t < 0.16$ GeV^2/c^2 (STAR) oraz $10^{-5} < \xi < 0.16$, $0.02 < -t < 1$ GeV^2/c^2 (ATLAS). W analizach zmierzono produkcję naładowanych cząstek o pędach poprzecznych większych od 200 MeV/c (STAR) i 100 MeV/c (ATLAS) oraz o bezwzględnej wartości pseudorapidity mniejszej niż 0.7 (STAR) i 2.5 (ATLAS). W obu analizach wymagano przynajmniej dwóch cząstek naładowanych w podanych wyżej zakresach.

Rozprawa doktorska rozpoczyna się od krótkiego wstępu do tematyki zaprezentowanej w pracy. W kolejnym rozdziale zostały przedstawione aspekty teoretyczne dotyczące Modelu Standardowego ze szczególnym uwzględnieniem procesów dyfrakcyjnych. W drugim rozdziale omówiono akceleratory RHIC i LHC oraz eksperymenty STAR i ATLAS. Rozdziały trzeci i czwarty zawierają szczegółowy opis przeprowadzonych analiz. W rozdziale piątym porównano otrzymane wyniki z danymi nieelastycznymi. Rozprawa kończy się podsumowaniem i wnioskami, które są przedstawione w rozdziale szóstym.

Najważniejsze wyniki analiz, to rozkłady krotności cząstek naładowanych oraz ich gęstości w funkcji pędu poprzecznego i pseudorapidity. Dla danych eksperymentu ATLAS otrzymano dodatkowo rozkłady średniego pędu poprzecznego w funkcji krotności cząstek oraz rozkłady ξ i $-t$ protonu do przodu. Wyniki porównane zostały z modelami zaimplementowanymi w generatorach Monte Carlo: PYTHIA 8, EPOS, HERWIG oraz QGSJET. Większość tych modeli wykazuje zgodność z danymi eksperymentu STAR oraz w sposób niedostateczny opisuje dane eksperymentu ATLAS.

Dla obu zbiorów danych przeprowadzono analizę stosunków krotności zidentyfikowanych cząstek naładowanych (pionów, kaonów, protonów) i ich antycząstek w funkcji pędu poprzecznego. Dla danych eksperymentu STAR w obszarze $0.02 < \xi < 0.05$ zaobserwowano znaczącą asymetrię w stosunku krotności antyproton-proton, wskazującą na transfer liczby barionowej z obszaru do przodu do centralnego obszaru w przestrzeni rapidity.

Treść przedstawiona w rozdziałach trzecim i czwartym jest samodzielną pracą autora, z wyjątkiem niektórych wspólnych części oprogramowania, które są takie same dla każdej analizy w danym eksperymencie.

Contents

Introduction **1**

1 Theoretical Framework **4**
- 1.1 The Standard Model 4
  - 1.1.1 Strong Interactions 4
  - 1.1.2 Soft QCD 7
- 1.2 Diffractive Interactions 12
  - 1.2.1 Kinematic Variables 12
  - 1.2.2 Soft Diffraction 14
  - 1.2.3 Hard Diffraction 16
  - 1.2.4 Diffractive Models 17
- 1.3 Baryon Number Transport 19
- 1.4 Monte Carlo Generators 20

2 Experimental Setup **22**
- 2.1 Accelerator Physics 22
- 2.2 Relativistic Heavy Ion Collider 23
- 2.3 The STAR experiment 24
- 2.4 The Large Hadron Collider 33
- 2.5 The ATLAS Experiment 35

3 STAR Data Analysis **48**
- 3.1 Roman Pot Simulation 48
- 3.2 Monte Carlo Samples 49
- 3.3 Data Sample and Event Selection 50
- 3.4 Fiducial Region of the Measurement 53
- 3.5 Background Contribution 56
- 3.6 Control Plots 66
- 3.7 Corrections 69
- 3.8 Migrations into and out of the Fiducial Region 91
- 3.9 Event Corrections and Unfolding Procedure 95
- 3.10 Systematic Uncertainties 109
- 3.11 Results 115

4 ATLAS Data Analysis 123
4.1 Monte Carlo Samples 123
4.2 Data Sample and Signal Selection 125
4.3 Fiducial Region of the Measurement 131
4.4 Background Contribution 131
4.5 Corrections 145
4.6 Migrations into and out of the Fiducial Region 151
4.7 Event Corrections and Unfolding Procedure 157
4.8 Systematic Uncertainties 165
4.9 Results 172

5 Comparison of Charged-Particle Densities at Central Rapidities 186

6 Summary and Conclusions 189

Acknowledgements 191

Acronyms 195

Bibliography 212

Introduction

Physics, as a natural science, deals with the study of the most basic and universal properties of matter. Its roots date back to ancient times, in which it was known as a philosophy of nature. Later during the Renaissance, physics became the science we know today. Its greatest growth occurred in the 20th century, when Albert Einstein formulated his special and general theories of relativity, which led to a change in our view of time and space. At the same time, the Quantum Mechanics was formulated in order to describe the behaviour of matter at short distances. This laid the foundation for many new branches of modern physics. One of them is particle physics, which is focused on investigating the fundamental interactions and the structure of matter. Three of the four known fundamental interactions are covered by the Standard Model (SM) theory, in which strong interactions are described by the Quantum Chromodynamics (QCD). However, the perturbative calculations of the QCD are limited and can not be used for processes characterised by a small momentum transfer between the interacting partons. These processes must be described by the phenomenological models. On the other hand, there are processes, e.g. diffraction, that extend from perturbative (hard) to non-perturbative (soft) region.

Diffractive scattering has usually been an important part of the physics programs implemented by the experiments investigating both pp and $p\bar{p}$ collisions. The hard diffraction was firstly measured at the SPS accelerator at CERN. However, the most sizeable discovery was made at HERA, where it turned out that a significant fraction of hard events were diffractive. Later, the measurements performed at the Tevatron brought new questions, e.g. about the gap survival probability. Modern experiments at the LHC and RHIC allow the investigations of processes with very high diffractive masses. Some of them (STAR, TOTEM, ATLAS) provide an opportunity to measure the intact forward-scattered protons.

Hadronic final states have been widely studied starting from the very first low-energy hadron-hadron collisions [1–10] to contemporary measurements at very high centre-of-mass energies at the LHC and RHIC [11–25]. However, the available measurements dedicated to diffractive processes are very limited [3, 26–28]. Therefore, there is a need to perform such studies since they allow to validate some phenomenological models and may be used to constrain free parameters of the general purpose Monte Carlo (MC) generators.

In this thesis, measurements of charged-particle distributions with single forward-scattered proton tagging are presented. Moreover, the identified particle/antiparticle (pion, kaon, proton and their antiparticles) ratios as a function of transverse momentum are studied, with special emphasis on the proton-antiproton production asymmetry, which quantifies the phenomena of baryon number transport. The analyses use the data from proton-proton collisions at centre-of-mass energies of $\sqrt{s} = 200$ GeV and $\sqrt{s} = 13$ TeV, collected by the STAR experiment at RHIC and the ATLAS experiment at the LHC, respectively. The forward-scattered protons are tagged in the Roman Pot systems while the charged-particle tracks are reconstructed in the STAR Time Projection Chamber and the ATLAS Inner Detector, respectively. Ionization energy loss of charged particles is used for their identification.

The thesis begins with an introduction to the SM, with special emphasis on diffractive interactions. Chapter 2 contains description of the experimental setups (the LHC and RHIC accelerators, the STAR and the ATLAS experiments). Details of the analyses are presented in Chapters 3 and 4. In Chapter 5 all results are compared with previous measurements if available. The thesis ends with summary and conclusions.

Almost all content presented in Chapters 3 and 4 is the author's original contribution, except of some common parts of the experiments' software which are required to be used in every analysis (e.g. track reconstruction efficiencies and corresponding systematic uncertainties).

The author participated also in the alignment survey of the Roman Pot detectors during RHIC Runs 15 and 17. In this procedure the position of the first strip of each silicon layer was determined with respect to the RHIC coordinate system. Moreover, the author was responsible for implementing the GEANT4 model that describes the RHIC magnets system from the Interaction Point to the Roman Pot stations. In total the author has spent 6 months at BNL and CERN during his PhD studies. The author participated also in the preparation of RHIC Runs 15 and 17 for the STAR experiment, and also took part in shifts during data taking in 2015-2018 and 2020.

Talks given by the author at the international and national conferences:

- Ł. Fulek (on behalf of the STAR Collaboration), *Measurements of particle spectra in diffractive $p+p$ collisions with the STAR detector at RHIC*, International Workshop on Diffraction in High-Energy Physics, Diffraction and Low-x 2018, 26 August - 1 September 2018, Reggio Calabria, Italy, Acta Phys. Polon. Supp. 12 (2019) 999.

- Ł. Fulek (on behalf of the STAR Collaboration), *Measurements of identified particle spectra in diffractive pp collisions with the STAR detector at RHIC*, International Workshop on Diffraction in High-Energy Physics, Diffraction 2016, 2 - 8 September 2016, Acireale, Italy, AIP Conf. Proc. 1819 (2017) 040007.

- Ł. Fulek, *Feasibility studies of the exclusive diffractive bremsstrahlung measurement at RHIC energies*, XXXVI-th IEEE-SPIE Joint Symposium Wilga 2015, 24-31 May 2015, Wilga, Poland, J. Chwastowski *et al.* (Ł. Fulek), Proc. SPIE Int. Soc. Opt. Eng. 9662 (2015) 96622R.

- Ł. Fulek (on behalf of the STAR Collaboration), *Identified particle spectra in single diffractive dissociation process in pp at $\sqrt{s} = 200$ GeV measured with the STAR detector*, XXIII Low-x Meeting, 1-5 September 2015, Sandomierz, Poland.

The results obtained by the author in this thesis are expected to be published by the STAR and ATLAS collaborations in the near future. The author made also significant contributions to the three published papers:

- STAR Collaboration, J. Adam *et al.* (Ł. Fulek), *Measurement of the central exclusive production of charged particle pairs in proton-proton collisions at* $\sqrt{s} = 200$ *GeV with the STAR detector at RHIC*, arXiv:2004.11078 [hep-ex] (2020).
- STAR Collaboration, J. Adam *et al.* (Ł. Fulek), *Results on Total and Elastic Cross Sections in Proton-Proton Collisions at* $\sqrt{s} = 200$ *GeV*, arXiv:2003.12136 [hep-ex] (2020).
- J. Chwastowski *et al.* (Ł. Fulek), *Feasibility Studies of Exclusive Diffractive Bremsstrahlung Measurement at RHIC Energies*, Acta Phys. Polon. B 46 (2015) 10, 1979.

As the member of the STAR Collaboration, I am co-author of 69 publications of the Collaboration.

Chapter 1

Theoretical Framework

1.1 The Standard Model

The SM of particle physics [29–33], proposed for the first time in the seventies of the 20th century, is a theory describing the elementary particles and their interactions. It classifies particles into two groups, distinguished by the spin: fermions with half-integer spin and bosons with integer spin. Fermions are grouped into quark (down d, up u, strange s, charm c, bottom b and top t) and lepton (electron e, muon μ, tau τ, electron neutrino ν_e, muon neutrino ν_μ and tau neutrino ν_τ) families. Each fermion has its own antiparticle with the same mass but opposite electric charge. The first two quarks (u and d) and leptons (e and ν_e) belong to so-called the first generation and form most of the visible matter of the Universe. Quarks and leptons from subsequent generations are heavier, unstable and decay into lighter particles. The existence of only three generations of quarks and leptons was confirmed by the experiments at the Large Electron Positron Collider (LEP) [34].

The SM is formulated as a Quantum Field Theory (QFT), which provides a description of the three known fundamental interactions: the electromagnetic, weak, and strong interactions [35–37]. The gravity is not incorporated into the QFT of the SM. The interactions in the SM are mediated by the exchange of the spin-1 bosons: photon (γ) in electromagnetic, $W^\pm$ and Z in weak, eight gluons (g) in strong interactions. The generation of mass of the $W^\pm$, Z bosons and other fermions is explained by the existence of the scalar Higgs field [38, 39], whose quantum excitation produces the spin-0 Higgs boson (H). The summary of all SM particles with their masses, charges and spins is shown in Fig. 1.1.

Full description of the SM can be found in e.g. [30, 40]. The analyses presented in this thesis involve mainly strong interactions and only this type of interactions is discussed below in more detail.

1.1.1 Strong Interactions

The QCD [32, 40–45] is a QFT, which describes the strong interactions between quarks and gluons. The theory is based on the non-Abelian $\mathrm{SU}(3)_C$ symmetry with an additional

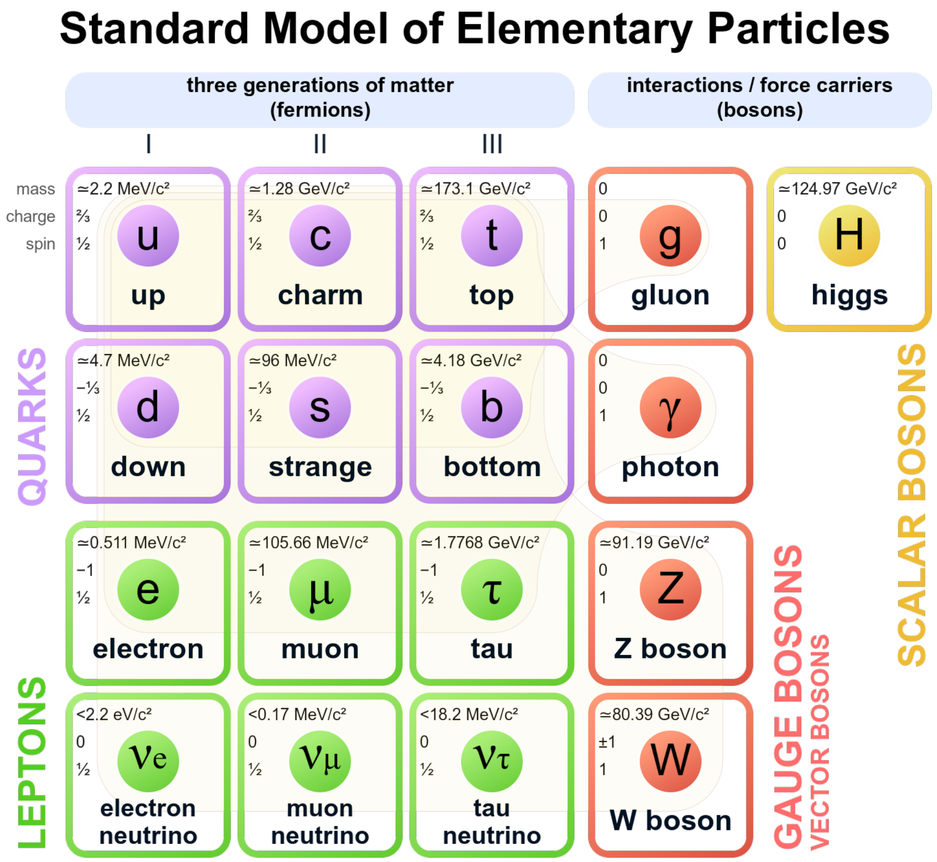

Figure 1.1: Particles of the SM are classified as matter particles and force carriers. Their main properties including mass, electric charge and spin are displayed in the figure.

quantum number known as colour charge, which allows the hadrons to be formed even by the same-spin quarks without violating the Pauli exclusion principle. The colour quantum number can take one of three values: red, green and blue with corresponding anticolours. Quarks exist in one of three colour states, while gluons carry the superposition of a colour and an anticolours. Antiquarks carry anticolours. The $\mathrm{SU}(3)_C$ is an unbroken symmetry, therefore, gluons are massless particles. In addition, gluons can interact with themselves (the so-called self-coupling), unlike the photon, which leads to key differences between strong and electromagnetic interactions.

The strong interaction plays an important role in the formation of hadrons, which consist of bound states of quarks and antiquarks. All hadrons have a net neutral colour charge and are classified into two groups, which are distinguished based on the number of valence quarks/antiquarks they contain:

- Baryons, which consist of three valence quarks, e.g. proton (uud), neutron (udd).
- Mesons, which are composed of a valence quark-antiquark pair, e.g. pion π^+ ($u\bar{d}$).

The strength of the interaction is regulated by a strong coupling parameter, g_s, which is related to the strong coupling constant, α_s, by $g_s^2 = 4\pi\alpha_s$ [42, 46]. α_s dependence on the scale Q^2 is given by (Fig. 1.2):

$$\alpha_s^2 \approx \frac{1}{\beta_0 \ln\left(Q^2/\Lambda^2_{\mathrm{QCD}}\right)} \tag{1.1}$$

where Λ^2_{QCD} is the QCD scale parameter and β_0 is a constant [47, 48]. For large $Q^2 \gg \Lambda^2_{\mathrm{QCD}}$, the strong coupling constant is small, $\alpha_s \to 0$, thus, quarks interact weekly and the perturbative calculations can be applied. This observation is known as the asymptotic freedom.

The other important phenomenon of the QCD is the colour confinement, which can be explained by the following parametrized form of the quark-antiquark potential [49]:

$$V = -\frac{4}{3}\frac{\alpha_s}{r} + \kappa r \tag{1.2}$$

where r is the distance between a quark and antiquark, κ is a constant approximately equal to 1 GeV/fm. At large distances, due to infinite potential, quarks are confined inside colour-neutral hadrons. Therefore, it is impossible to observe free quarks.

Parton Distribution Functions

In the Quark Parton Model [50], the proton consists of a number of point-like particles, called partons, which are associated with quarks and gluons in the SM. The structure of the proton at high Q^2 is complicated, i.e. in addition to three valence quarks, it is

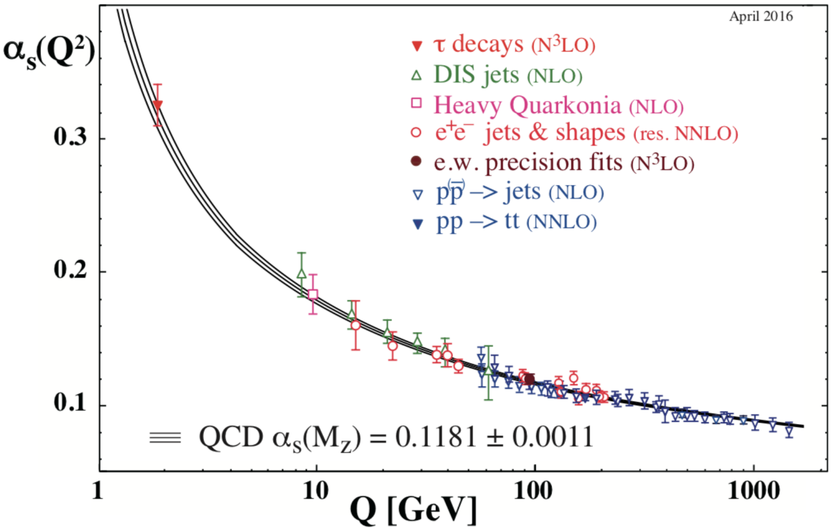

Figure 1.2: Summary of measurements of the strong coupling constant as a function of the energy scale Q. Figure taken from [42].

also composed of sea of virtual quark-antiquark pairs and gluons, what was observed in many experiments [51–53]. Therefore, the composition of the proton is parametrized by the so-called Parton Distribution Functions (PDFs), $f_p\left(x, Q^2\right)$, which give the probability of finding a parton in the proton carrying the proton momentum fraction x at energy scale Q of the hard interaction. Most of the PDFs were obtained from dedicated measurements in lepton-hadron scattering [54]. The DGLAP (Dokshitzer, Gribov, Lipatov, Altarelli, Parisi) equations [55–57] are used to describe the evolution of the parton density with Q^2.

Cross sections for hard hadron (proton) interactions, through the factorization theorem [58], can be written as a convolution of the PDFs and the cross section for hard parton-parton scattering:

$$d\sigma = f_p\left(x_1, Q^2\right) f_p\left(x_2, Q^2\right) d\sigma_{\text{hard}}\left(x_1, x_2, Q^2\right) \tag{1.3}$$

where x_1, x_2 are the proton momentum fractions carried by the interacting partons.

1.1.2 Soft QCD

The perturbative calculations are limited to the so-called hard processes, i.e. those with large Q^2 (small α_s). But the majority of interactions occurring during the proton-proton collisions are soft processes, which take place at small energy scales, i.e. $Q^2 < 1\ \text{GeV}^2/\text{c}^2$. They must be described by the phenomenological models. The total cross section for proton-proton interaction can be split into elastic and inelastic. The inelastic processes can be further divided into diffractive and Non-Diffractive (ND) [59] ones, thus the total cross section can be written as:

$$\sigma_{\text{tot}} = \sigma_{\text{elastic}} + \sigma_{\text{inelastic}} = \sigma_{\text{elastic}} + \sigma_{\text{diffractive}} + \sigma_{\text{non-diffractive}} \tag{1.4}$$

The contribution of hard parton-parton interactions to the σ_{tot} is a few orders of magnitude smaller than of soft processes [60].

Different physics processes in particle collisions are simulated using MC generators, which play a significant role in both experimental and theoretical particle physics. Usually, the algorithms for hard processes are based on the perturbative QCD, while the non-perturbative regime is described by phenomenological calculations. It is essential to understand the impact of soft processes, e.g. the hadronization process, on the measurements of hard scattering. In addition, models implemented in the MC generators provide a description of the Multiple Parton Interactions (MPI), which are a subject of many experimental and theoretical studies. Hence, there is a special need to constrain the free parameters of the phenomenological models, which are used to describe above phenomena.

Hadronization

The hadronization process combines free partons, from a parton cascade, into colour neutral hadrons. Since the energy scale of such process is smaller than $1\ \text{GeV}^2/\text{c}^2$, the hadronization can not be treated perturbatively.

The string model [42, 61] for hadron interactions assumes that the strong interaction field between two quarks can be approximated by a colour flux tube, so called a string. The quark-antiquark potential in this model is given by:

$$V\left(r\right) = \kappa r \tag{1.5}$$

where r is a distance between quark and antiquark, $\kappa \approx 1$ GeV/fm is the string tension. There may be an additional Coulomb term (as in Eq. 1.2), which is negligible for large distances. Hence, it is not included in the Lund String Model [42, 61, 62], which is the mostly used string hadronization model. The quark and antiquark are in back-to-back configuration, therefore when they move apart from each other, the potential energy increases. Then, the string breaks up and a pair of quark-antiquark is produced. The two new strings, consisting of initial and new quarks, are formed. The schema of such mechanism is shown in Fig. 1.3. The process is repeated until the energy of a quark-antiquark pair is not high enough to break the string. As a consequence, all the partons are confined inside the bound mesons. In this model, the production rate for quarks is given by [63]:

$$u : d : s : c \approx 1 : 1 : 0.3 : 10^{-11} \tag{1.6}$$

which implies that most of the heavy quarks are not produced in the hadronization process but during the hard interaction. In addition, gluons are represented as transverse kinks on the originally one-dimensional strings [42].

In the above procedure, only mesons are produced. There are two approaches in order to create baryons: the diquark model [64] and the popcorn model [65]. In the former, a pair of quark-antiquark is replaced by a pair of diquark-antidiquark. The hadronization procedure follows the one as for quark-antiquark pairs, therefore, systems of three quarks, i.e. baryons, are created. In the most common, the popcorn model, there are virtual colour fluctuations inside the strings. The quark-antiquark string can be broken up by production of quark-antiquark pair. However, it is also allowed to produce a pair of diquark-antidiquark, from which it is possible to create a baryon-antibaryon pair.

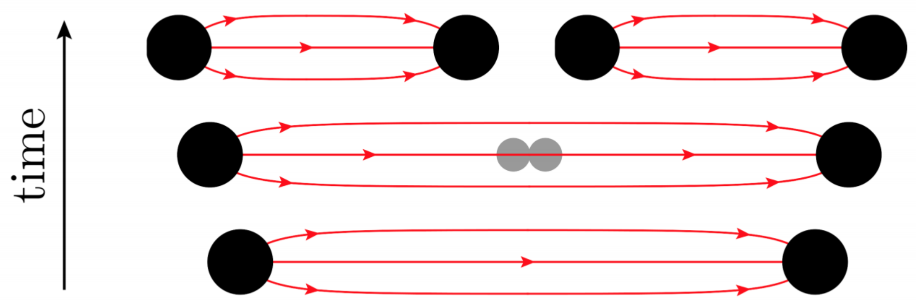

Figure 1.3: Schema of quark-antiquark creation in the string hadronization model. Figure taken from [42].

The Cluster Fragmentation Model [42, 63, 66] is an alternative description of the hadronization. This model is based on the idea of the preconfinement, in which the adjacent partons are grouped into colour-singlet clusters in the QCD parton branching process. Most clusters may be treated as superpositions of resonances. Hence, they follow the isotropic two-body decay into hadrons, what occurs in the final step of the process.

Multiple Parton Interactions

Since protons are complex objects consisting of partons, there is a probability of MPI within single proton-proton collision [67, 68]. In the MPI either one parton from one proton interacts with few different partons from the other proton or, what is more probable, there are separate $2 \rightarrow 2$ processes that are dominated by gluon exchange [69, 70]. Probability for such interactions increases with the centre-of-mass energy since more partons can interact at higher energy scales. In most of the models, there is an energy-dependent separation between hard and soft interactions. The former are calculated using perturbative QCD, while the latter are described by the phenomenological models. Moreover, the initial and final state partons can radiate gluons, which may contribute to the MPI. Theoretical models splits these parton showers into space-like Initial State Radiation (ISR) and time-like Final State Radiation (FSR). An additional mechanism, introduced in the Lund String Model, is the Colour Reconnection (CR) [71], in which the strings between final-state partons can be rearranged in order to shorten their lengths. All these processes affect the final-state particle multiplicity [69]. The CR mechanism is illustrated in in Fig. 1.4.

The MPI play an important role in the phenomenological description of the Underlying Events (UE) [72], in which soft or hard background interactions occur together with a hard process of interest.

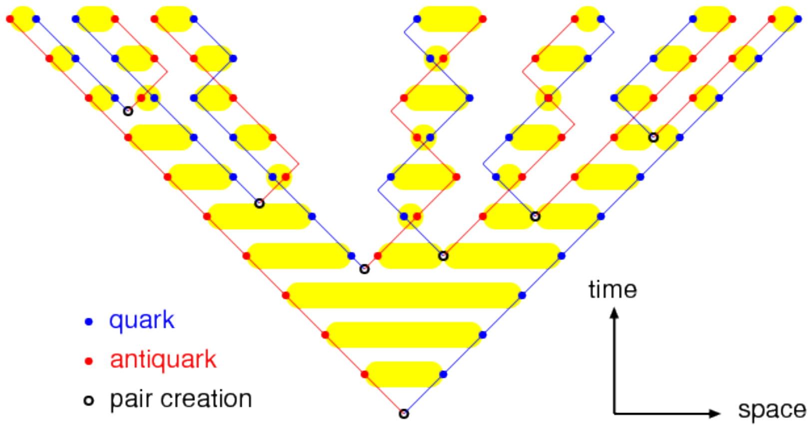

Figure 1.4: Schema of the CR mechanism in the Lund String Model. Yellow areas indicate the strings. Figure taken from [73].

Hadronic Final States

The properties of soft QCD can be studied by measuring the hadronic final states emerging from *pp* collisions. In order to describe their properties, phenomenological models have been developed and implemented in MC generators. However, free parameters of these models have to be constrained by the data. One way to perform such studies is to measure the charged-particle multiplicity, transverse momentum and pseudorapidity distributions.

The rapidity, which is additive under Lorentz boosts, is defined as:

$$y = \frac{1}{2} \ln \frac{E + p_{\mathrm{z}}c}{E - p_{\mathrm{z}}c} \tag{1.7}$$

where E is particle energy, and p_{z} is the component of its momentum along the beam axis (for *pp* collisions, the beam axis is the same as the z-axis defined by each experiment). In the limit, in which the mass of the particle is negligible in comparison to its momentum, $p \gg m$, rapidity can be approximated by pseudorapidity:

$$\eta = -\ln \left[\tan \left(\frac{\theta}{2} \right) \right] \tag{1.8}$$

where θ is the polar angle of the particle. In the case of events with tagged forward-scattered proton, we define a new observable $\bar{\eta}$, which is the pseudorapidity with the polar angle measured with respect to the beam axis oriented in the direction of forward-scattered proton, thus, $\bar{\eta} = \eta$ for events in which forward proton travels in the positive z-direction and $\bar{\eta} = -\eta$ for events in which forward proton travels in the negative z-direction. The transverse momentum of a particle is defined in the usual way as:

$$p_{\mathrm{T}} = p \sin \theta \tag{1.9}$$

The charged particle spectra are usually studied in Minimum Bias (MB) events[1]. In this thesis we concentrate on diffractive-like events and the following distributions are measured:

$$\frac{1}{N_{\mathrm{ev}}} \frac{dN_{\mathrm{ev}}}{dn_{\mathrm{ch}}}, \qquad \frac{1}{N_{\mathrm{ev}}} \frac{dN}{d\bar{\eta}}, \qquad \frac{1}{(2\pi p_T N_{\mathrm{ev}})} \frac{d^2N}{d\eta dp_{\mathrm{T}}}$$

where η ($\bar{\eta}$) is the particle's pseudorapidity, p_{T} its transverse momentum, n_{ch} is the number of primary charged particles in an event, N_{ev} is the total number of events and N is the total number of charged particles. In addition, both STAR and ATLAS analyses are completed with the average values of above observables. The mean transverse momentum as a function of charged-particle multiplicity, $\langle p_{\mathrm{T}} \rangle$ vs. n_{ch}, is measured using only data collected by the ATLAS experiment since the analysis of STAR data is characterized by low charged-particle multiplicities, and does not provide the possibility to separate events in different multiplicity categories.

---

[1] MB events are inelastic events selected with as little bias as possible.

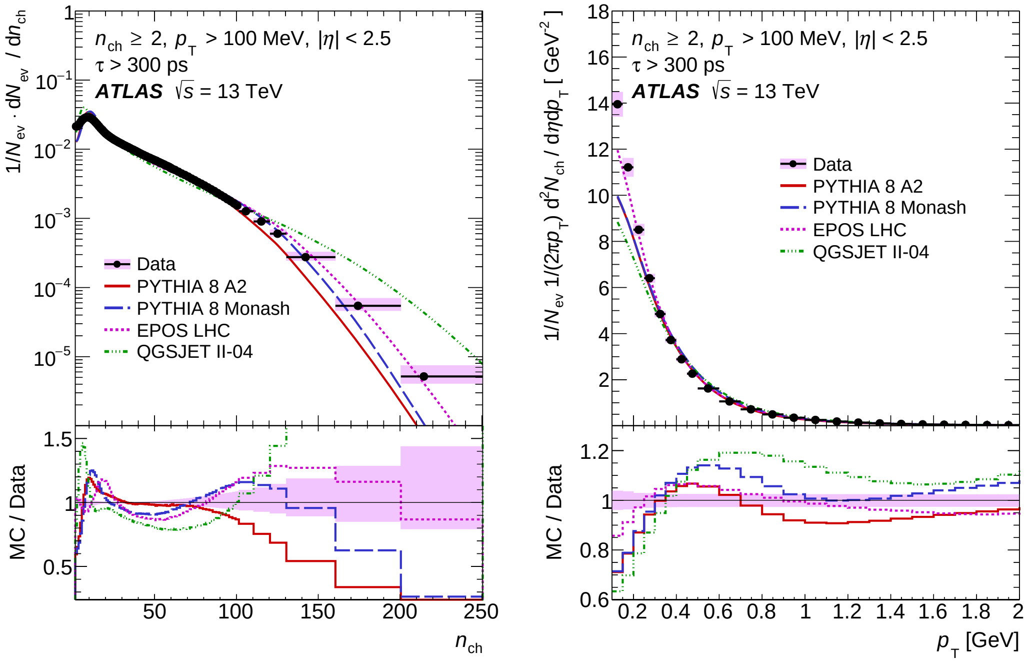

Figure 1.5: (left) Primary charged-particle multiplicity and (right) primary charged-particle multiplicity as a function of transverse momentum measured by the ATLAS experiment in pp collisions. Figure taken from [22].

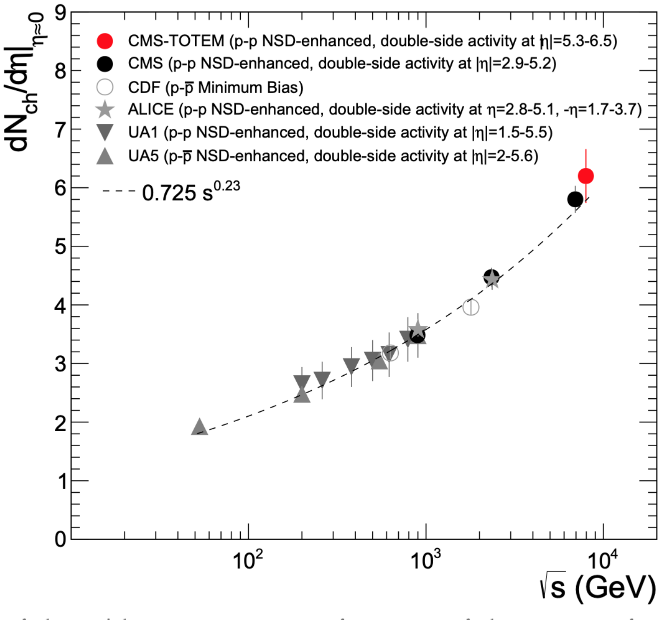

Figure 1.6: Distribution of $dN_{\mathrm{ch}}/d\eta$ at $\eta \approx 0$ as a function of the centre-of-mass energy in inelastic pp and $p\bar{p}$ collisions. Figure taken from [28].

Figure 1.5 shows an example of above distributions measured by the ATLAS experiment in MB events at the centre-of-mass energy of 13 TeV [22]. The charged-particle multiplicities are not well described by MC models. Therefore, there is a need to perform further tunning of free parameters of the models. In addition, it is interesting to study the centre-of-mass energy dependence of the charged-particle multiplicity at $\eta \approx 0$ (Fig 1.6) and identified antiparticle-to-particle ratios. The precise modelling of both can also help in a better understanding of the collision dynamics. This thesis provides results from the processes with forward proton tagging for two significantly different centre-of-mass energies, what makes them very unique.

1.2 Diffractive Interactions

Diffractive interactions are those in which only vacuum quantum numbers are exchanged between the interacting particles [74, 75]. Experimentally, diffraction is identified as a process with a large, non-exponentially suppressed, rapidity gap [76]. However, these two definitions are not equivalent. Diffractive interactions can be divided into four groups (shown schematically in Fig. 1.7):

- elastic scattering: $a + b \to a' + b'$,
- Single Diffractive Dissociation (or Single Diffraction (SD)): $a + b \to a' + X$, where particle b dissociates into state X,
- Double Diffractive Dissociation (or Double Diffraction (DD)): $a + b \to X_a + X_b$, where both particles a and b dissociate into states X_a and X_b, respectively,
- Central Diffraction (CD): $a+b \to a'+X+b'$, where additional state X with a quantum numbers of vacuum is produced. One can consider additional CD processes where one or both protons diffractivelly dissociate to state X_a and/or X_b.

Diffractive processes may be divided into two distinct classes: soft and hard diffraction. In the former, the energy scale is much lower than the typical hadronic scale (smaller than 1 GeV^2/c^2) and can not be treated perturbatively, whereas the latter, which involves much higher scales, can be described by the perturbative QCD.

1.2.1 Kinematic Variables

Kinematics of a two-body process, $1 + 2 \to 3 + 4$, can be described using the Mandelstam variables (Fig. 1.8), which are Lorentz-invariant quantities defined as:

$$\begin{aligned} s &= (p_1 + p_2)^2 = (p_3 + p_4)^2 \\ t &= (p_1 - p_3)^2 = (p_2 - p_4)^2 \\ u &= (p_1 - p_4)^2 = (p_2 - p_3)^2 \end{aligned} \tag{1.10}$$

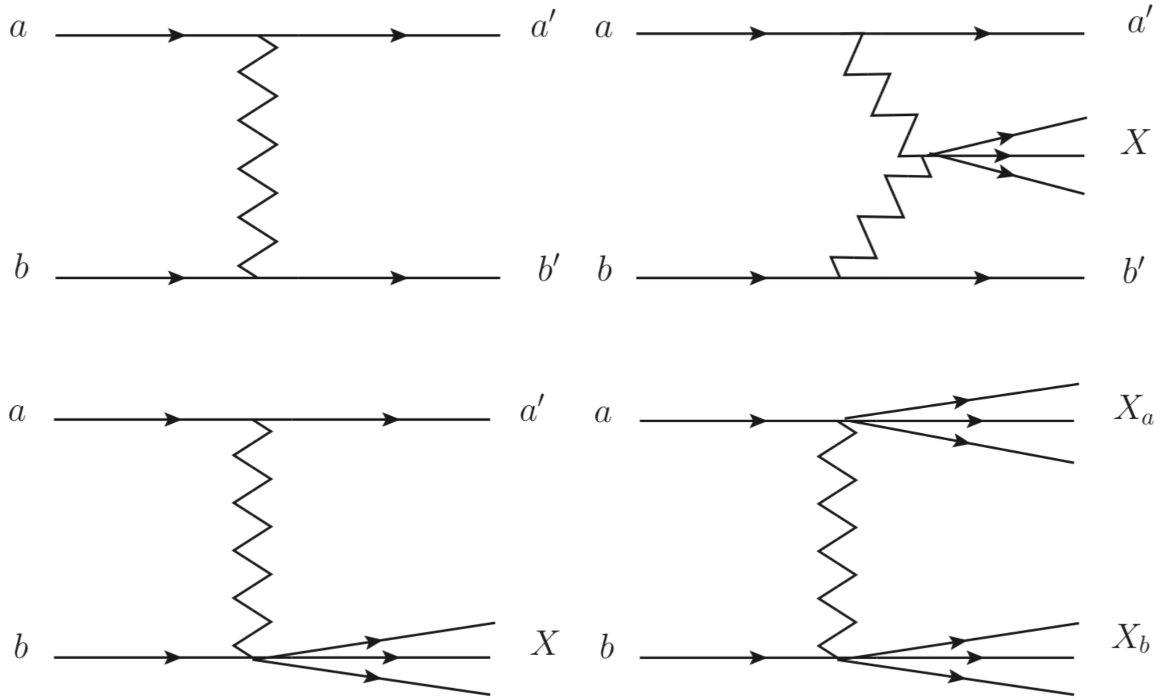

Figure 1.7: The Feynman diagrams of (top left) elastic, (top right) CD, (bottom left) SD (and analogous diagram in which particle a dissociates and b stays intact) and (bottom right) DD scattering.

where p_1 and p_2 are the four-momenta of the incoming particles, p_3 and p_4 are the four-momenta of the outgoing particles. The Mandelstam variables are not all independent and the following useful relation between them holds:

$$s + t + u = m_1^2 + m_2^2 + m_3^2 + m_4^2 \tag{1.11}$$

where m_i ($i = 1, 2, 3, 4$) are the masses of respective particles.

A particular process of interest in this thesis is the SD, $1 + 2 \to 3 + X$, which is usually described by three independent variables: s, t and the invariant mass of the system X:

$$M_X^2 = (p_1 + p_2 - p_3)^2 \tag{1.12}$$

In addition, the SD events are very often characterized by the ξ variable, which denotes the fractional energy loss of the diffractivelly scattered proton:

$$\xi = \frac{E_1 - E_3}{E_1} \simeq \frac{M_X^2}{s} \tag{1.13}$$

Then, the rapidity gap between the particle 3 and the X system is equal to:

$$\Delta y \simeq \ln \frac{s}{M_X^2} \simeq \ln \frac{1}{\xi} \tag{1.14}$$

A detailed derivation of above formulas can be found in e.g. [75].

1.2.2 Soft Diffraction

The Regge phenomenological theory [77–79], based on the scattering matrix (S-matrix) approach, was developed in the 1960s as an alternative to QFT for the description of the strong interactions. The two-body interaction, $1+2 \to 3+4$, is described by the S-matrix, which transforms the initial state to the final state:

$$\begin{aligned} S(s,t) =&\ \mathbb{I} + iT(s,t) \Longrightarrow \\ S_{if} =&\ \langle f|S|i\rangle = \delta_{if} + iT_{if} = \delta_{if} + i(2\pi)^4 \delta^4(p_f - p_i)\, A(i \to f) \end{aligned} \tag{1.15}$$

where $\mathbb{I}$ is the unit matrix, T is the transition matrix, s and t are Mandelstam variables, $|i\rangle$ and $|f\rangle$ are the initial and final states, and p_i and p_f their four-momenta, respectively, $A(i \to f)$ is the scattering amplitude. The assumptions about the S-matrix in the Regge theory are: relativistic invariance, unitarity, analyticity and crossing symmetry. In general, the Regge theory is based on expansion of the scattering amplitude, $A(s,t)$, into its partial waves. Due to the diveregency of partial-wave functions in the high-energy limit, $s \to \infty$, the angular momentum l is allowed to take any values from the complex plane. The singularities of such partial-waves amplitudes, $A(l,t)$, are poles (called Regge poles), and the amplitude in the high-energy limit, $s \to \infty$, is given by:

$$A(s,t) \propto -\beta(t) \frac{s^{\alpha(t)}}{\sin \pi\alpha(t)} \tag{1.16}$$

where $\alpha(t)$ is the location of the leading pole of $A(l,t)$ (the one with the largest real component) and is called a Regge trajectory, $\beta(t)$ is its residue. The partial wave amplitude near the Regge pole is then expressed as:

$$A(l,t) \propto \frac{1}{l - \alpha(t)} \tag{1.17}$$

where $\alpha(t)$ can be further expanded into the Taylor series and approximated as:

$$\alpha(t) = \alpha(0) + \alpha' t \tag{1.18}$$

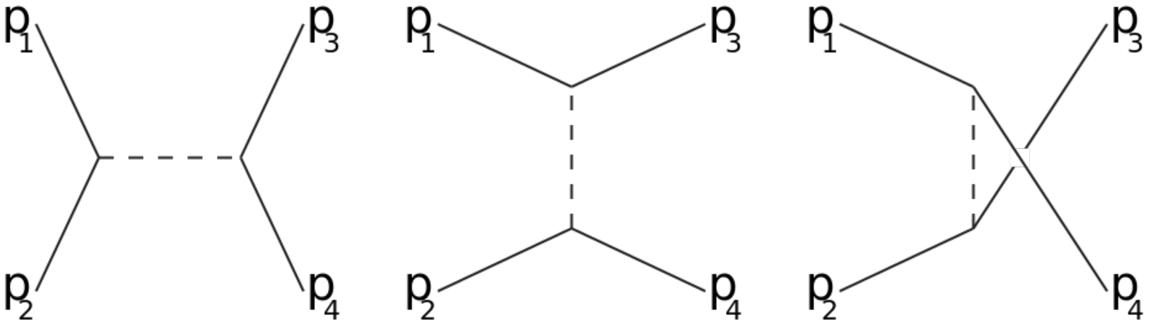

Figure 1.8: Feynman diagrams for the Mandelstam variables: s (left), t (middle) and u (right).

The Regge trajectories correspond to a family of particles, i.e. resonances, with all the same quantum numbers but the spin [80]. Figure 1.9 shows the so called Chew-Frautschi plot [81], which presents an example of Regge trajectories for four families of particles. All of these resonances can be used as an exchange objects, which provide an input to the total cross section. The contribution of one Regge pole is expressed via optical theorem as:

$$\sigma_{\mathrm{tot}} \underset{s\to\infty}{\approx} \frac{1}{s}\mathrm{Im}A\left(s,t=0\right) \underset{s\to\infty}{\sim} s^{\alpha(0)-1} \tag{1.19}$$

The total cross section for pp and $p\bar{p}$ collisions is reproduced well with $\alpha\left(0\right)=0.5$ in the low energy regime, i.e. $\sqrt{s} \lesssim 10$ GeV. At higher energies, the cross section starts to increase as shown in Fig. 1.10. Due to that, an another trajectory with the intercept $\alpha\left(0\right) \geq 1$, called the Pomeron, was introduced [82]. The Pomeron is a colour singlet with quantum numbers of the vacuum and its trajectory is often written as:

$$\alpha_{\mathbb{P}}\left(t\right) = \alpha_{\mathbb{P}}\left(0\right) + \alpha'_{\mathbb{P}}t = 1 + \epsilon + \alpha'_{\mathbb{P}}t \tag{1.20}$$

where ϵ describes the deviation from unity of the Pomeron intercept, while the values of $\alpha_{\mathbb{P}}\left(0\right) = 1.08$ and $\alpha'_{\mathbb{P}} = 0.25$ GeV^{-2} were obtained experimentally [83, 84]. The value of the Pomeron intercept does not satisfy the Froissart-Martin bound [85, 86], which determines the limit on the cross section rise at high energies. However, this bound is considered to be important at energies beyond those that are accessible at current colliders. In addition, the existence of the Pomeron allows to satisfy Pomeranchuk's theorem [87], in which

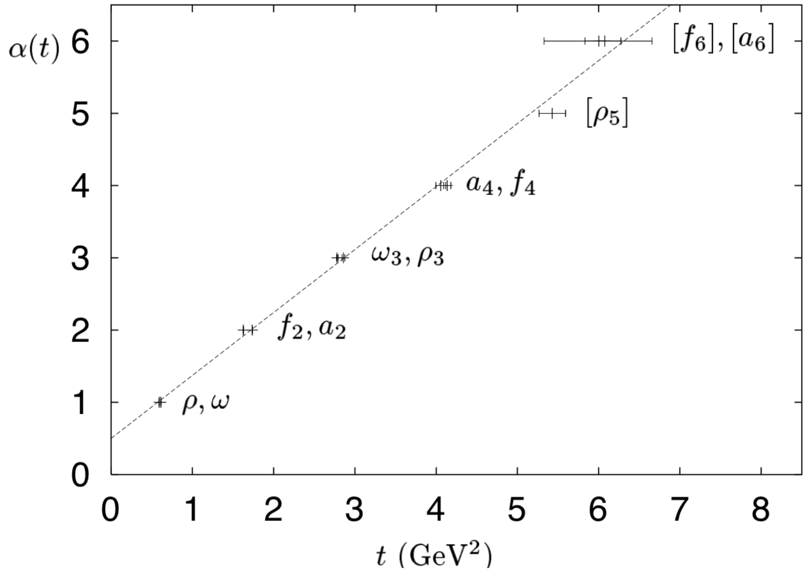

Figure 1.9: The Chew-Frautschi plot of the particles spin as a function of their squared masses for four families of particles. The straight line is $\alpha\left(t\right) = 0.5 + 0.9t$. Figure taken from [74].

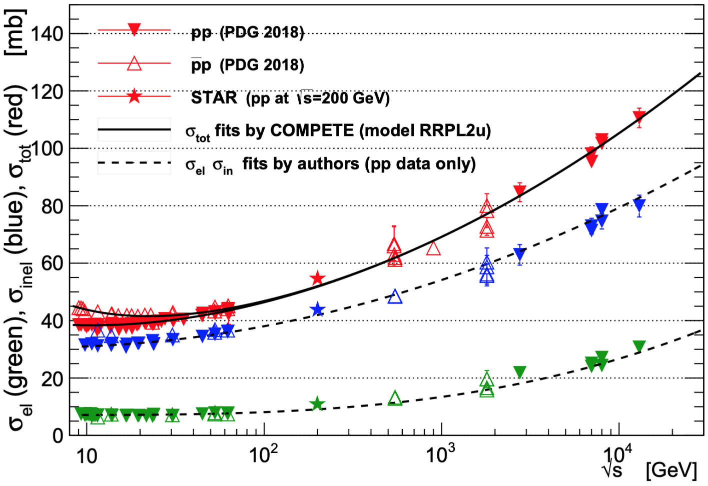

Figure 1.10: Total, elastic and inelastic cross section for pp and $p\bar{p}$ collisions as a function of $\sqrt{s}$. Figure taken from [88].

the nucleon and anti-nucleon total cross sections are equal at high energies. Moreover, the total cross section is the sum of the Pomeron and Regge trajectory contribution:

$$\sigma_{\text{tot}} = X s^{\alpha_{\mathbb{P}}(0)-1} + Y s^{\alpha_{\mathbb{R}}(0)-1} \tag{1.21}$$

where the terms with $\alpha_{\mathbb{P}}$ and $\alpha_{\mathbb{R}}$ specify the Pomeron and Reggeon trajectory contribution, respectively [83].

In the Mueller's generalization of the optical theorem [89, 90], the SD interaction is expressed as an elastic three-body interaction $ab\bar{a}' \to ab\bar{a}'$. This allows to determine the SD differential cross section in the so called triple-Regge limit, $s \gg M_X^2 \gg |t|$ [75, 91–93]:

$$\frac{d^2\sigma^{\text{SD}}}{dM_X^2\,dt} \propto s^{2\alpha_{\mathbb{P}}(t)-2} \left(\frac{1}{M_X^2}\right)^{2\alpha_{\mathbb{P}}(t)-1} \left(M_X^2\right)^{\alpha_{\mathbb{P}}(0)-1} \tag{1.22}$$

where the $(1/M_X^2)^{2\alpha_{\mathbb{P}}(t)-1}$ component is the Pomeron flux factor, which determines the probability that a Pomeron is emitted from a proton, while $(M_X^2)^{\alpha_{\mathbb{P}}(0)-1}$ component is the cross section for the interaction $p\mathbb{P} \to X$. The ratio of the SD to the total cross section is predicted by the Regge theory to be increasing with s, $\sigma^{\text{SD}}/\sigma^{\text{total}} \sim s^{\epsilon}$,what is in contrast with the data, in which this ratio is decreasing with energy [75]. Hence, the probability that the spectator parts of the colliding protons do not produce particles in the rapidity gap (called the rapidity gap survival probability) was introduced to properly describe the data.

1.2.3 Hard Diffraction

In the hard diffraction processes, the Pomeron can be interpreted in terms of a particle having partonic structure. This was first proposed by Ingelman and Schlein for the description of the diffractive jet production [94]. As a consequence, hard diffractive interactions can be described by Diffractive Parton Distribution Functions (DPDFs), that may be further decomposed into Pomeron flux component $\phi_{\mathbb{P}/p}(\xi,t)$, and the term $f_{\mathbb{P}}(x/\xi,Q^2)$, which describes the partonic structure of the Pomeron [95]:

$$f_d\left(x,Q^2,\xi,t\right)=\phi_{\mathbb{P}/p}(\xi,t)\,f_{\mathbb{P}}\left(x/\xi,Q^2\right) \tag{1.23}$$

where Q^2 is the scale of the hard process and x denotes the proton momentum fraction carried by the interacting parton. The DPDFs were successfully used to interpret data from the UA8 experiment at SPS [96, 97], while the Deep Inelastic Scattering (DIS) experiments at HERA determined them with high precision [98, 99]. However, to properly describe the data [98], additional contributions are considered by adding the Reggeon term:

$$f_d\left(x,Q^2,\xi,t\right)=\phi_{\mathbb{P}/p}(\xi,t)\,f_{\mathbb{P}}\left(x/\xi,Q^2\right)+\phi_{\mathbb{R}/p}(\xi,t)\,f_{\mathbb{R}}\left(x/\xi,Q^2\right) \tag{1.24}$$

Then, the cross section for hard proton-proton SD interaction is expressed in terms of the DPDFs, ND PDFs and cross section for hard parton-parton scattering as:

$$d\sigma=S^2\phi_{\mathbb{P}/p}(\xi,t)\,f_{\mathbb{P}}\left(x_1/\xi,Q^2\right)f_p\left(x_2,Q^2\right)d\sigma_{\text{hard}}\left(x_1,x_2,Q^2\right) \tag{1.25}$$

where x_1, x_2 are the proton momentum fractions carried by the interacting partons, S^2 is the rapidity gap survival probability. The Pomeron in hard diffraction has partonic structure and is represented by two gluons or a gluonic ladder in higher order approximation.

1.2.4 Diffractive Models

There are many models available, which are widely used in order to describe diffractive interactions. Most common parametrizations of the diffractive cross section and the Pomeron flux are described below. In all of these models, the inelastic cross section is obtained as:

$$\sigma_{\text{inelastic}}(s)=\sigma_{\text{tot}}(s)-\sigma_{\text{elastic}}(s) \tag{1.26}$$

while the ND cross section is then given by:

$$\sigma_{\text{ND}}(s)=\sigma_{\text{inelastic}}(s)-\left[\sigma_{\text{SD}}(s)+\sigma_{\text{DD}}(s)+\sigma_{\text{CD}}(s)\right] \tag{1.27}$$

The SaS and DL models

In the Schuler and Sjöstrand (SaS) model [100], the total cross section follows the Donnachie and Landshoff (DL) data-driven parametrization with Pomeron and Reggeon contributions [75, 83]:

$$\sigma_{\text{tot}}(s)=21.70s^{0.808}+56.08s^{-0.4525} \tag{1.28}$$

Then, the elastic cross section at small t is approximated by an exponential decrease and is related to the total cross section through the optical theorem.

In the low-mass diffraction, a valence quark or a gluon is kicked out from the diffractively excited proton and a string is produced, which is hadronized using the string model (Sec. 1.1.2). In the high-energy regime, the Pomeron has partonic structure. The SaS model is based on the Pomeron trajectory given by $\alpha_{\mathbb{P}}(t) = 1 + (0.25\ \text{GeV}^{-2})t$ and the following Pomeron flux parametrization [101]:

$$\phi_{\mathbb{P}/p}(\xi, t) = \beta^2(0)\frac{1}{\xi}\exp\left[2t\left(2.3 + 0.25\ln\left(\frac{1}{\xi}\right)\right)\right] \tag{1.29}$$

where $\beta(0)$ is the coupling of the Pomeron to the proton.

The diffractive cross section for the SD is scaled by the factor, which is introduced in order to describe the full phase space, i.e. suppress the cross sections in the high-mass region and enhance them in the low-mass region [70]. This factor is defined as:

$$F_{\text{SD}} = \left(1 - \frac{M_X^2}{s}\right)\left(1 + \frac{c_{\text{res}}M_{\text{res}}^2}{M_{\text{res}}^2 + M_X^2}\right) \tag{1.30}$$

where $c_{\text{res}} = 2$ and $M_{\text{res}} = 2\ \text{GeV/c}^2$ were obtained from a fit to pp and $\bar{p}p$ data [70]. The model also contains DD and CD contributions to the total cross section [101]. However, the latter was not originally included in the model and is parametrized using a simple scaling assumption.

The DL model is based on the Pomeron trajectory with $\epsilon = 0.085$ and $\alpha'_{\mathbb{P}} = 0.25\ \text{GeV}^{-2}$ [102, 103]. The Pomeron flux parametrization follows the ξ dependence predicted by the triple Pomeron cross-section and is assumed:

$$\phi_{\mathbb{P}/p} = \frac{9\beta^2(0)}{4\pi^2}\xi^{1-2\alpha_{\mathbb{P}}(t)}F_1^2(t) \tag{1.31}$$

where the proton form factor F_1 is determined experimentally [104]:

The MBR model

The Minimum Bias Rockefeller (MBR) model [105] was developed in order to describe the measurements performed by the CDF experiment [106, 107]. In this model, the total cross section is parametrized as:

$$\sigma_{\text{tot}} = \begin{cases} 16.79s^{0.104} + 60.81s^{-0.32} - 31.68s^{-0.54} & \text{for } \sqrt{s} < 1.8\ \text{TeV} \\ \sigma_{\text{tot}}^{\text{CDF}} + \dfrac{\pi}{s_0}\left[\left(\ln\dfrac{s}{s_{\text{F}}}\right)^2 - \left(\ln\dfrac{s_{\text{CDF}}}{s_{\text{F}}}\right)^2\right] & \text{for } \sqrt{s} \geq 1.8\ \text{TeV} \end{cases} \tag{1.32}$$

where $\sigma_{\text{tot}}^{\text{CDF}}$ is the measured total cross section by the CDF experiment at the centre-of-mass energy $\sqrt{s_{\text{CDF}}} = 1.8$ TeV, $s_0 = 3.7 \pm 1.5\ \text{GeV}^2$, $\sqrt{s_{\text{F}}} = 22$ GeV. For $\sqrt{s} < 1.8$ TeV the parametrization of the total cross section is obtained from a global fit to the lower-energy measurements [108], while for $\sqrt{s} \geq 1.8$ TeV, an unitarized model based on a saturated Froissart bound is used [109].

The elastic cross section is calculated by scaling the total cross section by the ratio $(\sigma'_{\mathrm{elastic}}/\sigma'_{\mathrm{total}})_{\mathrm{fit}}$, which is obtained from the fit to the lower-energy data. The diffractive contributions (SD, DD and CD) to the total cross section are parametrized using the renormalized model described in [107]. The Pomeron trajectory is given by $\alpha_{\mathbb{P}}(t) = 1.104 + 0.25\left(\mathrm{GeV}^{-2}\right) \cdot t$. In addition, the diffractive cross section for small rapidity gaps (large diffractive masses) is suppressed, similarly to the SaS model, but a different scaling factor is used:

$$S = \frac{1}{2}\left[1 + \mathrm{erf}\left(\frac{\Delta y - \Delta y_S}{\sigma_S}\right)\right] \tag{1.33}$$

where $\Delta y_S = 2$ and $\sigma_S = 0.5$.

In the MBR model, the Pomeron flux for high-mass diffraction is normalized to unity and is parametrized as:

$$\phi_{\mathbb{P}/p}(\xi, t) = \frac{1}{N(s)} \frac{\beta^2(0)}{16\pi} F_1^2(t)\, \xi^{1-2\alpha_{\mathbb{P}}(t)} \tag{1.34}$$

where F_1 is the proton form factor, $\beta(0)$ denotes the coupling of the Pomeron to the proton, $N(s)$ is the factor used in the renormalization procedure.

1.3 Baryon Number Transport

In the SM, the baryon number is a conserved quantity in all interactions. Most of the baryons are created as baryon-antibaryon pairs in the hadronization process, what leads to the equal amount of baryons and antibaryons in the central rapidity region, far away from the colliding baryons. There are alternative scenarios, known as so-called large baryon number transport (or transfer) [110–117], in which initial baryon number is transferred from the very forward to central rapidity region. Experimentally, this phenomenon is quantified by measuring the mid-rapidity baryon to antibaryon ratios, e.g. $p/\bar{p}$, which are often expressed in terms of the transfer size in the rapidity space:

$$\Delta y = y_{\mathrm{beam}} - y_{\mathrm{baryon}} \tag{1.35}$$

where y_{beam} is the rapidity of the incoming beam protons and y_{baryon} is the rapidity of the produced baryons.

There are many theoretical models, that are proposed in order to describe the baryon number transport. In the Dual Parton Model [110], the incoming proton is described as a pair of quark and diquark, where the latter possesses the baryon number information. Since most of the initial proton momentum is kept by the diquark, therefore it is expected that the extra baryons should appear in the very forward direction. In the String Junction Model [111, 112], the colliding baryons are described as a topological structure where three gluons emitted from the three valence quarks must join in one point (string junction), forming so-called the Mercedes-star configuration. Hence, the string junction is described by the non-perturbative QCD calculations, where gluons are represented by strings which may break up and produce a pair of quark and antiquark. In the Regge based approach to this model, the baryon number transport is proportional to $\exp\left[(\alpha_{SJ} - 1)\,\Delta y\right]$, where α_{SJ} denotes the string-junction Regge intercept, which can take two values: 0.5 and 1. For the former, the baryon number is carried by the valence quarks and is exponentially suppressed with Δy [111, 113], while for the latter, there is a pure gluonic process (baryon number is associated to the string junction) and the baryon number transport is uniformly distributed over the rapidity [114, 115]. There exist also models dedicated only to diffractive processes, which predict a non-zero probability that an extra baryon can appear close to the rapidity gap edge (so-called backward peak) [118].

Experimentally, it is natural to expect that possible baryon number transport will be better visible at small ξ where rate of particle-antiparticle creation is smaller due to the generally smaller particle multiplicity or due to the fact that the gap edge is inside the central rapidity region, which is fully covered by experimental apparatus.

1.4 Monte Carlo Generators

The analyses described in this thesis use a few MC generators, which are briefly discussed below.

PYTHIA 8 [71, 101] is a multipurpose event generator, which is the rewritten in C++ successor of PYTHIA 6 [70] (written in Fortran). As a part of this framework, various phenomenological models are implemented in order to describe soft and hard processes, including MPI, ISR and FSR, beam remnants, CR, hadronization and particle decays. The SD, DD and DD models are based on the Regge formalism with the Lund string hadronization model. By default PYTHIA 8 uses the SaS parametrization of diffractive cross section and Pomeron flux, however, it is also possible to choose alternative models, e.g. the DL or MBR parametrizations. The program implementation contains many parameters, hence, there are some prepackaged tunes, e.g. 4C [71] (default in version 8.1), Monash [119] and the ATLAS tunes (A2 [120], A3 [121]), in which groups of parameters are adjusted in order to deliver a sensible description of the experimental data. In addition, these tunes are very often based on the specific PDFs, e.g. MSTW2008LO [122] or CTEQ6L1 [123] for proton parton densities, H1 2006 Fit B [98] (default) for diffractive parton densities. Usually, PYTHIA 8 serves as the main MC generator used by most modern experiments.

EPOS [124] is a MC event generator, which was primarily used for the simulation of cosmic-ray air showers [125]. Each hadron-hadron interaction is described as a parton ladder between the projectile and the target remnants, where the parton ladder is represented by flux tubes (strings) consisting of the hard and soft parts (partons and the Pomerons). Hence, there are two sources of particle production, the two off-shell remnants and the parton ladder, for which the energy density and hydrodynamical evolution is computed [126]. The mathematical formulation of such model is given by the parton-based Gribov-Regge theory [127], which provides a simultaneous description of the hard and soft interactions.

Thus, the PDFs are not used as in PYTHIA 8. EPOS has one set of parameters for all energies and systems, which can not be tuned by the users and are adjusted in order to describe the available data.

EPOS predicts very large contribution of forward-scattered protons, which originate from non-diffractive events but are well separated in rapidity from other final state particles (Sec. 3.2). This is the result of low mass excitation of the proton remnant (< 1 GeV) leading to hadronization of the beam remnant back to the proton. Therefore, EPOS predictions in this thesis are separated in two classes: diffractive (EPOS SD), modelled by Pomeron exchange, and non-diffractive, modelled by low mass excitation of the proton remnant (EPOS SD$'$). Such a remnant treatment is very unique in EPOS compared to other string models, e.g the one used in PYTHIA 8, where ND forward-scattered protons are rare and arise from string fragmentation and hadronization.

In HERWIG (version 7.1) [128–130] event generator, the diffractive cross sections are calculated in the triple-Regge approach, similarly to PYTHIA 8. However, the kinematics of the soft particles from the dissociation state is constructed according to a multiperipheral particle production model [131]. In addition, HERWIG simulates proton-proton interactions with special emphasis on an accurate description of the MPI and hadronization of the final-state particles, where an implementation of the latter is based on the cluster model [132]. These two features are the main differences between HERWIG and PYTHIA 8 generators.

QGSJET-II [133] event generator, similarly to EPOS, used to be a tool for the simulation of high energy cosmic ray. The model is based on the Regge theory, where soft and semi-hard interactions are described by the semi-hard Pomerons. In addition, the PDFs are not used as in PYTHIA 8. This model differs from the previously described generators by its treatment of nonlinear interaction effects, based on a resummation of the corresponding enhanced Pomeron diagrams.

Chapter 2

Experimental Setup

2.1 Accelerator Physics

There are few parameters of an accelerator [42, 134, 135], which are important for further reading of this thesis. The betatron function at the Interaction Point (IP), referred to as β^*, which denotes the distance from the IP where the transverse beam size is doubled. The luminosity defines the rate of collisions at the experiment. The number of events of a given process per unit time, dN/dt, can be expressed as:

$$\frac{dN}{dt} = \mathcal{L}\sigma \tag{2.1}$$

where $\mathcal{L}$ is the instantaneous luminosity, σ is the cross section for this process. The instantaneous luminosity does not depend on the process and is defined as:

$$\mathcal{L} = fn\frac{N_1 N_2}{4\pi\sigma_x\sigma_y}F \tag{2.2}$$

where f is the revolution frequency, n is the number of bunches per beam, N_1 and N_2 are the number of protons in the crossing beam bunches, σ_x and σ_y describe the horizontal and vertical beam size, F is the luminosity reduction factor due to e.g. the crossing angle at the IP, and is given by:

$$F = \frac{1}{\left(1+\phi^2\right)^{1/2}} \tag{2.3}$$

where $\phi = \theta_c\sigma_z/\left(2\sigma_x\right)$ is so-called Piwinski angle, θ_c is the crossing angle at the IP, σ_z describes the longitudinal beam size. In order to obtain the total number of events of a particular process, the instantaneous luminosity is integrated over the time interval.

The last parameter useful in this thesis [136], μ, denotes the number of inelastic collisions per bunch crossing averaged over all colliding bunches and is given by:

$$\mu = \frac{\mathcal{L}\cdot\sigma_{\text{inelastic}}}{fn_{\text{b}}} \tag{2.4}$$

where $\sigma_{\text{inelastic}}$ is the total inelastic cross section and n_{b} is the number of colliding bunches.

2.2 Relativistic Heavy Ion Collider

The Relativistic Heavy Ion Collider (RHIC) [137, 138], located at the Brookhaven National Laboratory (BNL) in the USA, is one of the two currently operating heavy-ion colliders in the world and the only collider of protons with polarized spin (longitudinally or transversely). In heavy-ion collisions, the properties of Quark Gluon Plasma (QGP) are studied, whereas polarized proton collisions give the opportunity to explore the spin structure of the proton.

Since first collisions in the year 2000, RHIC has collided protons or different pairs of heavy ions, such as Au, Al, d, ^{3}He, U, Ru and Zr at various energies. It is also possible to produce asymmetrical collisions by colliding e.g. protons with the gold ions. RHIC was constructed to accelerate gold ions up to 100 GeV/nucleon and reach centre-of-mass energy of 510 GeV/c for pp collisions [139].

The RHIC accelerator consists of two independent accumulation rings (Blue and Yellow) with a length of 3.8 km each. To maintain high energy beams of protons or heavy ions on the right trajectory, RHIC is equipped with 1740 superconducting magnets (dipoles, quadrupoles, sextupoles and corrector magnets) made of niobium and titanium alloy working at 4.6 K and generating a magnetic field of 3.45 T in the arc dipoles [140]. Additionally, the Siberian Snake devices [141] are used to keep polarized-proton spin stable.

The RHIC injector chain [142], shown in Fig. 2.1, consists of several accelerators connected by beam transfer lines. The polarized hydrogen ions, created in the Optically Pumped Polarized Ion Source (OPPIS) [143], are first accelerated by Radio Frequency Quadrupole (RFQ) and Linac to 200 MeV and stripped to protons. In the Booster, protons are accelerated to 2.5 GeV before entering Alternating Gradient Synchrotron (AGS), where they reach an energy of 25 GeV. Beams are then injected to RHIC and are further accelerated to the nominal energy.

The ions are produced in a Laser Ion Source (LION) and transferred to an Electron Beam Ion Source (EBIS), where their energy reaches 17 keV/nucleon and their charge is multiplied (to +32 for Au) [145]. In RFQ and Linac, the ions are accelerated to 2 MeV/nucleon before entering the Booster, where they reach an energy of 100 MeV/nucleon and their charge is stripped (to +77 for Au). Inside the AGS, the ions are accelerated to 8.87 GeV/nucleon and stripped to the nominal charge (to +79 for Au). In RHIC, the heavy ions reach the nominal energy. The EBIS is the primary source of ions. However, the Tandem Van de Graaff, which was replaced by the EBIS, is still used in some special cases.

The STAR (Solenoidal Tracker at RHIC) experiment is currently the only operational experiment at RHIC. Two other experiments completed their operation: PHOBOS [146] in 2005, BRAHMS [147] in 2006. The PHENIX [148] experiment was decommissioned in 2015 because its successor, sPHENIX [149, 150], is being developed and will start taking data in 2023. The other experiment, pp2pp, was incorporated into STAR experiment in 2009 [151].

The scientific program of RHIC is planned to be completed by mid-to-late 2020s to make a room for a new Electron-Ion Collider [152].

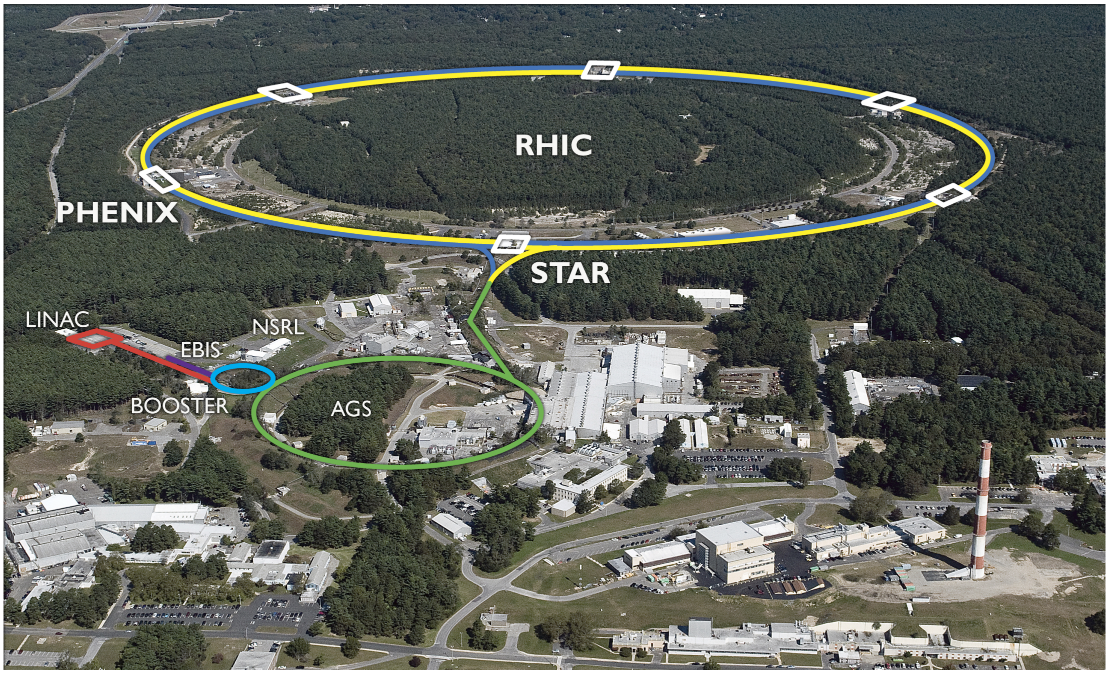

Figure 2.1: The RHIC accelerator complex. Figure taken from [144]

2.3 The STAR experiment

STAR [153] is a general purpose detector, located at the 6 O'clock position in the RHIC ring (near the AGS-to-RHIC Transfer Line). It consists of multiple detectors with different characteristics and responsible for measuring different quantities. Figure 2.2 shows the subsystems of the STAR detector, which were present during RHIC Run 15. The whole detector is enclosed in a solenoidal magnet that provides a uniform magnetic field of 0.5 T.

The STAR coordinate system a right-handed Cartesian system, in which the origin is defined by the nominal IP, while the direction of the two interacting beam particles determines the z-axis and $x - y$ plane is transverse to it. Positive x points away from centre of RHIC (South) and the positive y points upwards. The clockwise beam travels toward positive z (West) and the counter-clockwise beam moves toward negative z (East).

In the following sections, only detectors used in the analysis described in this thesis will be introduced in detail.

Time Projection Chamber

The heart of the STAR experiment is Time Projection Chamber (TPC), which is the primary detector for tracking and particle identification [154]. The TPC is 4.2 m long and 4 m in diameter, whereas its active part is limited by radii of 200 cm and 50 cm. Thus, it provides full azimuthal coverage and pseudorapidity interval of ±1 unit.

The TPC, shown schematically in Fig. 2.3, consists of the negatively-charged high voltage membrane, which divides the TPC into two parts and is held at −28 kV, and

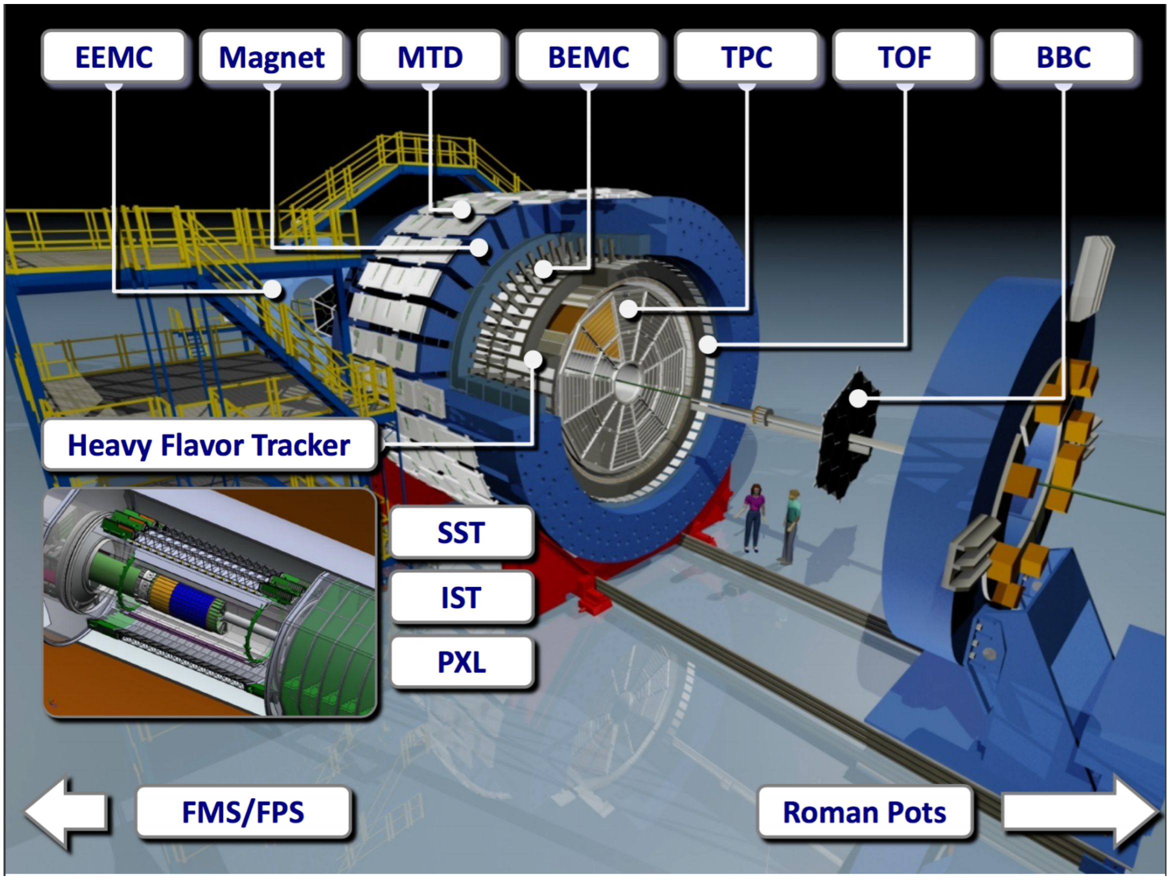

Figure 2.2: The STAR detector with selected subsystems. Figure courtesy of A. Schmah (STAR Collaboration).

two anodes at each end of the TPC. Inner and outer field cages and the attached resistor chains provide 182 equipotential rings from the high voltage membrane to the anode planes. The volume of the TPC is filled with P10 gas (a mixture of 10% methane and 90% argon) at 2 mbar above atmospheric pressure. When charged particles pass through the TPC volume, they ionize the gas. The positive ions drift towards the cathode in the centre of the TPC, whereas the electrons drift towards the anodes. Both ends of the TPC are divided into 12 Multi Wire Proportional Chambers (MWPC), shown schematically in Fig. 2.4, which are further divided into 13 inner and 32 outer pad rows, giving 136560 pads in total for the whole TPC. Each of these 45 pad rows allow to measure the spatial location in the $x-y$ plane of electron clusters and the number of electrons in each cluster. The electron drift velocity through the P10 gas (equal to 5.45 cm/µs) [155] together with the secondary electrons drift time determine the z position of electron clusters.

In addition to the position measurement, the TPC is able to determine charged particles momenta from 100 MeV/c to 30 GeV/c and identify them in the momentum range of 100 MeV/c to 1 GeV/c. The momentum resolution for pions in the TPC is approximately 2% at $p_{\mathrm{T}} \approx 1$ GeV/c.

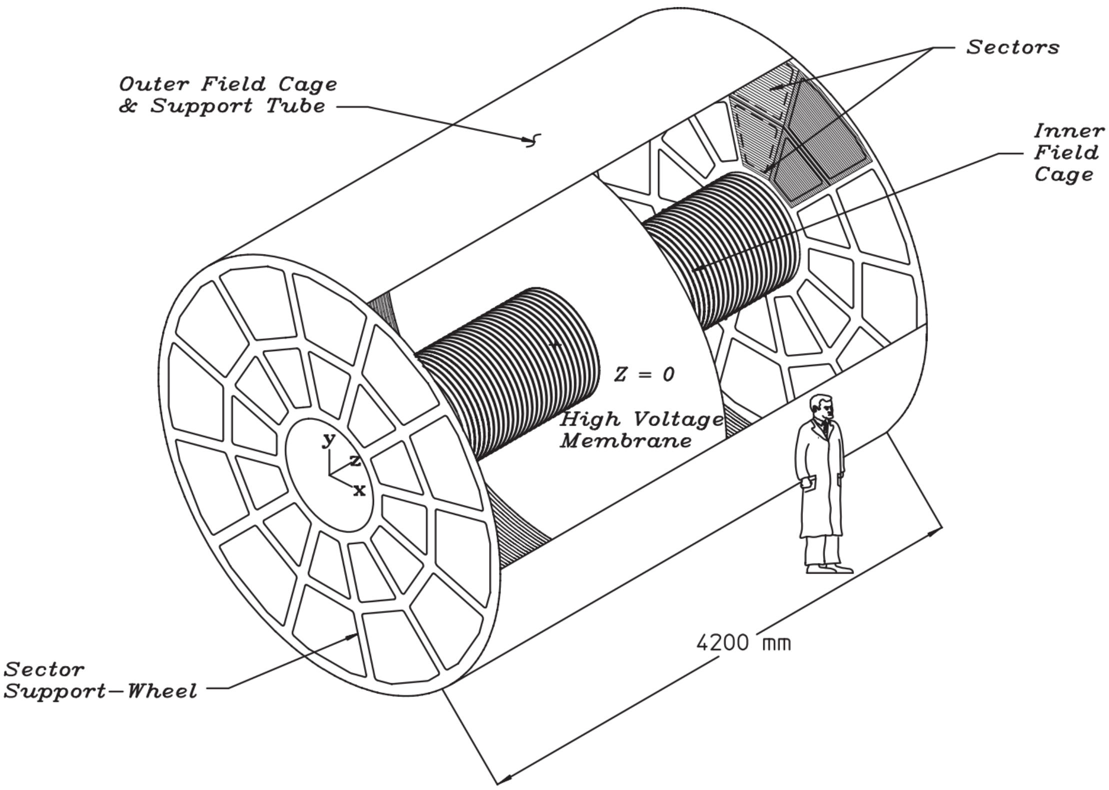

Figure 2.3: Schema of the STAR Time Projection Chamber. Figure taken from [154].

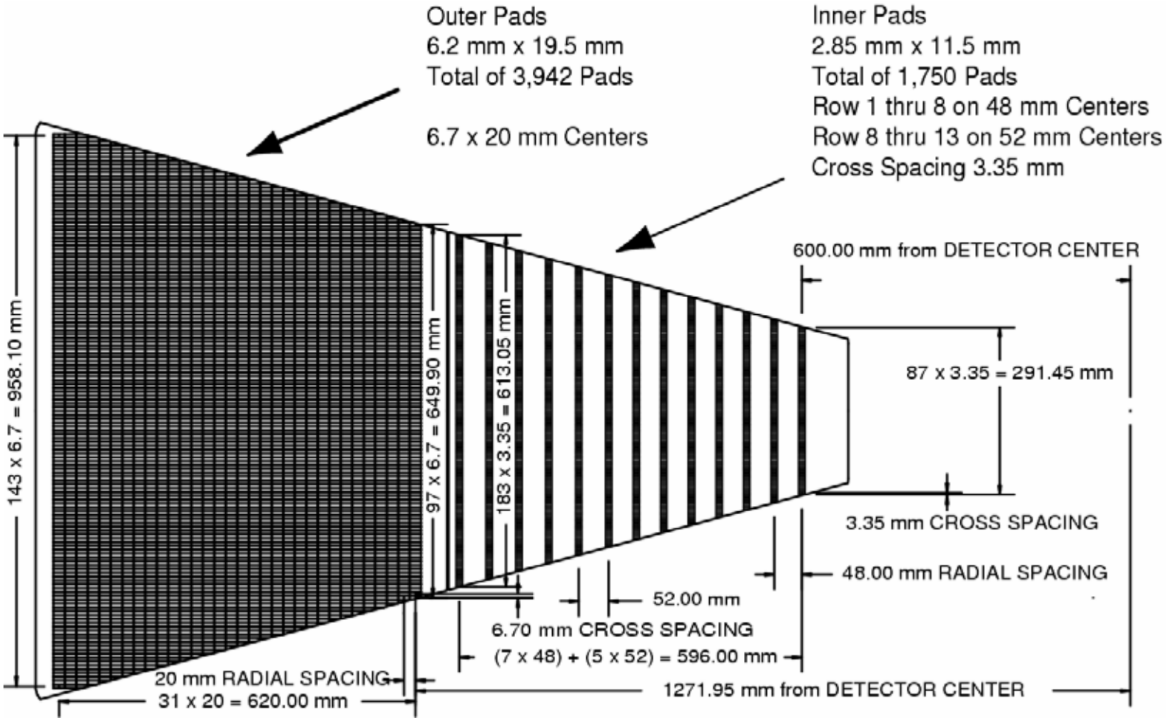

Figure 2.4: Schema of one full TPC sector. Figure taken from [154].

Time-of-Flight Detector

The barrel Time of Flight (TOF) detector [156–158] was fully installed in 2010 to complement the TPC detector and extend the momentum range for the particle identification. Additionally, it serves as a fast midrapidity trigger detector.

The TOF detector consists of 120 trays, 60 on each side of the high voltage membrane. With respect to the IP the TOF uniformly covers a pseudorapidity region of approximately 0.9 with axial symmetry, for a total coverage of 1.8 units of pseudorapidity in the full azimuthal angle. Each tray contains 32 individual Multi-gap Resistive Plate Chambers (MRPC) modules and each MRPC contains 6 channels (cells). The MRPC module, illustrated schematically in Fig. 2.5, is made of glass resistive layers, which are separated by gas gaps (a mixture of 95% freon and 5% isobutane). Electrodes are applied to the outer surface of the outer plates and held at the a potential difference of $10-15$ kV. When charged particles pass through the MRPC, an avalanches of electrons are produced in the gas gaps through ionization. The signal, measured by the pads located outside the electrodes, is the sum of avalanches from all the gas gaps.

In order to calculate the velocity of particle for its identification, information from three systems is usually combined:

- particle path length and momentum measured with the TPC,
- collision time measured with the Vertex Position Detector (VPD) [159],
- particle stop-time measured with the TOF.

The TOF system achieves a total time resolution of about 100 ps [159]. Instead of applying the VPD information for collision time measurement, it is also possible in high-multiplicity events that collision time is determined from the pions using only the TOF information. However, both methods of collision time calculation are not applicable in the analysis described in this thesis.

BBC and ZDC Detectors

The Beam Beam Counter (BBC) and Zero Degree Calorimeter (ZDC) detectors provide input to the triggering system [160, 161] and measure the location of an interaction vertex used in triggering.

The ZDC detectors [162] are placed ±18 m from the IP and were designed to measure energy and the multiplicity of neutrons produced at a small angle during a collision. The coincidence between the two ZDCs, placed on each side of the IP, provides the information about interaction rates. Each ZDC detector consists of three identical modules tilted at a 45° angle to the beam, and each module contains tungsten plates, fibres and photomultiplier tubes. In addition, the Shower Maximum Detector (SMD), located between the first and second ZDC modules, measures the position of the neutron beam.

There are two BBC detectors [163] which are placed ±3.75 m from the IP and cover a pseudorapidity region from 2.2 to 5.0. Each module consists of 18 small (with pseudorapidity coverage from 3.4 to 5.0) and 18 large scintillator tiles, and each tile is equipped

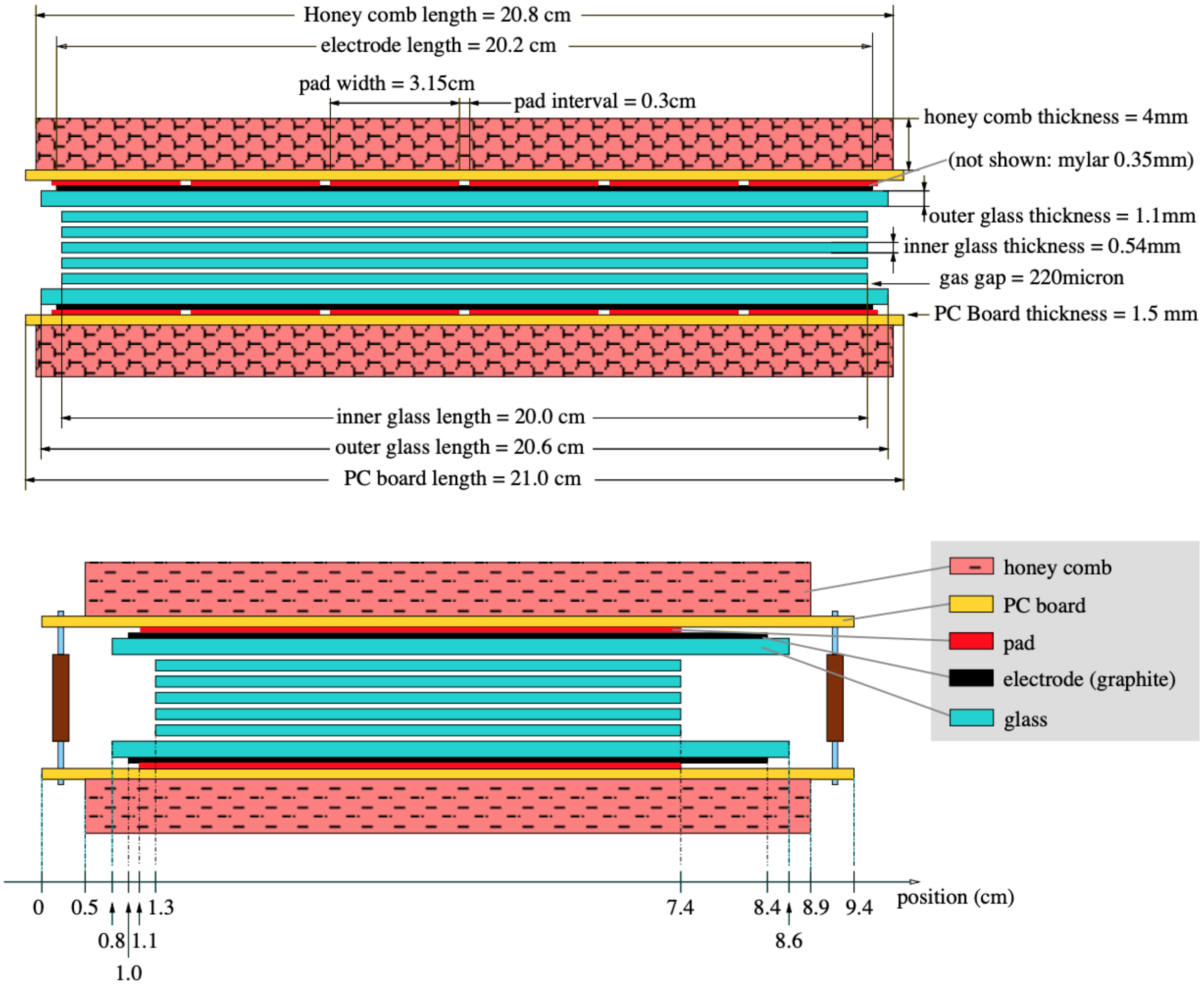

Figure 2.5: Schema of the MRPC module used in the STAR TOF [156].

with optical fibres and photomultiplier. The coincidence between BBC modules serves as the main MB trigger used for proton-proton collisions. In addition, they provide the information about luminosity and polarization of the beams.

Roman Pot Detectors

The system of Roman Pot (RP) detectors is used to measure protons that are scattered at very small angles (a few µrad) in the proton-proton interactions of low momentum exchanges, i.e. elastic and diffractive interactions.

During RHIC Run 15, there were two RP stations installed to the outgoing beam-pipe on either side of the IP near the STAR detector (15.8 m and 17.6 m from the IP) [88]. Figure 2.6 shows the scheme of the RP system. The location of the detectors between RHIC DX and D0 magnets ensures that no special beam conditions, e.g. high β^* optics, are needed to successfully operate the RPs. In each station there are two RP movable vessels (above

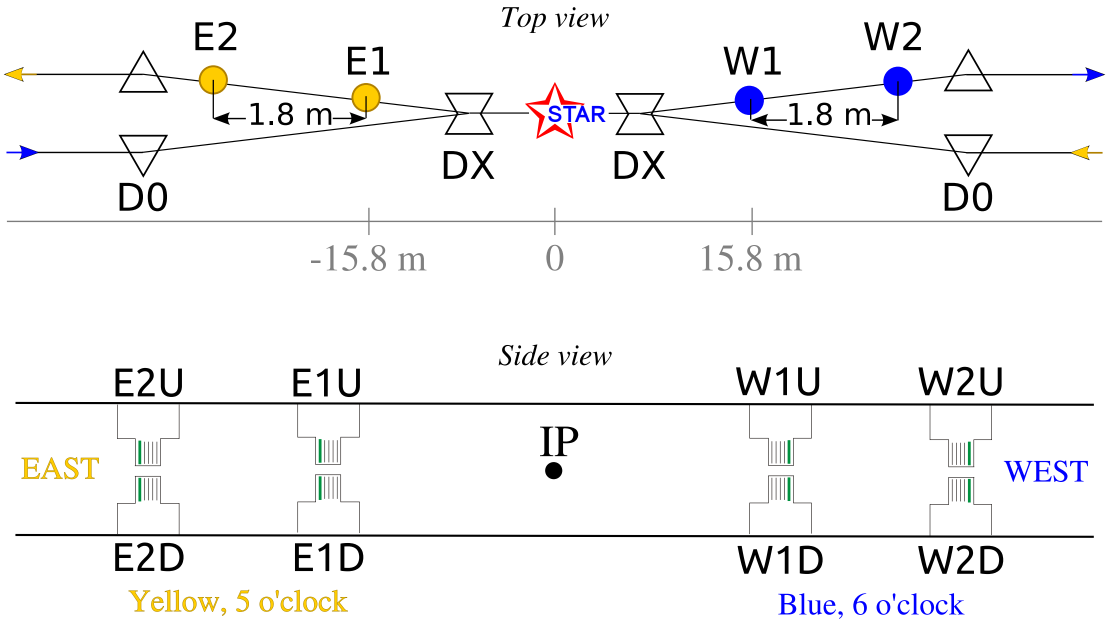

Figure 2.6: Experimental layout of the Roman Pot subsystem.

and below the beam-pipe), which approach the beam vertically. The detector assembly, mounted in each RP vessel, consists of four layers of Silicon Strip Detectors (SSD) [151], which are used for the proton position measurement in the $x-y$ plane (two of them measure the x and two the y position). The active area of the SSD detectors with a strip pitch of about 100 µm is approximately 79 × 48 mm^2. Figure 2.7 shows the photographs of single RP station, RP vessel and SSD detector package, taken during the preparation of the RP system for RHIC Run 15.

The idea of the SSD detectors is based on $p-n$ junction diodes, which are working in reverse-biased mode. Such detector is made of thin strips of p-type silicon implemented over an n-type silicon layer. Aluminum electrodes are connected to p-type strips. When charged particles pass through the SSD volume, electron-hole pairs are produced through ionization. Holes drift towards the p strips, whereas electrons drift towards positively-charged n-type layer. The charge deposited in the strips determines the position.

In addition to the SSDs, each detector assembly includes a scintillator (8 cm × 5 cm) combined with two photomultipliers, that provide fast signal for triggering of forward-scattered protons.

The naming convention denotes the position of each detector assembly in the RP system: side of the IP (East or West), station (1 or 2) and the orientation (Up or Down).

Trigger System

The aim of the STAR Trigger System [160, 161, 164] is to select those collisions which are of high interest for further analysis. Only fast systems are used as trigger detectors, e.g. BBC, ZDC, VPD, TOF or RP detectors. The maximum trigger rate that the TPC can

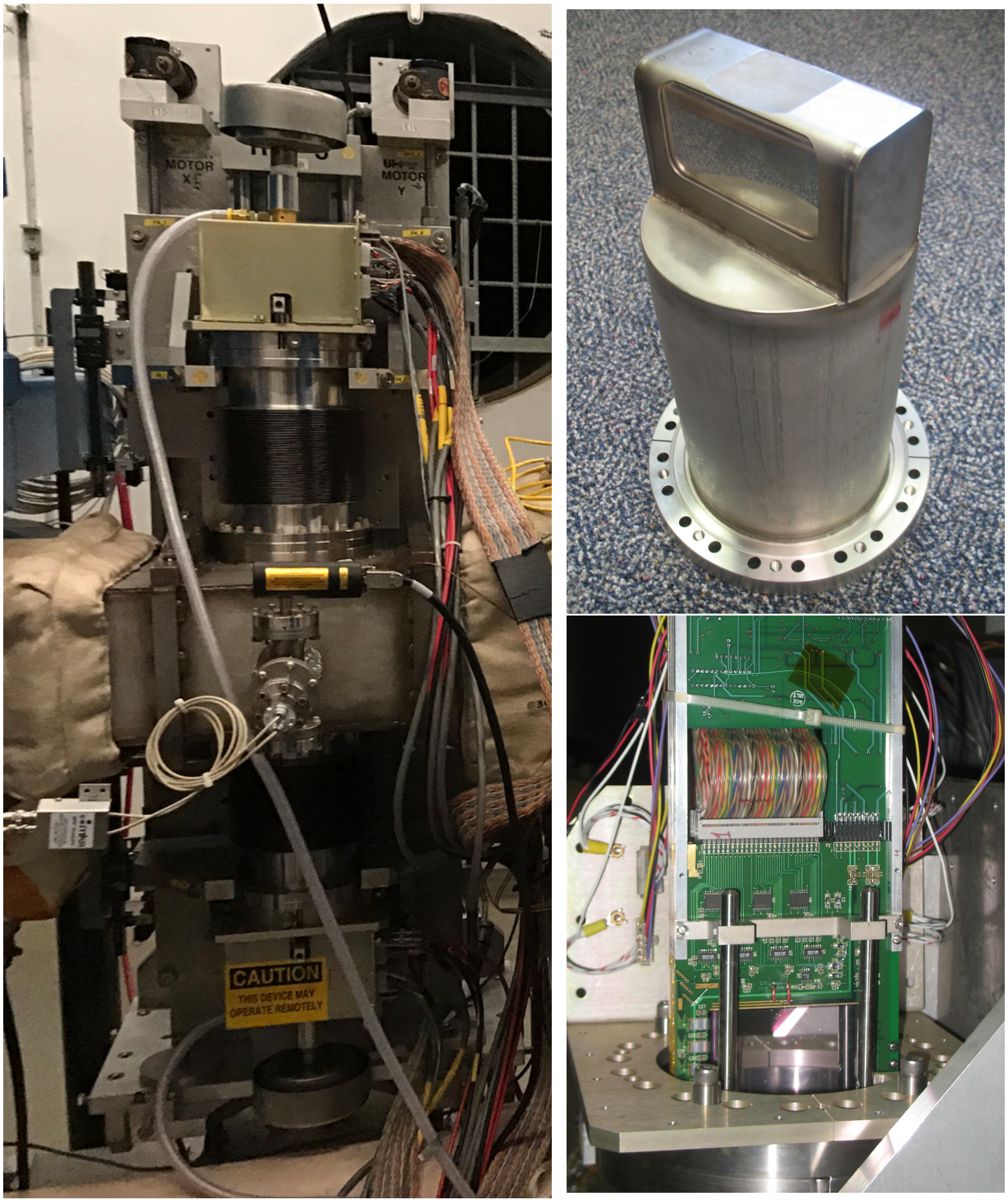

Figure 2.7: (left) Photographs of single RP station, (top right) RP vessel and (bottom right) SSD detector package.

operate is approximately 1.8 kHz, thus, the Trigger System reduces the rate of the data to be stored from 9.37 MHz (RHIC collision rate) to that level.

The STAR Trigger System consists of four levels for historical reasons. During each collision at STAR, the Level 0 trigger used to be working on the output information from fast detectors. Due to the drift time of the TPC, which is about 40 μs, the Level 1 trigger was introduced. Additionally, it could analyse data from fast detectors more deeply. The analysis of the calorimeter information and transfer of the TPC data to the Data Acquisition System (DAQ), which is about 5 ms, could be made at Level 2 trigger. The final decision, whether to accept or reject an event, could be made at Level 3 trigger, where the TPC tracks could be reconstructed. Since there were many improvements in the STAR Trigger System over the years, nowadays, the Level 1 and Level 2 are used only to control the trigger rate and send data to the DAQ. However, the trigger rate for some processes may be still too high, hence there are prescaled triggers, which sample only some fraction of events of interest.

TPC Event Reconstruction

The cluster-finding algorithm forms a three-dimensional space points (hits or electron clusters) for each pad row. Then, the track-finder algorithm [165], starting from the outer pad rows, forms tracks from hits. It finds short tracks, which usually consist of few hits only and serves as an input to the Kalman finder (a procedure based on the Kalman filter). In this iterative procedure, the detector is divided into several virtual layers. The Kalman finder extends the tracks by adding matching hits from the next layers. At the same time, the state vector (position, direction and momentum) of the existing track is updated and the corrections due to energy loss (calculated under pion hypothesis) and multiple Coulomb scattering effects are introduced. The transverse momentum and the charge of a particle are determined from the curvature of the track. When there are no matching hits in the next layer or the last layer of the detector is reached, this step is complete. In the algorithm used for the reconstruction of RHIC Run 15 data, each hit can belong only to one track.

When charged particles with relativistic velocities, $\beta = v/c$, travel through matter, e.g. detector dead-material, they interact with it and lose their energy. An example of such interaction is ionization process, which is used in detectors for charged particle identification. The mean rate of ionization energy loss per unit length travelled by charged particles heavier than the electron ($M \gg m_e$) is given by the Bethe-Bloch equation [42] :

$$\left\langle -\frac{dE}{dx} \right\rangle = Kz^2 \frac{Z}{A} \frac{1}{\beta^2} \left[\frac{1}{2} \ln \frac{2m_e c^2 \beta^2 \gamma^2 W_{\max}}{I^2} - \beta^2 - \frac{\delta(\beta\gamma)}{2} \right] \tag{2.5}$$

where $K = 4\pi N_A r_e^2 m_e^2 c^2 \approx 0.307$ MeV mol^{-1} cm^2, N_A is the Avogadro's number, $r_e \approx 2.818$ fm is the classical electron radius, m_e is the electron mass, M is the mass of the incident particle, c is the speed of light, z is the particle's charge in units of e, Z and A are the atomic and mass numbers, $W_{\max} = 2m_e c^2 \beta^2 \gamma^2 / \left(1 + 2\gamma m_e/M + (m_e/M)^2\right)$ is the maximum energy transfer to an electron in a single collision, γ is the Lorentz factor, I is the mean excitation energy, $\delta(\beta\gamma)$ describes the density effect correction. Since $\beta\gamma = p/M$, where p is the momentum of a particle, it is possible to distinguish particles of different masses but with the same momentum.

The TPC provides an information about the number of electrons in each hit, which is proportional to the amount of ionization energy loss of the particle traversing the TPC volume. Each hit provides a separate dE/dx measurement following a Landau distribution. Therefore, the mean energy loss, calculated for each track, may be biased due to a single hit with very high dE/dx. Hence, two methods were developed. The first, primary used for heavy-ion collision data, rejects 30% of the hits with the highest dE/dx values and determines the truncated mean from the remaining 70% of the hits. In the second method, introduced due to instability of the first method in high pile-up proton-proton collisions, the track's dE/dx is obtained by the Most Probable Value (MPV) from a maximum likelihood fit.

The vertex-finder algorithm [166, 167] extrapolates tracks to the z-axis. The tracks, which do not pass certain cuts on the number of hits and the distance of the closest approach to the z-axis, are rejected from further analysis. In the next step, each track is given a weight based on the probability that it can be extrapolated to either a Barrel Electromagnetic Calorimeter (BEMC) or TOF hit. Then, the iterative procedure groups tracks into primary vertices along z-axis. All tracks with a distance to a given primary vertex smaller than 3 cm, are refitted including the primary vertex.

The vertex reconstruction algorithm, applied to the data analysed in this thesis, uses only TOF-matched tracks to suppress number of tracks from out-of-time collisions. Matching of reconstructed tracks to TOF hits is obtained by extrapolating the TPC tracks to the TOF detector. If the extrapolated track is close enough to a TOF hit, then it is marked as TOF-matched. With presence of the Heavy Flavor Tracker (HFT) detector [168] in tracking algorithms, an improvement in track momentum resolution is observed. However, the information from the HFT was not stored in the data stream used in the analysis described in this thesis.

STAR uses the naming convention of global and primary tracks. The global tracks are obtained without a vertex information, whereas the fit of primary tracks includes the vertex.

Proton Track Reconstruction in RP system

When a proton passes through the SSD volume, the digitized signal for each strip in a given detector layer is stored as raw data. A proton may spread its energy over several neighbour strips, which together form a cluster. The reconstruction algorithm assigns to each cluster its length, which is equal to the number of strips forming a cluster, total energy, and position, which is energy weighed mean of the strip positions. Two layers of each SSD measure either x or y position of the proton. Therefore, pair of clusters from two layers is compared and combined if the position difference between these two clusters is at most equal to the width of two strips. As a result, the track points, consisting of a pair of matched clusters in x and y coordinates, are formed. Position of each track point is determined as a mean of the matched cluster positions. There may be more than one track point for each SSD, thus, the algorithm calculates all combinations of the matching clusters. However, in approximately 80% of events, only one cluster in each layer is found. Finally, the track points from two detectors are formed into a track, which is identified as a particle travelling through the RP system. In case of many track points, the algorithm forms tracks from all possible combinations of track points.

The procedure of detector alignment was done separately for each of the detector layers in order to obtain the position of the proton in the STAR coordinate system. First, during a survey, the position of the first strip of each SSD layers were determined with respect to the RHIC coordinate system at a 1 mm precision level. In the next and the final step of the procedure, the corrections to the survey alignment were obtained from elastic events.

Finally, the proton momentum is reconstructed for each track. In order to calculate the ξ variable and the scattering angle of the proton at the IP, information about the geometry of the RHIC DX magnet, its magnetic field and the position of each track point in a track are used [169]:

$$\tan\theta_x^{\mathrm{RP}} = \frac{x_2 - x_1}{d_{\mathrm{RP}}} \qquad \tan\theta_y^{\mathrm{RP}} = \tan\theta_y = \frac{y_2 - y_1}{d_{\mathrm{RP}}} \tag{2.6}$$

$$\theta_x = \frac{x_1 - x_{\mathrm{IP}} - \left(d_2 + \frac{1}{2}l_{\mathrm{DX}}\right)\theta_x^{\mathrm{RP}}}{d_1 - z_{\mathrm{IP}} + \frac{1}{2}l_{\mathrm{DX}}} \tag{2.7}$$

$$\xi = \left(1 + \frac{\alpha_0\left(d_1 + \frac{1}{2}l_{\mathrm{DX}} - z_{\mathrm{IP}}\right)}{\theta_x^{\mathrm{RP}}\left(d_1 + l_{\mathrm{DX}} + d_2 - z_{\mathrm{IP}}\right) - x_1 + x_{\mathrm{IP}}}\right)^{-1} \tag{2.8}$$

where (x_1, y_1) and (x_2, y_2) are track point positions measured in the first and the second RP station, respectively, (θ_x, θ_y) are the scattering angles at the IP, $\left(\theta_x^{\mathrm{RP}}, \theta_y^{\mathrm{RP}}\right)$ are the local angles measured between track points, d_{RP} is the distance between RP detectors along the beamline, $(x_{\mathrm{IP}}, y_{\mathrm{IP}}, z_{\mathrm{IP}})$ is the vertex position, l_{DX} is the length of the RHIC DX magnet, α_0 is the bending angle of the RHIC DX magnet for beam protons, d_1 is the distance between the centre of the STAR detector and the entrance of the RHIC DX magnet, d_2 is the distance between the exit of the RHIC DX magnet and the first RP detector. Additionally, variable t is determined from the relation:

$$t = -2p_0^2\left(1 - \xi\right)\left(1 - \cos\theta\right) \tag{2.9}$$

where $\theta^2 = \theta_x^2 + \theta_y^2$ and p_0 is the momentum of beam protons.

2.4 The Large Hadron Collider

The Large Hadron Collider (LHC) [170, 171], located at the European Laboratory for Particle Physics (CERN) on the French-Swiss border near Geneva, Switzerland, is the largest and highest-energy particle accelerator ever built. Proton-proton collisions give the opportunity to study the interactions and forces among the elementary particles and search for the signs of new physics beyond the Standard Model, whereas, heavy-ion collisions provide insight into the properties of QGP.

Since first collisions in year 2010, the LHC has collided protons or pairs of heavy ions, such as Pb, Xe, at various centre-of-mass energies. It is also possible to produce asymmetrical collisions of protons and lead ions. The LHC was constructed to accelerate proton beams to energies up to 7 TeV.

The LHC consists of two underground rings, placed at depth of 50–175 m, with a length of 27 km each. To keep the beams on their circular path, the LHC is equipped with about 9593 superconducting magnets made of niobium and titanium alloy working at temperature of 1.9 K and generating a magnetic field of 8 T in the arc dipoles.

The LHC injection chain [173], shown in Fig. 2.8, consists of several accelerators. Protons, created in a duoplasmatron ion source [174], are first accelerated to 50 MeV by Linac 2. In the Proton Synchrotron Booster (PSB), protons are accelerated to 1.4 GeV before entering the Proton Synchrotron (PS), where they reach an energy of 25 GeV. Beams are then injected to the Super Proton Synchrotron (SPS), where they reach an energy of 450 GeV. In the final step, protons are transferred to the LHC, where they are further accelerated to their nominal energy.

The Pb ions are produced in the Electron Cyclotron Resonance (ECR) ion source [175] and transferred to Linac 3 [176], where they reach an energy of 4.2 MeV/nucleon and their charge is stripped from +27 to +54. Inside the Low-Energy Ion Ring (LEIR), the ions are

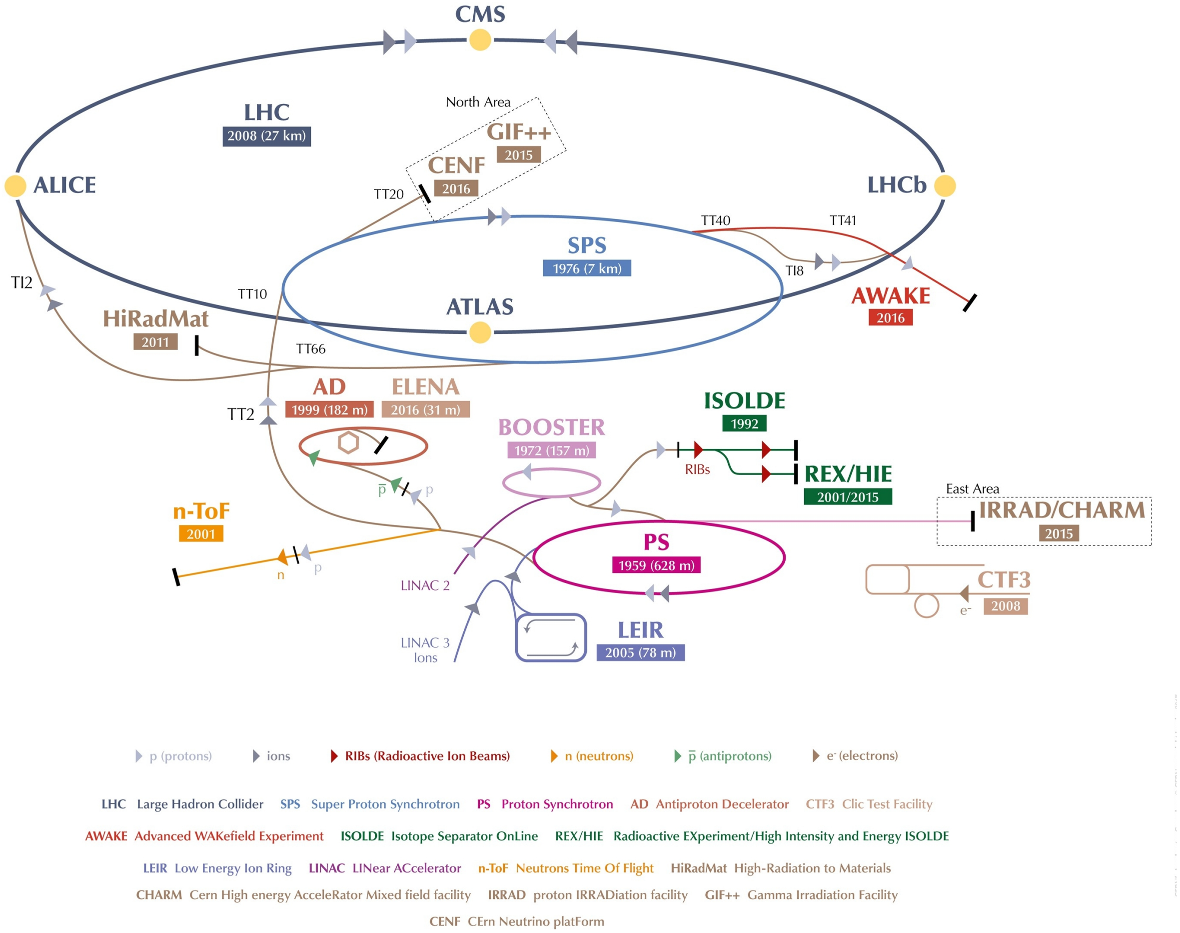

Figure 2.8: The CERN accelerator complex. Figure taken from [172]

accelerated to 72.2 MeV/nucleon. In the PS, the ions are accelerated to 5.9 GeV/nucleon and stripped to the nominal charge (+82) before entering the SPS, where they reach an energy of 177 GeV/nucleon. In the LHC, the heavy ions reach the nominal energy.

There are four IPs at the LHC where the main detectors are located: ATLAS [177], CMS [178], LHCb [179] and ALICE [180]. The former two are general purpose detectors, dedicated to precise measurements of interactions predicted by the Standard Model and searching for new physics. The ALICE studies the properties of QGP in heavy-ion collisions, whereas the LHCb is devoted to measurements of rare B decays and CP violation.

2.5 The ATLAS Experiment

A Toroidal LHC Apparatus (ATLAS) [177] is a general purpose detector, located in a cavern at Point 1 at CERN (near the Meyrin site). It consists of multiple detectors with different characteristics and responsible for measuring different quantities. Figure 2.9 shows the subsystems of the ATLAS detector. The whole inner detector is enclosed in a solenoidal magnet which provides a uniform magnetic field of 2 T, whereas barrel and two end-cap magnets, situated outside of the calorimeters and within the muon system, produce a toroidal magnetic field of 1.5 to 5.5 Tm in the pseudorapidity range of the barrel toroid, and approximately 1 to 7.5 Tm in the region of the end-cap magnets.

The ATLAS coordinate system a right-handed Cartesian system, in which the origin is defined by the nominal IP, while the direction of the two interacting beam particles determines the z-axis and $x-y$ plane is transverse to it. Positive x points to the centre of the LHC and the positive y points upwards. The clockwise beam travels toward negative z (side-C) and the counter-clockwise beam moves toward positive z (side-A). Polar angle θ is measured from the z-axis, azimuthal angle ϕ corresponds to the angle in the $x-y$ plane.

In the following sections, only detectors used in the analysis described in this thesis will be introduced in detail.

Inner Detector

The Inner Detector (ID) is the innermost sub-detector, surrounded by the 2 T magnetic field generated by the solenoid magnet. The ID is 6.2 m long with a diameter of 4 m, which ensures the pseudorapidity coverage in the range of $|\eta| < 2.5$. The ID comprise three sub-detectors employing different technologies, as shown in Figs. 2.10 and 2.11: the Pixel Detector, the Semiconductor Tracker (SCT) and the Transition Radiation Tracker (TRT). The active parts of the ID allow to precisely reconstruct tracks and determine vertex position. The transverse momentum resolution for charged particles in the ID is approximately $\sigma_{p_{\mathrm{T}}}/p_{\mathrm{T}} \sim 0.5\% p_{\mathrm{T}} \oplus 1\%$.

The Pixel Detector [182] is the innermost part of the ID. It contains four layers of barrel sensors and three end-cap disks on each side of the IP. The barrel layers are located at radii of 3.2, 5.1, 8.9 and 12.3 cm and have a length of 664 mm for the innermost layer and 800 mm for the rest layers. The end-cap sensors are placed at $|z| = 495$,

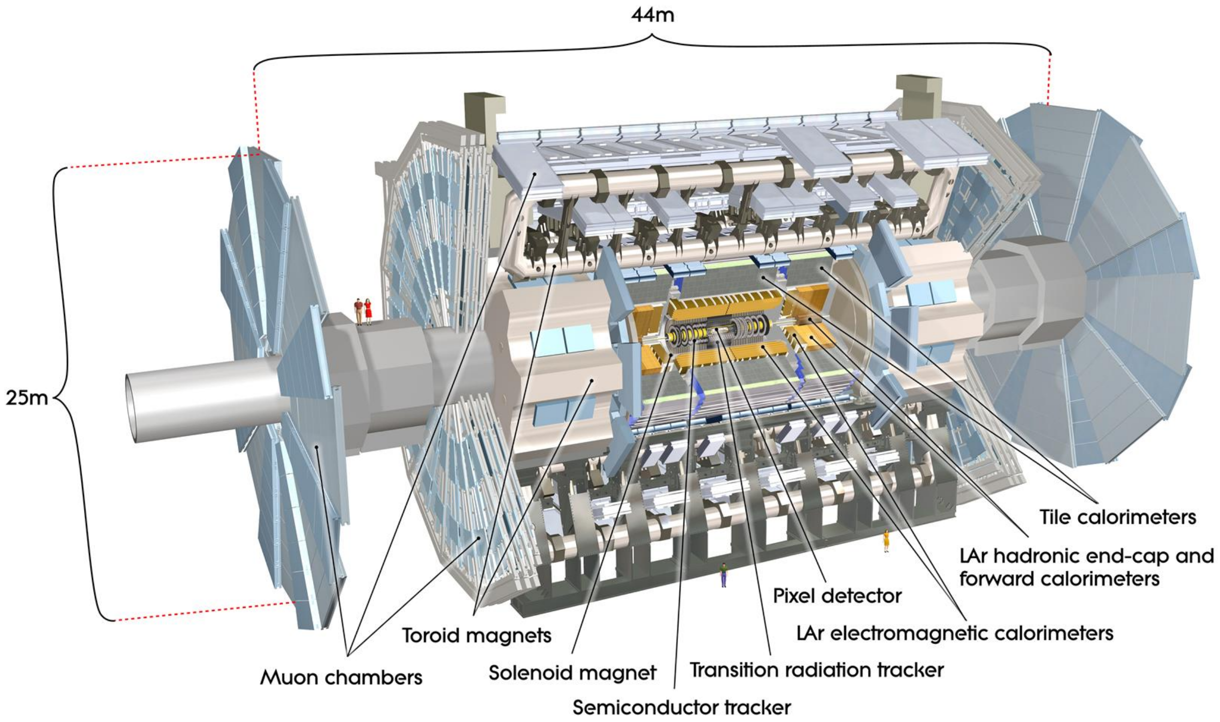

Figure 2.9: The ATLAS detector with selected subsystems. Figure taken from [177]

580 and 650 mm with radii ranging from 88.8 to 149.6 mm. The Insertable B-Layer (IBL) [183], which is the innermost part of the Pixel Detector, was installed in 2015 in order to improve the resolution of track impact parameters, mainly for b hadron physics, and maintain the ATLAS performance despite possible aging-induced effects. The outermost sensors have a pixel size of 50 μm $\times$ 400 μm, whereas the size of pixels in the IBL is about 50 μm$\times$250 μm. When a charged particle traverse the silicon sensor, it loses its energy due to ionization and electron-hole pairs are produced. The charge collected by the electrodes gives a measure of a hit position.

The Pixel Detector contains more than 92 million channels in total (about 12M channels in the IBL and about 80M in the rest three layers), which allow to measure the position with a resolution of 10 μm for the transverse plane coordinates and 115 μm for the longitudinal coordinate.

The Pixel is surrounded by the Patch Panel (PP) regions for electrical, optical and cooling services. It is crucial to properly simulate the dead-material of such structures, since it has an impact on the track reconstruction through the particle-matter interactions.

The SCT [184] is built of silicon strip sensors, which are distributed in four layers of barrel modules and nine end-cap disks on each side of the IP. The barrel layers are located at radii of 299, 371, 443 and 514 mm with a length of 1498 mm, whereas the end-cap sensors are installed along the z-axis in a range of $|z| = 853.8 - 2720.2$ mm with radii

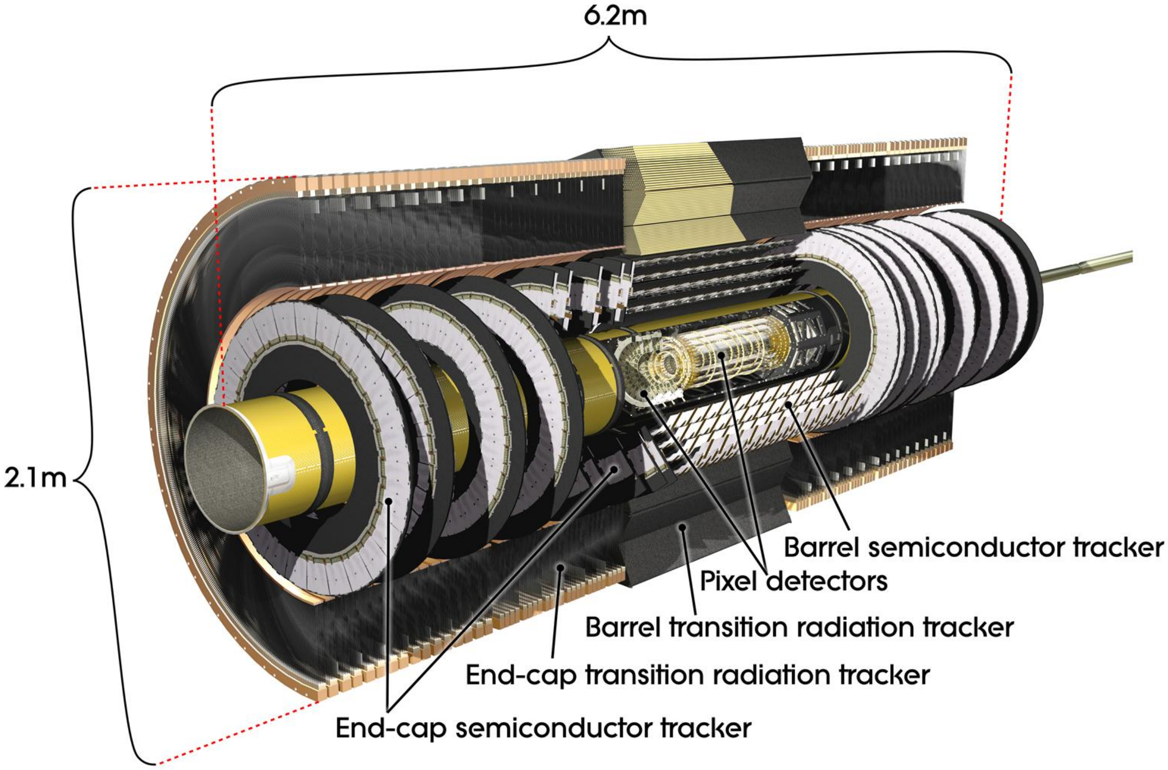

Figure 2.10: The ATLAS Inner Detector. Figure taken from [177]

from 27 to 44 cm. Each layer contains four silicon sensors, two on the top and two on the bottom side. In order to provide high resolution of the position measurement, each sensor contains stereo strips, which are oriented with an angle of 40 mrad between them. The 1536 strips in each barrel and end-cap modules, are 12.6 cm long with a pitch size of 80 µm.

The SCT contains about 6.3 million channels in total, which allow to measure the position with a resolution of 17 µm for the transverse plane coordinates and 580 µm for the longitudinal coordinate.

The TRT [185, 186] section of the ID is formed from a central TRT barrel detector and two TRT end-cap detectors. Each section consists of drift tubes (straws) of 4 mm in diameter, which are filled with a mixture of Xe, CO_2 and O_2 gases. In addition, the tubes are interleaved with transition radiation material in order to provide electron identification. The straws are 144 and 37 cm long in the barrel and end-caps, respectively. In the barrel, they are distributed along the z-axis with radii from 56 to 107 cm, while the straws in end-caps cover the z-axis in a range of $85 < |z| < 271$ cm with radii from 64 to 100 cm.

The TRT contains about 50k straws in the barrel and 120k straws in each end-cap, which allow to measure the position with a resolution of 130 µm for the transverse plane coordinates (it was not designed to provide the longitudinal coordinate).

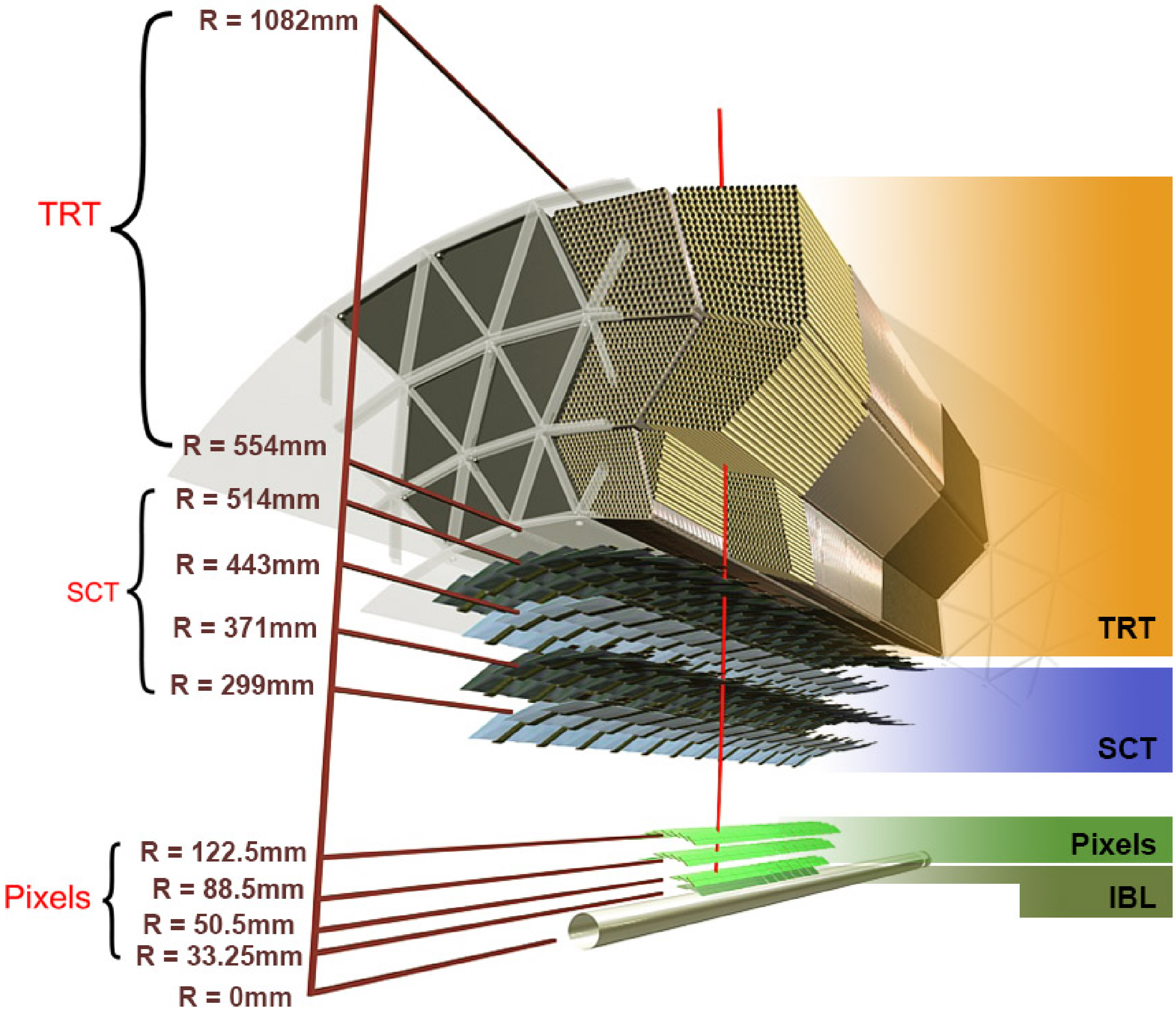

Figure 2.11: Detailed layout of the ATLAS Inner Detector, including the Pixel Detector (with the IBL), the SCT and the TRT. Figure taken from [181].

Calorimeters

The ATLAS Calorimeter System, which is shown in Fig. 2.12 provides the information about the energy of all charged and neutral particles except for muons and neutrinos.

The ATLAS Calorimeter System consists of the Electromagnetic (EM), the Hadronic and the Forward calorimeters. The EM calorimeter, surrounded by the hadronic calorimeter, covers the pseudorapidity $|\eta| < 3.2$. The forward calorimeter, which also contains EM and hadronic sections, covers the pseudorapidity range of of $3.1 < |\eta| < 4.9$. All calorimeters together reach pseudorapidity coverage over $|\eta| < 4.9$.

The EM calorimeters measure the energy and direction of photons, electrons and positrons. The EM calorimeter, made of liquid argon (LAr) samplers and lead absorbers,

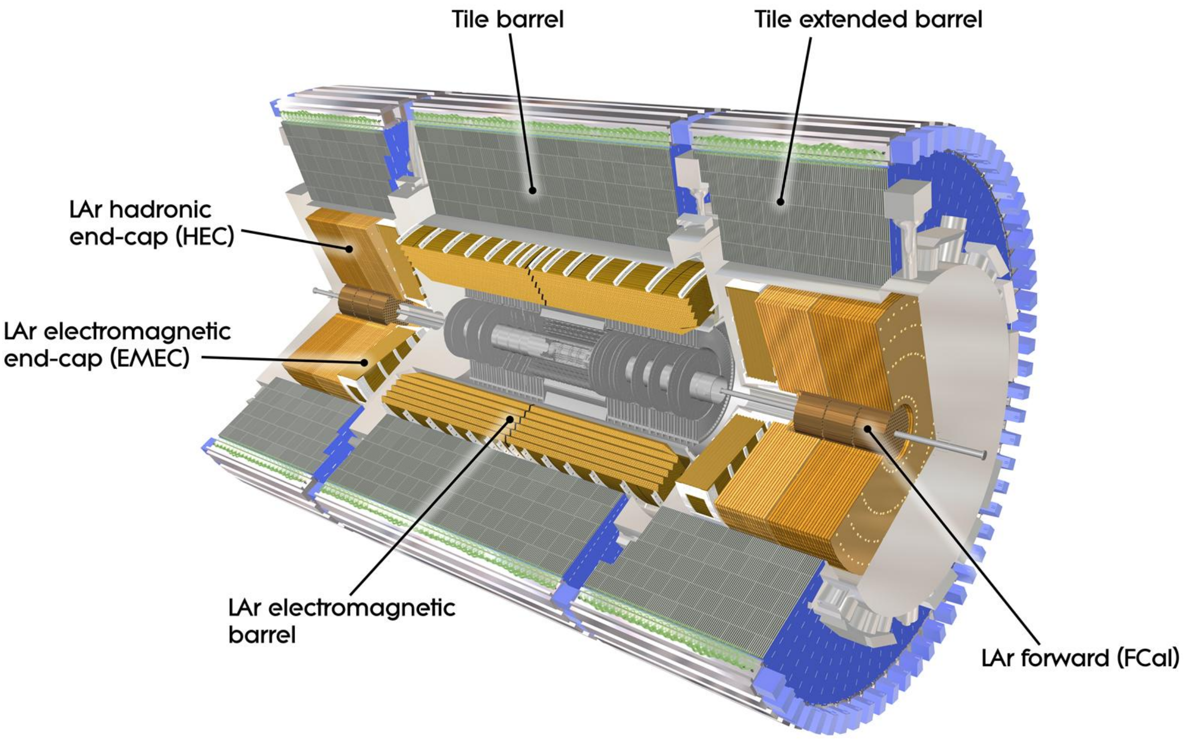

Figure 2.12: The ATLAS Calorimeter system. Figure taken from [177]

is housed in three cryostats, one barrel ($|\eta| < 1.475$) and two end-caps ($1.375 < |\eta| < 2.5$ and $2.5 < |\eta| < 3.2$).

The barrel calorimeter [187], being 6.4 m long and 4 m in diameter, consists of three layers and a presampler module [188]. The first layer has a granularity in η and ϕ of $\Delta\eta \times \Delta\phi = 0.003 \times 0.1$, which provides precision information about the particle position. The second and third layers have smaller granularity of $\Delta\eta \times \Delta\phi = 0.025 \times 0.025$ and $\Delta\eta \times \Delta\phi = 0.05 \times 0.025$, respectively. In addition, the thickness of each layer is described by the radiation length X_0, which is defined as a thickness of material over which an electron loses $1 - 1/e$ of its initial energy. The largest fraction of the electromagnetic shower energy is collected by the second layer, which is $16X_0$ thick. The first and the third layers are $4.3X_0$ and $2X_0$ thick, respectively.

The EM end-cap calorimeter [189] consists of two wheels, one on each side of the EM barrel calorimeter. As in the barrel calorimeter, each wheel in the region of $|\eta| < 2.5$ is divided into three layers. In addition, a presampler in front of the end-cap calorimeter was mounted in the region of pseudorapidity $1.5 < |\eta| < 1.8$. The granularity of the end-cap calorimeter is η-dependent and varies between $\Delta\eta \times \Delta\phi = 0.003 \times 0.1$ and $\Delta\eta \times \Delta\phi = 0.1 \times 0.1$.

The energy resolution for electrons in both, barrel and end-cap EM calorimeters, is approximately $\sigma_E/E \sim 10\%/\sqrt{E} \oplus 0.7\%$.

When electrons or photons pass through the absorber, they lose their energy by different processes. At high energies, photons mainly lose their energy by the e^+e^- pair creation in the field of absorber nucleus, whereas electrons or positrons emit photons (Bremsstrahlung) as they cross the material. Next, the particle multiplication continues through a cascade of Bremsstrahlung radiation and pair production until the products reach low energies. The sampler acts as an ionization chamber, i.e. it is ionized by charged particles passing through its volume. The generated charge, which is a measure of energy loses, is collected by electrodes due to presence of an electric field.

The Hadronic Calorimeter (HCAL) measures the energy of hadrons and jets originating from quark and gluon hadronization. It consists of two parts - the Tile and the Hadronic End-Cap (HEC) calorimeters.

The Tile calorimeter [190] is divided into a central barrel section covering the range $|\eta| < 1$ and two extended barrel sections covering $0.8 < |\eta| < 1.7$. Its radius ranges from 2.28 to 4.45 m. As in the EM calorimeter, each section is divided into three layers, which are made of iron as an absorber and scintillating plastic tiles as a sampler. The granularity in η and ϕ is equal to $\Delta\eta \times \Delta\phi = 0.1 \times 0.1$ in two first layers and $\Delta\eta \times \Delta\phi = 0.2 \times 0.1$ in the last layer. In addition, the thickness of each layer is described by the nuclear interaction length λ, which is defined as a thickness of material over which hadrons reduce their number by a factor of $1/e$. The thickness of the layers is approximately 1.5, 4.1 and 1.8λ for the barrel segment and 1.5, 2.6, and 3.3λ for the extended barrel segment.

The HEC calorimeter [191] consists of two wheels, one on each side of the barrel calorimeter, and covers the pseudorapidity range of $1.5 < |\eta| < 3.2$. The HEC's absorber is made of copper and its sampler of LAr. The granularity in η and ϕ is η-dependent and varies from $\Delta\eta \times \Delta\phi = 0.1 \times 0.1$ to $\Delta\eta \times \Delta\phi = 0.2 \times 0.2$.

The energy resolution for both, barrel and end-cap HCALs, is approximately $\sigma_E/E \sim 50\%/\sqrt{E} \oplus 3\%$.

Each of the Forward Calorimeters (FCAL) [192] consists of one EM and two hadronic calorimeters and covers the pseudorapidity range of $3.1 < |\eta| < 4.9$. They use LAr as an active material in all layers, whereas the absorber is made of copper and tungsten for the EM and hadronic modules, respectively. In addition, they are approximately 10 interaction lengths deep and their granularity in x and y is η-dependent. The energy resolution for hadronic modules is approximately $\sigma_E/E \sim 100\%/\sqrt{E} \oplus 10\%$.

Minimum Bias Trigger Scintillators

There are two Minimum Bias Trigger Scintillator (MBTS) detectors [193] which are placed at ±3.56 m from the IP and cover pseudorapidity region $2.08 < |\eta| < 3.86$. Each module consists of eight inner (with pseudorapidity coverage $2.76 < |\eta| < 3.86$) and four outer azimuthally arranged sectors, which are made of 2 cm thick polystyrene scintillator. The MBTS serves as the main MB trigger detector used for proton-proton collisions.

The ALFA Detectors

The system of the Absolute Luminosity For ATLAS (ALFA) detectors [194, 195] measures the protons that are scattered at very small angles in the forward direction. There are two ALFA stations installed to the outgoing beam-pipe on either side of the central ATLAS detector at distances of 237 m and 245 m from the IP. Figure 2.13 shows the scheme of the ALFA subsystem. The magnets (insertion dipole and quadrupole magnets) provide special beam conditions, i.e. parallel-to-point focusing optics, where the vertical position of the scattered protons in ALFA is insensitive to the transverse position of the IP.

Each station consists of an upper and lower RP movable vessels, which approach the beam vertically and allow to detect protons scattered down to 10 µrad. The detector assembly mounted in each RP vessel (Fig. 2.14), contains Main Detector (MD), for tracking and an Overlap Detector (OD) used for the relative alignment of two detectors within one station. The detectors are made of scintillating fibres to detect scattered protons and measure their position in the transverse plane. When protons pass through the detector, they excite the electrons in the scintillator and a light is emitted as the electrons return to their ground state. Then, the signal is read by Multi Anode Photomultiplier Tube (MAPMT).

The MD is built of 20 layers of 64 scintillating fibres. The size of each fibre is 0.5 mm in a diameter, whereas the space between them is about 70 µm. These layers are installed on ten planes, where each two layers within one plane are perpendicular to each other, in directions called U and V, and arranged at angles ±45° with respect to the y-axis.

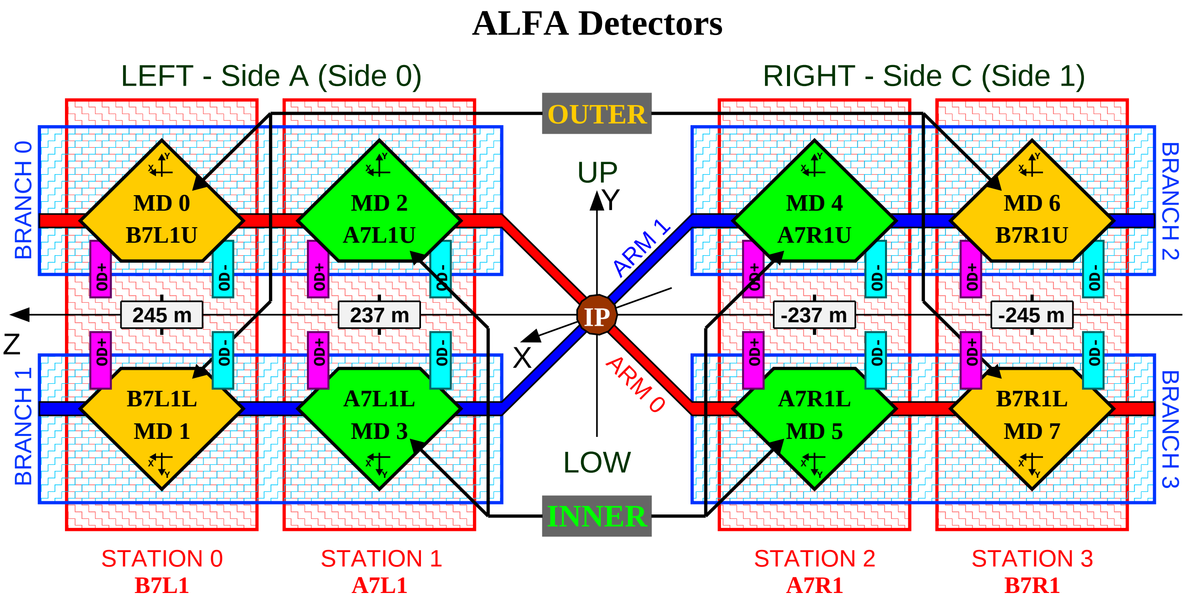

Figure 2.13: Experimental layout of the ALFA subsystem. Figure taken from [196].

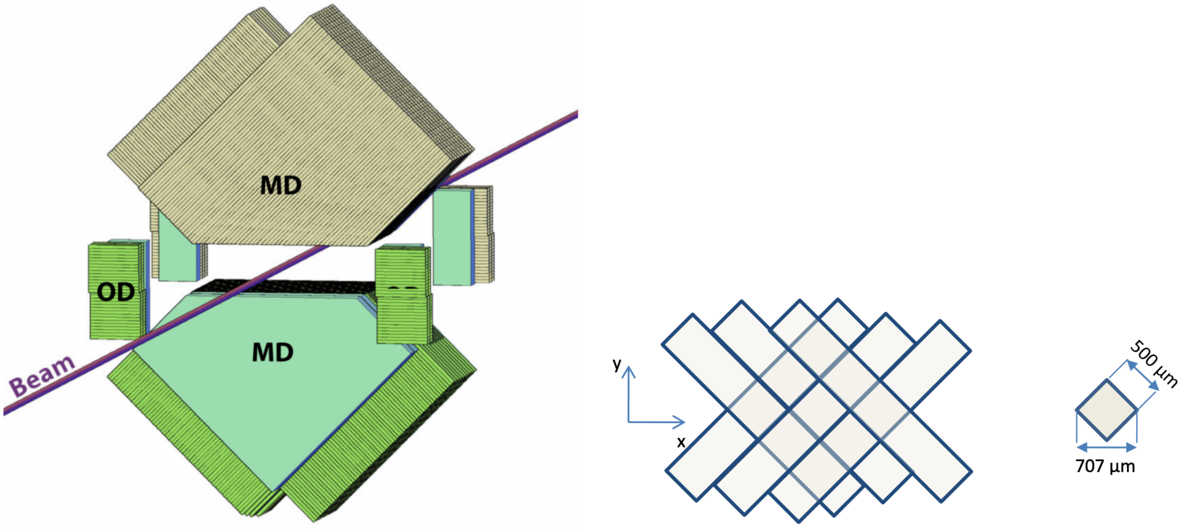

Figure 2.14: (left) Schematic drawing of two ALFA detectors and (right) the layout of scintillating fibres in the ALFA detector. Figures taken from [197] and [198].

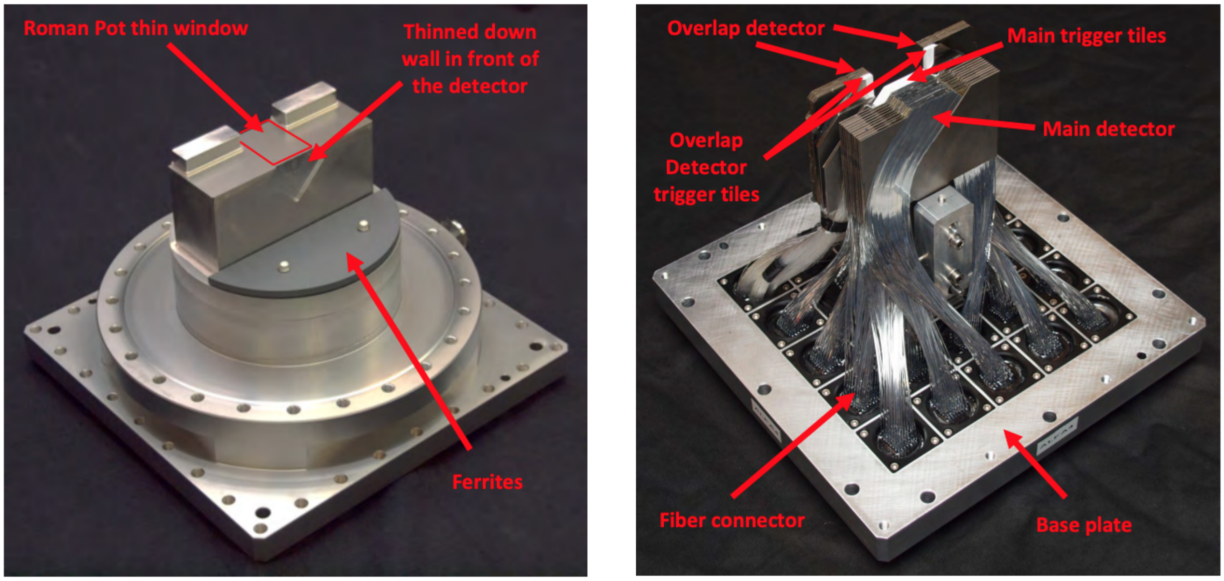

Figure 2.15: Photographs of (left) ALFA RP vessel and (right) ALFA detector. Figures taken from [198].

On the other hand, the OD is built of 3 layers with 30 fibres in each. It is able to measure the distance between upper and lower MD detectors, which is further used in the alignment procedure. In addition, each MD and OD are equipped with plastic scintillator tiles, that are used in triggering of forward-scattered protons. The MD contains trigger tiles on each side of the detector, whereas only one tile is mounted in the OD detector. Figure 2.15

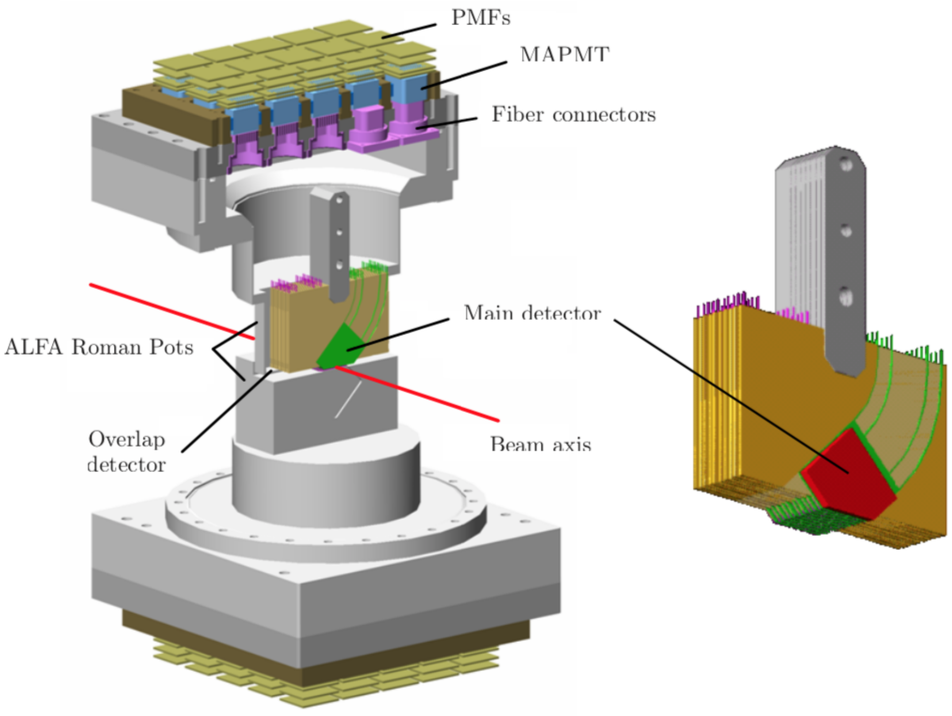

Figure 2.16: Schema of two ALFA RPs. Figure taken from [199].

shows photographs of the ALFA detector assembly and its RP vessel, while the schema of two RPs is presented in Fig. 2.16.

The spatial resolution for one single layer in the MD is approximately 144 μm, whereas the resolution of tracks made of hits from 10 planes is about 30 μm.

In this thesis, the RPs are denoted by the numbers from $0-7$. There are two stations on the A-side, the further station ($z = 245$ m) with RPs situated above (0) and below (1) the beam-pipe. In the closer station ($z = 237$ m), the RPs 2 and 3 are located above and below the beam-pipe, respectively. Similarly, there are two stations on the C-side, one closer with the RPs 4, 5 and one further with pots 6, 7. The RPs 4 and 6 are placed above the beam-pipe, whereas 5 and 7 below.

The ATLAS Forward Proton (AFP) detector [200] is an extension to the physics program of ALFA. However, the author of this thesis focuses only on the ALFA data.

Trigger and Data Acquisition

The ATLAS Trigger and Data Acquisition (TDAQ) system [201, 202], whose structure is shown in Fig. 2.17, was designed to select only the collisions of high-interest for physics. The TDAQ consists of hardware-based Level-1 (L1) trigger and software-based High Level Trigger (HLT). During each collision, the L1 trigger is checking the activity in Muon and Calorimeter detectors. It is also working on the output information from the fast

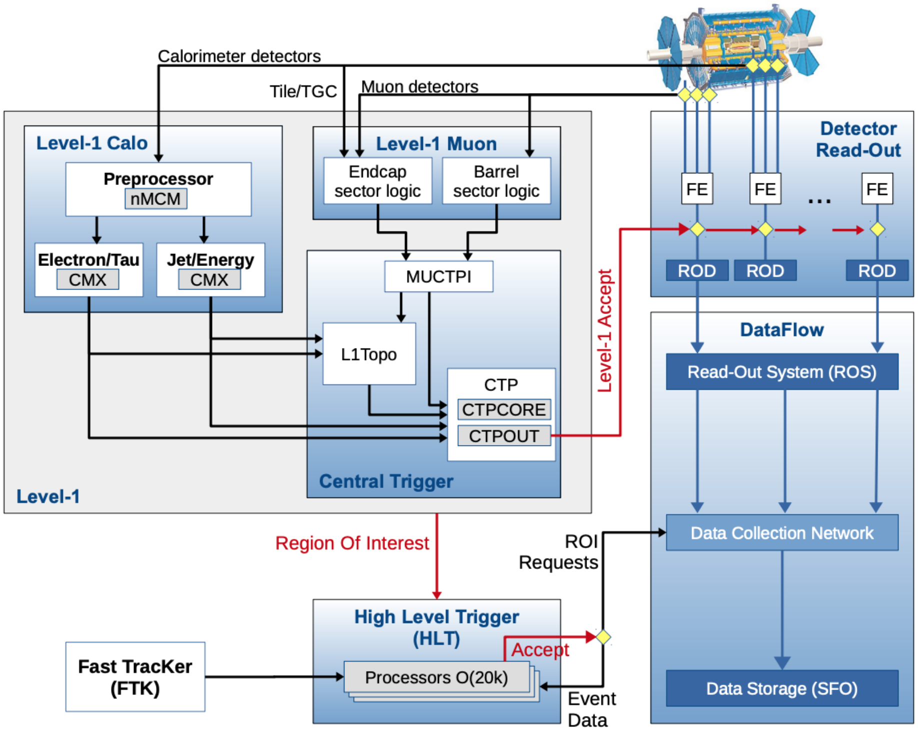

Figure 2.17: Layout of the ATLAS TDAQ system. Figure taken from [201].

detectors, e.g. MBTS, ALFA. Once the signal is received, the L1 defines the location of the Regions-of-Interest (ROI) in the detector. The L1 reduces the event rate from 30 MHz to 100 kHz and makes a decision within 2.5 µs. It also checks whether a prescale should be applied. The event rate is further reduced to 1 kHz within 200 ms at the HLT, which receives the ROI from the L1 and makes a decision, based on the reconstructed events, whether to store the data for further analysis.

Track and Vertex Reconstruction in the ATLAS

In this section, the method of track reconstruction used in this analysis is described. It starts with a formation of tracks in Pixel and SCT detectors, which are further extended to the TRT detector.

A trajectory of a charged particle in a magnetic field follows the parametrization τ with uncertainties encoded in the covariance matrix [203]:

$$\tau = (d_0, z_0, \phi, \theta, q/p) \tag{2.10}$$

where d_0 and z_0 are the transverse and longitudinal impact parameters with respect to the beamline, ϕ is the azimuthal angle of the track, θ its polar angle, and the ratio q/p is the charge of the particle divided by its momentum.

The procedure of track fitting starts from grouping hits in a given detector into clusters (space-points) [204–206], which consist of a multiple adjacent pixels or sensors. In the Pixel detector, each cluster forms a space-point, whereas in the SCT detector, a space-point is a combination of clusters in the front and back layers of the module. Then, the pattern recognition algorithm forms seeds from sets of three space-points. The iterative procedure, based on the combinatorial Kalman filter [207], extends the tracks to the remaining layers of the Pixel and SCT detectors. Each seed may provide multiple track candidates. Therefore, a procedure of ambiguity solving is introduced. In a given set of tracks with common space-points, each track is given a score, which depends on the content of clusters, number of holes (expected hit in an active layer of the detector but none found), number of shared hits, fit quality. Moreover, loose track quality cuts are introduced. The algorithm stores the track with the lowest χ^2 (with its clusters), and repeat the procedure on the remaining tracks with common clusters. In addition, an artificial neutral network is used to identify merged clusters and improve the efficiency of ambiguity solver algorithm in dense environment [208]. Figure 2.18 shows the logics of the ambiguity solver algorithm. In the final step of track fitting, the pattern recognition may extend silicon tracks into the TRT, what improves the momentum resolution of the reconstructed tracks.

The Pixel detector provides an information about the energy loss for each particle traversing its volume. The dE/dx for each cluster is obtained from the measured charge Q and is expressed as [209]:

$$\frac{dE}{dx} = \frac{Q}{e}\frac{W\cos\alpha}{\rho d} \tag{2.11}$$

where e is the elementary electric charge, W is the average energy needed to create an electron-hole pair, $W = 3.68 \pm 0.02$ eV/pair, α is the angle of incidence, ρ is the silicon density and d is the sensor thickness. Each cluster provides a separate dE/dx measurement following a Landau distribution and the mean dE/dx, calculated for each track, may be biased due to one hit with very high dE/dx. Hence, the algorithm removes one cluster for tracks with $2, 3, 4$ clusters and two clusters for tracks with 5 or more clusters in order to obtain the truncated mean from the remaining clusters [210].

The vertexing algorithm [211], extrapolates tracks to the z-axis. The tracks, which do not pass quality cuts on the number of hits and distance of the closest approach to the z-axis, are removed from further procedure. The iterative adaptive algorithm [212], applied to the data analysed in this thesis, has the ability to reconstruct multiple vertices. In the first step, the seed for a vertex is selected. The z-coordinate is determined by the weighted mean of longitudinal impact parameters of selected tracks. Then, the remaining tracks are used to find the seed for an another vertex. In the next step, each track is given a weight based on the probability that it originate from one of the two vertices, which are then refitted. The procedure is repeated until no new vertices can be found. The primary vertex is defined as the reconstructed vertex with the highest sum of the squared transverse momenta of tracks that originate from it. Each of the reconstructed vertices must have the transverse coordinates consistent with the beam-spot position and contain at least two tracks with $p_{\mathrm{T}} > 100$ MeV/c.

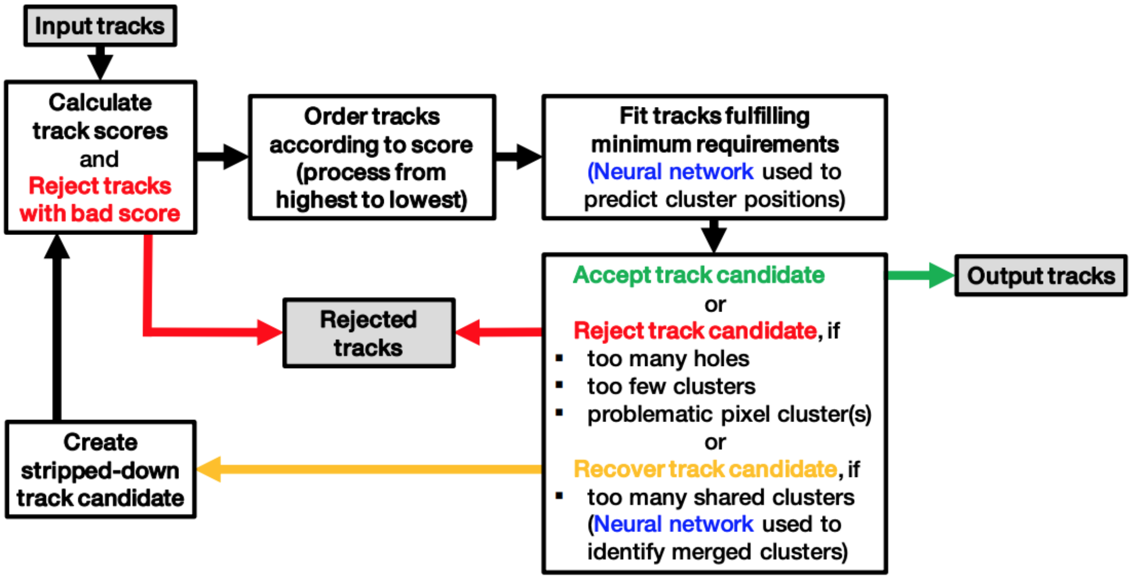

Figure 2.18: Logics of the ambiguity solver algorithm. Figure taken from [204]

Topological Cell Clustering in the Calorimeters

The reconstruction of the final-state particles in the ATLAS Calorimeter System is based on a three-dimensional topological clustering algorithm [213, 214]. In this procedure the significance parameter ς_{cell} is defined for each cell of the calorimeter:

$$\varsigma_{\text{cell}} = \frac{E_{\text{cell}}}{\sigma_{\text{noise, cell}}} \tag{2.12}$$

where E_{cell} is the energy deposited in a cell and $\sigma_{\text{noise, cell}}$ is an average cell noise. The algorithm searches for cluster seeds, which are formed by the cells with the significance $\varsigma_{\text{cell}} > 4$. Then, the surrounding cells are collected into the seed cluster if they satisfy the condition $\varsigma_{\text{cell}} > 2$. Finally, all the nearest neighbours with $\varsigma_{\text{cell}} > 0$ are also added. Therefore, the topological clusters have no predefined shape (in contrast to the Sliding Window Clustering Algorithm [214]).

The algorithm is able to find a cell which is close to more than one seed cluster (cluster splitting). In this case, the procedure shares the cell energy between clusters according to the geometrical and energy-dependent weights. The cluster kinematics, i.e. its energy and direction in (η, ϕ), is calculated in the final step.

Track Reconstruction in the ALFA

The proton passes through the ALFA detector and a hit pattern is formed, as illustrated in Fig. 2.19. Since, the fibres in a layer are shifted with respect to the previous layer, the centre of the hit pattern gives the position in the U or V coordinates, whereas the width

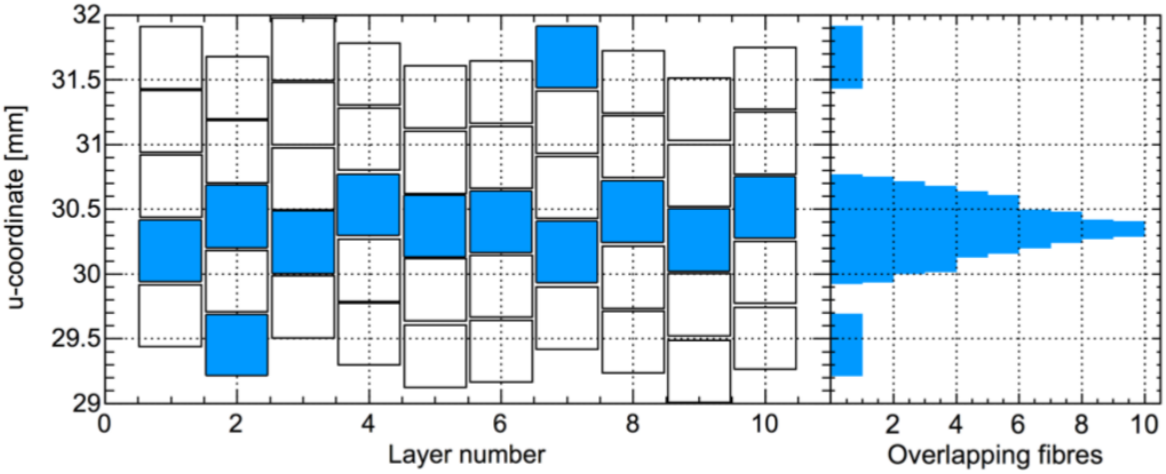

Figure 2.19: Hit pattern in the U coordinate of a reconstructed proton trajectory in one ALFA detector. Figure taken from [197]

determines the resolution. There may be more than one proton passing the detector. All of these are found by the reconstruction algorithm and stored as a possible track candidates. It is crucial to precisely determine the position of the detectors with respect to the beam in order to reconstruct the proton kinematics. Therefore, the two-step alignment procedure is introduced [196], that is based on the beam-halo and elastic events analyses. In the next step, track U and V coordinates in each of the detector are transformed to the beam reference frame (x, y).

The proton coordinates $u = x, y$ in each of the ALFA detectors is parametrized by [199]:

$$u\left(u_{\mathrm{IP}}, \frac{p_{u,\mathrm{IP}}}{p}, \frac{\Delta p}{p}\right) = F_u\left(\frac{\Delta p}{p}\right) u_{\mathrm{IP}} + G_u\left(\frac{\Delta p}{p}\right)\left(\frac{p_{u,IP}}{p}\right) + H_u\left(\frac{\Delta p}{p}\right) \tag{2.13}$$

where p is the proton momentum, p_u is the component of its transverse momentum, F_u, G_u and H_u are quartic polynomials of the proton momentum loss, $\Delta p/p$. The subscript "IP" denotes the values at the IP. Finally, the F_u, G_u and H_u functions are fitted to the output from a MC simulation. A detailed description of the above parametrization can be found in [199].

Chapter 3

STAR Data Analysis

3.1 Roman Pot Simulation

The RP detectors and the related beam line modifications are not implemented in the standard STAR detector simulation within the GEANT3 framework [215]. Therefore, a standalone simulation of the RP system [216, 217] together with the RHIC magnet lattice [218, 219] was developed within the GEANT4 framework [220]. The application was originally dedicated to the configuration of the RPs for RHIC Run 2009 [151]. When the RPs were moved to their current location in the RHIC tunnel, the configuration was updated. The geometry of RHIC, i.e. magnets and beampipe, is based on the technical drawings of RHIC, whereas the MAD-X [221] output provided information about the magnetic field of the RHIC DX magnets. In case of the RP vessels and SSDs, technical drawings together with a dedicated survey were used to best implement their geometry.

Figure 3.1 shows the GEANT4 visualisation of the RP setup together with all beam-line elements. In addition, the implementation of the RP vessels and SSDs is presented.

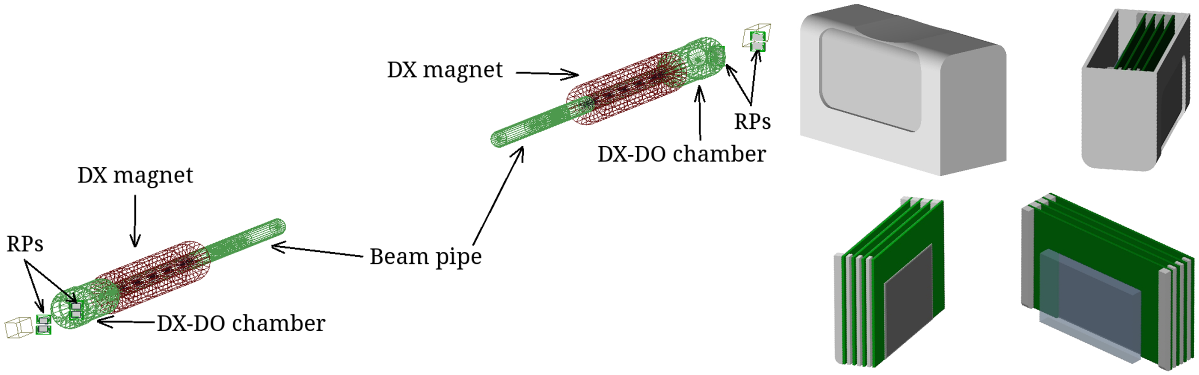

Figure 3.1: (left) GEANT4 implementation of the RP system and (right) RP vessel together with SSD. Figure courtesy of R. Sikora (STAR Collaboration).

3.2 Monte Carlo Samples

MC samples used to correct data for detector effects were obtained by the embedding MC technique [154], in which particles produced by MC event generators are mixed with the real Zerobias (ZB) events at the raw data level. ZB data events used in the embedding MC were sampled over the entire data-taking period in order to properly describe the data set used in the analysis. Two samples of embedding MC were produced:

1. single particle MC, in which particles are generated from flat distributions in η and p_{T}, in order to have similar statistics in all bins,
2. the SaS model implemented in PYTHIA 8 with 4C tune.

Generated particles were passed through the full simulation of the STAR TPC and RP system detectors using GEANT3 and GEANT4, respectively, and then embedded into real data sample. These embedding events were next processed through the full event reconstruction chain.

It is preferred to get the detector corrections from a MC, which is dedicated to simulate the studied physics process. However, for this purpose, the statistics in the MC should be several times greater than in the analysed data sample. Since this is not possible with low efficiency of TPC and TOF, the basic method of corrections used in the analysis for p_{T} and $\bar{\eta}$ distributions is a method of factorization of global efficiency into the product of single-particle efficiencies. In this way, statistically precise multidimensional corrections on TPC and TOF were obtained from the single particle MC. The energy loss correction was also determined from the same MC sample. The charged-particle multiplicity distributions were unfolded from the measured multiplicities of TPC tracks based on the response matrix, which takes into account all detector effects. In this procedure single particle MC samples were not used.

All other detector corrections were obtained from PYTHIA 8 4C (SaS). In order to keep statistical precision coming from the corrections high, samples filtered on true-level values of ξ and t (not necessarily with reconstructed proton track in RP) are used.

Systematic uncertainty related to hadronization of the diffractive system was determined by using alternative hadronization models as implemented in HERWIG and EPOS. In these simulations particles were propagated through the full simulation and reconstruction chain, but were not embedded into ZB events.

Results are compared to model predictions from PYTHIA 8 4C (SaS), HERWIG, EPOS and alternative PYTHIA 8 model MBR with A2 tune. In all PYTHIA 8 models, diffractive cross sections are scaled by some factors (Sec. 1.2.4). As a result, diffractive cross sections are artificially suppressed at relatively large values of ξ ($>$0.05). This artificial suppression significantly changes predicted distribution of ξ and fractions of different processes in our fiducial phase space. Therefore, data is also compared to expectations obtained without suppression of the diffractive cross sections (MBR-tuned).

Figure 3.2 (left) shows the distribution of ξ generated with EPOS (SD and SD+SD$'$) and PYTHIA 8 SD (SaS, MBR and MBR-tuned). PYTHIA 8 (MBR) predicts a strong

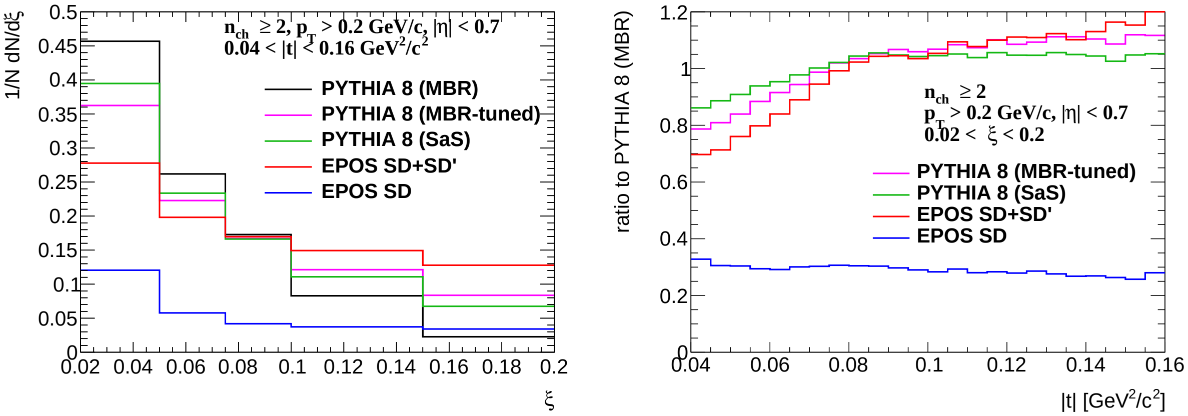

Figure 3.2: (left) ξ distribution for various MC generators and (right) ratios of different MCs to PYTHIA 8 (MBR) predictions as a function of $|t|$ at $\sqrt{s} = 200$ GeV.

dependence of the cross section on ξ, which is much weaker in PYTHIA 8 (SaS and MBR-tuned) and the weakest in EPOS. This difference between PYTHIA 8 SaS and MBR models is expected since they are based on different Pomeron trajectories (Sec. 1.2.4). Only 30% of events in EPOS are SD, while the rest are SD′. Since all MC samples were generated with forward proton filter (a cut on the proton position in front of the RPs), the shapes of $|t|$ distributions for these samples are biased. In order to compare them with each other, only their ratio to PYTHIA 8 (MBR) predictions is presented as a function of $|t|$. EPOS SD is only relevant for very small $|t|$ (below 0.04 GeV^2/c^2) and is suppressed in the STAR acceptance region, $0.04 < |t| < 0.16$, where EPOS SD′ contribution dominates. The t-slope is very different for EPOS SD and EPOS SD′, while it is similar for EPOS SD+SD′ and PYTHIA 8 (SaS and MBR-tuned), EPOS SD and PYTHIA 8 (MBR). This is related to the smaller average value of ξ for EPOS SD and PYTHIA 8 (MBR) compared to EPOS SD+SD' and PYTHIA 8 (SaS and MBR-tuned).

3.3 Data Sample and Event Selection

The data sample used in this analysis was collected in proton-proton collisions at centre-of-mass energy of $\sqrt{s} = 200$ GeV during RHIC Run 15, i.e. in year 2015.

All of the studies in this analysis use data from only the SDT trigger condition, which was the main trigger designed for SD studies in Run 15. The logic of the trigger was formed by the following conditions combined with the logical AND:

1. RP_EOR || RP_WOR - signal in at least one RP on any side of the STAR central detector,
2. veto on any signal in small BBC tiles or ZDC on the triggered RP side of the STAR central detector,

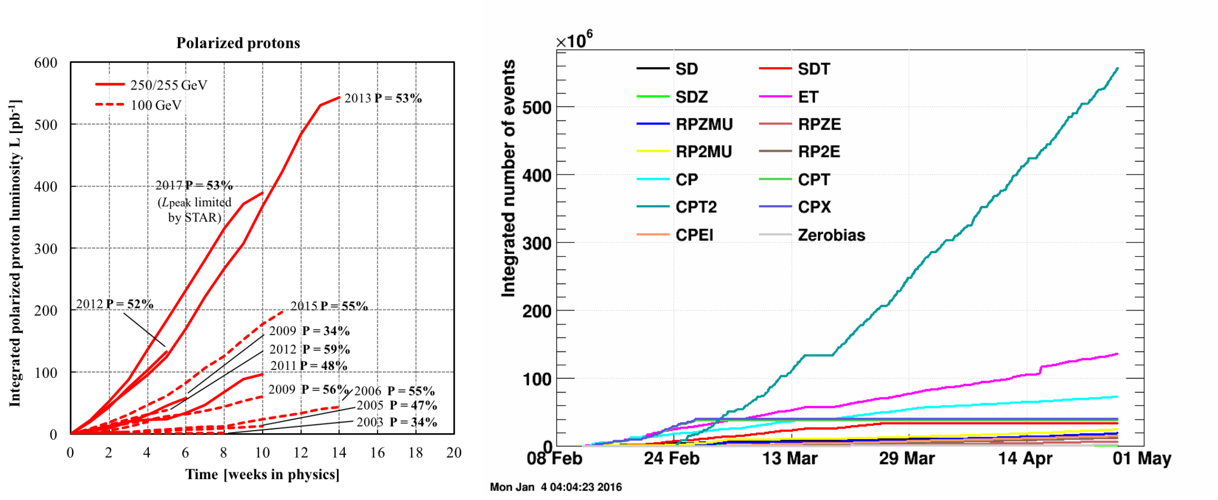

Figure 3.3: (left) Integrated luminosity delivered by the collider over the seventeen years of operation of RHIC [139]. Dashed lines are for 100 GeV/c proton momentum mainly for transverse spin physics programs, while continuous lines are for 250/255 GeV/c proton beams aimed predominantly at the *W*-physics program. The percentage polarization reached in each run is indicated next to the curves. (right) Cumulative number of events collected for each trigger in the RP data stream during Run 15.

3. at least two TOF hits.

The above requirements were imposed in accordance with the diffractive event topology. Veto on any signal in small BBC tiles and ZDC allowed to accept only events with rapidity gap and reject diffractive events with simultaneous pile-up event. The requirement of at least two TOF hits was applied to ensure activity in the mid-rapidity.

Integrated luminosity delivered by the RHIC to the STAR experiment in *pp* collisions during Run 15 amounts to 185.1 pb^{-1} [139], shown in Fig. 3.3, whereas about 34.4M SDT events were gathered by the STAR detector, which corresponds to 16 nb^{-1} of integrated luminosity.

Event Selection

Events were selected from those passing the SDT trigger condition. In order to remove events of poor quality and to suppress background the following conditions were required:

1. trigger signals in exactly two stations of one arm of RP system (this requirement divides the sample into four sub-samples, which were later analysed independently, e.g. for background studies),

2. any trigger signal in small BBC tiles on the opposite side of the STAR central detector to the triggered RP station,

3. exactly one proton track in the above RP stations with $0.02 < \xi < 0.2$ and $0.04 < -t < 0.16$ GeV^2/c^2.

4. exactly one vertex reconstructed from TPC tracks matched with hits in TOF (later in the text such vertex is referred as a TOF vertex),

5. TOF vertex within $|V_z| < 80$ cm - events with vertices away from the nominal IP have low acceptance for the central and forward tracks,

6. at least two but no more than eight primary TPC tracks, $2 \leq n_{\mathrm{sel}} \leq 8$, matched with hits in TOF and satisfying the selection criteria described in Sec. 3.3,

7. if there are exactly two primary tracks satisfying the above criteria and exactly two global tracks used in vertex reconstruction (Sec. 3.7), the longitudinal distance between these global tracks should be smaller than 2 cm, $|\Delta z_0| < 2$ cm.

Figure 3.4 shows the multiplicity of TOF vertices n_{vrt} (left) and the z-position of reconstructed vertices in single TOF vertex events (right). Data are compared to embedded PYTHIA 8 SD sample. These distributions are not significantly process-dependent, therefore, contributions from other processes are not included in these plots. Most events with $n_{\mathrm{vrt}} > 1$ originate from in-time pile-up and are excluded from the analysis.

Track Selection

The following quality cuts had to be passed by the selected primary tracks:

1. the tracks must be matched with hits reconstructed in TOF,

2. the number of the TPC hits used in the helix fit $N^{\mathrm{fit}}_{\mathrm{hits}}$ must be greater than 24,

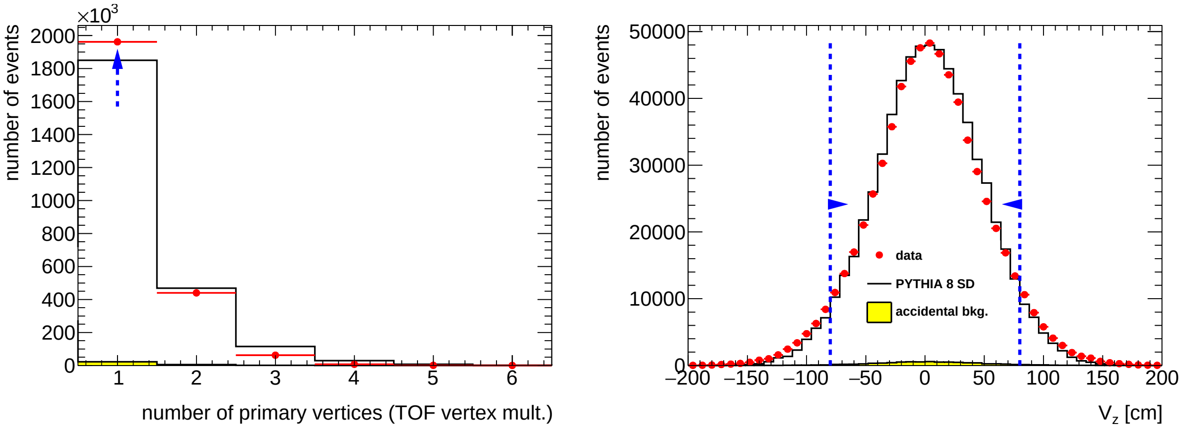

Figure 3.4: (left) Vertex multiplicity and (right) the z-position of reconstructed vertices in single TOF vertex events before applying the cut on the quantity shown. Blue lines indicate regions accepted in the analysis.

3. the ratio of $N_{\text{hits}}^{\text{fit}}$ to the number of all possible TPC hits, $N_{\text{hits}}^{\text{fit}}/N_{\text{hits}}^{\text{possible}}$, must be greater than 0.52,
4. the number of the TPC hits used to determine the dE/dx information $N_{\text{hits}}^{\text{dE/dx}}$ must be greater than 14,
5. the transverse impact parameter with respect to the beamline d_0 must be less than 1.5 cm,
6. the radial component of the distance of the closest approach between the global helix and the vertex DCA_{xy} must be less than 1.5 cm,
7. the absolute magnitude of longitudinal component of the distance of the closest approach between the global helix and the vertex $|\text{DCA}_z|$ must be less than 1 cm,
8. the track's transverse momentum p_{T} must be greater than 0.2 GeV/c,
9. the track's absolute value of pseudorapidity $|\eta|$ must be smaller than 0.7.

The $N_{\text{hits}}^{\text{fit}}$ and $N_{\text{hits}}^{\text{fit}}/N_{\text{hits}}^{\text{possible}}$ cuts are used to reject low quality TPC tracks and avoid track splitting effects. The d_0 and global DCA_{xy}, $|\text{DCA}_z|$ cuts are used to select tracks that originate from the primary interaction vertex. The cut on $N_{\text{hits}}^{\text{dE/dx}}$ is used to ensure that selected tracks have sufficient energy loss information for particle identification purposes. In this analysis tracks without identification are required to have $p_{\text{T}} > 0.2$ GeV/c and $|\eta| < 0.7$ due to high track reconstruction and TOF matching efficiencies in this region. For the identified particle-antiparticle ratio analysis, where charged pions, charged kaons and (anti)protons are measured, the p_T cut was increased for kaons and (anti)protons to 0.3 and 0.4 GeV/c, respectively. The distributions of the DCA_{xy}, $|\text{DCA}_z|$, d_0, $N_{\text{hits}}^{\text{fit}}$ and $N_{\text{hits}}^{\text{dE/dx}}$ quantities together with applied cuts are shown in Fig. 3.5, while the p_T, η and the azimuthal angle, ϕ, of the reconstructed tracks are shown in Fig. 3.6. Data are compared to embedded PYTHIA 8 SD sample. The azimuthal angle of the reconstructed tracks is not described by the simulation in the region of dead TPC sector.

3.4 Fiducial Region of the Measurement

A fiducial phase space of measurement is defined by the following criteria. Primary charged particles are defined as charged particles with a mean lifetime $\tau > 300$ ps, either directly produced in pp interaction or from subsequent decays of directly produced particles with $\tau < 30$ ps. Primary charged particles had to be contained within the kinematic range of $p_{\text{T}} > 0.2$ GeV/c and $|\eta| < 0.7$. The results are corrected to the region of the total number of primary charged particles (without identification), $2 \leq n_{\text{ch}} \leq 8$. In identified charged antiparticle to particle ratio measurement, the lower transverse momentum limit was set for the analysed particles as follows: 0.2 GeV/c (pions), 0.3 GeV/c (kaons), 0.4 GeV/c (protons and antiprotons).

The measurements were performed in a fiducial phase space of the forward-scattered protons of $0.04 < -t < 0.16$ GeV^2/c^2 and $0.02 < \xi < 0.2$. Figure 3.7 shows that the fraction of events containing at least two primary charged particles, $\epsilon_{n_{\rm ch}\geq 2}(\log_{10}\xi)$, is reduced by half for $\xi < 0.02$ compared to the region of larger ξ. In addition, the accidental back-

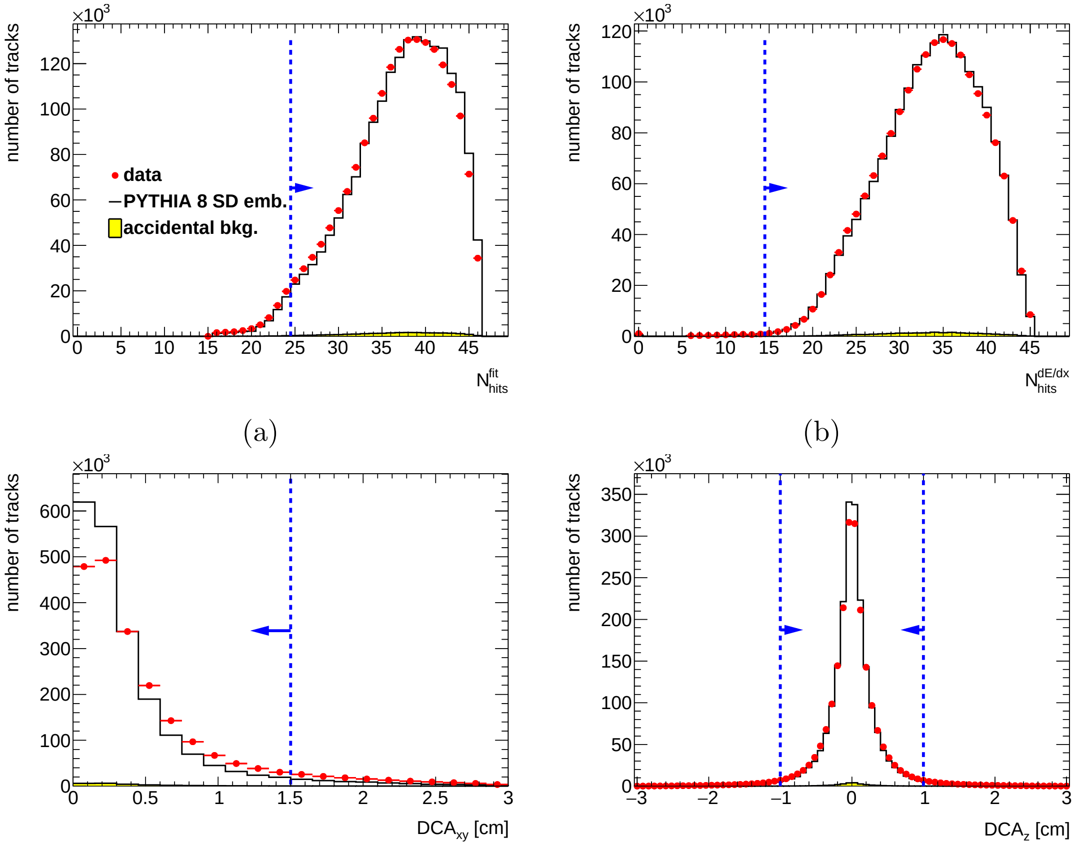

(a) (b)

(c) (d)

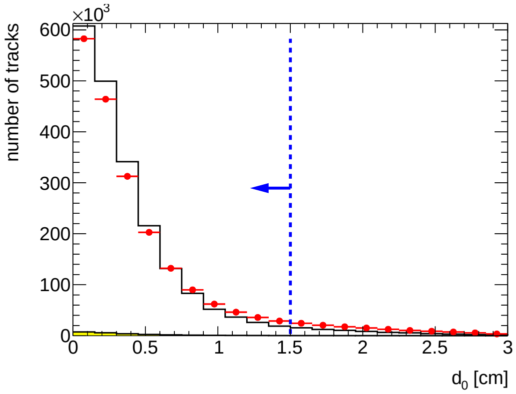

(e)

Figure 3.5: Number of the TPC hits used in the helix fit (a) and number of the TPC hits used to determine the dE/dx (b), the radial component (c) and the absolute magnitude of the longitudinal component (d) of the distance of the closest approach between the global helix and the vertex, transverse impact parameter w.r.t. beamline (e). All distributions are shown before applying the corresponding cuts. Blue lines indicate regions accepted in the analysis.

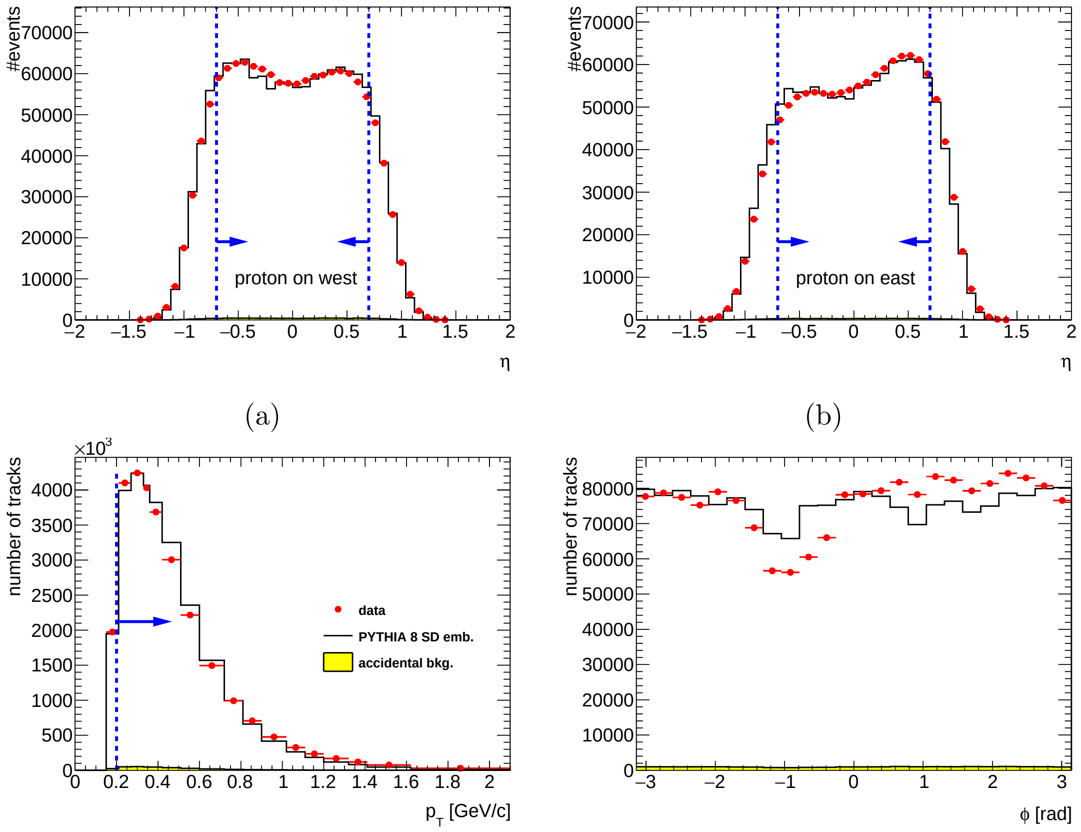

(a) (b)

(c) (d)

Figure 3.6: Pseudorapidity of the reconstructed tracks for events in which forward-scattered proton is on west (a) and east (b) side of the IP, track transverse momentum (c) and track azimuthal angle (d). All distributions are shown before applying the corresponding cuts. Blue lines indicate regions accepted in the analysis.

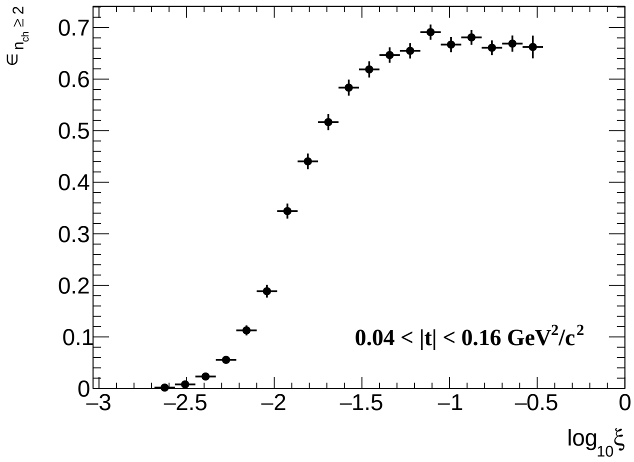

Figure 3.7: $\epsilon_{n_{\rm ch}\geq 2}$ as a function of $\log_{10}\xi$ calculated from PYTHIA 8 (MBR).

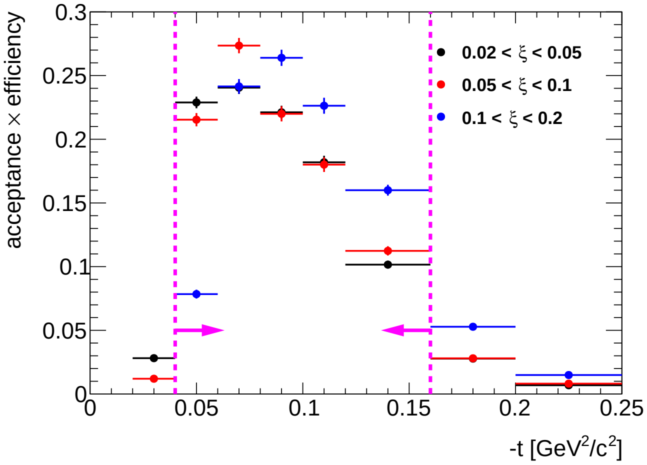

Figure 3.8: RP acceptance and track reconstruction efficiency as a function $-t$ in three ranges of ξ, calculated using PYTHIA 8 4C (SaS). Magenta lines indicate region accepted in the analysis.

ground contribution at $\xi < 0.02$ is significant and approximately equal to 10% (Sec. 3.5). For these reasons the lower ξ cut was introduced. The upper ξ cut was required since the region of larger ξ is dominated by DD and ND (Sec. 3.6). The joint RP acceptance and track reconstruction efficiency was defined as the probability that true-level proton was reconstructed as a track passing the selection criteria. This efficiency was calculated as a function of $-t$ for three ranges of ξ separately and is shown in Fig. 3.8. Events were accepted only if the reconstructed values of $-t$ for protons fall within $> 5\%$ acceptance regions, which were required to be the same for each ξ region and similar to those defined in the elastic analysis [88]. Therefore, cuts on $0.04 < -t < 0.16$ GeV^2/c^2 were introduced. All measured observables are presented in three ξ regions: $0.02 < \xi < 0.05$, $0.05 < \xi < 0.1$ and $0.1 < \xi < 0.2$.

3.5 Background Contribution

The background contributions to the charged-particle distributions can be divided into event-level and track-level backgrounds, and are described in detail below:

- Accidental background refers to events which do not originate from a single collision of two protons.
- Track backgrounds from non-primary tracks consist of secondary tracks and fake tracks; the first come mostly from decays, the short-lived particles with mean life $30 < \tau < 300$ ps, or secondary interactions with the detector dead material, while the second comes from the track reconstruction algorithms and out-of-time pile-up with no corresponding true particles.

Accidental Background

The accidental backgrounds (same bunch pile-up background) are quantified using data-driven method and defined as a process where in single bunch crossing there is coincidence of two interactions, where any single-side proton signal is collected in coincidence with an independent signal in the TPC+TOF+BBC detector. This type of background may come from the overlap of a signal in RP (proton from beam-halo, low mass SD process without activity in TOF, elastic or low mass CD processes with undetected proton on the other side) with a signal in TPC+TOF+BBC (mainly ND events without forward-scattered proton).

The accidental background contribution was calculated from ZB data (colliding bunches), where two signatures of such background were investigated: the reconstructed proton in RP and the reconstructed vertex from TPC tracks matched with TOF. The analysis was done for each RP arm separately and thus the ZB data was firstly required to pass the following criteria:

1. no trigger in any RP or trigger in exactly one arm (two RPs) with exactly one reconstructed proton track in that arm,
2. veto on any signal in small BBC tiles or ZDC on the same side of the IP as the RP arm under consideration,
3. no or exactly one reconstructed vertex with at least two TOF-matched tracks passing the quality criteria. The latter includes also signal in BBC small tiles on the opposite side of the IP to the RP arm under study.

The sample of selected ZB data with total number of events N was divided into four classes:

$$N = N_{PS} + N_{RS} + N_{PT} + N_{RT} \tag{3.1}$$

where: N_{PS} is the number of events with reconstructed proton in exactly one RP and reconstructed TOF vertex, N_{RS} is the number of events with no trigger in any RP and reconstructed TOF vertex, N_{PT} is the number of events with reconstructed proton in exactly one RP and no reconstructed TOF vertex, N_{RT} is the number of events with no trigger in any RP and no reconstructed TOF vertex.

Since the signature of the signal is a reconstructed proton in exactly one RP and a reconstructed TOF vertex, the number of such events can be expressed as:

$$N_{PS} = N\,(p_3 + p_1 p_2) \tag{3.2}$$

where: p_1 is the probability that there is a reconstructed proton in RP and there is no reconstructed TOF vertex, p_2 is the probability that there is no reconstructed proton in RP and there is a reconstructed TOF vertex, p_3 is the probability that there is a reconstructed proton in RP and there is a reconstructed TOF vertex (not accidental).

The other classes of events given in Eq. (3.1) can be expressed in terms of the above probabilities as:

$$\begin{aligned} N_{RS} =& N(1-p_1)p_2(1-p_3) \\ N_{PT} =& N(1-p_2)p_1(1-p_3) \\ N_{RT} =& N(1-p_1)(1-p_2)(1-p_3) \end{aligned} \tag{3.3}$$

Finally, the accidental background contribution $A_{\text{bkg}}^{\text{accidental}}$ is given by:

$$A_{\text{bkg}}^{\text{accidental}} = \frac{p_1 p_2}{p_3 + p_1 p_2} = \frac{N_{RS} N_{PT} N}{N_R N_T N_{PS}} \tag{3.4}$$

where: $N_R = N_{RS} + N_{RT}$ and $N_T = N_{PT} + N_{RT}$.

The shapes of the accidental background related to TPC distributions come from the above ZB data events which pass all the analysis selection except having no trigger in any RP. The templates corresponding to RP distributions are from protons in the above data sets but with no reconstructed TOF vertex. The normalization is given by Eq. (3.4). Figure 3.9 shows distributions of the reconstructed ξ with the accidental background contribution for events with proton reconstructed in EU, ED, WU and WD arms. Accidental background in the range of $0.02 < \xi < 0.2$ is below 1% and increases to 10% at $\xi < 0.02$. Unphysical negative values of reconstructed ξ are due to the detector resolution.

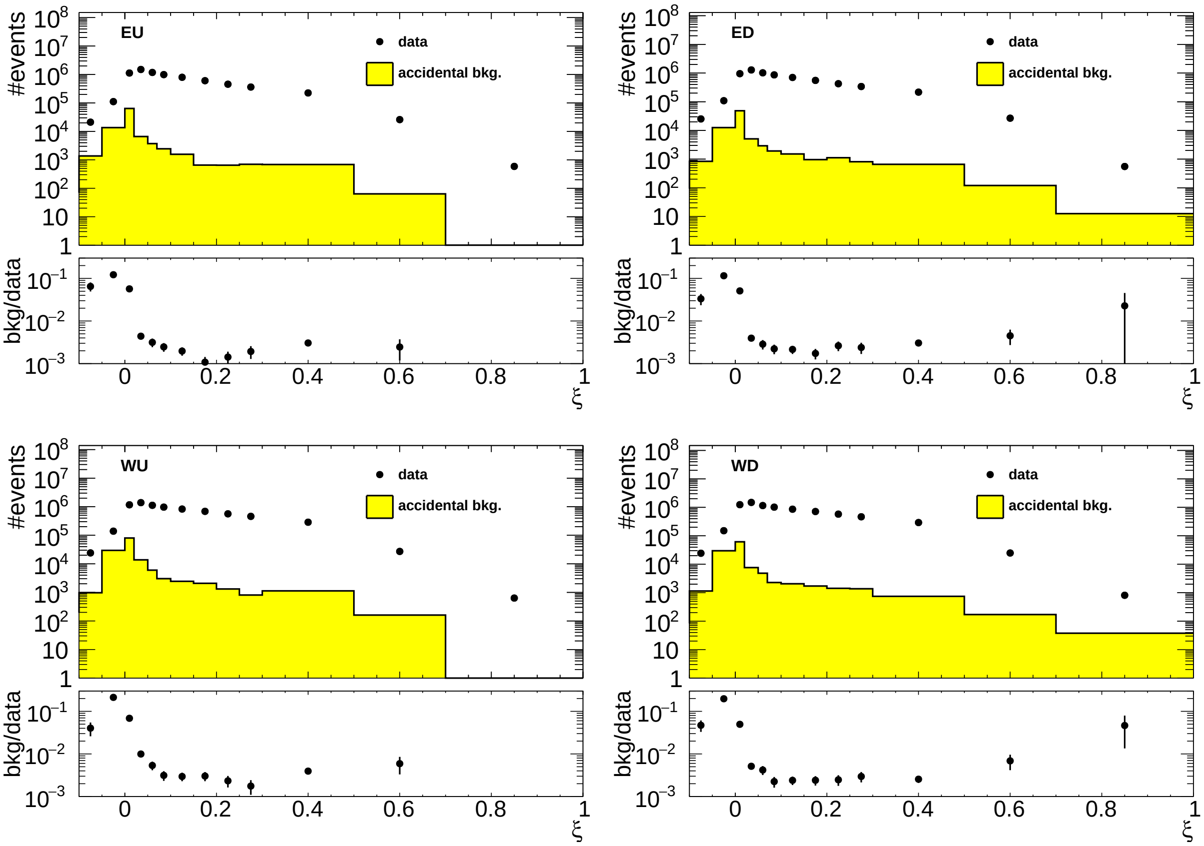

Figure 3.9: Uncorrected distributions of the reconstructed ξ for events with proton reconstructed in (top left) EU, (top right) ED, (bottom left) WU and (bottom right) WD arms. Data is shown as black markers, whereas the accidental background contribution is shown as yellow histogram. The ratio of accidental background and data is shown in the bottom panels.

The selection of ZB events, which is not unique, may provide some bias to the normalization of the accidental background. As a systematic check, two criteria for ZB selection were changed to:

1. no trigger in any RP or trigger in exactly one arm (two RPs) with *no more* than one reconstructed proton track in that arm, i.e. events with trigger signals in exactly one arm and without reconstructed proton track in that arm were also used,

2. no or exactly one reconstructed TOF vertex (*without any additional requirements*), i.e. events with a reconstructed TOF vertex that does not have at least two primary tracks satisfying the selection criteria (Sec. 3.3), or with a reconstructed TOF vertex that is out of the range of $|V_z| < 80$ cm, were also accepted. The requirement of signal in BBC small tiles remains unchanged.

As a result of this change, the accidental background normalization increases of about 50% with respect to the nominal value. A symmetric systematic uncertainty of 50% of the normalization of accidental background is applied to the measurement.

Background from Non-Primary Tracks

Reconstructed tracks matched to a non-primary particle, so-called background tracks, originate mainly from the following sources:

- decays of short-lived primary particles with strange quark content (mostly K^0, Λ^0),
- photons from π^0 and η decays which are converting to e^+e^-,
- hadronic interactions of particles with the beam-pipe or detector dead material.

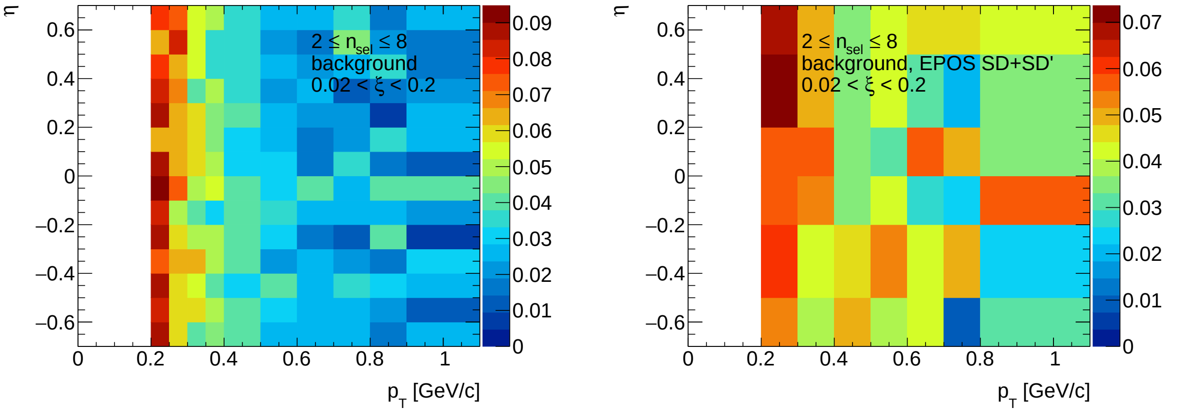

Figure 3.10: Distribution of fraction of selected tracks associated with non-primary particles in the range $0.02 < \xi < 0.2$ as predicted by (left) PYTHIA 8 4C (SaS) embedding and (right) EPOS SD+SD′.

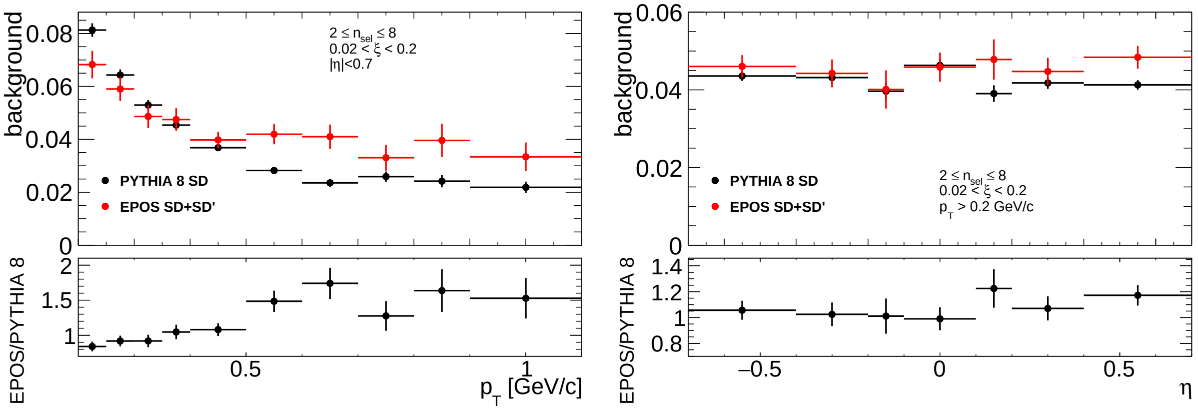

Figure 3.11: PYTHIA 8 SD and EPOS SD+SD′ predictions of fraction of selected tracks associated with non-primary particles as a function of (left) p_{T} and (right) η. The ratio of EPOS and PYTHIA 8 predictions is shown in the bottom panels.

Figure 3.10 (left) shows the background from non-primary tracks, $f_{\mathrm{bkg}}\,(p_{\mathrm{T}}, \eta)$, as a function of tracks' p_{T} and η, predicted by PYTHIA 8 SD model. There were no differences observed in the background contribution in different ξ ranges, hence, all three ξ ranges were merged for this study. The highest background fraction, which varies between $5 - 10\%$, was found to be at low p_{T}.

Figure 3.10 (right) shows the background track contribution to reconstructed tracks as a function of p_{T} and η calculated from EPOS SD+SD′. The differences between PYTHIA 8 and EPOS, which are up to 50% for $p_{\mathrm{T}} > 0.5$ GeV/c (as shown in Fig. 3.11), were symmetrized and taken as a systematic uncertainty.

There is also a small ($< 0.5\%$) contribution from fake tracks, $f_{\mathrm{fake}}\,(p_{\mathrm{T}}, \eta)$, i.e. tracks not associated with true-level particles, coming from out-of-time pile-up or formed by a random combination of TPC hits. The change by ±100% in this contribution was taken as a systematic uncertainty.

Proton Background

Secondary particles can be created due to the interaction of particles with detector dead-material. The proton sample contains background from such protons knocked out from the detector materials [25]. Most of these protons have large DCA to the primary vertex and are not associated with it. However, the protons with small DCA are included in the primary track sample. Antiprotons do not have knock-out background, hence the DCA tail is almost absent in their DCA distributions.

The fraction of knock-out background protons depends on a number of factors, including the amount of detector material, analysis cuts and the ξ of diffractive proton. While it is natural to calculate the fractions of primary and background protons in the MC sample, the MC models do not necessarily predict the fraction of knock-out background protons without any bias. Hence, data-driven methods should be used to calculate this type of background.

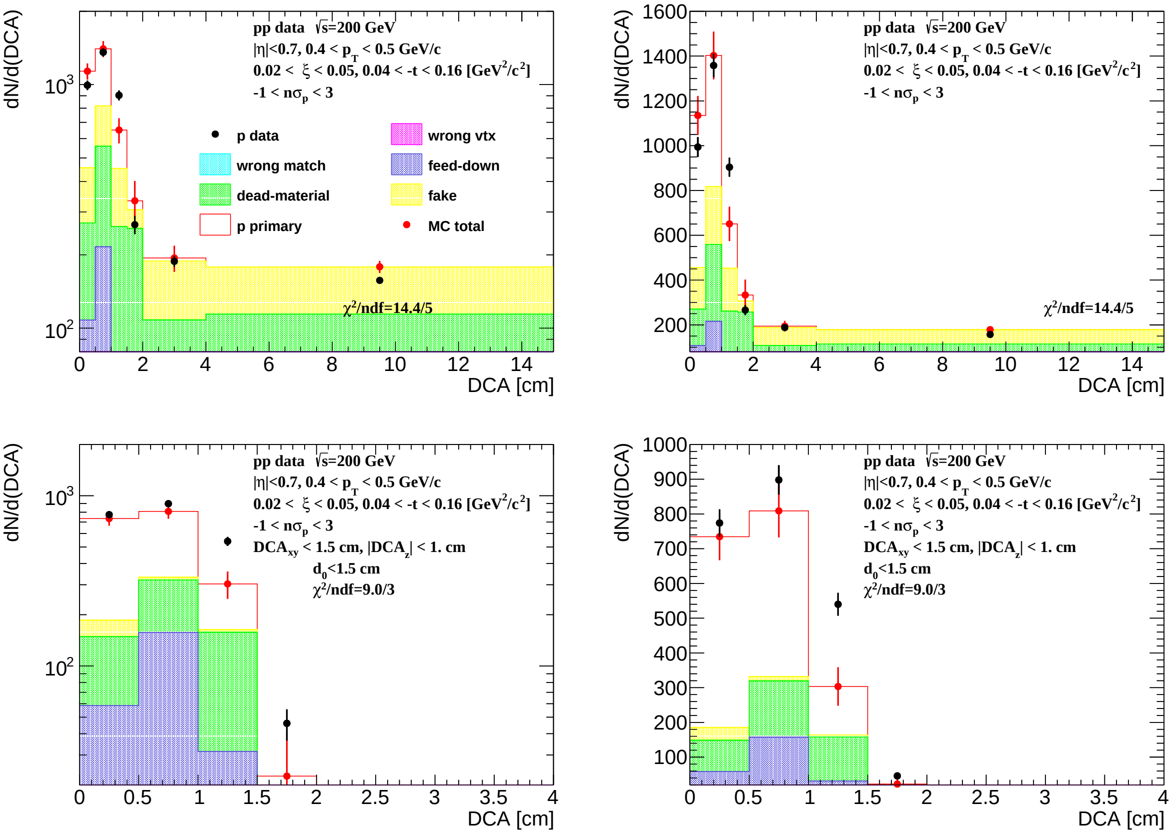

Figure 3.12: The DCA distributions of protons for $0.4 < p_T < 0.5$ GeV/c shown for single range of $0.02 < \xi < 0.05$ (shown in log and linear scale in left and right column, respectively). The MC contributions are shown after scaling the dead-material template to the tail of large DCA values, $2 <$ DCA < 15 cm. (top) Background enriched samples were used in the normalization procedure, whereas (bottom) the proton background was estimated from the nominal sample.

In order to correct for the knock-out background protons, sample enriched in proton background was used for background normalization, where DCA$_{xy}$, DCA$_z$ and d_0 cuts were abandoned. Additionally, at least one, instead of exactly one, reconstructed vertex was allowed in this sample. Figures 3.12 and 3.14 show the DCA distributions of protons and antiprotons, respectively, for nominal (bottom) and background enriched (top) samples. The protons and antiprotons are selected by a dE/dx cut of $-1 < n\sigma_{p,\bar{p}} < 3$ where $n\sigma_{p,\bar{p}}$ is given by Eq. (3.30). In some p_{T} regions, the dE/dx of (anti)protons starts to overlap with kaons and pions, hence, the asymmetric $n\sigma_{p,\bar{p}}$ cut was introduced in order to select as clean (anti)proton sample as possible. The fraction of knock-out protons within the selected sample is determined via MC template fits. The templates of reconstructed tracks with dE/dx corresponding to the proton and antiproton are obtained from PYTHIA 8 embedding MC separately for:

- primary (anti)protons,
- knock-out background protons (labelled as dead-material),
- fake tracks,
- tracks associated with primary (anti)protons, but with the reconstructed vertex not matched to the true-level primary vertex (labelled as wrong vtx),
- reconstructed track is partially matched to the true-level particle (labelled as wrong match, track to true-level particle matching is described in 3.7), i.e. track and true-level particle have appropriate number of common hit points but the distance between true-level particle and track is too large, $\delta^2(\eta,\phi) > (0.15)^2$, thus, track is not considered as corresponding to a primary particle,
- (anti)proton as a product of short-lived decays, mainly Λ^0 (labelled as feed-down).

First, the background enriched sample was analysed (Fig. 3.12, top), where the template of knock-out background protons was normalized to the number of events in the fake-subtracted tail of the DCA distribution, $2 < \mathrm{DCA} < 15$ cm. Next the knock-out proton and fake background was subtracted from the DCA distribution and the sum of other templates was normalized to the number of events in the signal region, $\mathrm{DCA} < 1.5$ cm.

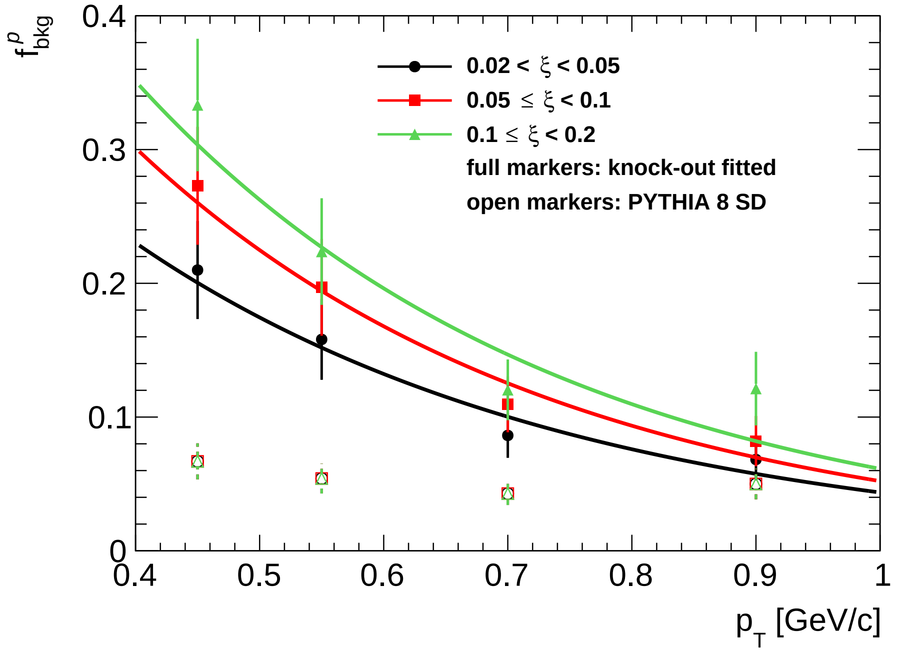

Figure 3.13: The fraction of knock-out proton background as a function of p_{T} in three ranges of ξ with fitted parametrizations. Full markers represent fitted knock-out background and open markers represent PYTHIA 8 SD predictions.

The fraction of the knock-out proton background in the signal region, DCA < 1.5, was estimated from the nominal sample (Fig. 3.12, bottom), where DCA$_{xy}$, DCA$_z$ and d_0 track cuts were applied and exactly one reconstructed vertex was required. The normalization of each MC contribution was kept the same as that estimated for the background enriched sample. Figure 3.13 shows the knock-out proton background as a function of p_{T} in three ranges of ξ. The following functional form was found to describe the background protons:

$$f^{p}_{\mathrm{bkg}}\left(p_{\mathrm{T}}\right) = p_0 \exp\left(p_1 p_{\mathrm{T}}\right) \tag{3.5}$$

where p_0 and p_1 are free parameters obtained from a fit.

The obtained fraction of knock-out background protons is approximately 20% at $p_{\mathrm{T}} = 0.45$ GeV/c and less than 10% at $p_{\mathrm{T}} = 1.0$ GeV/c. In PYTHIA 8 SD predictions (also shown in Fig. 3.13), such fraction is much smaller and equals to approximately 7% at $p_{\mathrm{T}} = 0.45$ GeV/c and about 5% at $p_{\mathrm{T}} = 1.0$ GeV/c. This may suggest that there are differences in the amount of dead material in front of TPC between data and simulation, which is consistent with the studies described in Sec. 3.7.

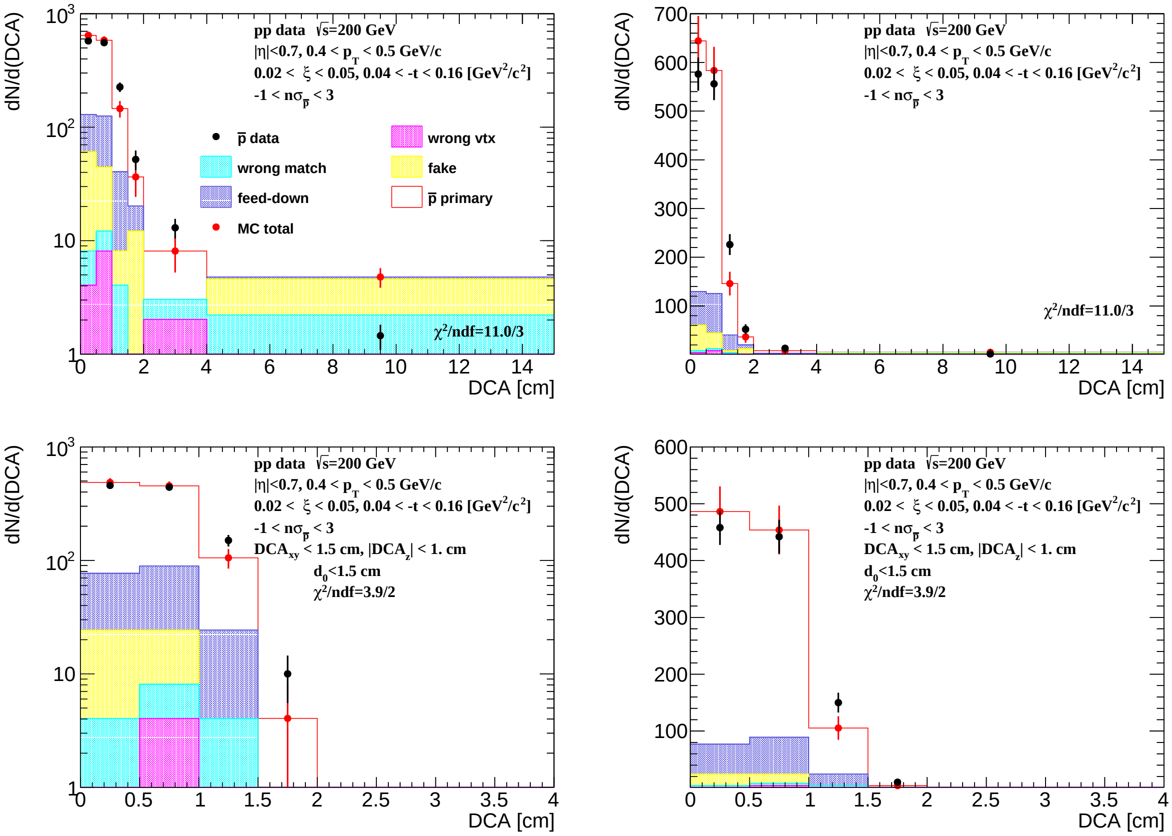

Figure 3.14: The DCA distributions of antiprotons for $0.4 < p_{\mathrm{T}} < 0.5$ GeV/c shown for one range of $0.02 < \xi < 0.05$ (log and linear scale in left and right column, respectively). The MC contributions are shown as colour histograms. (top) Background enriched and (bottom) nominal samples were used.

Figure 3.14 shows the corresponding DCA distributions with MC templates for antiprotons, where the background from knock-out particles is not present. Therefore, there was no need for any fit to be performed in this comparison. The MC templates fairly well describe the DCA distribution for both, protons, after tunning the fraction of knock-out background to data, and antiprotons.

Systematic Uncertainty Related to Proton Background

The knock-out proton background estimation introduces systematic uncertainties. First, the normalization interval of the knock-out proton background template in the background enriched sample was changed to $4 < \mathrm{DCA} < 15$ cm. This introduced a relative systematic uncertainty of up to 30% for $p_\mathrm{T} \approx 0.9$ GeV/c.

The knock-out proton background contribution was parametrized as it is shown in Eq. (3.5). The systematic uncertainty related to the parametrization procedure was es-

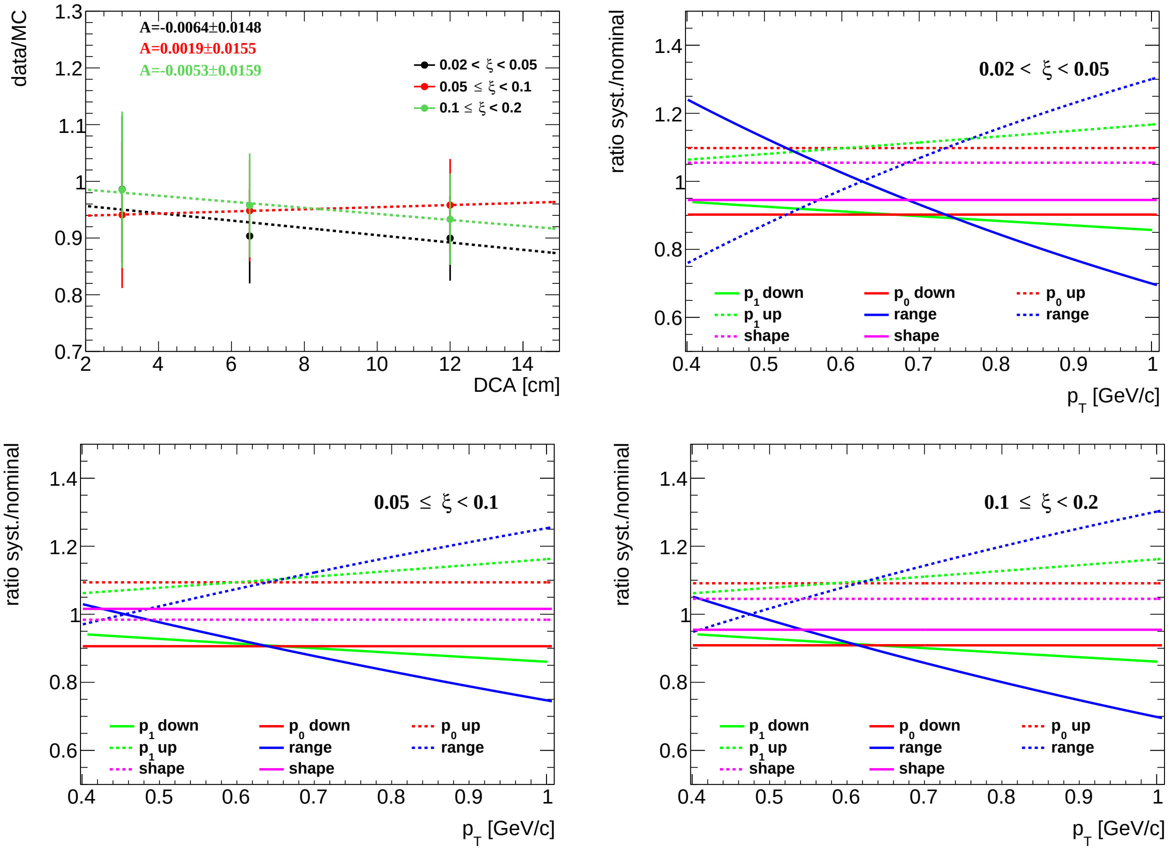

Figure 3.15: (top left) Data to MC ratio of the number of events in the background dominated region in three ranges of ξ with fitted functional form given by Eq. (3.6). (top right and bottom) Components of the systematic uncertainty related to the knock-out background protons contribution in three ξ ranges.

timated by varying the parameters, p_0 and p_1, by their statistical uncertainties ($\pm 1\sigma$). As a result, a relative systematic uncertainties of about 10% were obtained.

Differences in the shape of the DCA distribution between data and MC can affect the knock-out proton background estimation procedure. Figure 3.15 (top left) shows the data to MC ratio of the number of events in the background dominated region, $2 < \mathrm{DCA} < 15$ cm. Since this region is used to estimate background normalization, and the shape of the DCA distribution in the data differs from that observed in the simulation, the predicted background in the DCA < 1.5 cm region can change. Thus, the following functional form was used to estimate the slope between data and MC:

$$\frac{\mathrm{data}}{\mathrm{MC}}(\mathrm{DCA}) = A(\mathrm{DCA} - 8.5 \text{ cm}) + B \tag{3.6}$$

where A (slope) and B are fit free parameters. Differences in slope between data and MC were used to estimate how many more background tracks would fit into the signal region and a systematic uncertainty, which varies up to 5% for $0.02 < \xi < 0.05$, was introduced.

All above components of the systematic uncertainty related to the knock-out proton background, shown in Fig. 3.15, are added in quadrature. Those related to the fit range and the shape of the proton background are symmetrized. Figure 3.16 shows the fraction of knock-out proton background in three ranges of ξ and the total systematic uncertainty related to it.

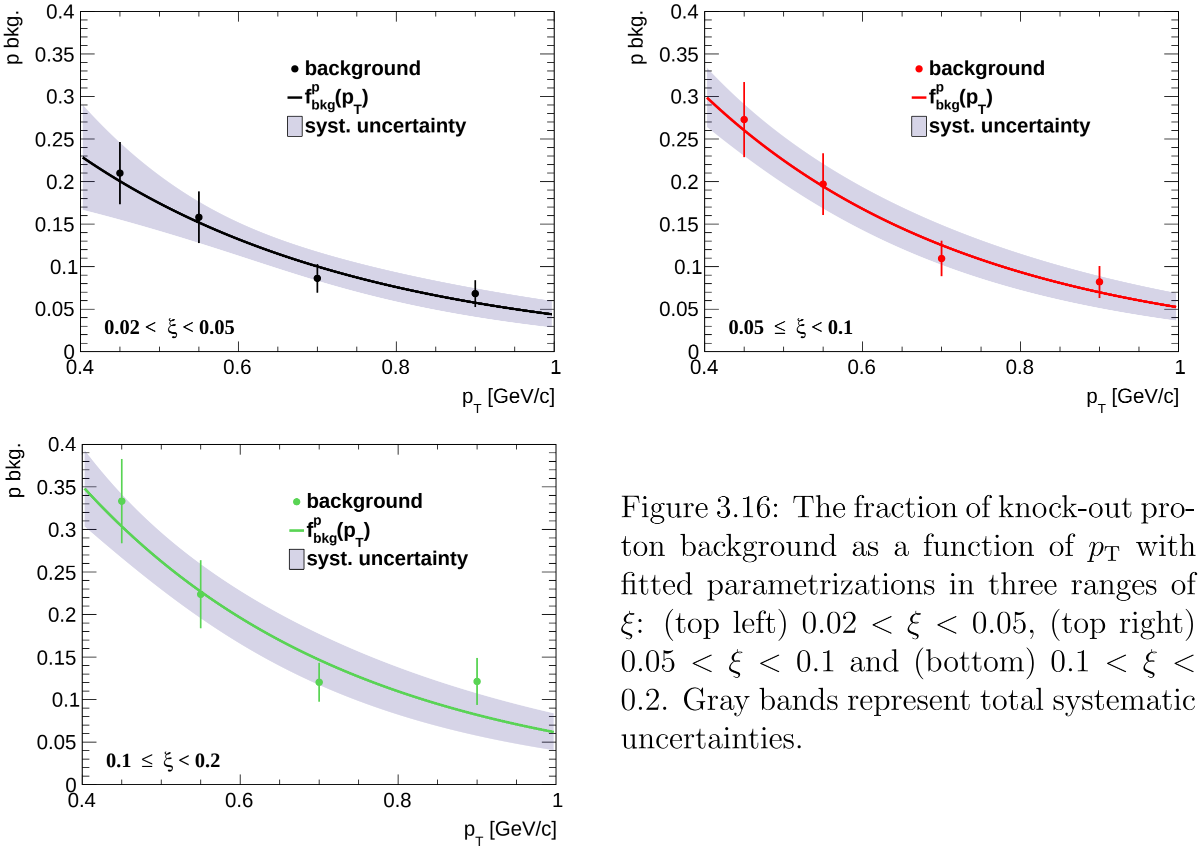

Figure 3.16: The fraction of knock-out proton background as a function of p_T with fitted parametrizations in three ranges of ξ: (top left) $0.02 < \xi < 0.05$, (top right) $0.05 < \xi < 0.1$ and (bottom) $0.1 < \xi < 0.2$. Gray bands represent total systematic uncertainties.

Pion Background

The pion spectra are corrected for weak decays (mainly of K^0_S and Λ^0), muon contribution and background from the detector dead-material interactions. The pion decay muons can be identified as pions due to the similar masses. These background contributions are obtained from PYTHIA 8 SD. Figure 3.17 shows the background contribution to the pion spectra as a function of p_T in three ranges of ξ, separately for π^- and π^+. Since there were negligible differences observed between these three ranges of ξ, the background contribution was averaged over ξ. The following parametrization was found to describe it:

$$f^{\pi}_{\mathrm{bkg}}(p_\mathrm{T}) = a_0 \exp(a_1 p_\mathrm{T}) + a_2 p_\mathrm{T}^2 + a_3 p_\mathrm{T} \tag{3.7}$$

where a_i, $i = 0, \ldots, 3$ are free parameters of the fitted function.

The pion background contribution varies between 5% at low-p_T ($p_\mathrm{T} = 0.25$ GeV/c) and about 1% at $p_\mathrm{T} = 1.0$ GeV/c for both negatively and positively charged pions. In addition, the background was calculated from EPOS SD+SD′ for the full range of ξ. The differences between PYTHIA 8 and EPOS are up to 1% for π^-.

3.6 Control Plots

Events, in which forward-scattered proton and reconstructed TOF vertex are the result of the same *pp* interaction, may originate from ND, DD, SD, and CD processes. It is preferred to estimate the background contribution from data, using dedicated control regions. Since

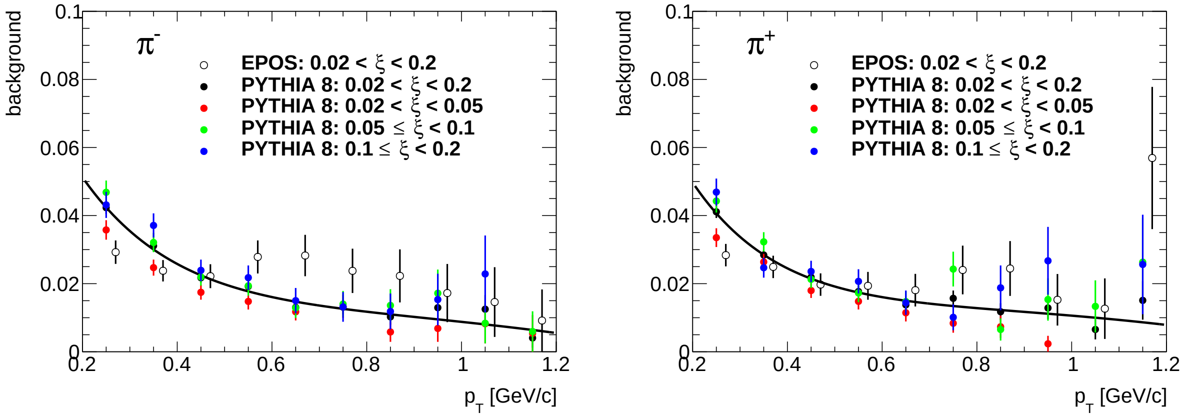

Figure 3.17: Pion background fraction as a function of p_T shown separately for (left) negatively and (right) positively charged pions in three ranges of ξ: (red) $0.02 < \xi < 0.05$, (green) $0.05 < \xi < 0.1$, (blue) $0.1 < \xi < 0.2$. (full black points) The pion background averaged over three ranges of ξ with fitted parametrization is also shown. Open black points represent EPOS predictions for the full ξ range.

such regions were not found, the relative contributions from the above processes were estimated from MC models and are therefore model dependent. Tracks reconstructed in RPs may also be:

- forward-scattered protons produced in the SD, CD or DD diffractive systems or from ND events,
- secondary particles from showering initiated by interaction of forward-scattered protons with beam-line elements. This contribution is negligible.

Figure 3.18 shows the uncorrected ξ and t distributions in data compared to various MC models: PYTHIA 8 A2 (MBR), PYTHIA 8 A2 (MBR-tuned), PYTHIA 8 4C (SaS) and EPOS. The MC distributions are split into SD, ND, DD and CD components. For EPOS, SD$'$ is separated from the ND events. Additionally, the accidental background is also shown. PYTHIA 8 A2 (MBR) predictions, shown in Fig. 3.18 (a-b), do not agree with the data, especially there is small number of events in the region of large values of ξ. This effect may be due to the scaling factors (Sec. 1.2.4), which are introduced in PYTHIA 8 to artificially suppress diffractive cross sections in the high mass region, or due to too large Pomeron intercept ($\epsilon = 0.104$). Therefore, additional two samples of PYTHIA 8 were generated: without this artificial suppression (MBR-tuned) and with $\epsilon = 0$ (SaS). Their predictions, shown in Fig. 3.18 (c-f), agree much better with the data than PYTHIA 8 A2 (MBR) and result also in a suppression of non-SD events. Amongst PYTHIA 8 models, PYTHIA 8 A2 (MBR-tuned) shows the best agreement with the data. EPOS predictions, shown in Fig. 3.18 (g-h), describes data better than PYTHIA 8 but shows a dominant contribution of SD$'$ events. The CD contribution in EPOS is several times greater than in PYTHIA 8 (MBR), but it was never tuned to describe any data, as opposed to PYTHIA 8 (MBR) in which the CD cross sections are constrained by CDF measurements [222]. The CD component in the SaS model is based on simple scaling assumption (Sec. 1.2.4), therefore, it is not usually used by the experimental communities [223]. All MCs predict significant DD and ND background at large ξ, thereby the analysis was limited to $\xi < 0.2$.

Figures 3.19 to 3.21 show the uncorrected distributions of variables used in the later analysis: n_{sel}, p_{T} an $\bar{\eta}$. The contributions from non-SD (except EPOS SD$'$) interactions differ a bit between each other, i.e. EPOS predicts significantly larger CD contribution, whereas DD and ND are suppressed in PYTHIA 8 A2 (MBR-tuned) and PYTHIA 8 4C (SaS). PYTHIA 8 A2 (MBR) is used as the default model of non-SD contribution subtracted from the data with systematic uncertainty ±50%, which covers all differences between the models except EPOS SD$'$. In this analysis EPOS SD$'$ is considered as an alternative to PYTHIA 8 SD model of events with forward-scattered proton in the final state, where one of the proton remnants hadronizes back to a single proton (non-diffractive process), while in PYTHIA 8 the initial proton stays intact (diffractive process). As a consequence, results are compared with the sum of SD and SD$'$ processes for EPOS model.

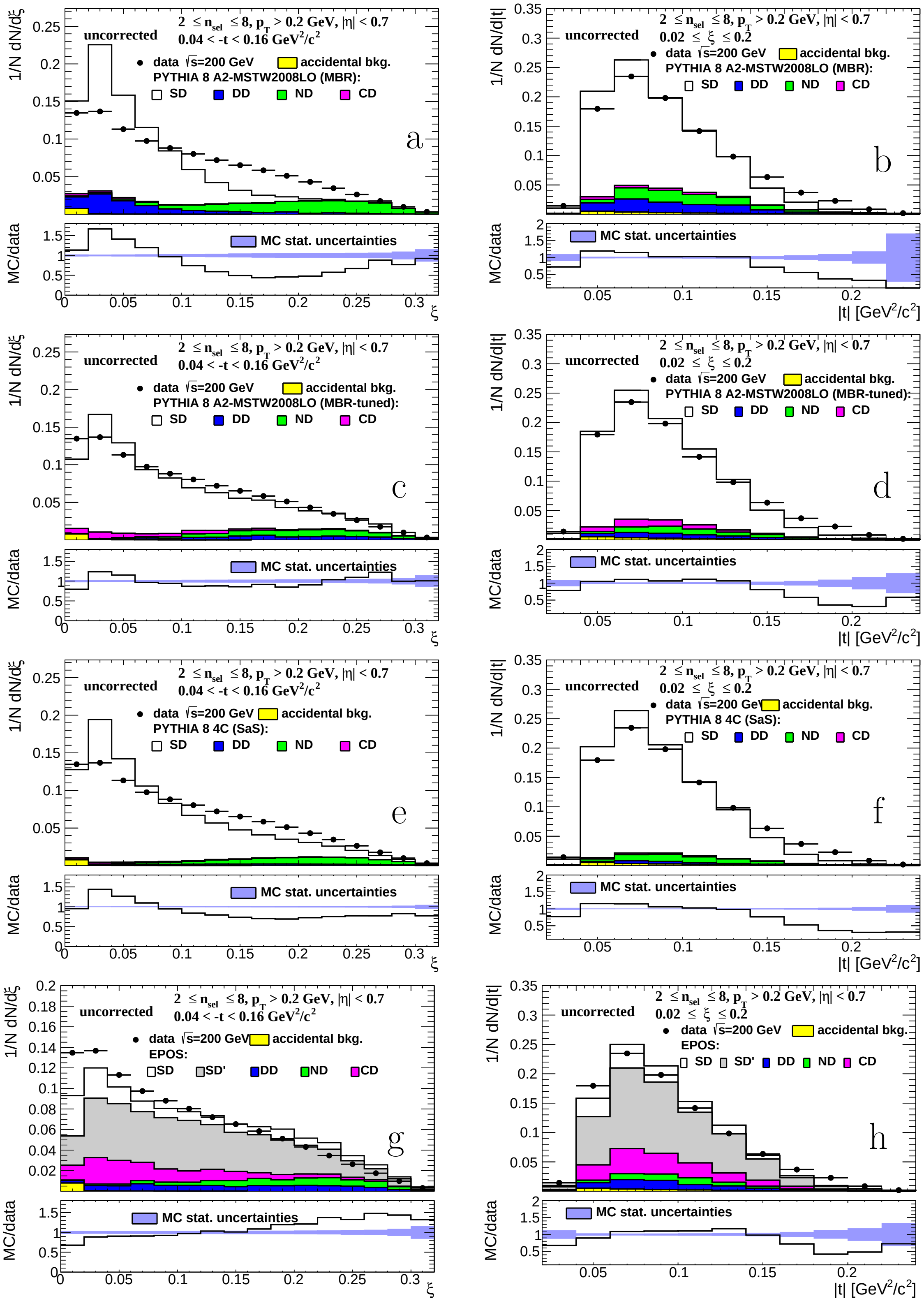

Figure 3.18: Uncorrected distributions of data compared to various MC models: (a-b) PYTHIA 8 A2 (MBR), (c-d) PYTHIA 8 A2 (MBR-tuned), (e-f) PYTHIA 8 4C (SaS) and (g-h) EPOS, as a function of (left column) ξ and (right column) $|t|$. The ratio of MC predictions and data is shown in the bottom panels.

3.7 Corrections

TPC Track Reconstruction

The TPC track reconstruction efficiency and acceptance, $\epsilon_{\text{TPC}}\left(p_{\text{T}},\eta,V_z\right)$, is defined as the probability that a true-level primary particle is reconstructed as a global track passing the selection criteria. The efficiency is measured as a function of p_{T}, η and V_z, separately for each particle type, and is expressed as:

$$\epsilon_{\text{TPC}}\left(p_{\text{T}},\eta,V_z\right)=\frac{N_{\text{reco}}^{\text{global}}\left(p_{\text{T}},\eta,V_z\right)}{N_{\text{gen}}\left(p_{\text{T}},\eta,V_z\right)} \tag{3.8}$$

where p_{T}, η and V_z are true quantities, $N_{\text{reco}}^{\text{global}}\left(p_{\text{T}},\eta,V_z\right)$ is number of reconstructed global tracks matched to a given true-level primary particle, $N_{\text{gen}}\left(p_{\text{T}},\eta,V_z\right)$ is the number of true-level primary particles in a given $\left(p_{\text{T}},\eta,V_z\right)$ bin. A global TPC track matching to

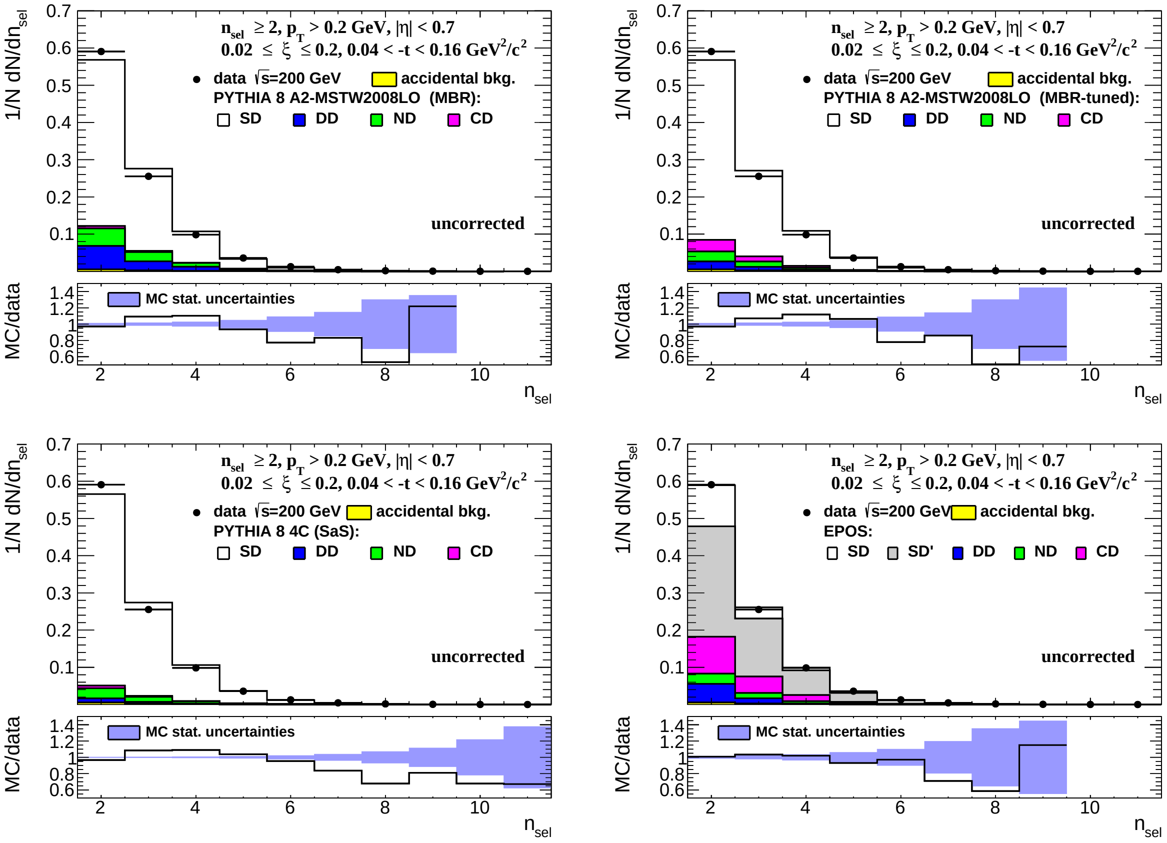

Figure 3.19: Uncorrected distributions of data compared to various MC models: (top left) PYTHIA 8 A2 (MBR), (top right) PYTHIA 8 A2 (MBR-tuned), (bottom left) PYTHIA 8 4C (SaS) and (bottom right) EPOS, as a function of n_{sel}. The ratio of MC predictions and data is shown in the bottom panels.

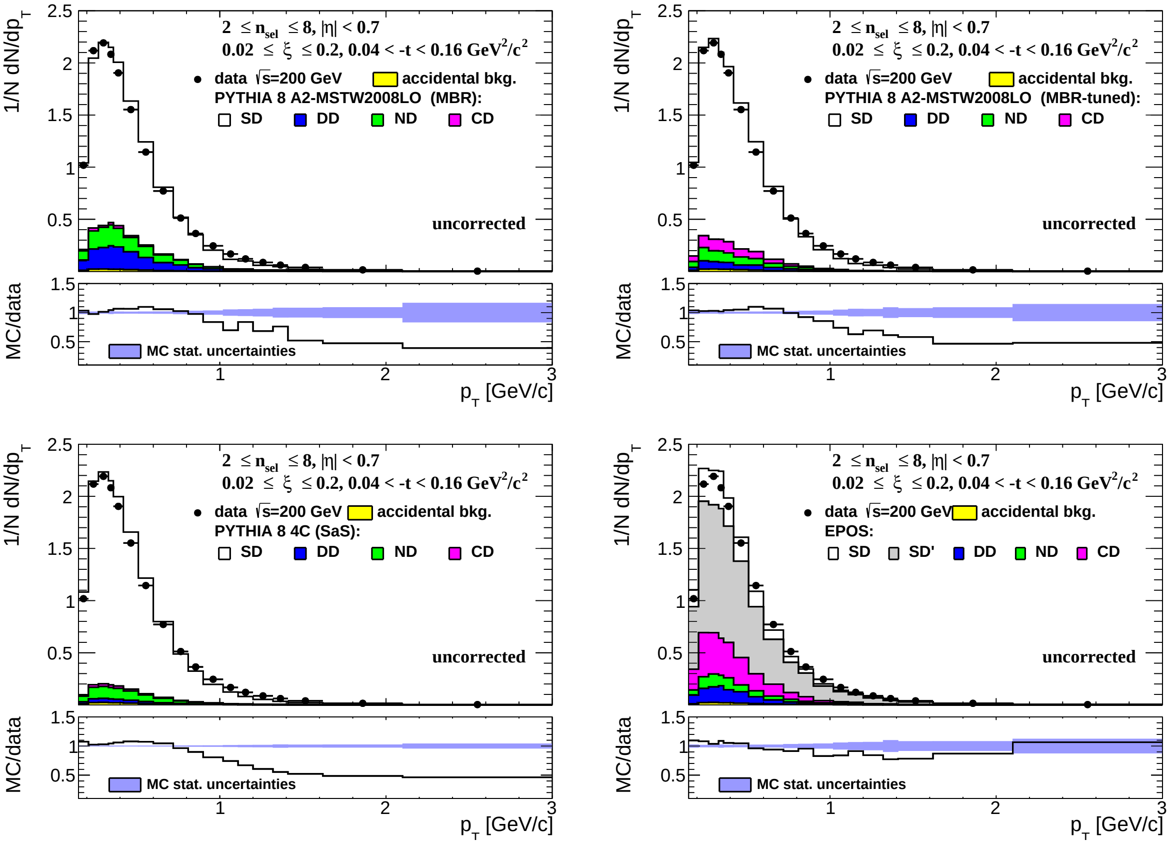

Figure 3.20: Uncorrected distributions of data compared to various MC models: (top left) PYTHIA 8 A2 (MBR), (top right) PYTHIA 8 A2 (MBR-tuned), (bottom left) PYTHIA 8 4C (SaS) and (bottom right) EPOS, as a function of p_{T}. The ratio of MC predictions and data is shown in the bottom panels.

a true-level particle proceeds in two steps. First, it is required that the generated true-level particle and a reconstructed global track have the appropriate number of common hit points. This is the nominal STAR definition of true-level particle and global track matching.

In about 1% of events there were more than one reconstructed global track matched with the same true-level particle. The true-level particles can interact with the dead material or decay. The location where it occurs is given by the radial component of the true-level secondary vertex V_r^{end}. Above 1% of the reconstructed tracks were matched to a true-level particle which lost identity ($V_r^{\mathrm{end}} < 48$ cm) before entering TPC. To avoid ambiguity, the following correlation in $\eta - \phi$ space between matched pair was defined:

$$\delta^2(\eta,\phi) = \left(\eta^{\mathrm{true}} - \eta^{\mathrm{reco}}\right)^2 + \left(\phi^{\mathrm{true}} - \phi^{\mathrm{reco}}\right)^2 \tag{3.9}$$

The distance $\delta^2(\eta,\phi)$, obtained with PYTHIA 8 4C (SaS), for π^-, K^- and $\bar{p}$, is shown in Fig. 3.22 for particles with only one matched global track and Fig. 3.23 for particles with at least two matched global tracks. It indicates that some particles are matched to two reconstructed tracks, even if there are no secondary vertices. Hence, the definition of true-level particle and global track matching was expanded. In addition to the requirement of the appropriate number of common hit points, the distance between true-level particle and track was required to be smaller than 0.15, $\delta^2(\eta,\phi) < (0.15)^2$ [169]. This value was chosen by the requirement that only small amount, less than 0.3%, of Central Exclusive Production (CEP) events which passed all selection criteria would not satisfy matching criteria. All tracks, which do not satisfy the above criteria, are treated as fake tracks (even if they are matched to the true level particle in the standard way).

During Run 15, the sector #19 in the TPC was dead for some runs (run number < 16073050). Hence, the TPC reconstruction efficiency was calculated separately for two periods: runs up to 16073050 and after 16073050. Only results for runs with the sector #19 alive are shown in the sections related to the TPC track reconstruction efficiency. Nevertheless, the correction procedure for earlier runs was the same.

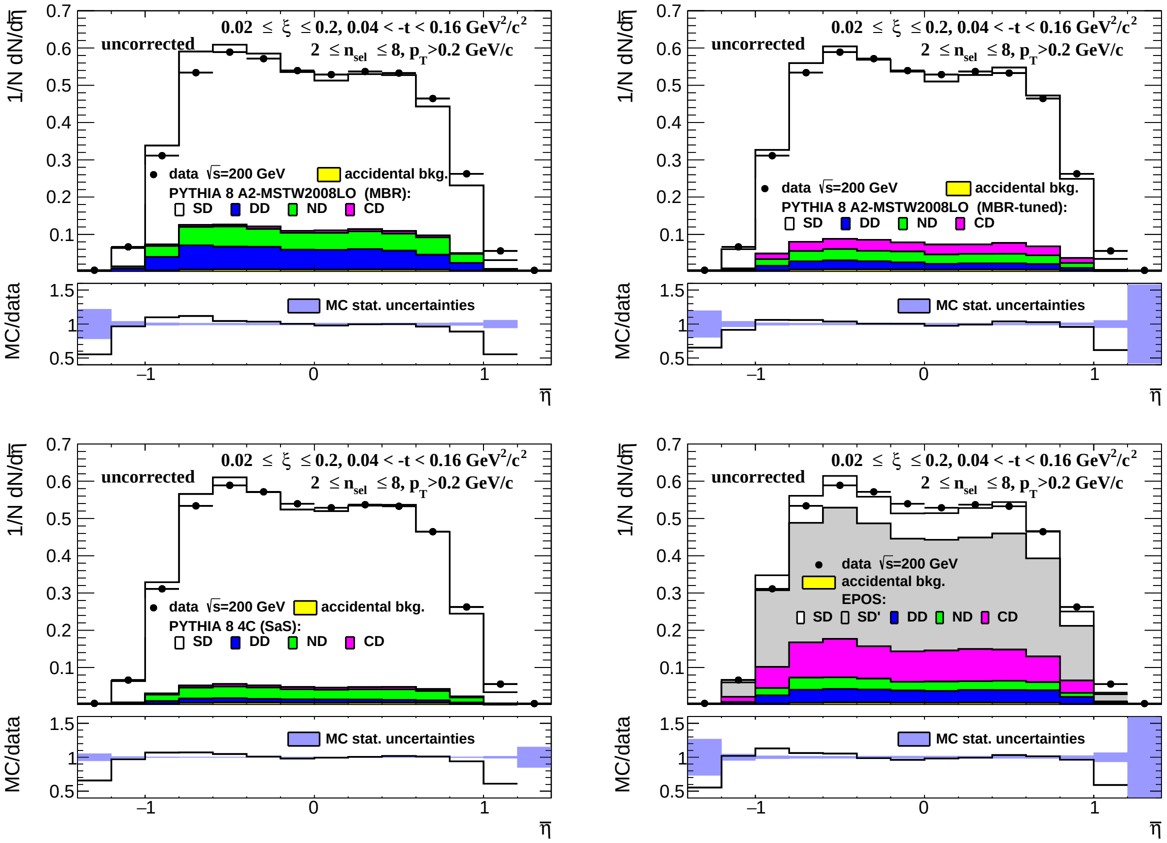

Figure 3.21: Uncorrected distributions of data compared to various MC models: (top left) PYTHIA 8 A2 (MBR), (top right) PYTHIA 8 A2 (MBR-tuned), (bottom left) PYTHIA 8 4C (SaS) and (bottom right) EPOS, as a function of $\bar{\eta}$. The ratio of MC predictions and data is shown in the bottom panels.

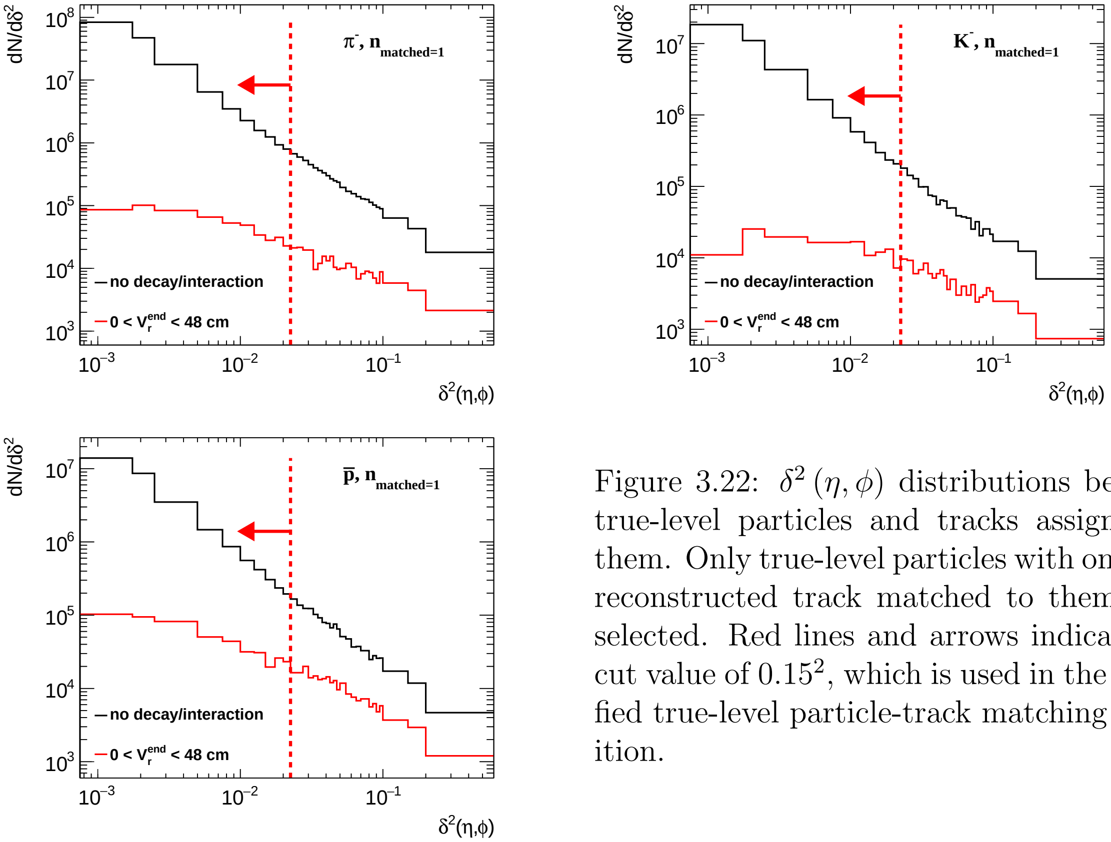

Figure 3.22: $\delta^2(\eta,\phi)$ distributions between true-level particles and tracks assigned to them. Only true-level particles with only one reconstructed track matched to them were selected. Red lines and arrows indicate the cut value of 0.15^2, which is used in the modified true-level particle-track matching definition.

The off-time pile-up significantly reduces the TPC track reconstruction efficiency due to high density of pile-up hits. That effect is taken into account by using single particle MC events embedded into ZB real data. The sample TPC track reconstruction efficiency for π^- in three V_z bins is shown in Fig. 3.24. In order to minimize the systematic uncertainties related to TPC and TOF and to avoid V_z-dependent (p_T,η) cuts, a rectangular (p_T,η) space with limits independent from V_z was applied, where the efficiency is higher than 50% of the maximum value. In addition, the cut on $|V_z| < 80$ cm was set to exclude the region of V_z where the efficiency for $|\eta| < 0.7$ is very small. All above cuts are listed in Section 3.3. The TPC track reconstruction efficiency for $\pi^\pm$ is approximately 80%, $55-65$% for $K^\pm$, 75% for $\bar{p}$ and 85% for p.

The following sources of systematic uncertainties on TPC track reconstruction were considered:

a) Pile-Up Effect

In order to estimate the systematic uncertainty related to a different density of pile-up TPC hits in the data and embedding MC, the luminosity dependence of the track reconstruction efficiency was compared between data-driven tag&probe method [169] and embedding method.

The data and MC were divided into three samples based on mean BBC coincidence: $\langle$BBC_AND$\rangle$ = 700 kHz, $\langle$BBC_AND$\rangle$ = 1100 kHz, $\langle$BBC_AND$\rangle$ = 1400 kHz, as shown in Fig. 3.25 (left). Figure 3.25 (right) shows the change of $N_{\text{hits}}^{\text{fit}}$ in three $\langle$BBC_AND$\rangle$ regions, which is the main effect of different pile-up. The same cut on $N_{\text{hits}}^{\text{fit}}$ in these three samples results in different TPC track reconstruction efficiency. Using the data-driven tag&probe method, $N_{\text{hits}}^{\text{fit}}$ cut was modified for samples with $\langle$BBC_AND$\rangle$ = 700 kHz and $\langle$BBC_AND$\rangle$ = 1400 kHz in order to provide the same TPC track reconstruction efficiency for these samples as for sample with $\langle$BBC_AND$\rangle$ = 1100 kHz and nominal $N_{\text{hits}}^{\text{fit}}$ cut. In order to obtain the best agreement between these samples, $N_{\text{hits}}^{\text{fit}}$ was allowed to be a real number, although normally it is an integer. Therefore, $N_{\text{hits}}^{\text{fit}}$ was increased for each reconstructed track by adding a random number from the uniform distribution $U(0,1)$. The obtained values of $N_{\text{hits}}^{\text{fit}}$ cut were $N_{\text{hits}}^{\text{fit}} > 23.8$ and $N_{\text{hits}}^{\text{fit}} > 26$ for high and low BBC rate runs, respectively.

The above values of $N_{\text{hits}}^{\text{fit}}$ cut were used to obtain the TPC track reconstruction efficiencies from the single particle embedding MC. If the embedding procedure is compatible with data-driven tag&probe method, the TPC track reconstruction efficiencies should be the same for three samples. To be in agreement with data-driven tag&probe method, in which true-level information is not available, the TPC track reconstruction efficiency was defined as the probability that a global TPC track, passing d_0 quality cut and compat-

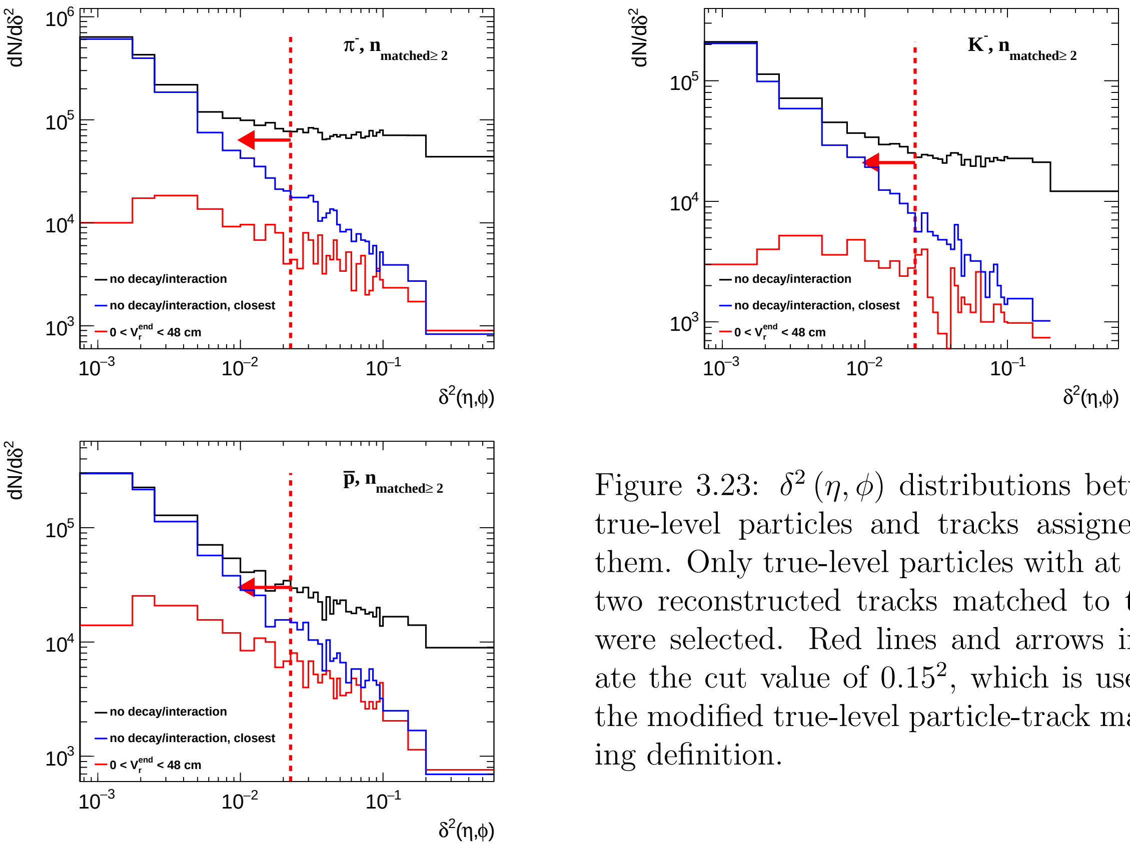

Figure 3.23: $\delta^2(\eta,\phi)$ distributions between true-level particles and tracks assigned to them. Only true-level particles with at least two reconstructed tracks matched to them were selected. Red lines and arrows indicate the cut value of 0.15^2, which is used in the modified true-level particle-track matching definition.

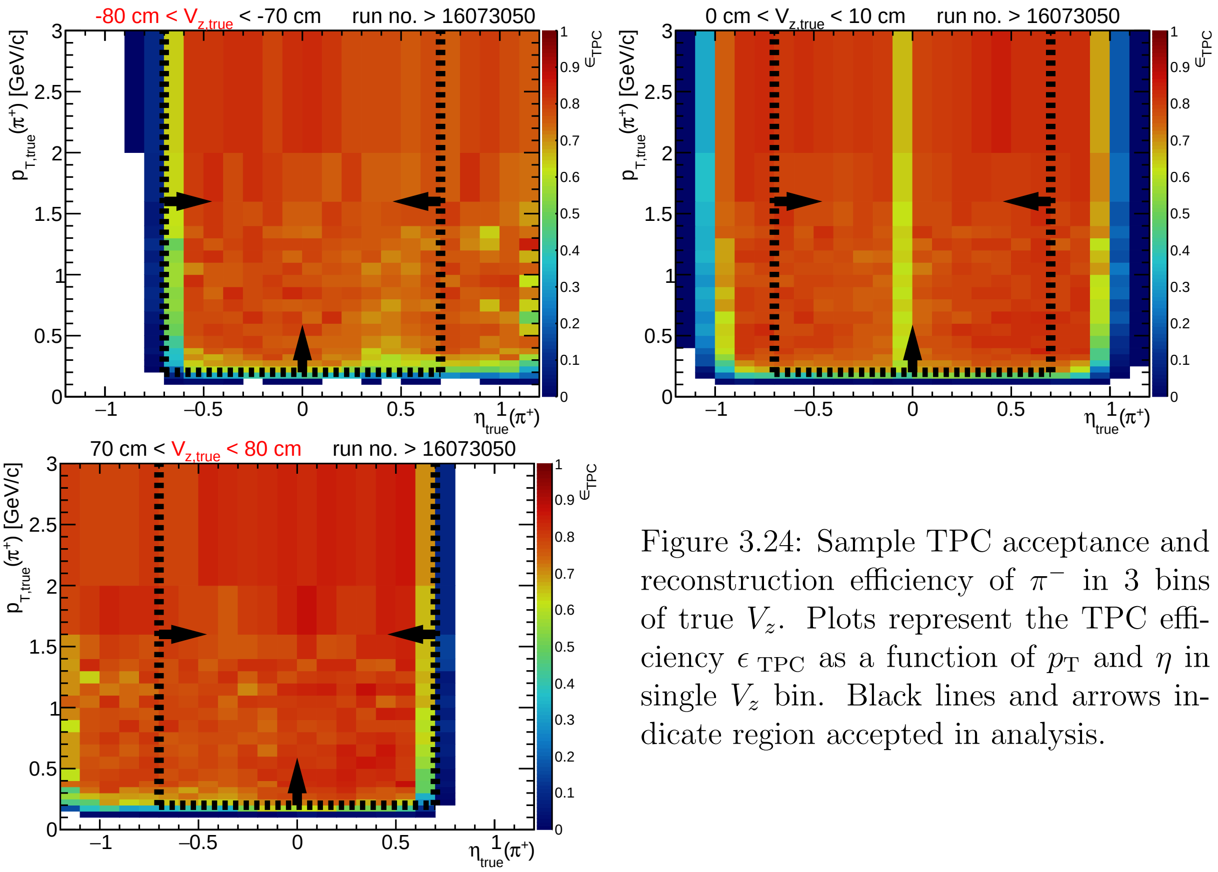

Figure 3.24: Sample TPC acceptance and reconstruction efficiency of π^{-} in 3 bins of true V_z. Plots represent the TPC efficiency $\epsilon_{\text{ TPC}}$ as a function of p_{T} and η in single V_z bin. Black lines and arrows indicate region accepted in analysis.

ible with pion hypothesis $|n\sigma_{\pi^{\pm}}| < 3$ (Sec. 3.9), is matched with TOF hits and true-level primary particle satisfies $N_{\text{hits}}^{\text{fit}}$ quality cut. Figure 3.26 shows the TPC track reconstruction efficiency with nominal, for $\langle\text{BBC\_AND}\rangle$ = 1100 kHz sample, and modified quality cut on $N_{\text{hits}}^{\text{fit}}$, for $\langle\text{BBC\_AND}\rangle$ = 700 kHz and $\langle\text{BBC\_AND}\rangle$ = 1400 kHz samples. The systematic uncertainty on TPC track reconstruction efficiency related to embedding procedure was defined as an offset between medium and low (high) pile-up runs, as shown in Fig. 3.26:

$$\Delta\epsilon_{\text{TPC}}^{(1100,i)} = \epsilon_{\text{TPC}}^{\left(1100,N_{\text{hits}}^{\text{fit}}>24\right)} - \epsilon_{\text{TPC}}^{i} \tag{3.10}$$

where $\epsilon_{\text{TPC}}^{\left(1100,N_{\text{hits}}^{\text{fit}}>24\right)}$ is the TPC track selection efficiency calculated from sample with $\langle\text{BBC\_AND}\rangle$ = 1100 kHz with nominal $N_{\text{hits}}^{\text{fit}}$ cut, ${\epsilon^{i}}_{\text{TPC}}$ is the modified TPC track reconstruction efficiency calculated from samples with $\langle\text{BBC\_AND}\rangle$ = 700 kHz and $\langle\text{BBC\_AND}\rangle$ = 1400 kHz with modified $N_{\text{hits}}^{\text{fit}}$ quality cut. As shown in Fig. 3.26, the above offset is about 1% for $\pi^{\pm}$.

b) Representation of Data in Embedding

Only small fraction of ZB data was available for embedding MC production. Therefore, a systematic uncertainty related to the proper representation of whole data sample in embedding should be calculated. The BBC_AND rate varies between data and embedding of about 5%, as shown in Fig. 3.27. The effect of different TPC track reconstruction efficiency depending on TPC occupancy (the BBC rate) is about 5% for extreme cases (Fig. 3.26). Thus, an additional systematic uncertainty due to different mean BBC_AND rate in the data and embedding MC was set as 0.25%.

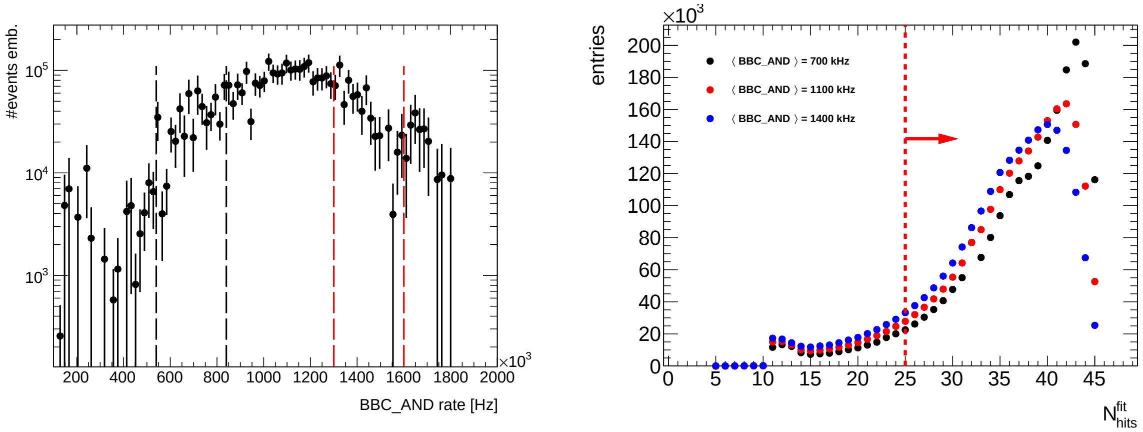

Figure 3.25: (left) Number of events in embedding MC as a function of BBC_AND rate. The black and red lines represent the events with $\langle$BBC_AND$\rangle$ = 700 kHz and $\langle$BBC_AND$\rangle$ = 1400 kHz, respectively. The region between these two corresponds to events with $\langle$BBC_AND$\rangle$ = 1100 kHz. (right) Number of hits used in the helix fit $N^{\rm fit}_{\rm hits}$ for embedding MC samples selected with respect to average rate in BBC. Distributions are normalized to the number of events in $\langle$BBC_AND$\rangle$ = 700 kHz sample. Red line and arrow indicate the region accepted in the analysis for nominal $N^{\rm fit}_{\rm hits}$ cut value.

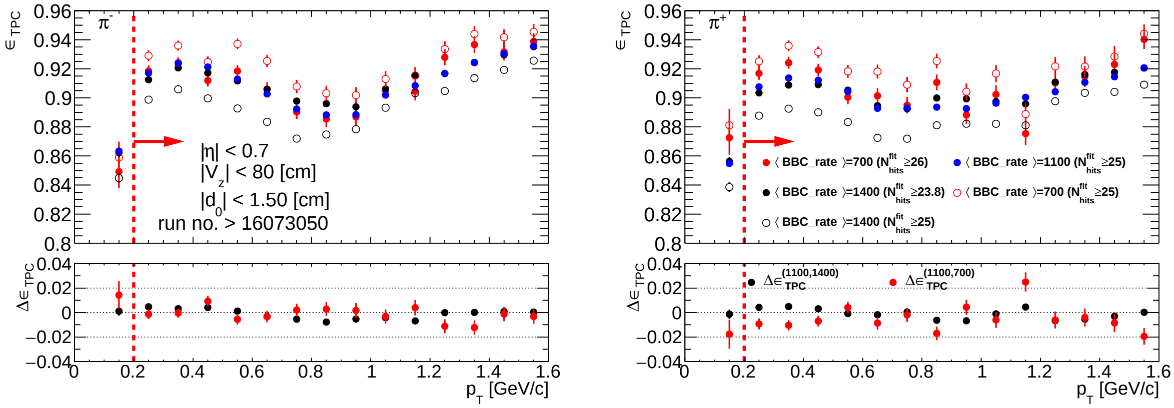

Figure 3.26: TPC track selection efficiency of $\pi^{\pm}$ as a function of p_T for embedding MC samples with $\langle$BBC_AND$\rangle$ = 700 kHz, $\langle$BBC_AND$\rangle$ = 1100 kHz and $\langle$BBC_AND$\rangle$ = 1400 kHz. The efficiencies from corresponding MC samples with changed cut on the number of hits used in the helix fit are also shown. Additionally, the offsets from Eq. (3.10) are drawn in the bottom panels of each plot. Red lines and arrows indicate region accepted in the analysis.

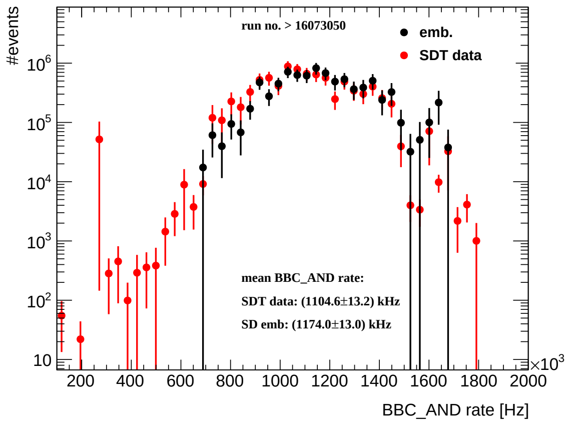

Figure 3.27: Comparison of the BBC_AND rate in the data and embedding MC for SD.

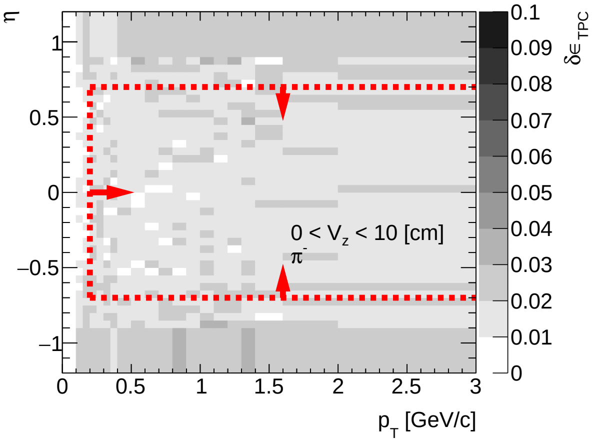

Figure 3.28: Fraction of lost π^- due to the interaction with dead material in front of TPC as a function of η and p_{T} in single V_z bin. Red lines and arrows indicate region accepted in the analysis.

c) Description of Dead Material

The amount of dead material in front of TPC differs up to 25% between data and simulation [169]. The symmetric systematic uncertainty on the TPC track reconstruction efficiency due to dead material $\Delta\epsilon_{\mathrm{TPC}}^{\mathrm{DM}}$ was introduced as:

$$\Delta\epsilon_{\mathrm{TPC}}^{\mathrm{DM}} = \pm 0.25 \cdot \delta\epsilon_{\mathrm{TPC}} \tag{3.11}$$

where $\delta\epsilon_{\mathrm{TPC}}$, estimated with no-pile-up MC, is the amount of lost particles due to the interaction with dead material in front of TPC. The sample distribution of $\delta\epsilon_{\mathrm{TPC}}$ for π^- as a function of p_{T} and η in one V_z bin is shown in Fig. 3.28.

d) Variation in the Track Quality Cuts

In order to check the sensitivity of any track based measurement to track selection (described in Sec. 3.3), additional four variations of track quality cuts have been implemented and corresponding TPC efficiencies are calculated:

- nHits loose: $N_{\mathrm{hits}}^{\mathrm{fit}} \geq 20$, $N_{\mathrm{hits}}^{\mathrm{dE/dx}} \geq 12$,

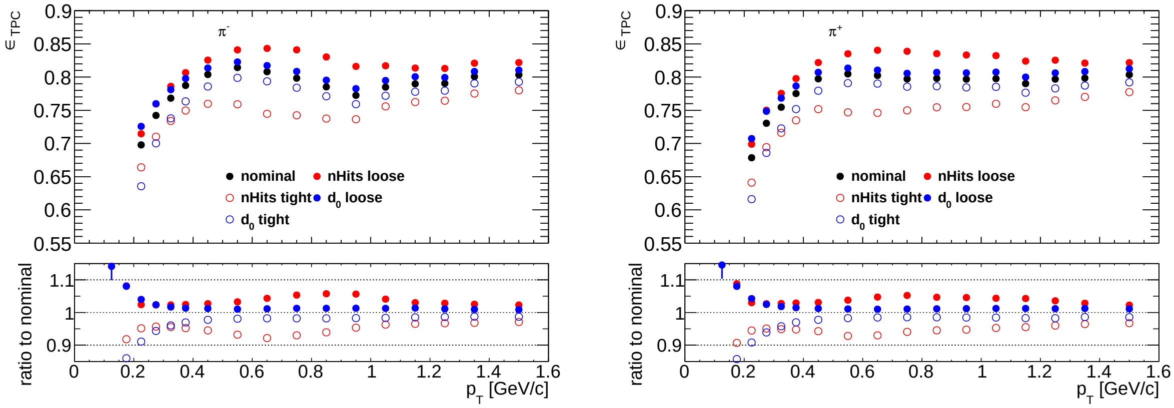

Figure 3.29: TPC acceptance and reconstruction efficiency of (left) π^- and (right) π^+ as a function of p_{T} ($|\eta| < 0.7$, $|V_z| < 80$ cm) obtained from embedding MC samples with respect to various track quality cuts. The ratios of TPC efficiencies for changed track quality cuts to nominal TPC efficiencies are shown in the bottom panels.

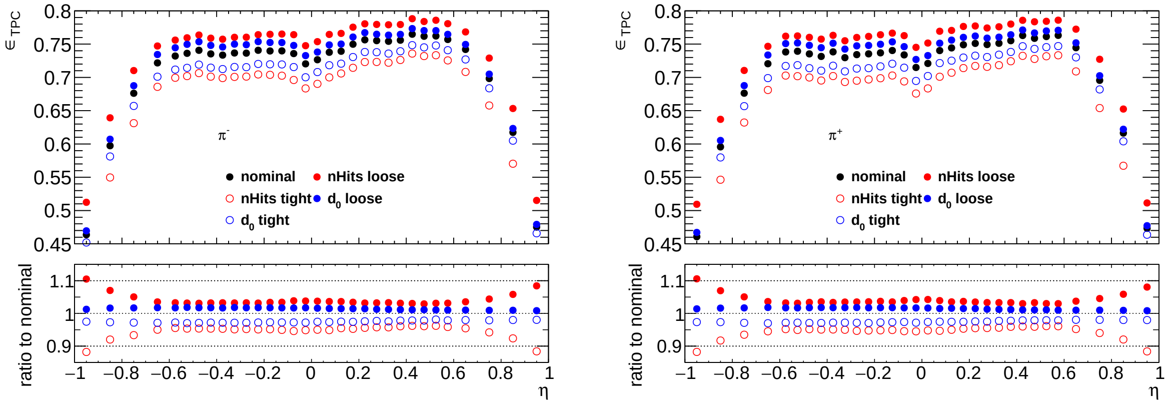

Figure 3.30: TPC acceptance and reconstruction efficiency of (left) π^- and (right) π^+ as a function of η ($p_{\mathrm{T}} > 0.2$ GeV/c, $|V_z| < 80$ cm) obtained from embedding MC samples with respect to various track quality cuts. The ratios of TPC efficiencies for changed track quality cuts to nominal TPC efficiencies are shown in the bottom panels.

- nHits tight: $N_{\text{hits}}^{\text{fit}} \geq 28$, $N_{\text{hits}}^{\text{dE/dx}} \geq 17$,
- d_0 loose: $|d_0| < 3.0$ cm,
- d_0 tight: $|d_0| < 1.0$ cm.

Figures 3.29 and 3.30 show TPC track reconstruction and acceptance efficiencies of $\pi^{\pm}$ as a function of p_{T} and η, respectively, obtained from embedding MC samples with respect to the above various track quality cuts. The variation of the $N_{\text{hits}}^{\text{fit}}$ and $N_{\text{hits}}^{\text{dE/dx}}$ cuts leads to a 5% change in the efficiencies, while the variation of the d_0 cut produces changes in

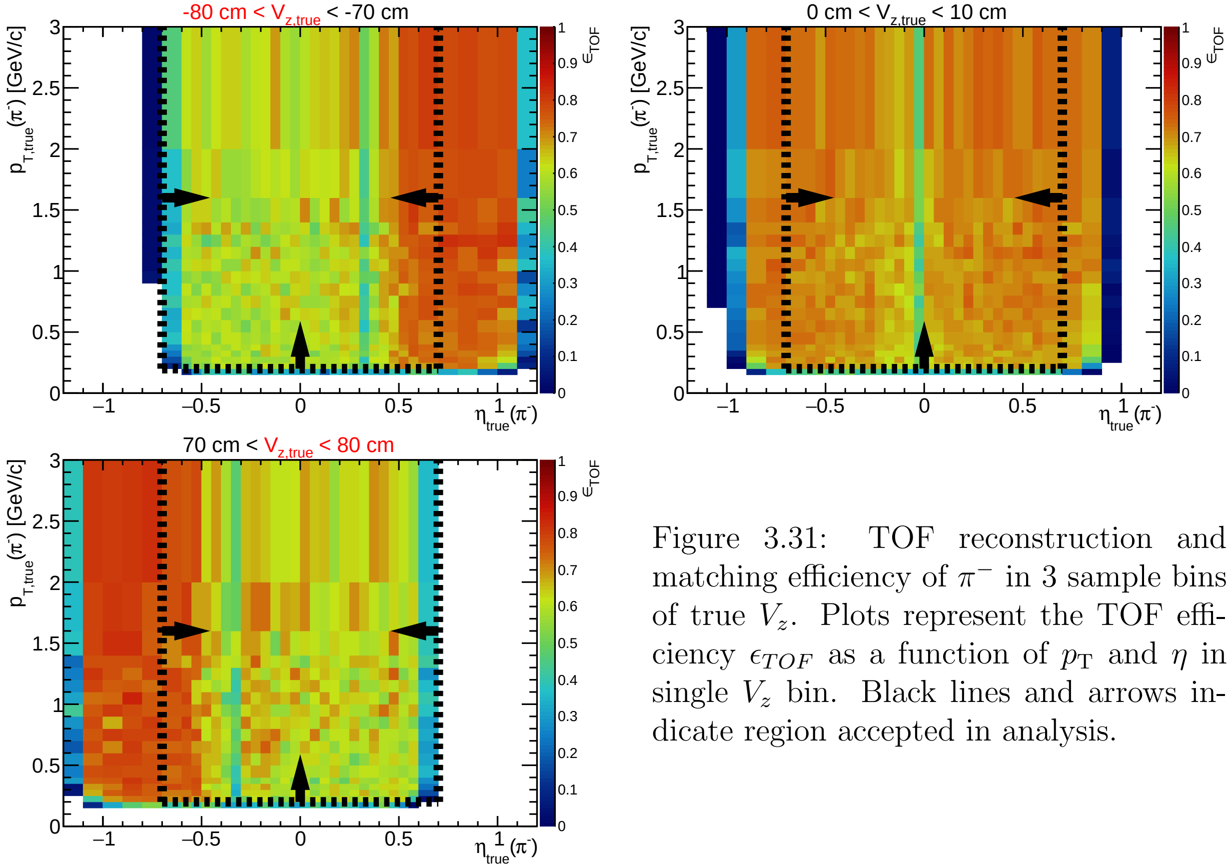

Figure 3.31: TOF reconstruction and matching efficiency of π^- in 3 sample bins of true V_z. Plots represent the TOF efficiency ϵ_{TOF} as a function of p_T and η in single V_z bin. Black lines and arrows indicate region accepted in analysis.

the efficiencies of about $1-2\%$ but 5% at low p_T. These changes in the efficiencies should not be treated as systematic uncertainties. For each measured quantity, the sensitivity of the results on different quality cuts is examined.

TOF Matching Efficiency

The TOF acceptance, which includes hit reconstruction efficiency and matching efficiency with TPC tracks, $\epsilon_\mathrm{TOF}\left(p_\mathrm{T},\eta,V_z\right)$, is defined as the probability that a global TPC track, that passed the selection criteria and is associated to a true-level primary particle, is matched with a hit in TOF. The efficiency was obtained from the single particle MC embedded into ZB data, as a function of p_T, η and V_z, separately for each particle type, and is expressed as:

$$\epsilon_\mathrm{TOF}\left(p_\mathrm{T},\eta,V_z\right)=\frac{N^\text{global-TOF}_\text{reco}\left(p_\mathrm{T},\eta,V_z\right)}{N^\text{global}_\text{reco}\left(p_\mathrm{T},\eta,V_z\right)} \tag{3.12}$$

where p_T, η, V_z are quantities related to a generated particle, $N^\text{global}_\text{reco}\left(p_\mathrm{T},\eta,V_z\right)$ is the number of reconstructed global tracks assigned to a given true-level primary particle, $N^\text{global-TOF}_\text{reco}$ $\left(p_\mathrm{T},\eta,V_z\right)$ is the number of global tracks assigned to a given true-level primary particle and matched with a hit in TOF. The TOF efficiency for π^- in three sample V_z bins is shown in Fig. 3.31.

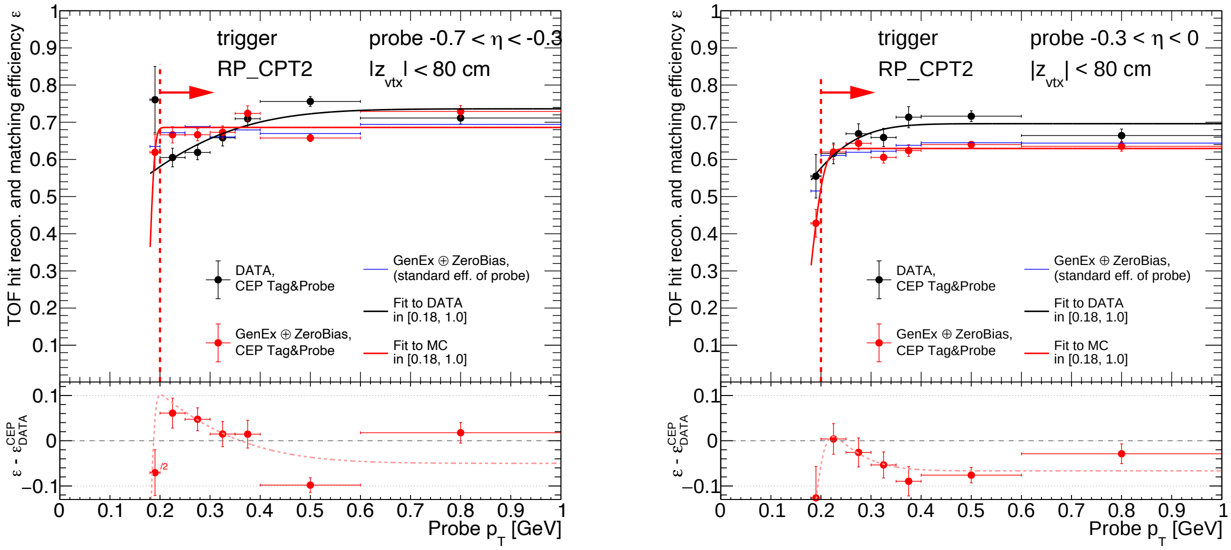

Figure 3.32: tag&probe TOF efficiency from CEP data compared with the result from embeddingCEP MC as a function of p_{T}. Blue lines denote the TOF efficiency calculated in the standard way. Differences between tag&probe TOF efficiency from embedding MC and data are shown in the bottom panels. Red lines with arrows indicate region accepted in analysis. Figure taken from [169].

There are some inaccuracies in the description of real detector geometry in the STAR detector simulation. Therefore, a correction to the TOF efficiency was derived by tag&probe method from the CEP of $\pi^+\pi^-$ data and embedding MC, and comparing the results between each other [169]. Figure 3.32 shows the sample comparison of tag&probe TOF efficiency as a function of p_T between data and MC. The difference between them was applied as an additive correction to the TOF efficiency estimated from single particle embedding MC. The TOF efficiency for $\pi^\pm$ is approximately 65%, $55-65\%$ for $K^\pm$, 60% for $\bar{p}$ and 65% for p.

The following sources of systematic uncertainties on TOF system are considered:

a) TOF System Simulation Accuracy

The systematic uncertainty on TOF system simulation accuracy was estimated by comparing the nominal TOF efficiency, including efficiency from single particle MC and data-driven correction, obtained with an independent method.

The alternative method uses TPC tracks containing hits in the HFT [169]. Since the time of response of HFT is much shorter than of TPC, it is very probable that TPC tracks containing hits in HFT are real, in-time tracks. As a result, the alternative correction to TOF efficiency correction was obtained. The difference between this correction and the correction from tag&probe method was used as the systematic uncertainty of the overall TOF efficiency, which is shown in Fig. 3.33.

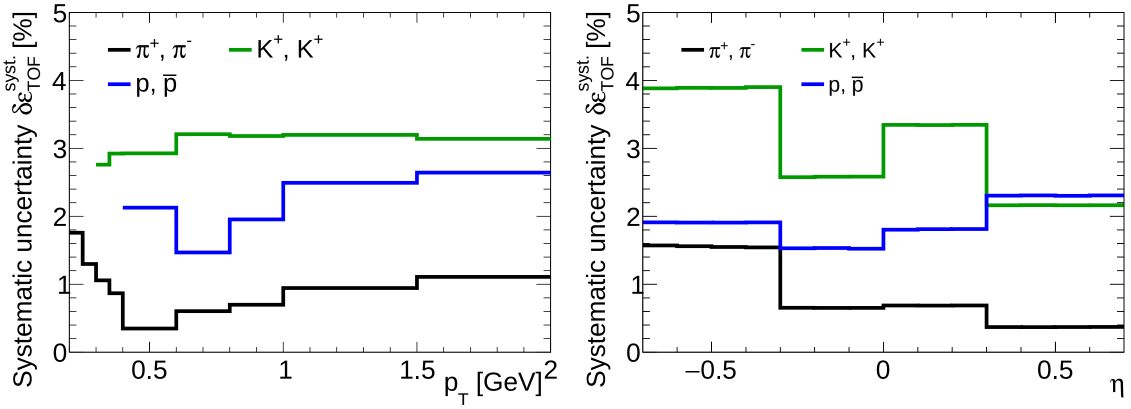

Figure 3.33: The systematic uncertainty on TOF efficiency related to the simulation accuracy, drawn as a function of (left) p_{T} and (right) η. Figure taken from [169].

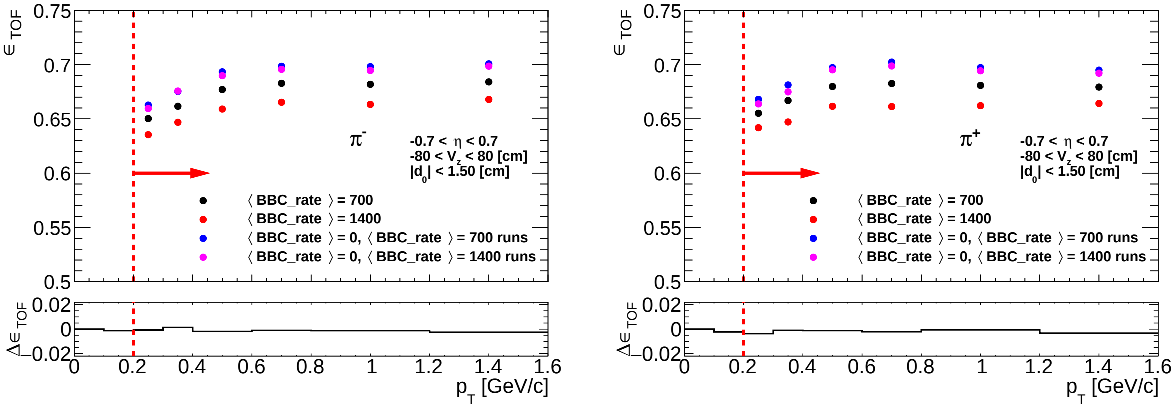

Figure 3.34: TOF matching efficiency for $\pi^{\pm}$ as a function of p_{T} for embedding MC samples with ⟨BBC_AND⟩ = 700 kHz and ⟨BBC_AND⟩ = 1400 kHz. The efficiencies from corresponding no-pile-up MC samples were also shown. The corresponding values of $\Delta\epsilon_{\mathrm{TOF}}$ are shown in the bottom panels. Red lines and arrows indicate region accepted in the analysis.

b) Embedding (Pile-Up) Effect

The effects of pile-up on TOF efficiency is taken into account by using single particle MC embedded into ZB data. To estimate the systematic uncertainty of the TOF efficiency related to the embedding procedure, the offset from the linearity of TOF efficiency as a function of the mean BBC_AND rate, ⟨BBC_AND⟩, was used. The embedding MC was divided into two samples in which ⟨BBC_AND⟩ rates differ by a factor of two: ⟨BBC_AND⟩ = 700 kHz and ⟨BBC_AND⟩ = 1400 kHz as shown in Fig. 3.25. Next, it was checked whether the difference between TOF efficiency in pile-up and no-pile-up MC also changes by a factor of two between these two samples. The TOF matching efficiency is conditional and depends on TPC track reconstruction efficiency. Hence, the difference between pile-up and no-pile-up MC was calculated as:

$$\Delta\epsilon_{\text{TOF}}^{1400/700\text{ kHz}} = \frac{N_{\text{TPC-TOF}}^{\text{no-pile-up}}}{N_{\text{TPC}}^{\text{no-pile-up}}} - \frac{N_{\text{TPC-TOF}}^{\text{pile-up}}}{N_{\text{TPC}}^{\text{pile-up}}} \tag{3.13}$$

where: $N_{\text{TPC-TOF}}^{\text{pile-up}}$ is the umber of reconstructed tracks, matched with true-level particles and TOF hit in pile-up MC, $N_{\text{TPC-TOF}}^{\text{no-pile-up}}$ is the number of reconstructed tracks, matched with true-level particles and TOF hit in no-pile-up MC, $N_{\text{TPC}}^{\text{pile-up}}$ is the number of reconstructed tracks, matched with true-level particles in pile-up MC, $N_{\text{TPC}}^{\text{no-pile-up}}$ is the number of reconstructed tracks, matched with true-level particles in no-pile-up MC.

Next the offset between high and low pile-up events was calculated with the formula:

$$\Delta\epsilon_{\text{TOF}} = \Delta\epsilon_{\text{TOF}}^{1400\text{ kHz}} - 2\cdot\Delta\epsilon_{\text{TOF}}^{700\text{ kHz}} \tag{3.14}$$

which is shown in Fig. 3.34. The obtained value of $\Delta\epsilon_{\text{TOF}}$ is smaller than 0.5% and can be neglected in comparison with other systematic uncertainties.

Energy Loss Correction

Particles passing through the detector material lose energy on their way. The track transverse momentum p_{T} is reconstructed by fitting a helical path to the hits. Fitting the track points to an ideal helical track tends to underestimate the momentum due to energy loss. To minimize biases due to this effect, a correction procedure is applied during standard track momentum reconstruction (Sec. 2.3). For this procedure pion hypothesis is used and the reconstructed momentum $p_{\text{T}}^{\text{meas}}$ is corrected by the amount of energy loss specific for a pion. For all particles but a pion some rest bias is still present since energy loss is specific for each particle type. This correction was determined from MC for each particle species as a function of $p_{\text{T}}^{\text{meas}}$, η and V_z. The sample energy loss corrections averaged over $|\eta| < 0.7$ for K^- and $\bar{p}$ are shown in Fig. 3.35.

Vertex Reconstruction

When the charged-particle multiplicity is low, the vertex-finding algorithm sometimes fails to find the primary vertex. In addition, at high luminosity, vertex finder can fail due to the contribution of pile-up interactions, providing a wrong reconstructed vertex. In the study of vertex reconstruction efficiency we required at least two reconstructed global tracks $n_{\text{sel}}^{\text{global}} \geq 2$ passing all the quality cuts listed in Sec 3.3, except vertex-related cuts on DCA$_{xy}$ and DCA$_z$, and associated to true-level primary particles. Additionally, MC events were accepted if the z-coordinate of the true-level primary vertex was between -80 and 80 cm and $n_{\text{ch}} \geq 2$. All corrections, described in this section, were calculated in three ranges of ξ separately using PYTHIA 8 SD embedding MC.

The global tracks (not necessarily associated to a true-level primary particles), which are used by the vertex-finder algorithm, had to pass the following quality cuts:

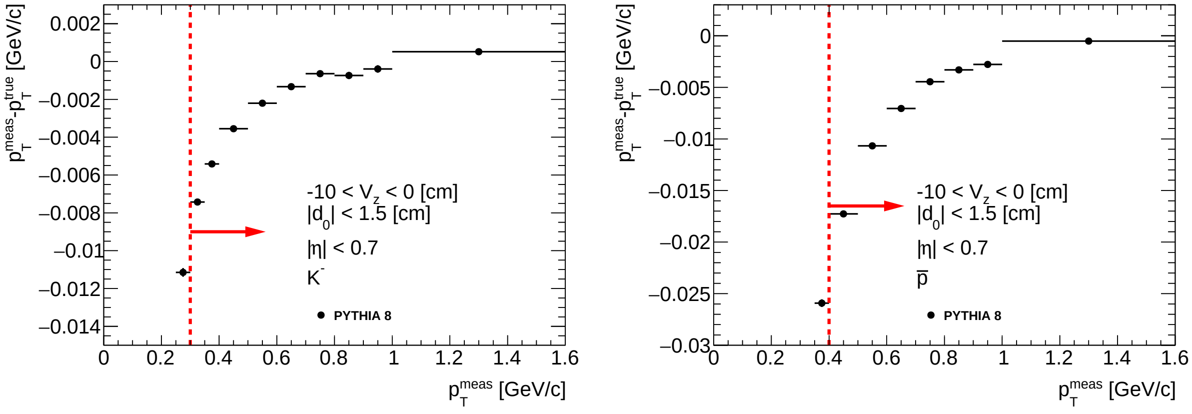

Figure 3.35: Sample energy loss correction for $p_{\mathrm{T}}^{\mathrm{meas}}$ for (left) K^- and (right) $\bar{p}$ as a function of reconstructed transverse momentum $p_{\mathrm{T}}^{\mathrm{meas}}$ ($|\eta| < 0.7$) in single z-vertex bin, $-10 < V_z < 0$ cm. Red lines and arrows indicate region accepted in analysis.

1. tracks must be matched with hits reconstructed in TOF,
2. the number of the TPC hits used in the helix fit $N_{\mathrm{hits}}^{\mathrm{fit}}$ must be greater than 20,
3. the ratio of the number of TPC hits used in the helix fit to the number of possible TPC hits $N_{\mathrm{hits}}^{\mathrm{fit}}/N_{\mathrm{hits}}^{\mathrm{poss}}$ must be greater than 0.52,
4. the transverse impact parameter with respect to the beamline d_0 must be less than 2 cm,
5. the track's transverse momentum p_{T} must be greater than 0.2 GeV/c.

The above track selection criteria are different than those used in the nominal analysis. Primary vertex reconstruction efficiency and fake vertex rate were calculated as a function of the number of global tracks used in vertexing $n_{\mathrm{vrt}}^{\mathrm{global}}$ instead of $n_{\mathrm{sel}}^{\mathrm{global}}$ ($n_{\mathrm{vrt}}^{\mathrm{global}} \geq n_{\mathrm{sel}}^{\mathrm{global}}$).

In the nominal analysis exactly one vertex with $n_{\mathrm{sel}} \geq 2$ is required. However, in the study of vertex reconstruction, events with additional vertices were studied. Therefore, we define the best vertex as the reconstructed vertex with the highest number of TOF-matched tracks. This vertex does not have to be associated to true-level primary vertex (fake or secondary vertex). The algorithm, which matches reconstructed vertices to true-level vertices, checks for reconstructed tracks originating from them. If at least one reconstructed track is assigned to a true-level particle, then the reconstructed vertex is assigned to the true-level vertex from which the true-level particle originates. Since the fake vertices (not matched to the true-level primary vertex) are allowed in the analysis, the overall vertex-finding efficiency, $\epsilon_{\mathrm{vrt}}\left(n_{\mathrm{vrt}}^{\mathrm{global}}\right)$, is expressed as:

$$\epsilon_{\mathrm{vrt}}\left(n_{\mathrm{vrt}}^{\mathrm{global}}\right) = \epsilon_{\mathrm{vrt}}^{\mathrm{best}}\left(n_{\mathrm{vrt}}^{\mathrm{global}}\right) + \delta_{\mathrm{vrt}}^{\mathrm{fake}}\left(n_{\mathrm{vrt}}^{\mathrm{global}}\right) \tag{3.15}$$

where:

$\epsilon_{\mathrm{vrt}}^{\mathrm{best}}\left(n_{\mathrm{vrt}}^{\mathrm{global}}\right)$ is the primary vertex reconstruction efficiency, determined as the ratio of the number of good reconstructed events (best primary vertex with $n_{\mathrm{sel}} \geq 2$ matched to the true-level primary vertex) to the number of input MC events,

$\delta_{\mathrm{vrt}}^{\mathrm{fake}}\left(n_{\mathrm{vrt}}^{\mathrm{global}}\right)$ is the fake vertex rate, determined as the ratio of the number of good reconstructed events (best primary vertex with $n_{\mathrm{sel}} \geq 2$ not matched to the true-level primary vertex) to the number of input MC events. Due to the contribution of pile-up, it is possible that the best vertex originates from fake tracks instead of true-level particles.

The vertex-finding efficiency as a function of $n_{\mathrm{vrt}}^{\mathrm{global}}$, shown in Fig. 3.36 (left), is larger than 75% for all $n_{\mathrm{vrt}}^{\mathrm{global}}$. However, for $n_{\mathrm{vrt}}^{\mathrm{global}} > 8$, there are more fake than true-level primary vertices. When there are exactly two global tracks used in the vertex reconstruction, $n_{\mathrm{vrt}}^{\mathrm{global}} = 2$, the vertex-finding efficiency depends on the longitudinal distance between these tracks $|\Delta z_0|$. Therefore, the vertex-finding efficiency for such events $\epsilon_{\mathrm{vrt}}\left(|\Delta z_0|\right)$ is given by:

$$\epsilon_{\mathrm{vrt}}\left(|\Delta z_0|\right) = \epsilon_{\mathrm{vrt}}^{\mathrm{best}}\left(|\Delta z_0|\right) + \delta_{\mathrm{vrt}}^{\mathrm{fake}}\left(|\Delta z_0|\right) \tag{3.16}$$

where: $\epsilon_{\mathrm{vrt}}^{\mathrm{best}}\left(|\Delta z_0|\right)$ is the primary vertex reconstruction efficiency, $\delta_{\mathrm{vrt}}^{\mathrm{fake}}\left(|\Delta z_0|\right)$ is the fake vertex rate.

Figure 3.36 (right) shows the vertex-finding efficiency for events with $n_{\mathrm{vrt}}^{\mathrm{global}} = 2$. This efficiency is smaller than 20% for tracks with $|\Delta z_0| > 2$ cm, hence the analysis was limited to events with $|\Delta z_0| < 2$ cm, when $n_{\mathrm{vrt}}^{\mathrm{global}} = 2$. The rate of fake vertices is negligibly low (open points overlap with full points).

Events are rejected if more vertices are reconstructed in addition to the best one. Rejected events can be classified as:

a) two or more additional vertices,

b) additional secondary vertex from interactions with the detector dead-material,

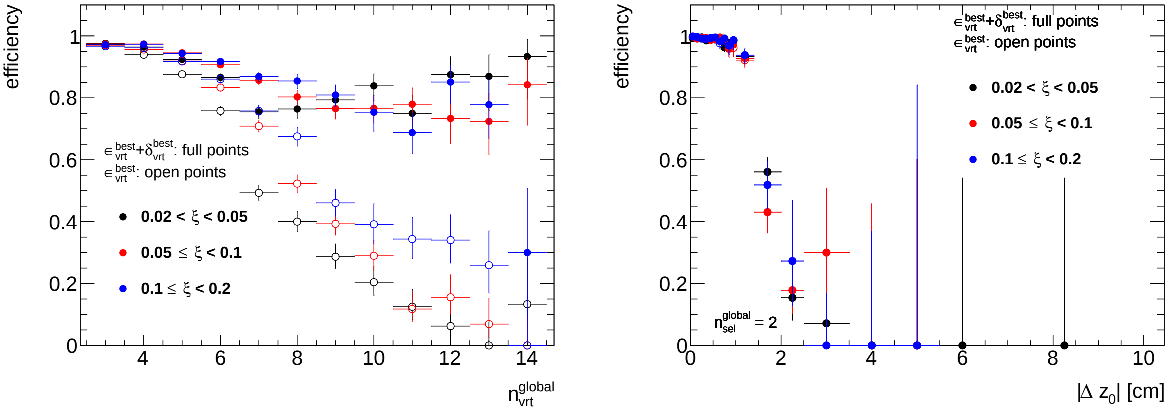

Figure 3.36: Vertex-finding efficiency in three ranges of ξ as a function of (left) $n_{\mathrm{vrt}}^{\mathrm{global}}$ and (right) with respect to the $|\Delta z_0|$ between reconstructed tracks in events with $n_{\mathrm{vrt}}^{\mathrm{global}} = 2$.

c) additional fake vertex,

d) additional primary vertex (vertex splitting or background vertex reconstructed as best vertex),

e) additional secondary vertex from the decay.

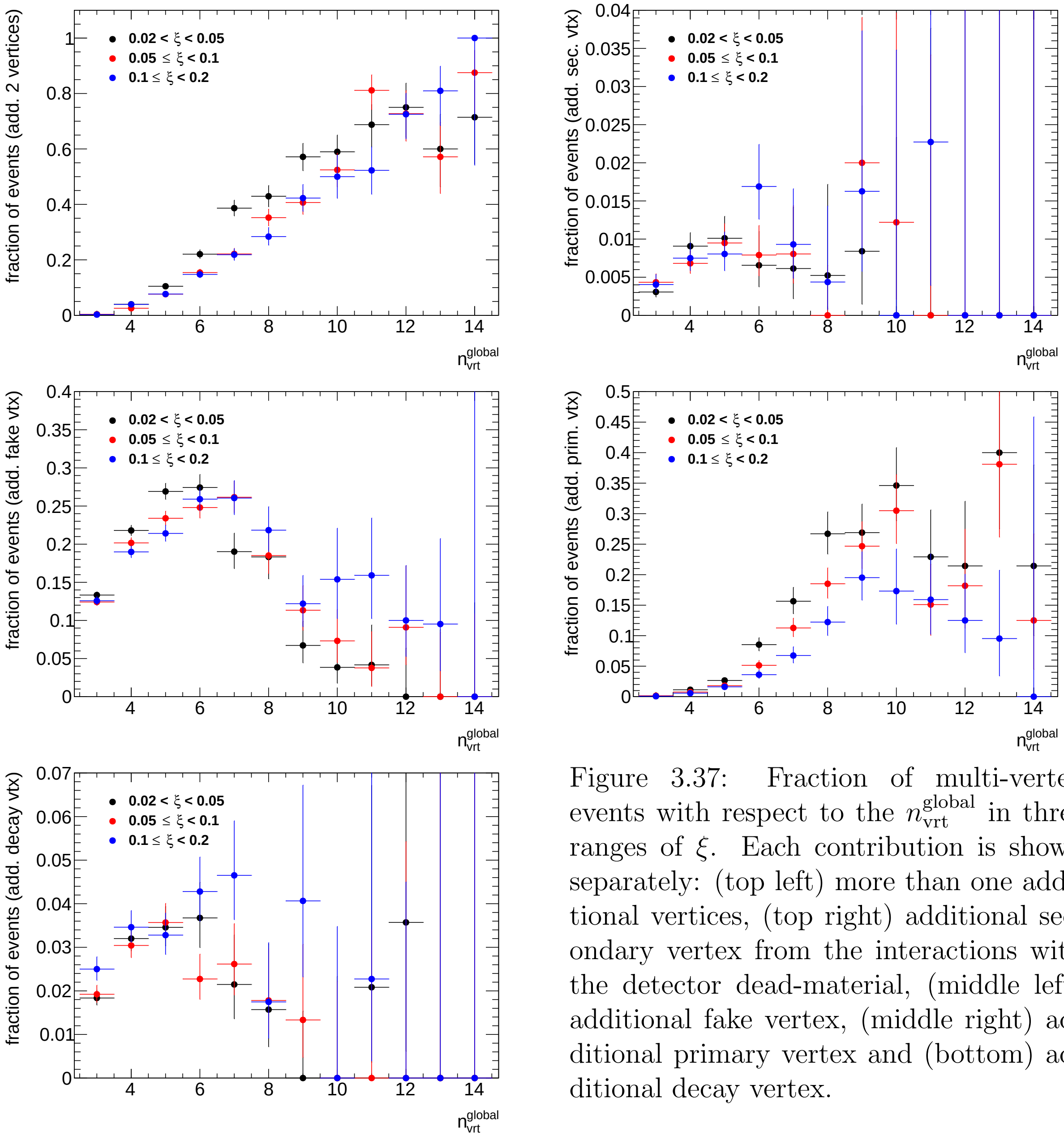

Figure 3.37: Fraction of multi-vertex events with respect to the $n_{\mathrm{vrt}}^{\mathrm{global}}$ in three ranges of ξ. Each contribution is shown separately: (top left) more than one additional vertices, (top right) additional secondary vertex from the interactions with the detector dead-material, (middle left) additional fake vertex, (middle right) additional primary vertex and (bottom) additional decay vertex.

The fraction of such events, $f_{\mathrm{vrt}}^{\mathrm{veto}}\left(n_{\mathrm{vrt}}^{\mathrm{global}}\right)$, is given by:

$$\begin{aligned} f_{\mathrm{vrt}}^{\mathrm{veto}}\left(n_{\mathrm{vrt}}^{\mathrm{global}}\right) &= \frac{\text{number of events with more than one reconstructed TOF vertex}}{\text{number of events with at least one reconstructed TOF vertex}} \\ &= f_a + f_b + f_c + f_d + f_e \end{aligned} \tag{3.17}$$

where f_a to f_e are the fractions of events with additional vertices, with labels corresponding to the items in the listing above.

As before, the fraction was calculated as a function of $|\Delta z_0|$ for events with $n_{\mathrm{vrt}}^{\mathrm{global}} = 2$. Figure 3.37 shows the fraction of multi-vertex events with respect to the $n_{\mathrm{vrt}}^{\mathrm{global}}$. There is a large fraction of events ($> 90\%$) with additional background vertices for $n_{\mathrm{vrt}}^{\mathrm{global}} \geq 9$, what would result in large correction factor. Hence, the analysis was limited to events with $n_{\mathrm{sel}}^{\mathrm{global}} \leq 8$ ($n_{\mathrm{sel}}^{\mathrm{global}} \leq n_{\mathrm{vrt}}^{\mathrm{global}}$). The total fraction of multi-vertex events, $f_a + f_b + f_c + f_d + f_e$, as a function of $n_{\mathrm{vrt}}^{\mathrm{global}}$ and $|\Delta z_0|$, shown in Fig. 3.38, demonstrates that $f_{\mathrm{vrt}}^{\mathrm{veto}}(|\Delta z_0|)$ is very small ($< 2\%$) for events with $n_{\mathrm{vrt}}^{\mathrm{global}} = 2$.

Although, the analysis was limited to $n_{\mathrm{sel}}^{\mathrm{global}} \leq 8$ ($n_{\mathrm{sel}}^{\mathrm{global}} \leq n_{\mathrm{vrt}}^{\mathrm{global}}$), a fraction of events with additional background vertices was still relatively large. Since most of these additional vertices are fake (and as accidental not correlated with true-level primary distributions), it was checked whether the charged-particle multiplicity distributions are different for events with and without reconstructed fake vertices. These distributions, as shown in Fig 3.39, are in good agreement, thus, above studies of vertex reconstruction were repeated using MC events that do not contain reconstructed fake vertices. It means that events with additional fake vertex were rejected (similarly to the analysis of real data) and no correction is needed for such losses since it only affects overall normalization (not the shapes of distributions under study). The vertex-finding efficiency, which was calculated from such events, is shown in Fig. 3.40. It is greater than 95% for events with $2 \leq n_{\mathrm{vrt}}^{\mathrm{global}} \leq 8$. In addition, the corresponding fraction of multi-vertex events, shown in Figs. 3.41 and 3.42, is smaller than 20%. Since fake vertices were rejected from this study, the f_c term from Eq. (3.17) is equal to 0. The correction factors calculated from MC events that do not contain reconstructed fake vertices were used in the analysis instead of the one obtained from the full MC sample.

Correction to BBC-Small

The SDT trigger conditions imposed a signal in RPs and a veto on any signal in the same-side small BBC tiles, whereas a signal in the opposite-side BBC-small was required by the offline event selection. These requirements were imposed in order to accept only events with rapidity gap and reduce DD, ND and accidental backgrounds. A joined BBC-small efficiency, ϵ_{BBC}, was obtained as a function of each measured quantity using PYTHIA 8 4C (SaS) SD embedded into ZB data, EPOS SD+SD′ and HERWIG SD MC. The efficiency was calculated for events within fiducial region as follows:

$$\epsilon_{\mathrm{BBC}} = \frac{\text{number of MC events satisfying the BBC-small selection criteria}}{\text{number of MC events}} \tag{3.18}$$

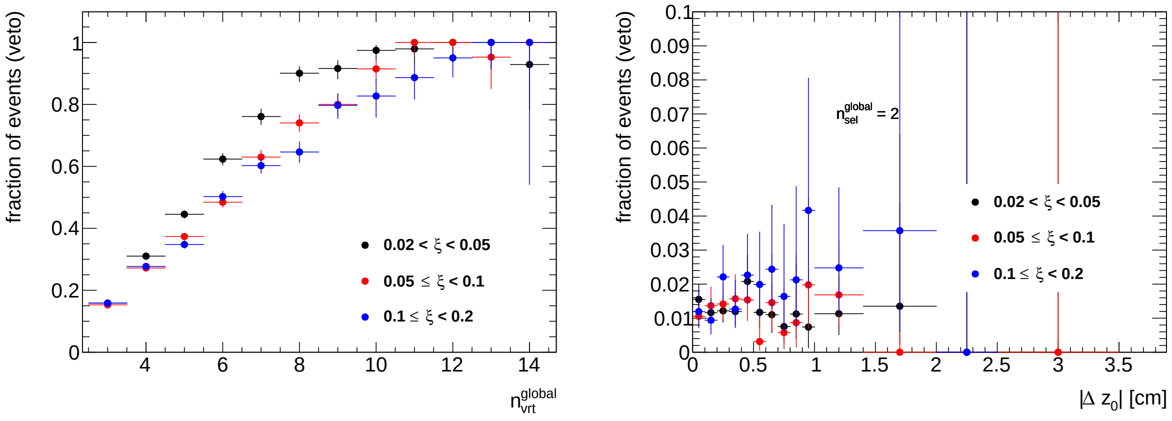

Figure 3.38: Total fraction of multi-vertex events as a function of (left) $n_{\rm vrt}^{\rm global}$ for events with $n_{\rm vrt}^{\rm global} > 2$ and (right) $|\Delta z_0|$ for events with $n_{\rm vrt}^{\rm global} = 2$ in three ranges of ξ.

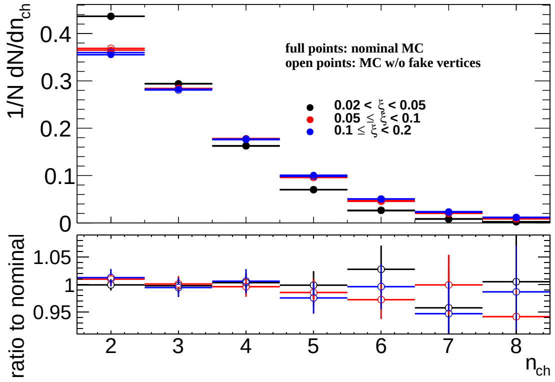

Figure 3.39: Normalized charged-particle multiplicity distributions in three ranges of ξ calculated from PYTHIA 8 SD embedding MC for (full points) all generated events and (open points) events without reconstructed fake vertices.

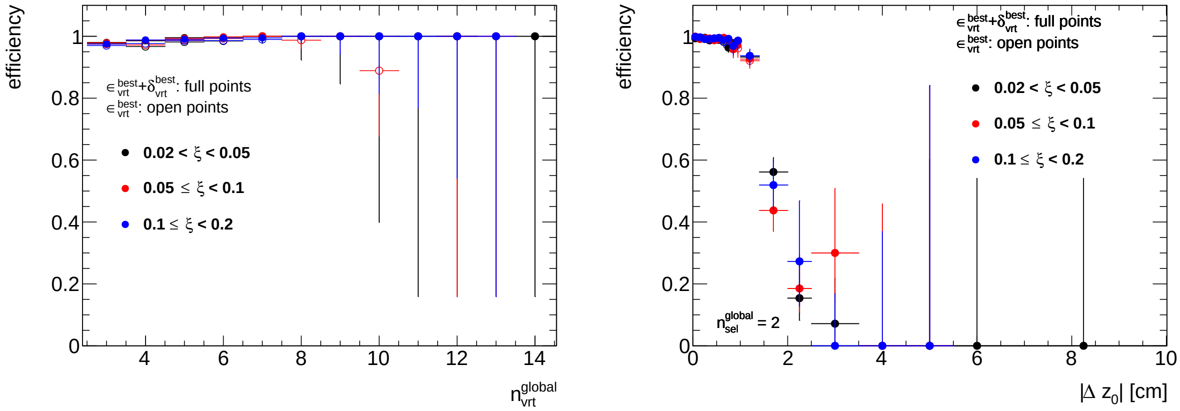

Figure 3.40: Vertex-finding efficiency in three ranges of ξ as a function of (left) $n_{\rm vrt}^{\rm global}$ and (right) with respect to the $|\Delta z_0|$ between reconstructed tracks in events with $n_{\rm vrt}^{\rm global} = 2$. Only events that do not contain additional fake vertices were used.

Figures 3.43 to 3.45 show the fraction of generated true-level MC events, within the fiducial region of the measurement, in which the selection criteria on BBC-small signal and veto are fulfilled. The efficiency weakly depends on the measured variables (n_{ch}, p_{T} and $\bar{\eta}$). In addition, veto, signal and joined BBC-small efficiencies are presented separately as a function of ξ in Fig. 3.46. The ϵ_{BBC} strongly depends on ξ and varies from about 90% for events with ξ within $0.02 - 0.05$ to about 60% for events with $0.1 < \xi < 0.2$. However, measurements of corrected ξ distributions are out of the scope of this analysis.

Data is corrected for BBC-small efficiency using PYTHIA 8 4C (SaS). The uncertainty related to this correction is estimated by using HERWIG and EPOS SD+SD′ samples, where the hadronization models are different from that used in PYTHIA 8. Figure 3.47 shows the PYTHIA 8 prediction on BBC efficiency divided by the HERWIG prediction in three ranges of ξ. The deviations between these two models are of the order of 4% at $0.02 < \xi < 0.05$, 2% at $0.05 < \xi < 0.1$ and about 10% at $0.1 < \xi < 0.2$. The differences

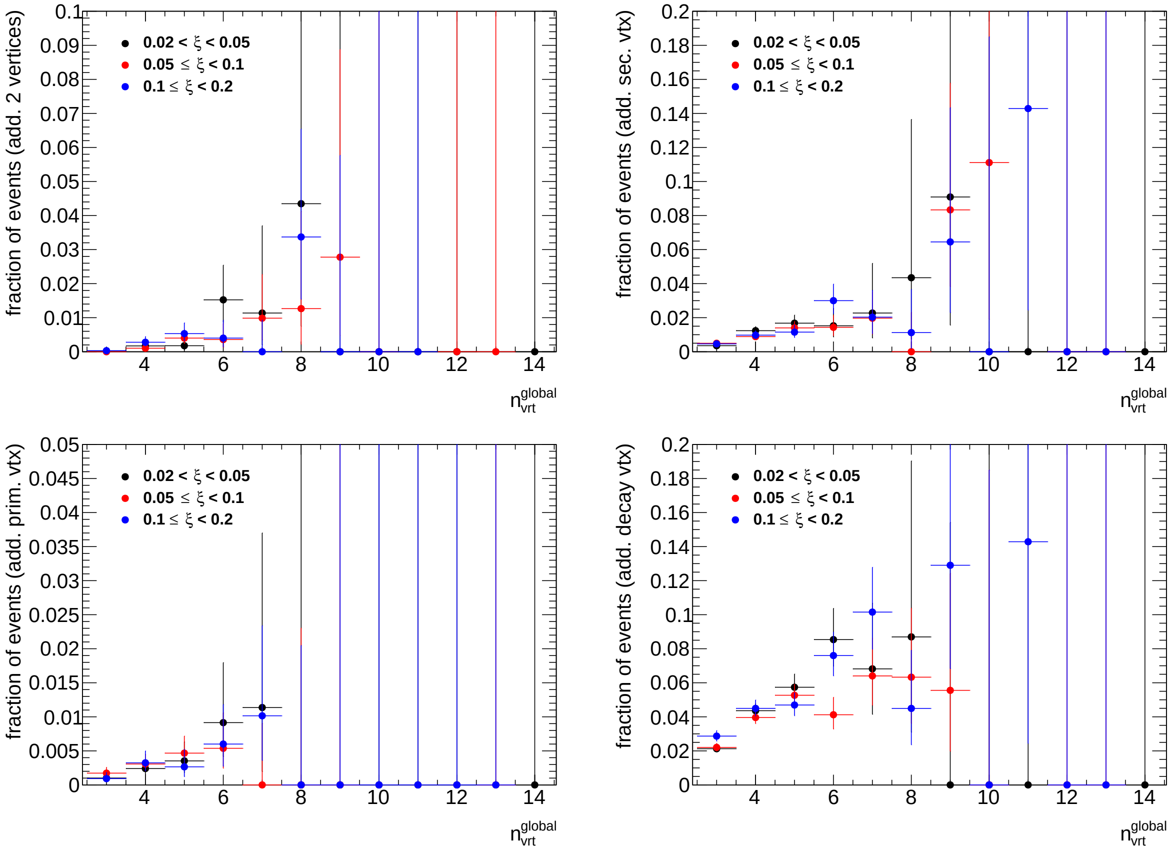

Figure 3.41: Fraction of multi-vertex events with respect to the $n_{\mathrm{vrt}}^{\mathrm{global}}$ in three ranges of ξ. Each contribution is shown separately: (top left) more than one additional vertices, (top right) additional secondary vertex from the interactions with the detector dead-material, (bottom left) additional primary vertex and (bottom right) additional decay vertex. Only events that do not contain additional fake vertices were used.

between PYTHIA 8 and EPOS SD+SD′ predictions are shown in Fig. 3.48. Most of them are of the order of 3%, except $n_{\rm ch} \leq 3$ for which the difference varies up to 6%. The maximum difference between PYTHIA 8 and HERWIG/EPOS hadronization models is used as systematic uncertainty.

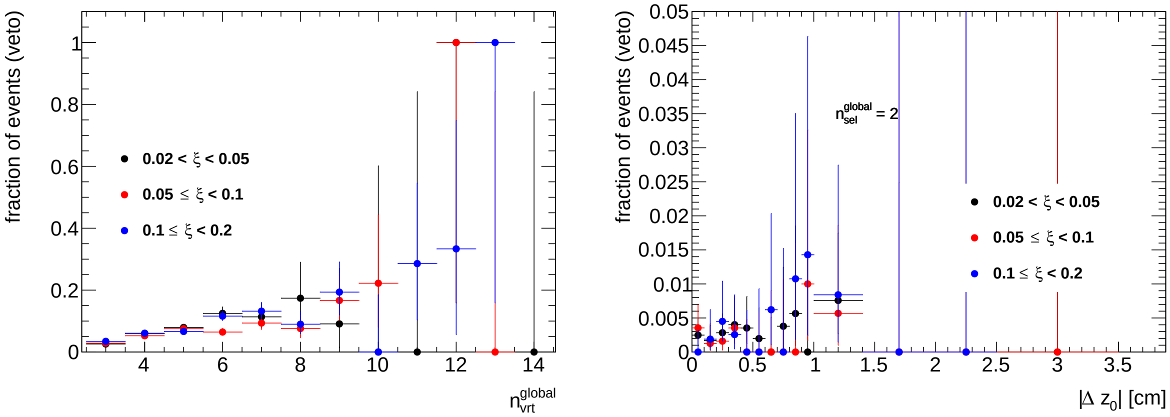

Figure 3.42: Total fraction of multi-vertex events as a function of (left) $n_{\rm vrt}^{\rm global}$ for events with $n_{\rm vrt}^{\rm global} > 2$ and (right) $|\Delta z_0|$ for events with $n_{\rm vrt}^{\rm global} = 2$ in three ranges of ξ. Only events that do not contain additional fake vertices were used.

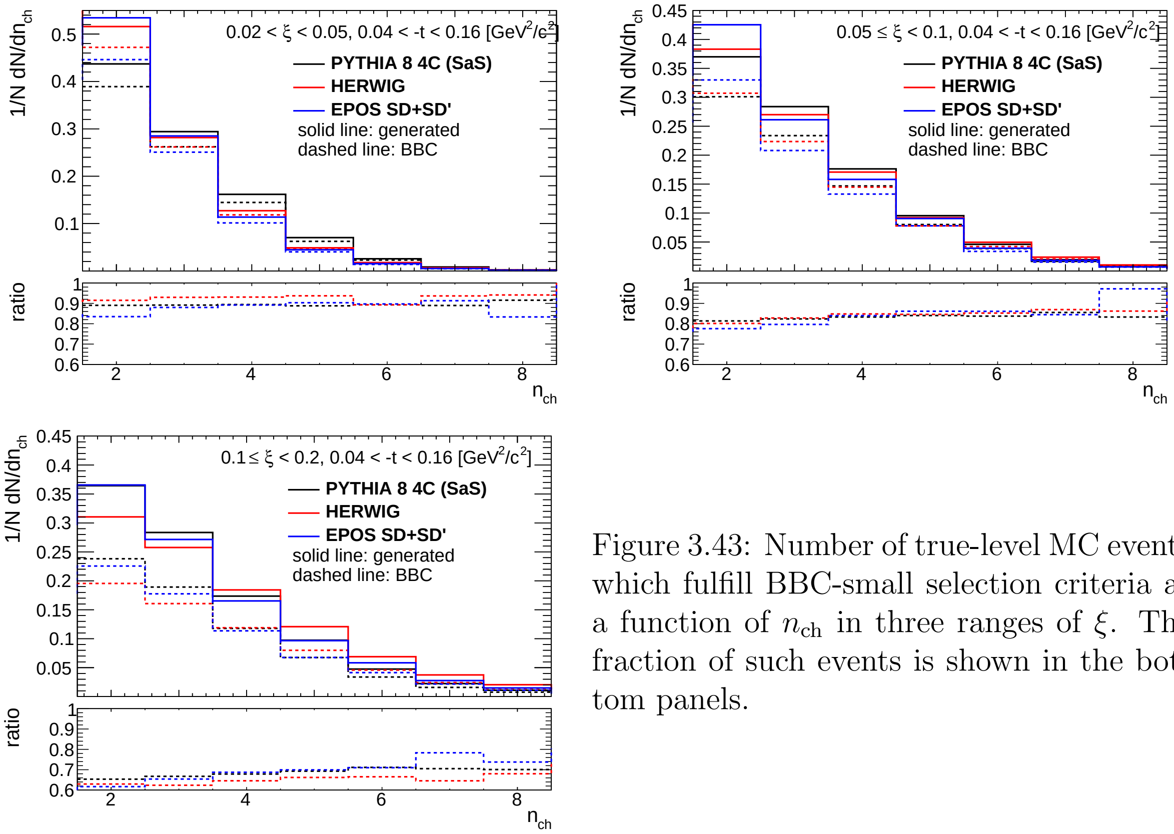

Figure 3.43: Number of true-level MC events which fulfill BBC-small selection criteria as a function of $n_{\rm ch}$ in three ranges of ξ. The fraction of such events is shown in the bottom panels.

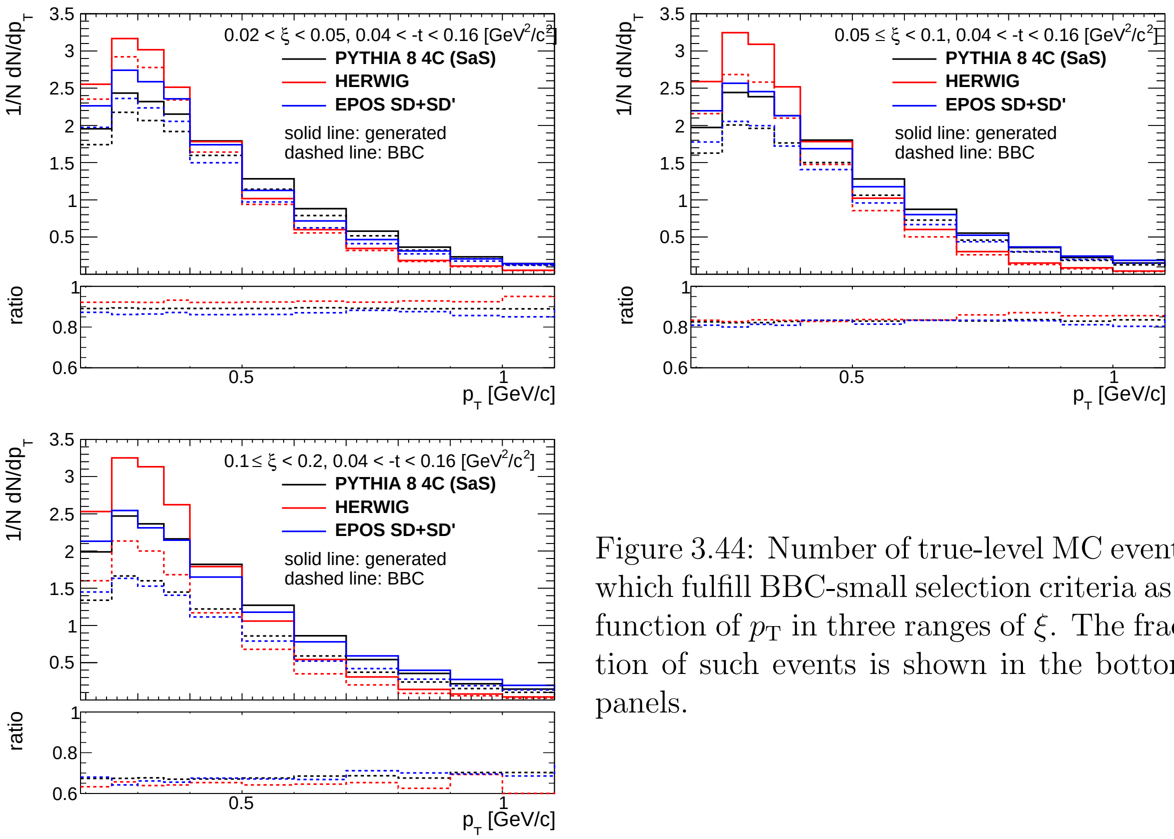

Figure 3.44: Number of true-level MC events which fulfill BBC-small selection criteria as a function of p_{T} in three ranges of ξ. The fraction of such events is shown in the bottom panels.

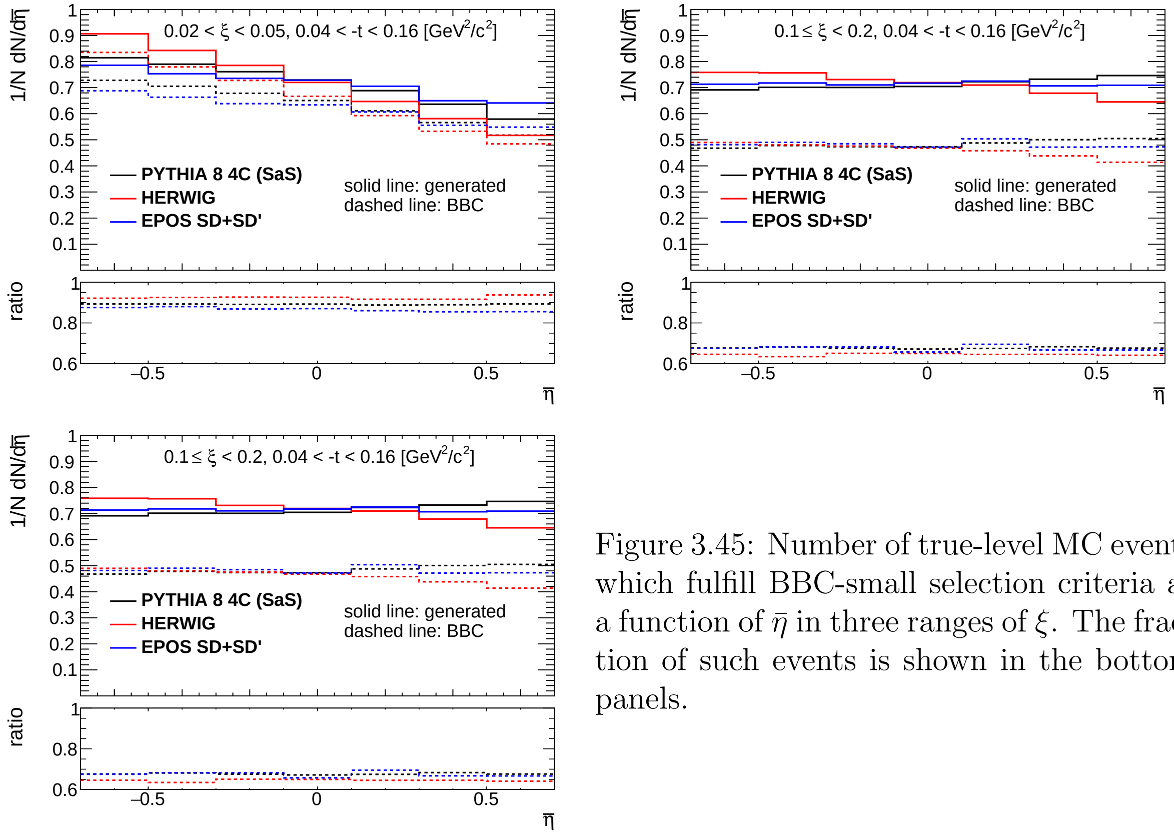

Figure 3.45: Number of true-level MC events which fulfill BBC-small selection criteria as a function of $\bar{\eta}$ in three ranges of ξ. The fraction of such events is shown in the bottom panels.

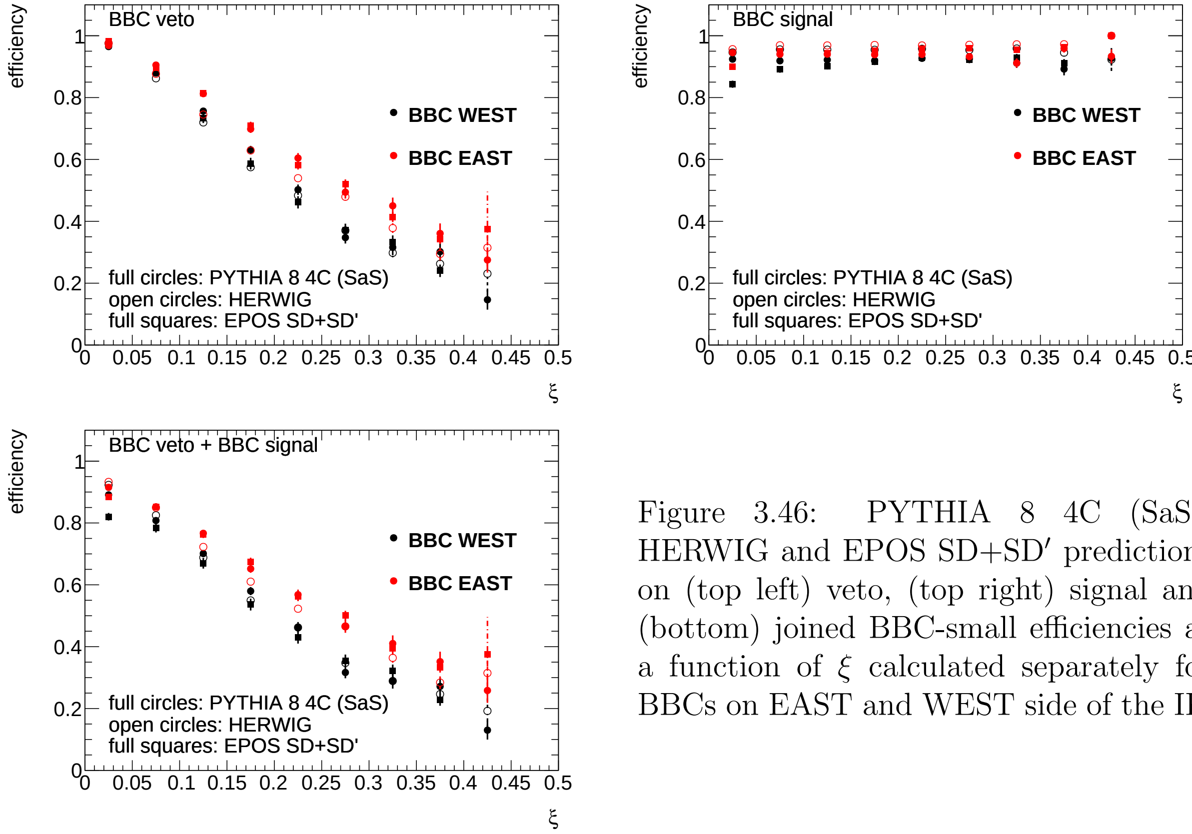

Figure 3.46: PYTHIA 8 4C (SaS), HERWIG and EPOS SD+SD′ predictions on (top left) veto, (top right) signal and (bottom) joined BBC-small efficiencies as a function of ξ calculated separately for BBCs on EAST and WEST side of the IP.

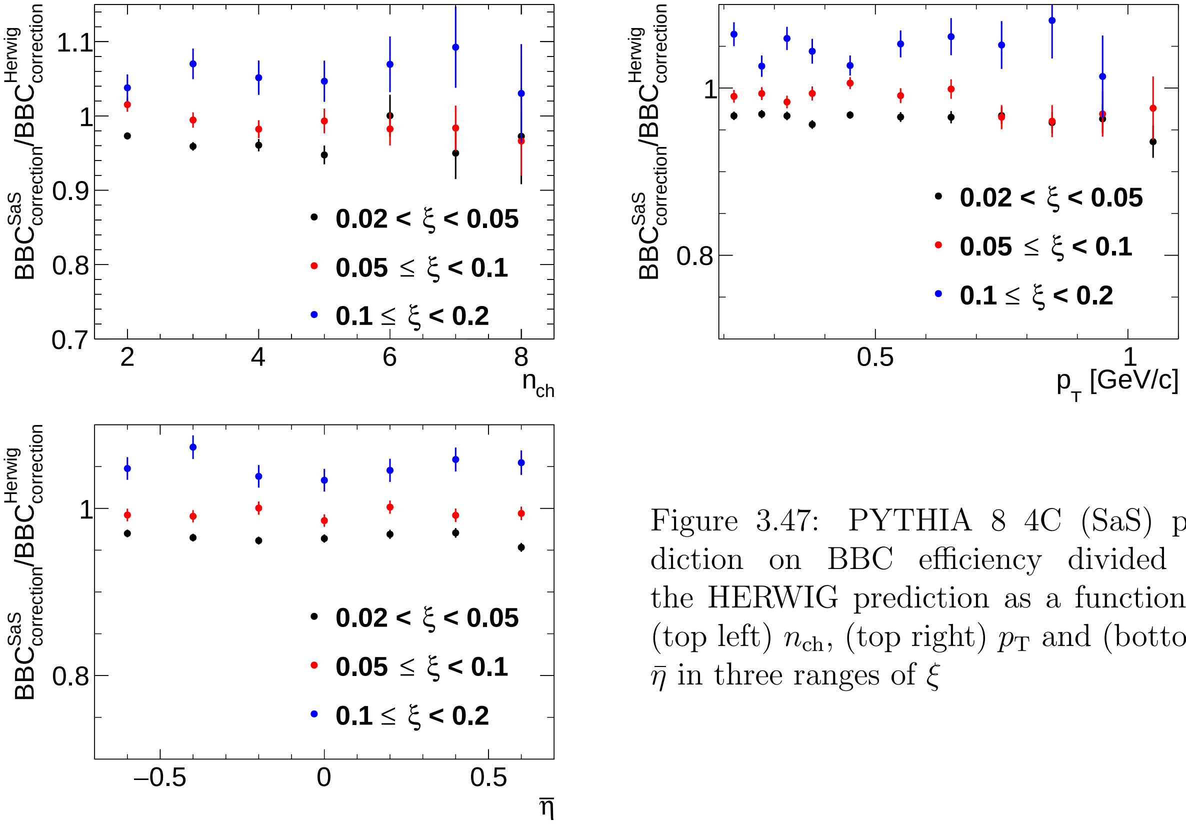

Figure 3.47: PYTHIA 8 4C (SaS) prediction on BBC efficiency divided by the HERWIG prediction as a function of (top left) n_{ch}, (top right) p_{T} and (bottom) $\bar{\eta}$ in three ranges of ξ

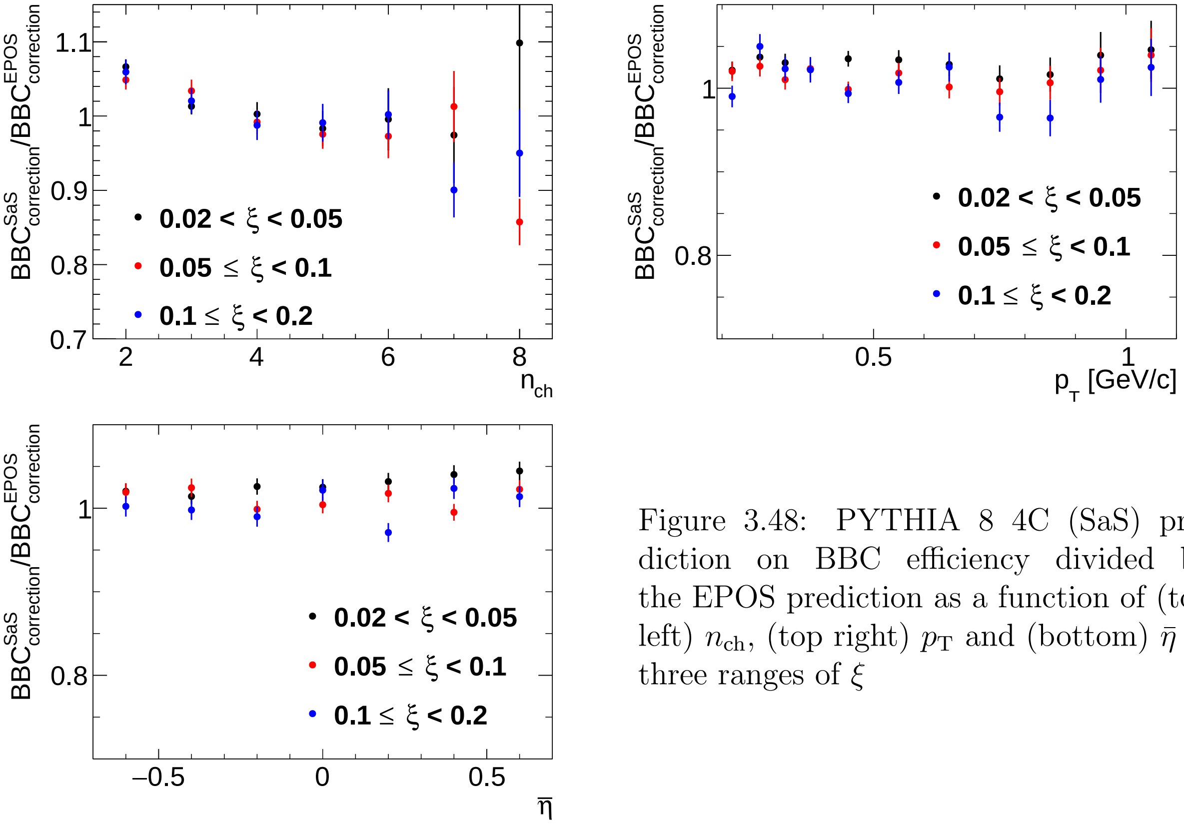

Figure 3.48: PYTHIA 8 4C (SaS) prediction on BBC efficiency divided by the EPOS prediction as a function of (top left) n_{ch}, (top right) p_{T} and (bottom) $\bar{\eta}$ in three ranges of ξ

3.8 Migrations into and out of the Fiducial Region

In this section the corrections due to the migrations of tracks and forward-scattered protons into and out of the fiducial region are described.

Migrations of Tracks into and out of the Fiducial Region

The procedure, described in this section, accounts for migrations of tracks into and out of the fiducial region, which originate from TPC resolution effects. The correction factor for such tracks, $f_{\mathrm{okr}}(p_T, \eta)$ is defined as follows:

$$f_{\mathrm{okr}}(p_{\mathrm{T}}, \eta) = \frac{1 - f^{-}_{\mathrm{okr}}(p_{\mathrm{T}}, \eta)}{1 - f^{+}_{okr}(p_{\mathrm{T}}, \eta)} \tag{3.19}$$

where $f^{-}_{\mathrm{okr}}(p_{\mathrm{T}}, \eta)$ is the fraction of reconstructed tracks for which the corresponding primary particle is outside of the kinematic range of the measurement and $f^{+}_{\mathrm{okr}}(p_{\mathrm{T}}, \eta)$ is the fraction of primary particles for which the corresponding reconstructed track is outside of the kinematic range of the measurement.

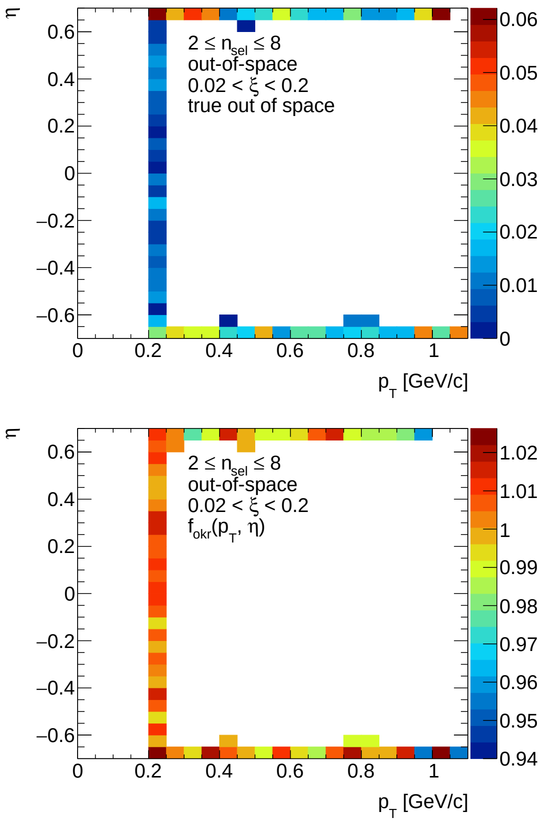

Figure 3.49: (top left) Fraction of selected tracks migrating from outside of the kinematic range to the signal region, (top right) fraction of particles for which the corresponding reconstructed track is outside the kinematic range of the measurement and (bottom) the correction factor for migrations of tracks.

The resulting residual migrations, shown in Fig. 3.49, were estimated using PYTHIA 8 SD embedding MC. The main effect was observed at $|\eta| \sim 0.7$, where about $2-6\%$ reconstructed tracks were associated to primary particle outside the fiducial region. However, above contributions to the correction factor, $f_{\mathrm{okr}}(p_T, \eta)$, cancel each other and the resulting factor is about 2% at $|\eta| \sim 0.7$.

Migrations in ξ

The analysis was performed in three ranges of ξ. Thus, there are migrations into and out of these ξ regions. They mainly originate from the resolution of ξ reconstructed from RP tracks. Figure 3.50 shows the resolution of ξ as a function of the true-level ξ (denoted as ξ_{true}) with fitted zeroth order polynomial. The resolution of ξ is fairly constant and equals to about 0.3%.

The corrections due to migrations into and out of ξ regions was defined as:

$$f_\xi = \frac{1 - f_\xi^-}{1 - f_\xi^+} \tag{3.20}$$

where f_ξ^- is the fraction of events for which the corresponding true-level, ξ_{true}, is outside of the ξ region and f_ξ^+ is the fraction of events for which the corresponding reconstructed, ξ_{reco}, is outside of the ξ region.

The f_ξ was calculated for each measured variable separately. Figures 3.51 to 3.53 show the fraction of events f_ξ^- and f_ξ^+ as a function of n_{ch}, p_{T} and $\bar{\eta}$. The lower panel in each figure shows the corresponding correction factor f_ξ. The largest differences between migrations into and out of the ξ regions were observed at $0.02 < \xi < 0.05$, where they are of the order of $2-4\%$. In the other ξ regions, the difference between f_ξ^- and f_ξ^+ is smaller than 1%.

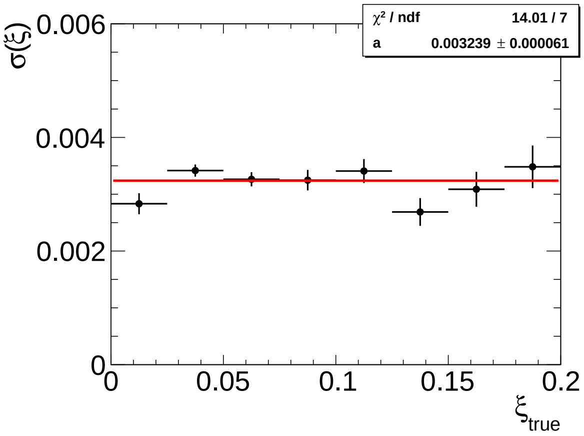

Figure 3.50: The resolution of ξ as a function of ξ_{true}. The zeroth order polynomial, shown as red line, was fitted.

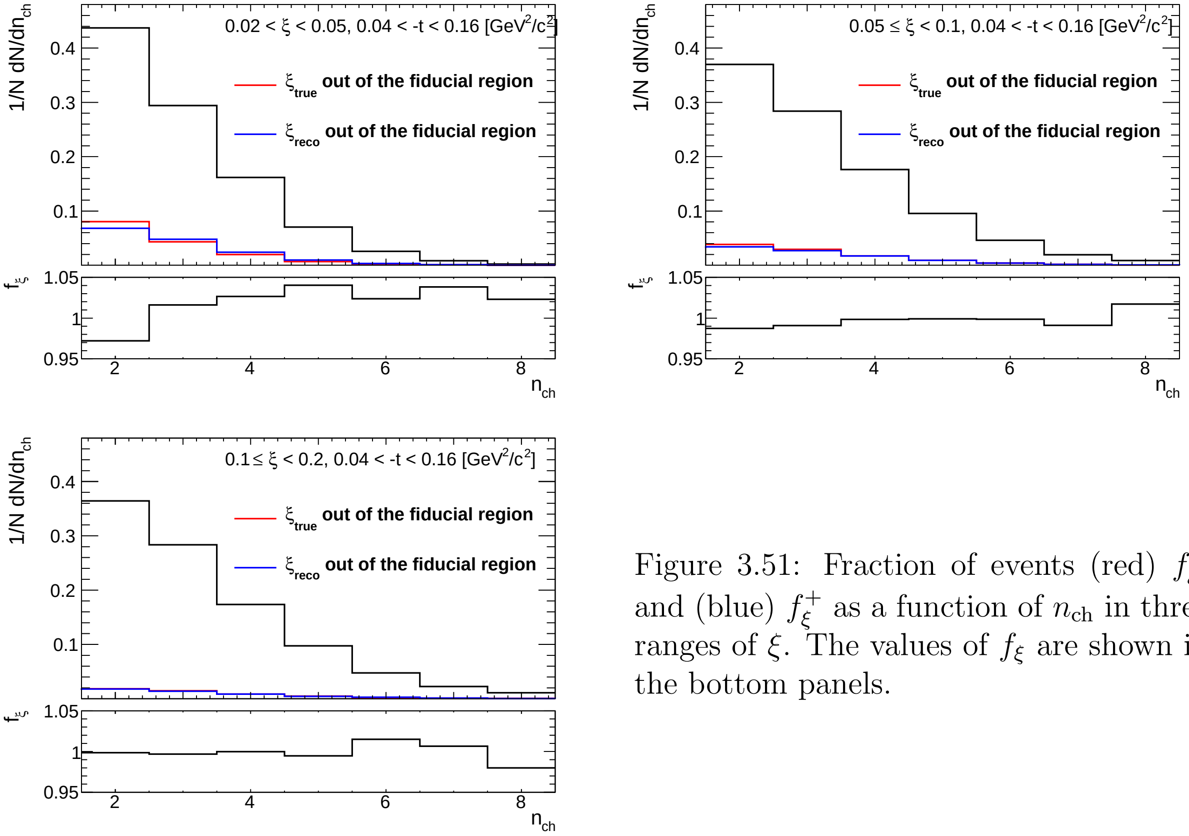

Figure 3.51: Fraction of events (red) f_ξ^- and (blue) f_ξ^+ as a function of n_{ch} in three ranges of ξ. The values of f_ξ are shown in the bottom panels.

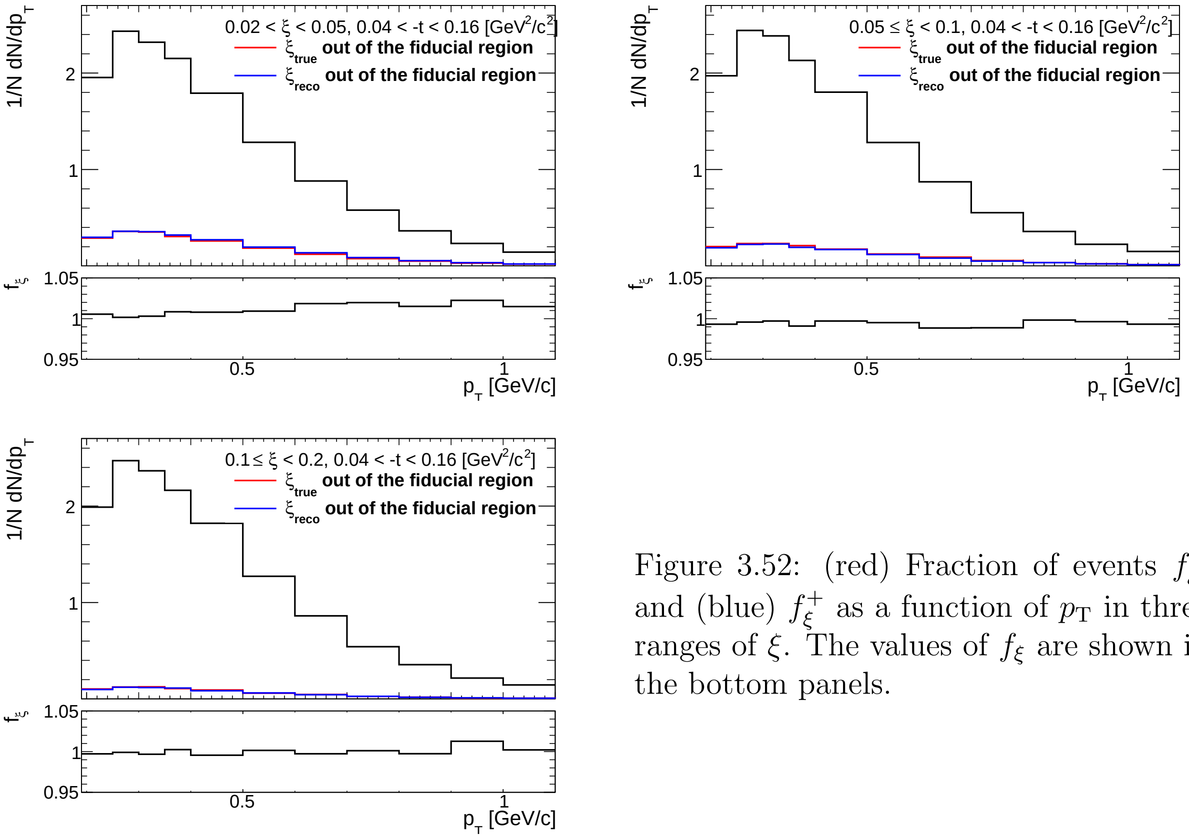

Figure 3.52: (red) Fraction of events f_ξ^- and (blue) f_ξ^+ as a function of p_T in three ranges of ξ. The values of f_ξ are shown in the bottom panels.

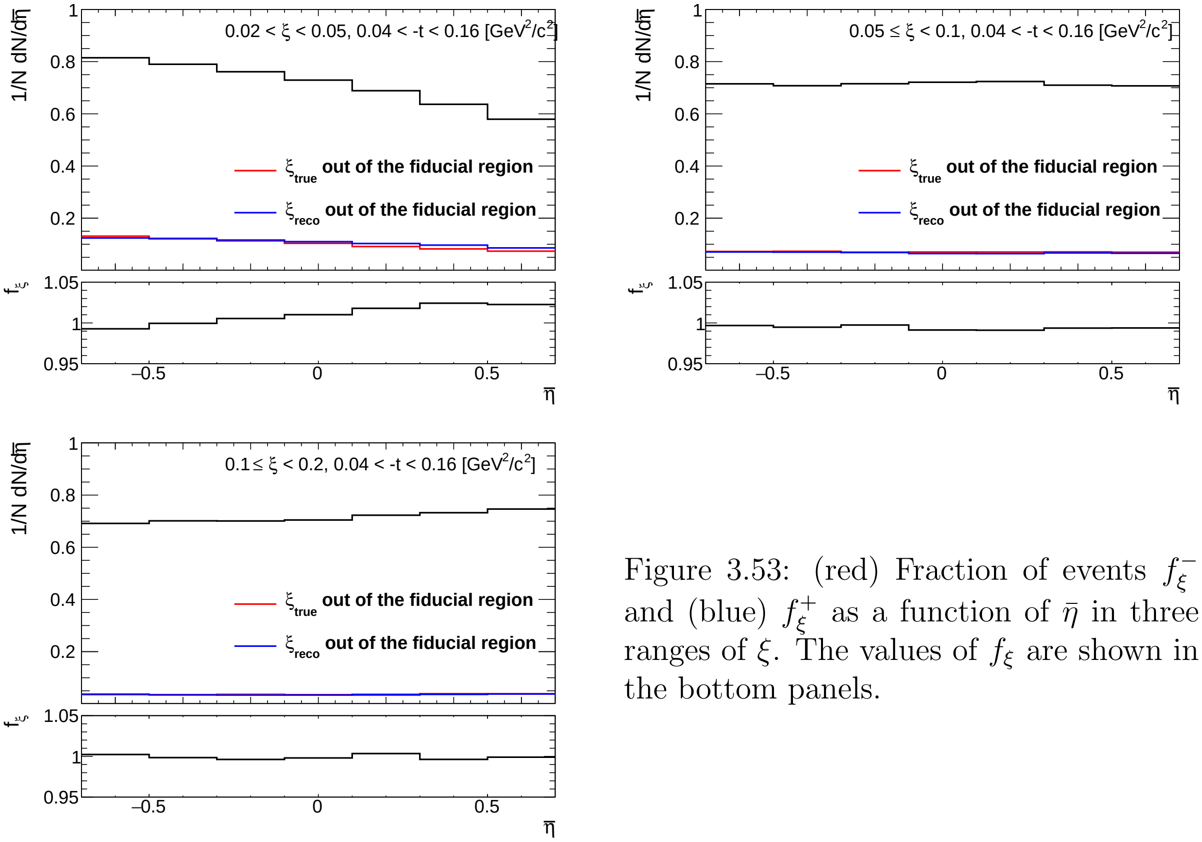

Figure 3.53: (red) Fraction of events f_ξ^- and (blue) f_ξ^+ as a function of $\bar{\eta}$ in three ranges of ξ. The values of f_ξ are shown in the bottom panels.

3.9 Event Corrections and Unfolding Procedure

After subtraction of accidental, DD, CD and ND backgrounds (as described in Sec. 3.5 and 3.6), the data was corrected for detector inefficiencies to obtain the distributions of charged particles and particle to antiparticle (pion, kaon, proton and their antiparticle) multiplicity ratios. These corrections include:

- event-by-event weights due to vertex reconstruction efficiency:

$$w_{\mathrm{ev}}^{\mathrm{vrt}}\left(n_{\mathrm{vrt}}^{\mathrm{global}}, |\Delta z_0|\right) = \frac{1}{\epsilon_{\mathrm{vrt}}\left(n_{\mathrm{vrt}}^{\mathrm{global}}, |\Delta z_0|\right)} \cdot \frac{1}{1 - f_{\mathrm{vrt}}^{\mathrm{veto}}\left(n_{\mathrm{vrt}}^{\mathrm{global}}, |\Delta z_0|\right)} \tag{3.21}$$

  where the $|\Delta z_0|$ dependence is only applicable for events with $n_{\mathrm{vrt}}^{\mathrm{global}} = 2$ as described in Sec. 3.7.

- track-by-track weights due to track reconstruction efficiency, track backgrounds, migrations of tracks into and out of the fiducial region:

$$w_{\mathrm{trk}}\left(p_{\mathrm{T}}, \eta, V_z\right) = \frac{1 - f_{\mathrm{bkg}}\left(p_{\mathrm{T}}, \eta\right) - f_{\mathrm{fake}}\left(p_{\mathrm{T}}, \eta\right)}{\epsilon_{\mathrm{TPC}}\left(p_{\mathrm{T}}, \eta, V_z\right)\epsilon_{\mathrm{TOF}}\left(p_{\mathrm{T}}, \eta, V_z\right)} f_{\mathrm{okr}}\left(p_{\mathrm{T}}, \eta\right) \tag{3.22}$$

  where: $\epsilon_{\mathrm{TPC}}\left(p_{\mathrm{T}}, \eta, V_z\right)$ is TPC track reconstruction efficiency (Sec. 3.7), $\epsilon_{\mathrm{TOF}}\left(p_{\mathrm{T}}, \eta, V_z\right)$ is TOF matching efficiency (Sec. 3.7), $f_{\mathrm{okr}}\left(p_{\mathrm{T}}, \eta\right)$ is a factor accounting for migrations of tracks into and out of the fiducial region, $f_{\mathrm{bkg}}\left(p_{\mathrm{T}}, \eta\right)$ is a fraction of background tracks, and $f_{\mathrm{fake}}\left(p_{\mathrm{T}}, \eta\right)$ is a fraction of fake tracks. These corrections were not applied for n_{ch} measurements since they were taken into account in the unfolding procedure.

- event-by-event (for n_{ch} distribution) or track-by-track (for p_{T}, $\bar{\eta}$ distributions) weights, f_{ξ}, due to migrations of events between three ξ regions.

Additionally, the obtained distributions were corrected for BBC-small efficiency, ϵ_{BBC}, using the following weight, which was calculated for each true-level quantity (n_{ch}, p_{T}, $\bar{\eta}$) in three ranges of ξ separately:

$$w_{\mathrm{BBC}} = \frac{1}{\epsilon_{\mathrm{BBC}}} \tag{3.23}$$

In the following sections, the correction procedure for each of the measured distributions is presented separately.

Correction to dN/dn$_{\mathbf{sel}}$

In order to express the multiplicity distribution in terms of the number of charged particles, n_{ch}, instead of the number of selected tracks, n_{sel}, the following procedure based on the Bayesian unfolding [21, 224] was used. First, the n_{sel} distribution was corrected for vertex reconstruction effects by applying event-by-event weights, $w_{\mathrm{ev}}^{\mathrm{vrt}}(n_{\mathrm{vrt}}^{\mathrm{global}}, |\Delta z_0|)$. The number of events in which n_{ch} are produced, $N_{\mathrm{ev}}(n_{\mathrm{ch}})$, can be associated with the number of events in which $n_{\rm sel}$ are reconstructed, $N_{\rm ev}(n_{\rm sel})$. Since there are several possible $n_{\rm sel}$ observed in $n_{\rm ch}$ event, $N_{\rm ev}(n_{\rm ch})$ is given by:

$$\begin{aligned} N_{\rm ev}(n_{\rm ch}) &= \sum_{n_{\rm sel}=0} P(n_{\rm ch}|n_{\rm sel}) \cdot N_{\rm ev}(n_{\rm sel}) \\ &= \frac{1}{\epsilon_m(n_{\rm ch})\epsilon_r(n_{\rm ch})} \sum_{n_{\rm sel}=2}^{8} P(n_{\rm ch}|n_{\rm sel}) \cdot N_{\rm ev}(n_{\rm sel}) \end{aligned} \tag{3.24}$$

where:

$P(n_{\rm ch}|n_{\rm sel})$ is the conditional probability of having $n_{\rm ch}$ charged particles in an event in which $n_{\rm sel}$ tracks were found,

$\epsilon_m(n_{\rm ch})$ is a factor, which recovers events that are lost due to TPC track reconstruction and TOF matching inefficiencies, i.e. those with $n_{\rm ch} \geq 2$ but $n_{\rm sel} < 2$,

$\epsilon_r(n_{\rm ch})$ is a factor, which recovers events which are lost due to fake tracks, i.e. those with $n_{\rm ch} \leq 8$ but $n_{\rm sel} > 8$. It was checked that this effect is negligible (smaller than 1‰) and can be omitted.

Figure 3.54 shows $\epsilon_m(n_{\rm ch})$ in three ranges of ξ. It was derived from PYTHIA 8 embedding MC and varies from about 25% for $n_{\rm ch} = 2$ to 95% for $n_{\rm ch} = 8$. Since there are additional data-driven corrections to TPC and TOF efficiencies, MC simulations were modified by randomly removing or adding tracks. This was done in accordance with differences in the efficiencies between data and MC. Figure 3.55 shows $\epsilon_m(n_{\rm ch})$ calculated in three ranges of ξ using no-pile-up PYTHIA 8 and EPOS SD+SD′. The differences between these two models, which are up to 8% for $n_{\rm ch} = 2$ and $0.1 < \xi < 0.2$, were symmetrized and taken as a systematic uncertainty.

The probability $P(n_{\rm ch}|n_{\rm sel})$ can be derived using Bayes' theorem, which can be stated mathematically in terms of charged particle and charged track multiplicities as:

$$P\left(n_{\rm sel}|n_{\rm ch}\right) \cdot P\left(n_{\rm ch}\right) = P\left(n_{\rm ch}|n_{\rm sel}\right) \cdot P\left(n_{\rm sel}\right) \tag{3.25}$$

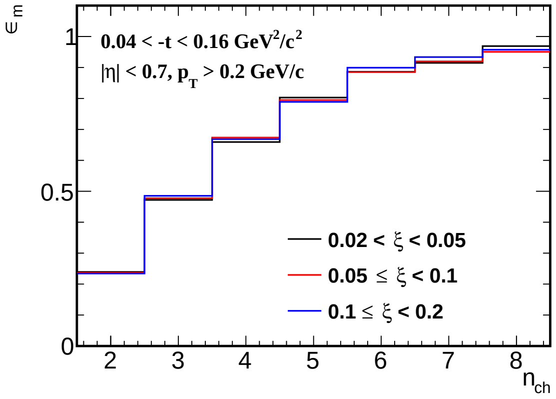

Figure 3.54: $\epsilon_m(n_{\rm ch})$ calculated separately in three ranges of ξ using PYTHIA 8 embedding MC.

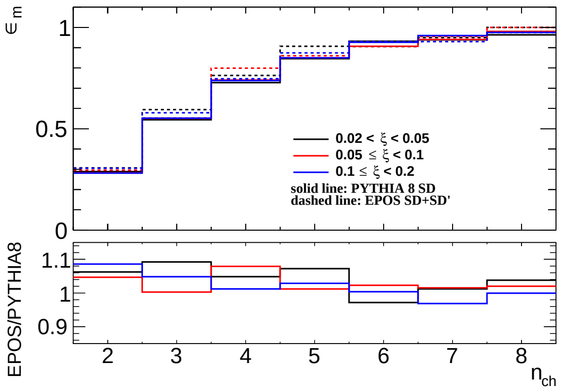

Figure 3.55: Comparison of $\epsilon_m(n_{\text{ch}})$ calculated separately in three ranges of ξ using PYTHIA 8 SD and EPOS SD+SD′ no-pile-up MCs. The ratios of EPOS to PYTHIA 8 predictions are shown in the bottom panel.

where: $P(n_{\text{sel}})$ and $P(n_{\text{ch}})$ are probabilities of observing n_{sel} and n_{ch} respectively, $P(n_{\text{ch}}|n_{\text{sel}})$ and $P(n_{\text{sel}}|n_{\text{ch}})$ are conditional probabilities.
In order to improve the estimate of $P(n_{\text{ch}}|n_{\text{sel}})$, the unfolding is done iteratively:

- In the first iteration, it is assumed that:

$$P(n_{\text{ch}}|n_{\text{sel}}) = P = P^{\text{MC}}(n_{\text{sel}}|n_{\text{ch}})\frac{P^{\text{MC}}(n_{\text{ch}})}{P^{\text{MC}}(n_{\text{sel}})} \tag{3.26}$$

$$N_{\text{ev}}(n_{\text{ch}}) = \frac{1}{\epsilon_m(n_{\text{ch}})}\sum_{n_{\text{sel}}=2}^{8} N_{\text{ev}}(n_{\text{sel}})\cdot P \tag{3.27}$$

  where $P^{\text{MC}}(n_{\text{sel}}|n_{\text{ch}})$, $P^{\text{MC}}(n_{\text{ch}})$ and $P^{\text{MC}}(n_{\text{sel}})$ are obtained from MC. $P^{\text{MC}}(n_{\text{sel}}|n_{\text{ch}})$ is the same for each iteration.

- In the $(i+1)$th iteration we have:

$$P^{i+1} = P^{\text{MC}}(n_{\text{sel}}|n_{\text{ch}})\frac{N^{i}_{\text{ev}}(n_{\text{ch}})}{N_{\text{ev}}(n_{\text{sel}})} \tag{3.28}$$

$$N^{i+1}_{\text{ev}}(n_{\text{ch}}) = \frac{1}{\epsilon_m(n_{\text{ch}})}\sum_{n_{\text{sel}}=2}^{8} N_{\text{ev}}(n_{\text{sel}})\cdot P^{i+1} \tag{3.29}$$

  where $N^{i}_{\text{ev}}(n_{\text{ch}})$ is calculated in the previous iteration, and $N_{\text{ev}}(n_{\text{sel}})$ is taken from data.

The unfolding matrices $P(n_{\text{ch}}|n_{\text{sel}})$ for each ξ region, shown in Fig. 3.56, were obtained from PYTHIA 8 embedding MC and used in all iterations of the above procedure. Similarly to $\epsilon_m(n_{\text{ch}})$, the matrices were modified by randomly removing or adding tracks in order to take into account additional data-driven corrections to TPC and TOF efficiencies. In order to increase statistical precision of the unfolding matrices, all simulated events were used,

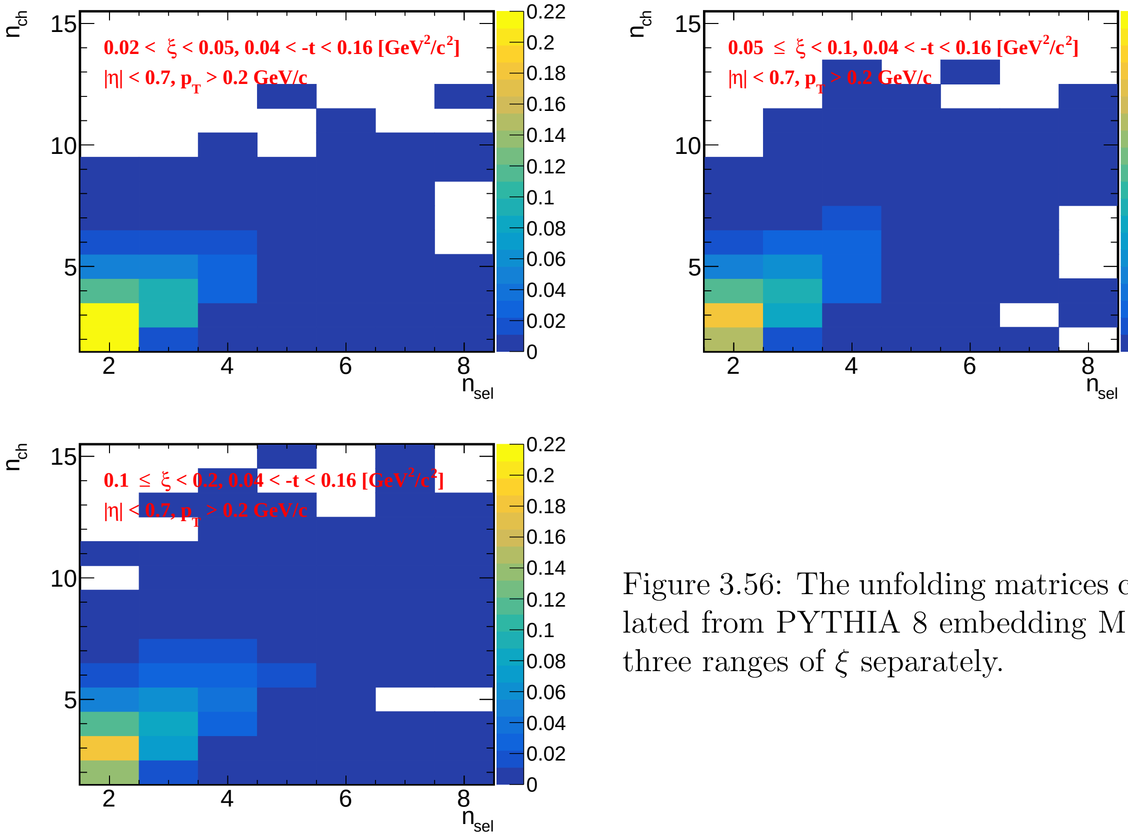

Figure 3.56: The unfolding matrices calculated from PYTHIA 8 embedding MC for three ranges of ξ separately.

i.e. also those with additional fake vertices (with n_{sel} defined as a number of primary tracks associated with the best vertex). The systematic uncertainty related to limited statistics in PYTHIA 8 was estimated by performing 50 pseudo-experiments, in which the unfolding matrices were smeared according to their statistical uncertainties. It affects mainly large charged-particle multiplicities, where it is about $8-10\%$ (as shown in Fig. 3.57), and is smaller or at the same level as other components contributing to the total systematic uncertainty.

The distribution dN/dn_{ch} obtained after the unfolding procedure was corrected for BBC-small efficiency, through $w_{\text{BBC}}(n_{\text{ch}})$ weights, and migrations of events between ξ ranges, through $f_{\xi}(n_{\text{ch}})$ weights. Since the unfolding matrices contain track reconstruction efficiencies, non-primary track backgrounds, migrations of tracks into and out of the fiducial region, the weight $w_{\text{trk}}\,(p_{\text{T}}, \eta, V_z)$ was not used.

Finally, the dN/dn_{ch} distribution was normalized to the total number of events, $N_{\text{ev}} = N$, which was calculated as the integral of the unfolded distribution.

Correction to Transverse Momentum and Pseudorapidity Distributions

First the accidental and non-SD backgrounds were subtracted from the p_{T} and $\bar{\eta}$ distributions. Next, each event was corrected for vertex reconstruction efficiency by applying $w_{\text{ev}}^{\text{vrt}}(n_{\text{vrt}}^{\text{global}}, |\Delta z_0|)$ weights. Then, the tracks were corrected for the track reconstruction efficiency, non-primary track background contribution, track and ξ migrations, BBC-small efficiency (the product of $w_{\mathrm{trk}}(p_{\mathrm{T}}, \eta, V_z)$, f_ξ and w_{BBC} weights was applied, f_ξ and w_{BBC} were calculated as a function of true-level p_{T} and $\bar{\eta}$ separately).

In order to obtain charged-particle densities, the p_{T} and $\bar{\eta}$ distributions were normalized to unity and scaled by the average charged particle multiplicity in an event $\langle n_{\mathrm{ch}} \rangle$. The latter was calculated from the corrected charged particle multiplicity distribution dN/dn_{ch} (Sec. 3.9). The above procedure was done to correct the data also for events that are lost due to $n_{\mathrm{sel}} < 2$ but $n_{\mathrm{ch}} \geq 2$ since such correction was not included in any event-by-event and track-by-track weights. There was an assumption that p_{T} and η distributions are the same for lost and measured events, but it was validated by the closure tests (Sec. 3.9). The mean p_{T} and $\bar{\eta}$ in an event, $\langle p_{\mathrm{T}} \rangle$ and $\langle \bar{\eta} \rangle$, were obtained from the measured distributions.

Closure Tests

In order to validate the correction procedures, closure tests were performed, i.e. full correction procedure was applied to the MC detector-level distributions and the results were directly compared to the true-level distributions. Figure 3.58 shows closure tests of multiplicity, transverse momentum and pseudorapidity distributions for three ranges of ξ, separately. PYTHIA 8 SD embedding MC was used as an input. In order to compare corrected

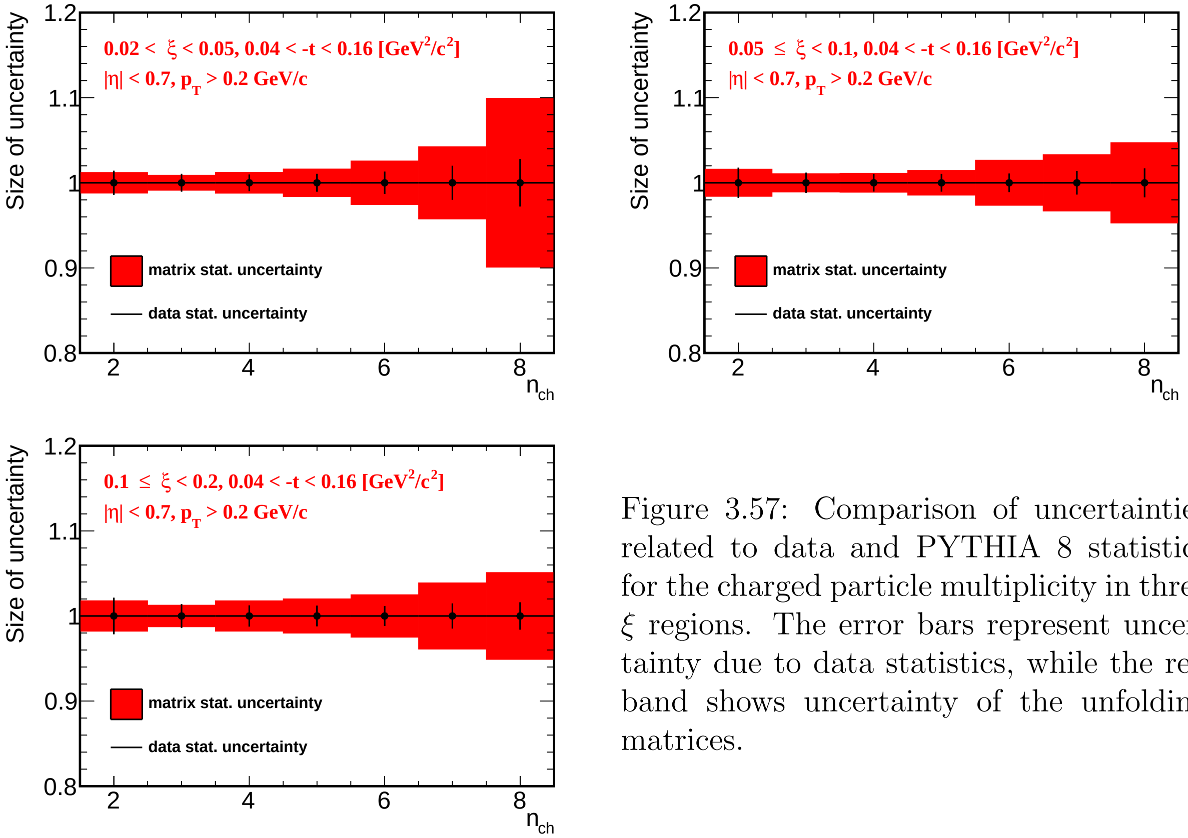

Figure 3.57: Comparison of uncertainties related to data and PYTHIA 8 statistics for the charged particle multiplicity in three ξ regions. The error bars represent uncertainty due to data statistics, while the red band shows uncertainty of the unfolding matrices.

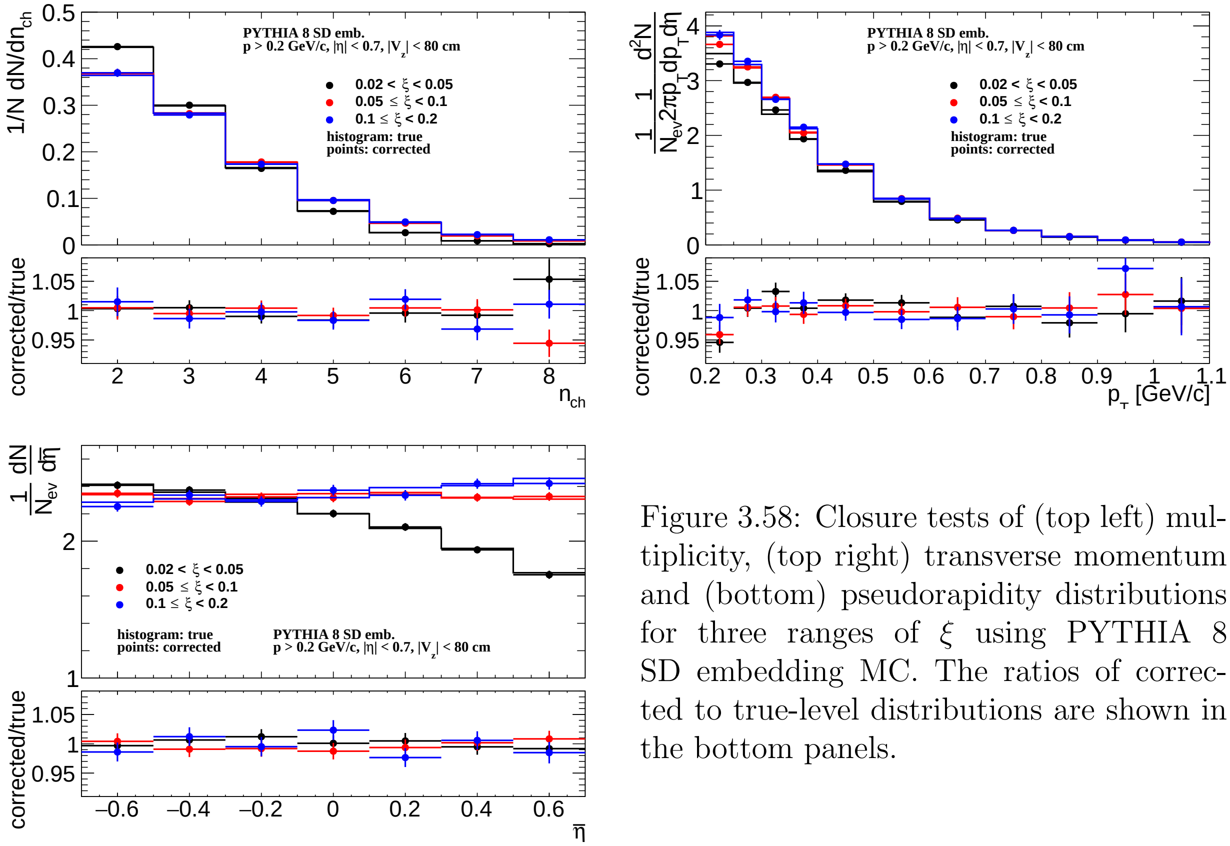

Figure 3.58: Closure tests of (top left) multiplicity, (top right) transverse momentum and (bottom) pseudorapidity distributions for three ranges of ξ using PYTHIA 8 SD embedding MC. The ratios of corrected to true-level distributions are shown in the bottom panels.

and true-level distributions, the statistical uncertainties of the true-level distributions were assumed to be 0. The difference between true-level and corrected distributions was taken as a systematic uncertainties.

EAST-WEST asymmetry

Another kind of consistency check can be performed by comparing the results obtained by tagging forward-scattered protons in different detectors. Therefore, each distribution was measured separately for events in which forward-scattered proton is on one and the other side of the IP (east-west). Figure 3.59 shows the tests of multiplicity, transverse momentum and pseudorapidity distributions for three ranges of ξ, separately. Both statistical uncertainty components, due to input data and due to unfolding matrix, are added in quadrature for n_{ch} distributions. The largest difference is observed for charged-particle multiplicity distributions, where it varies up to 20% for $n_{\mathrm{ch}} = 8$ and $0.02 < \xi < 0.1$. For the rest multiplicities and ξ ranges, the differences are smaller ($< 10\%$). In case of p_{T} and $\bar{\eta}$ distributions, a level of these disagreements is below 5%. As a result, half of the differences between east and west distributions were used to be systematic uncertainty.

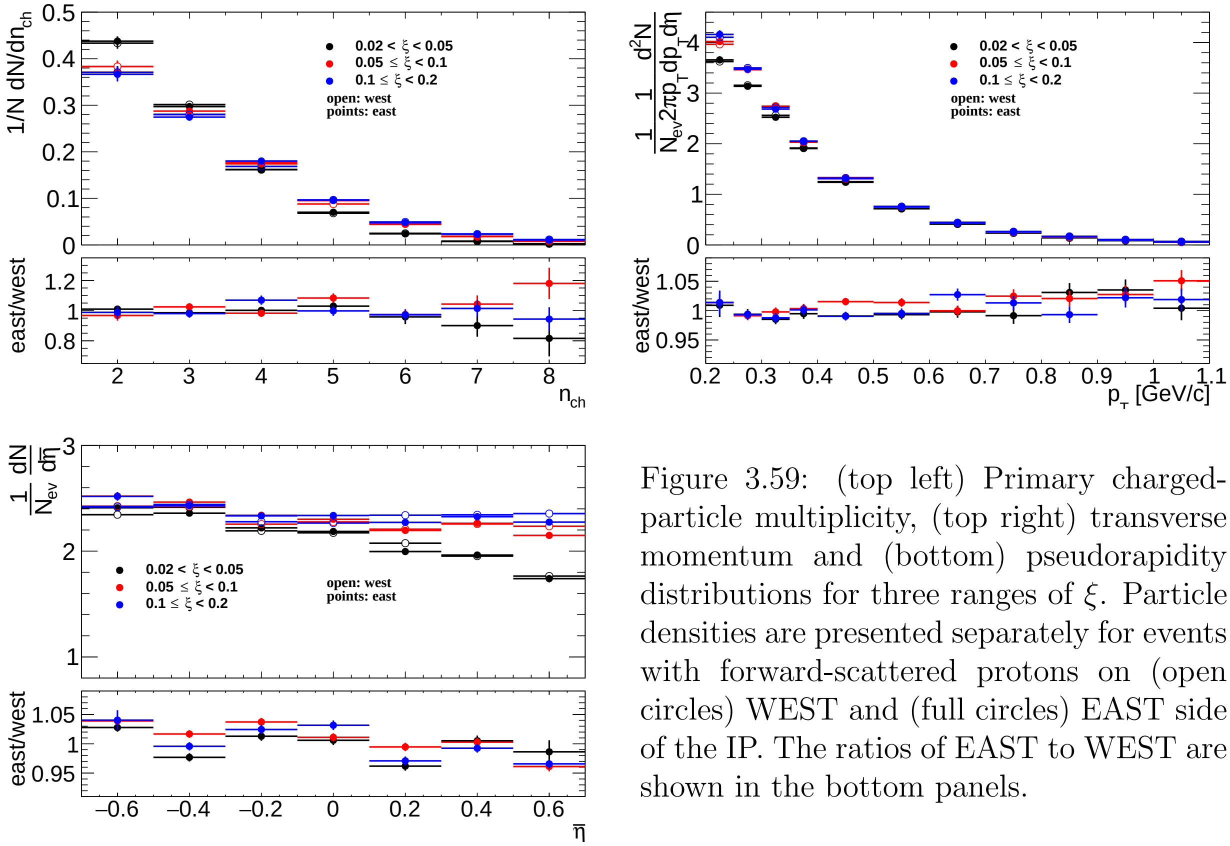

Figure 3.59: (top left) Primary charged-particle multiplicity, (top right) transverse momentum and (bottom) pseudorapidity distributions for three ranges of ξ. Particle densities are presented separately for events with forward-scattered protons on (open circles) WEST and (full circles) EAST side of the IP. The ratios of EAST to WEST are shown in the bottom panels.

Particle Identification

Specific ionization energy loss, the dE/dx, is a function of the magnitude of a particle momentum. In this section the particle identification with help of dE/dx is described. Due to a low particle multiplicity and lack of signal in VPDs on the outgoing proton side (presence of the rapidity gap) in SD events, the time of collision is not defined precisely enough, therefore, the particle identification by the TOF is not possible and the analysis was limited to identification only by dE/dx.

The ionization energy loss of charged particles in material is given by the Bethe-Bloch formula and for the STAR TPC by the more precise Bichsel formula [225]. The particle type can be determined by comparison of particle's dE/dx with the Bethe-Bloch (Bichsel) expectations. Figure 3.60 shows the dE/dx versus rigidity $q \times p$ for particles in $|\eta| < 0.7$. Particles are well separated at low $|q \times p|$, whereas at higher $|q \times p|$ the dE/dx of different particle species starts to overlap: $e^{\pm}$ and $K^{\pm}$ merge at ~ 0.4 GeV/c, $K^{\pm}$ and $\pi^{\pm}$ merge at ~ 0.65 GeV/c, and $p(\bar{p})$ and $\pi^{\pm}$ merge at ~ 1 GeV/c. Since the dE/dx distribution for a given particle type is not Gaussian, the following variable for each particle type was defined:

$$n\sigma^{i}_{dE/dx} = \ln\left(\frac{dE/dx}{(dE/dx)^{\mathrm{BB}}_{i}}\right)/\sigma \tag{3.30}$$

where $(dE/dx)_i^{\mathrm{BB}}$ is the Bethe-Bloch (Bichsel) expectation of dE/dx for the given particle type i ($i = \pi, K, p$), σ - the relative dE/dx resolution. The expected value of $n\sigma^i_{dE/dx}$ for the particle under consideration is 0 and the width equals to 1. The sample $n\sigma^i_{dE/dx}$ distribution for $\pi^\pm$, $K^\pm$ and $p(\bar{p})$ in one ξ range, $0.02 < \xi < 0.05$, is shown in Fig. 3.61. Figure 3.62 shows the $n\sigma^{\pi^\pm}_{dE/dx}$,$n\sigma^{K^\pm}_{dE/dx}$ and $n\sigma^{p(\bar{p})}_{dE/dx}$ distributions for $0.6 < p_{\mathrm{T}} < 0.65$ GeV/c in the ξ range, $0.02 < \xi < 0.05$, each corrected for the energy loss (mass of i-particle was assumed) and vertexing. To extract the particle yield for a given particle type, a multi-Gaussian fit is applied to the $n\sigma^i_{dE/dx}$ distribution in each p_{T} bin and ξ range. The parameters of the multi-Gaussian fit are the centroids μ_{i^-/i^+}, widths σ_{i^-/i^+}, sums and ratios of yields C_{i^-/i^+}, r_{i^-/i^+} for negative i^- and positive i^+ particles ($\pi^\pm$, $e^\pm$, $K^\pm$, p and $\bar{p}$). The positive and negative particle $n\sigma^i_{dE/dx}$-distributions are fitted simultaneously, where the centroids and widths are kept the same for particle and antiparticle. In some p_{T} regions, the fit does not converge, because different particle species are not well separated there. Therefore, multiple steps of the fitting procedure are performed to reduce the number of free parameters in the final fit and ensure its stability. Almost all centroids and widths are

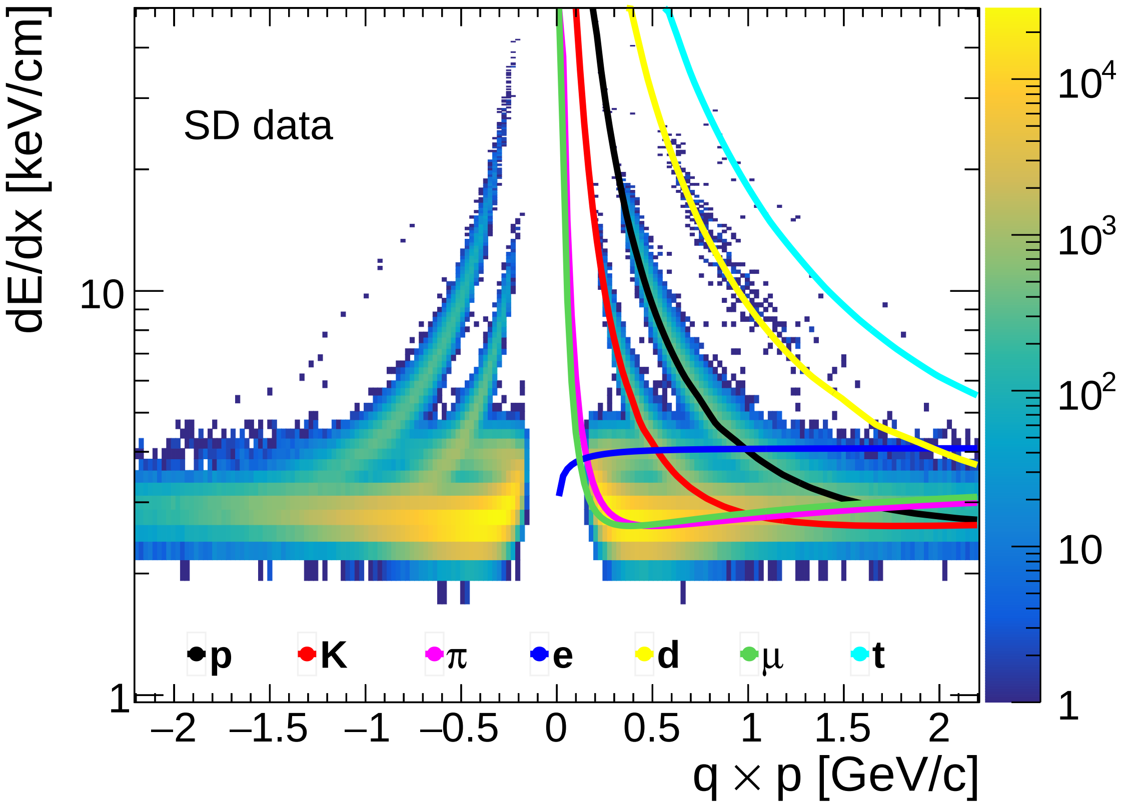

Figure 3.60: Specific ionization energy loss dE/dx as a function of rigidity $q \times p$ for particles in $|\eta| < 0.7$. The Bichsel predictions for each particle species are also shown.

constrained by a function with free parameters p_k, where $k \in \mathbb{N}$. The function is chosen to describe the data as best as possible. Since dE/dx is a function of the particle's momentum and its shape should be independent of the process under study, the values of p_k are obtained only for events with $0.02 < \xi < 0.05$ and kept the same for other ξ ranges. The electron contributions are fitted only in the first analysed p_T range, separately for each particle species and ξ range. For higher p_T ranges, they are estimated from PYTHIA 8 embedding MC, and scaled according to the ratio of PYTHIA 8 predictions and contributions fitted in the first p_T bin. The procedure slightly differs for different particle types. In each step, the multi-Gaussian fit is performed first, then the widths and centroids are fitted in p_T ranges in which the fit applied to $n\sigma^i_{dE/dx}$ converges. Later, the widths and centroids are extrapolated to other p_T ranges, in which particle species are not well separated:

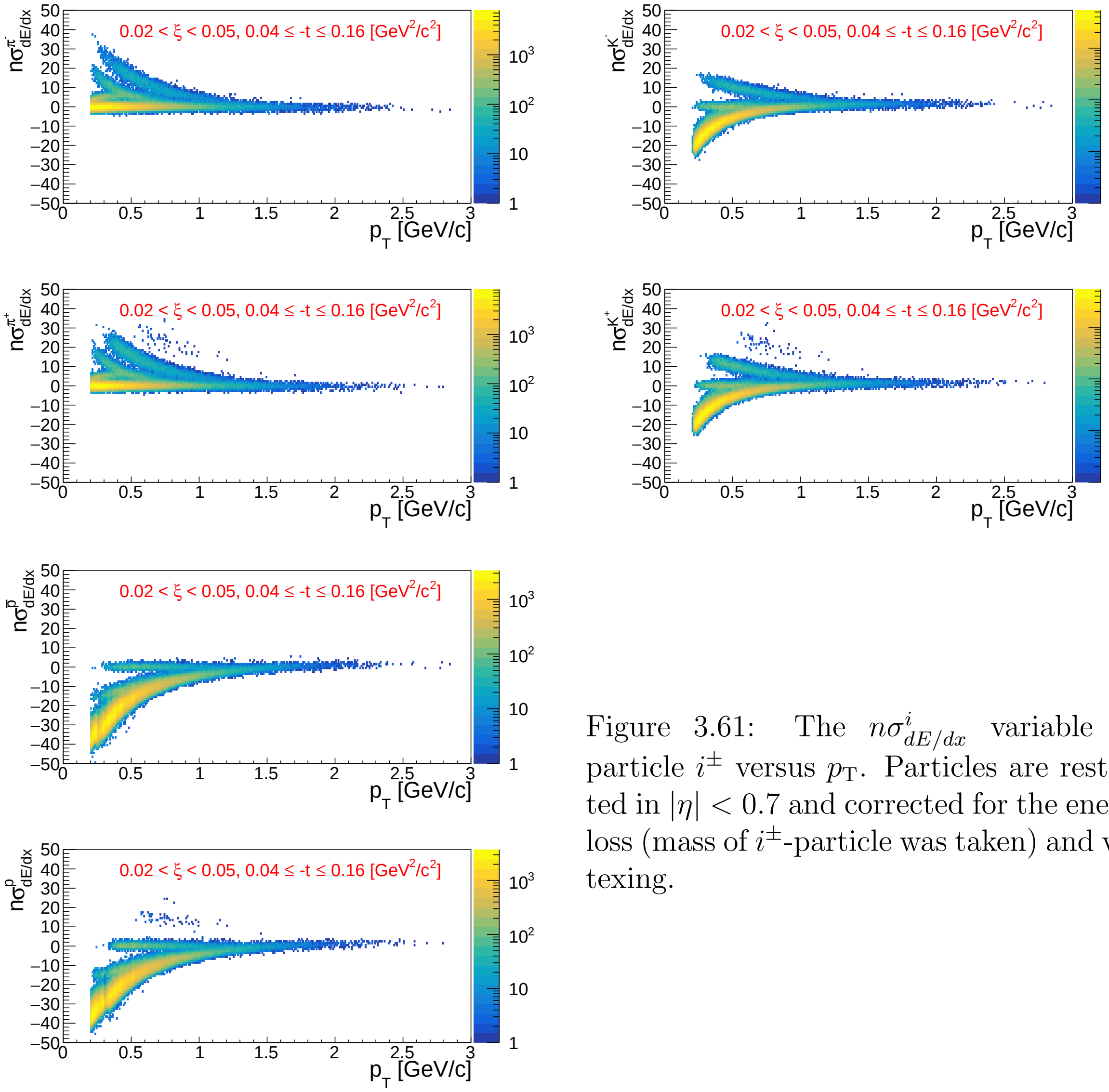

Figure 3.61: The $n\sigma^i_{dE/dx}$ variable for particle $i^\pm$ versus p_T. Particles are restricted in $|\eta| < 0.7$ and corrected for the energy loss (mass of $i^\pm$-particle was taken) and vertexing.

1. $\pi^{\pm}$:

   - Step 1 (Fig. 3.63):
     - Analyse data with $0.2 < p_{\mathrm{T}} < 0.65$ GeV/c
     - Fit μ_{π^-/π^+} and σ_{π^-/π^+} as a function of p_{T} with a polynomial $p_0 p_{\mathrm{T}}^3 + p_1 p_{\mathrm{T}}^2 + p_2 p_{\mathrm{T}} + p_3$
     - Fit r_{e^-/e^+} as a function of p_{T} with a polynomial $p_0 p_{\mathrm{T}}^2 + p_1 p_{\mathrm{T}} + p_2$
     - Fit C_{e^-/e^+}, μ_{K^-/K^+} as a functions of p_{T} with $p_0 \exp(p_1 p_{\mathrm{T}}) + p_2$
     - Fit μ_{e^-/e^+} as a function of p_{T} with $p_0 \exp\left[-(p_1 p_{\mathrm{T}})^{p_2}\right]$
     - Fit σ_{K^-/K^+} as a function of p_{T}, for $0.3 < p_{\mathrm{T}} < 0.5$ GeV/c, with constant p_0
     - Fit $\mu_{\bar{p}/p}$ and $\sigma_{\bar{p}/p}$ as a function of p_{T} with $p_0 \exp(p_1 p_{\mathrm{T}})$

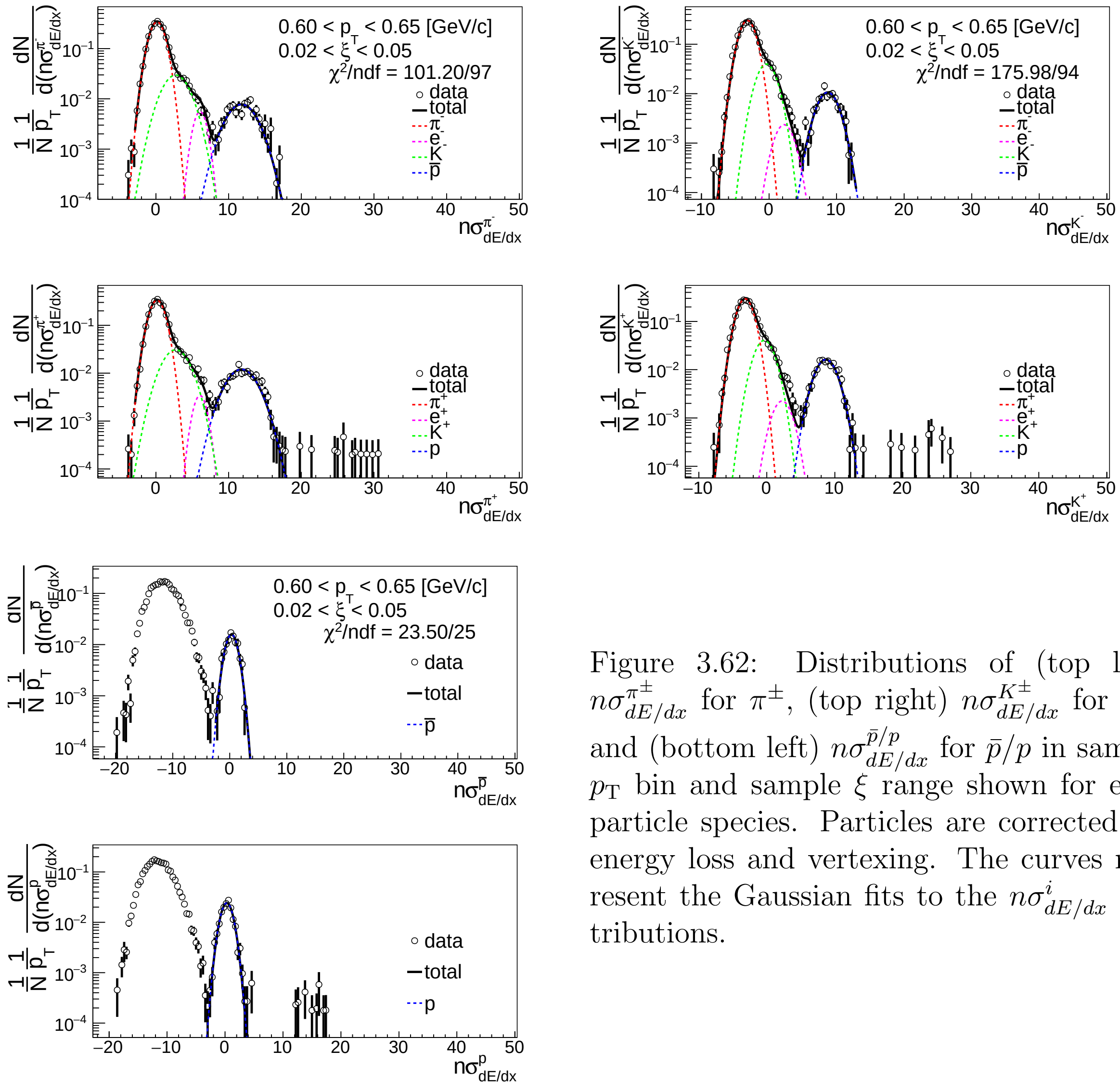

Figure 3.62: Distributions of (top left) $n\sigma^{\pi^{\pm}}_{dE/dx}$ for $\pi^{\pm}$, (top right) $n\sigma^{K^{\pm}}_{dE/dx}$ for $K^{\pm}$ and (bottom left) $n\sigma^{\bar{p}/p}_{dE/dx}$ for $\bar{p}/p$ in sample p_{T} bin and sample ξ range shown for each particle species. Particles are corrected for energy loss and vertexing. The curves represent the Gaussian fits to the $n\sigma^{i}_{dE/dx}$ distributions.

- Step 2:
  - σ_{e^-/e^+} fixed to 1.2 and 0.8 for $0.2 < p_{\mathrm{T}} < 0.4$ and $0.4 < p_{\mathrm{T}} < 0.7$, respectively
  - Fit σ_{K^-/K^+} as a function of p_{T}, for $0.3 < p_{\mathrm{T}} < 0.7$ GeV/c, with constant p_0 and fix it to the value of p_0
  - The rest parameters from Step 1 are fixed to the values calculated from functions obtained in Step 1: μ_{π^-/π^+}, σ_{π^-/π^+}, , r_{e^-/e^+}, C_{e^-/e^+}, μ_{e^-/e^+} , μ_{K^-/K^+}, $\mu_{\bar{p}/p}$, $\sigma_{\bar{p}/p}$

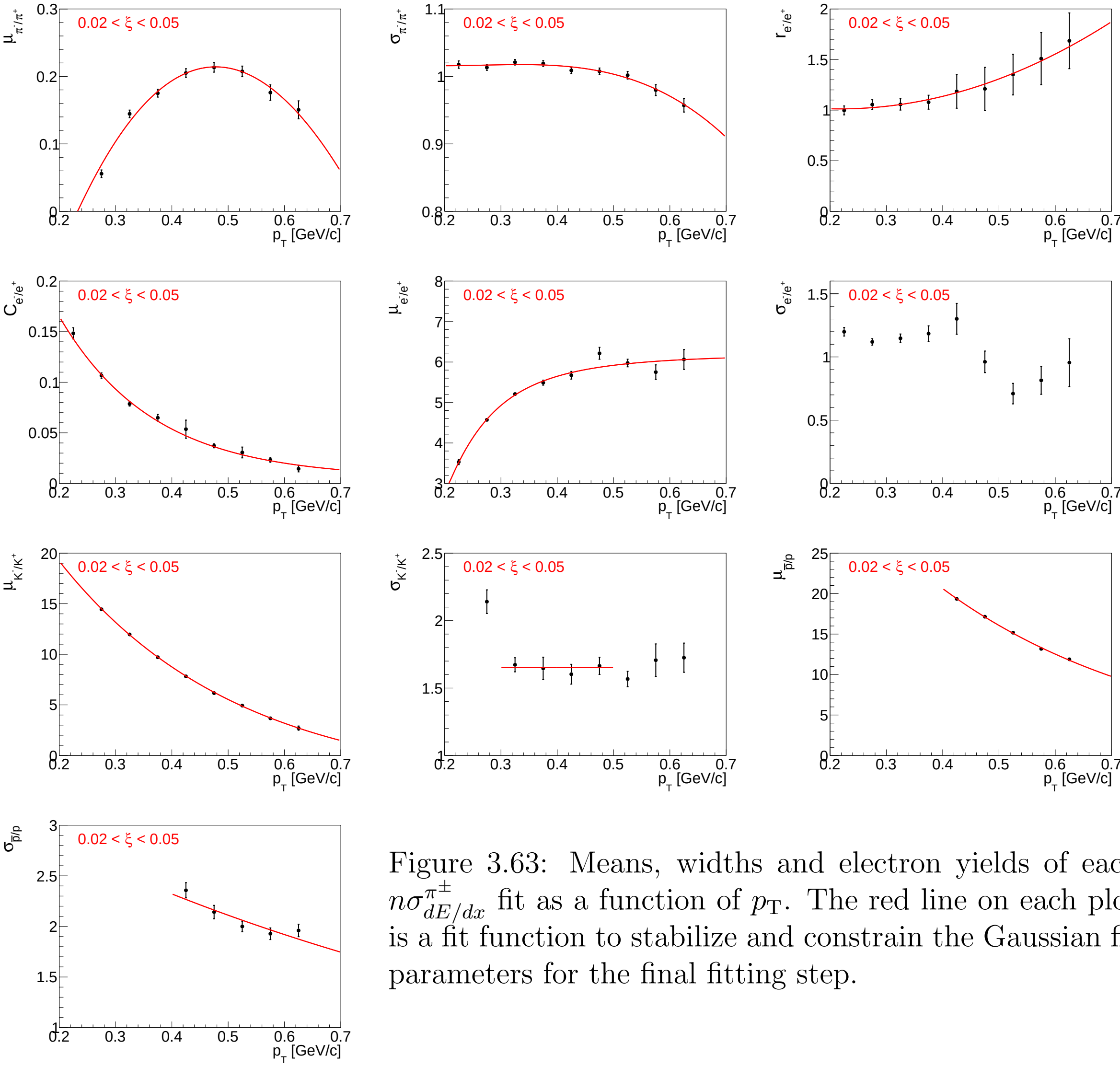

Figure 3.63: Means, widths and electron yields of each $n\sigma^{\pi^\pm}_{dE/dx}$ fit as a function of p_{T}. The red line on each plot is a fit function to stabilize and constrain the Gaussian fit parameters for the final fitting step.

2. $K^{\pm}$:
    - Step 1 (Fig. 3.64):
        - Analyse data with $0.2 < p_{\mathrm{T}} < 0.6$ GeV/c
        - Fit μ_{π^-/π^+} as a function of p_{T} with $-\exp(p_0 + p_1 p_{\mathrm{T}})$
        - Fit σ_{π^-/π^+}, C_{e^-/e^+}, σ_{e^-/e^+}, σ_{K^-/K^+} as a function of p_{T} with $\exp(p_0 + p_1 p_{\mathrm{T}})$
        - Fit r_{e^-/e^+} as a function of p_{T} with constant p_0
        - Fit μ_{e^-/e^+} as a function of p_{T} with a polynomial $p_0 p_{\mathrm{T}}^3 + p_1 p_{\mathrm{T}}^2 + p_2 p_{\mathrm{T}} + p_3$
        - Fit μ_{K^-/K^+} as a function of p_{T} with a polynomial $p_0 + p_1 p_{\mathrm{T}}^2$
    - Step 2:
        - All parameters from Step 1 except σ_{e^-/e^+} are fixed to the values calculated from functions obtained in Step 1
        - Fit σ_{e^-/e^+} as a function of p_{T}, for $0.45 < p_{\mathrm{T}} < 0.65$ GeV/c, with constant p_0
    - Step 3:
        - σ_{e^-/e^+} fixed to the values calculated from functions obtained in Steps 1 and 2 for $0.3 < p_{\mathrm{T}} < 0.45$ and $0.45 < p_{\mathrm{T}} < 0.65$, respectively.
        - The rest parameters from Step 1 are fixed to the values calculated from functions obtained in Step 1: μ_{π^-/π^+}, σ_{π^-/π^+}, , r_{e^-/e^+}, C_{e^-/e^+}, μ_{e^-/e^+} , μ_{K^-/K^+},σ_{K^-/K^+}

3. $\bar{p}, p$:
    - Step 1 (Fig. 3.65):
        - Analyse data with $0.4 < p_{\mathrm{T}} < 0.9$ GeV/c
        - Fit μ_{π^-/π^+}, μ_{K^-/K^+} as a function of p_{T} with a polynomial $p_0 p_{\mathrm{T}} + p_1$
        - Fit σ_{π^-/π^+} as a function of p_{T} with a polynomial $p_0 p_{\mathrm{T}}^2 + p_1 p_{\mathrm{T}} + p_2$
        - Fit σ_{K^-/K^+} as a function of p_{T} with $\exp(p_0 + p_1 p_{\mathrm{T}})$
    - Step 2:
        - μ_{K^-/K^+} fixed to the values calculated from a function obtained in Step 1
        - All the rest parameters from Step 1 are limited to the values calculated from functions obtained in Step 1
        - Fit μ_{π^-/π^+}, σ_{π^-/π^+}, σ_{K^-/K^+} as a function of p_{T} with a polynomial $p_0 p_{\mathrm{T}}^2 + p_1 p_{\mathrm{T}} + p_2$
        - Fit $\mu_{\bar{p}/p}$ as a function of p_{T}, for $0.7 < p_{\mathrm{T}} < 1.0$ GeV/c, with constant p_0
    - Step 3:
        - μ_{K^-/K^+} fixed to the values calculated from a function obtained in Step 1

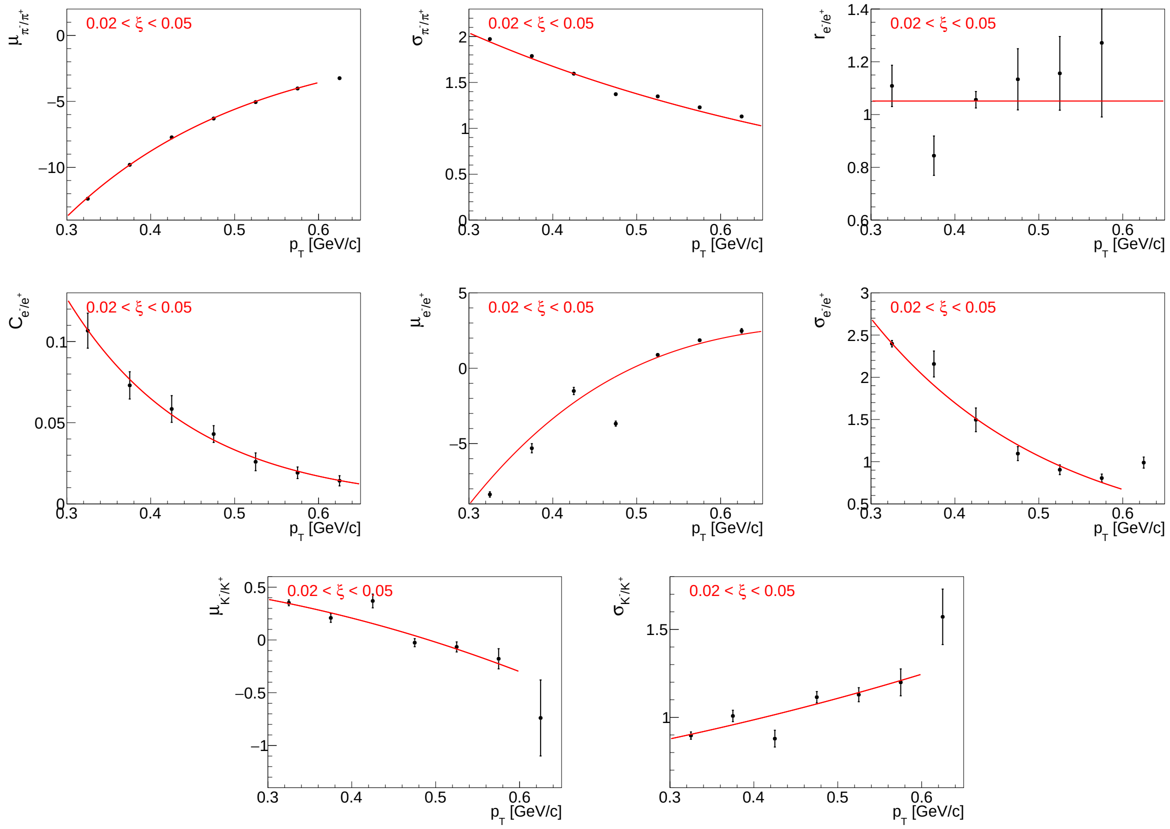

Figure 3.64: Means, widths and electron yields of each $n\sigma_{dE/dx}^{K^{\pm}}$ fit as a function of p_{T}. The red line on each plot is a fit function to stabilize and constrain the Gaussian fit parameters for the final fitting step.

  - $\mu_{\bar{p}/p}$ fixed to the values calculated from a function obtained in Step 2 for $0.7 < p_{\mathrm{T}} < 1.0$
  - The rest parameters from Step 2 are fixed to the values calculated from functions obtained in Step 2: μ_{π^-/π^+}, σ_{π^-/π^+}, σ_{K^-/K^+}

The particle yield is extracted from the fit to the corresponding $n\sigma_{dE/dx}^{i}$ distribution (corrected only for the energy loss and vertexing). As shown in Fig. 3.61, the dE/dx of each particle type merge at large p_{T}. Hence, the particle identification is limited. Pions can be identified in the momentum range of $0.2 - 0.7$ GeV/c, kaons in $0.3 - 0.65$ GeV/c and (anti)protons in $0.4 - 1.0$ GeV/c.

Antiparticle-to-Particle Ratios

The following steps were taken to correct the identified antiparticle to particle (pion, kaon, proton and their antiparticle) multiplicity ratios as a function of p_{T} in three ranges of ξ:

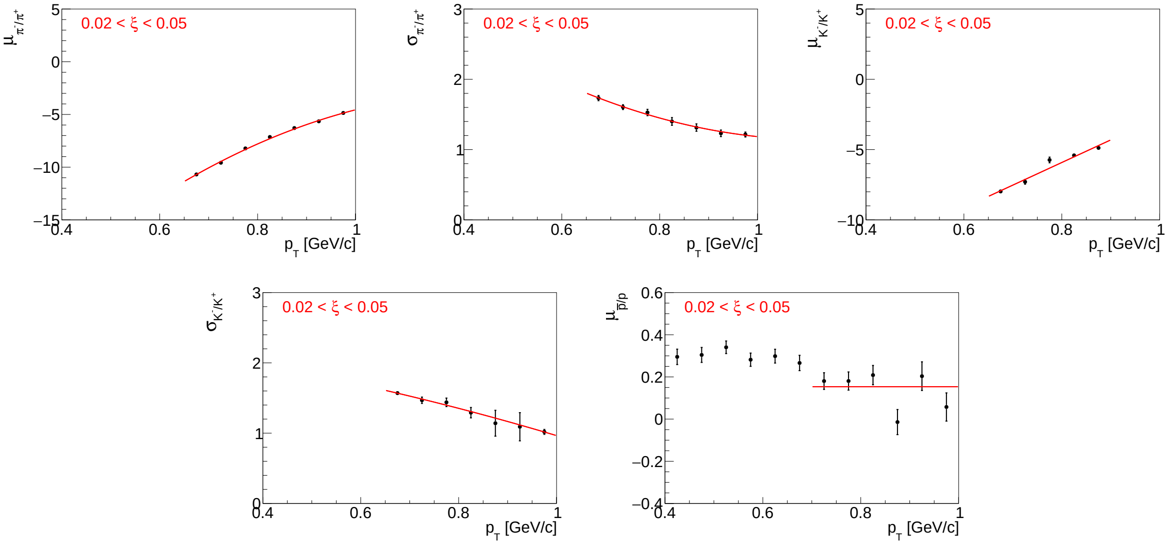

Figure 3.65: Means and widths of each $n\sigma^{\bar{p}/p}_{dE/dx}$ fit as a function of p_{T}. The red line on each plot is a fit function to stabilize and constrain the Gaussian fit parameters for the final fitting step.

- The raw identified particle yields were obtained through multi-Gaussian fits to the $n\sigma^{i}_{dE/dx}$ distributions (Sec. 3.9), where the vertex reconstruction and energy loss corrections were applied. The latter depends on the particle type.

- The non-SD background (Sec. 3.6) is the same for particles and antiparticles, thus, it was not subtracted. The accidental background contribution (Sec. 3.5) is very small, hence, any particle-antiparticle differences have a negligible effect on the result. Therefore, it was assumed that the accidental background does not depend on the particle type and for this reason it was not subtracted.

- The particle yields were corrected for track reconstruction efficiencies, which depend on the particle type and charge. These corrections are averaged over η and V_z. The ratio of particle to antiparticle TPC-TOF efficiencies is shown in Fig. 3.66. It weakly depends on ξ range, therefore, only sample results for single range of $0.02 < \xi < 0.05$ are presented.

- The background from non-primary tracks was subtracted (Sec. 3.5):
  - $\pi^{\pm}$: weak decays pions, muon contribution and background from detector dead-material interactions,
  - p: background from detector dead-material interactions,
  - $p, \bar{p}$: reconstructed tracks which have the appropriate number of common hit points with true-level particle, but the distance between them is too large (this background is negligibly small for other particle types),

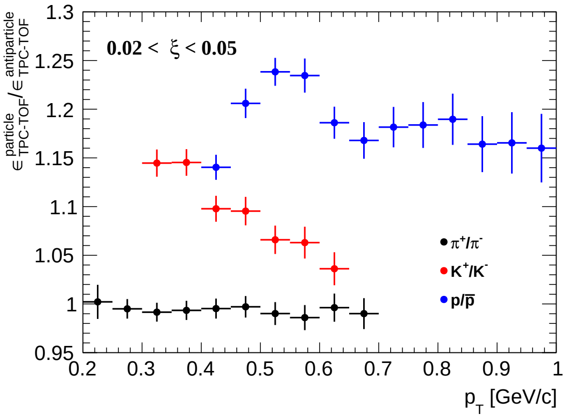

Figure 3.66: Ratio of particle to antiparticle TPC-TOF efficiencies for $0.02 < \xi < 0.05$.

  - fake track contribution was assumed to be the same for each particle type, hence, it was not subtracted.

- Since track and ξ migrations, and BBC-small efficiency, do not depend on the particle type and charge, these corrections are not applied.

- Finally, each antiparticle p_T distribution was divided by the corresponding particle p_T distribution to obtain fully corrected identified antiparticle to particle multiplicity ratios.

- Additionally, the average antiparticle to particle ratios over fiducial region of p_T in each ξ region were calculated.

3.10 Systematic Uncertainties

Apart from the statistical uncertainties there are also systematic uncertainties originating from inefficiencies and limitations of the measurement devices and techniques. The following sources of systematic uncertainties were considered:

- the effect of off-time pile-up on TPC track reconstruction efficiency (Sec. 3.7),

- the uncertainty of TPC track reconstruction efficiency related to the description of dead-material in simulation (Sec. 3.7),

- representation of data sample in embedding MC (Sec. 3.7),

- variation in the track quality cuts (Sec 3.7),

- non-primary track background contribution (Sec. 3.5),

- fake track background contribution (Sec. 3.5),

- TOF system simulation accuracy (Sec. 3.7),
- accidental background contribution (Sec. 3.5),
- the effect of alternative model of hadronization on BBC-small efficiency (Sec. 3.7),
- non-SD background contribution (Sec. 3.6),
- the effect of alternative model on ϵ_m correction (Sec. 3.9),
- non-closure (Sec 3.9),
- non-closure of N_{ev}, applied only to p_{T} and $\bar{\eta}$ distributions (Sec 3.9),
- difference in the distributions calculated separately for events in which forward-scattered proton is on one and the other side of the IP (east-west, Sec 3.9).

Some of the systematic uncertainties on $1/N\ dN/dn_{\mathrm{ch}}$ (related to TPC and TOF reconstruction efficiencies, fake track background contribution) are propagated by randomly removing and adding tracks in the n_{sel} distribution before unfolding procedure. For each track, a random number is generated. If this number is smaller than the absolute value of systematic uncertainty, then n_{sel} is increased or decreased, depending on the sign of systematic uncertainty.

Figures 3.67 to 3.69 show the components contributing to the total systematic uncertainty for charged particle distributions without the identification. The dominant systematic uncertainty for p_{T} and n_{ch} distributions is related to TOF system simulation accuracy. It affects mainly low-p_{T} particles, where it is about $6-8\%$, and large charged particle multiplicities, where it varies up to 50% for $n_{\mathrm{ch}} = 8$ and $0.02 < \xi < 0.05$. In case of $\bar{\eta}$ distribution, the systematic uncertainty on TOF mainly refers to charged particles produced at the edge of the fiducial region, for which it is about 4%. The largest (up to 30%) systematic uncertainty for $\langle\bar{\eta}\rangle$, is related to the observed difference in the distributions calculated separately with respect to the forward-scattered proton direction. The rest of the components have smaller contributions to the total systematic uncertainty. The systematic uncertainty on non-closure is on average at the level of 2% which proves the accuracy of the correction procedure.

Figures 3.70 to 3.73 show breakdown of all different systematics for the antiparticle-to-particle multiplicity ratio distributions. An additional systematic contribution for $\bar{p}/p$ multiplicity ratio due to proton background estimation was introduced. Since most of the corrections are the same for particle and its antiparticle, nearly all systematic uncertainties cancel out in the antiparticle-to-particle ratios. The largest sources of systematics, which do not, are related to proton background estimation and dead-material effect on TPC track reconstruction efficiency. The former was found to be up to 6%, whereas the latter varies up to 2% for low-p_{T} $\bar{p}/p$ multiplicity ratio.

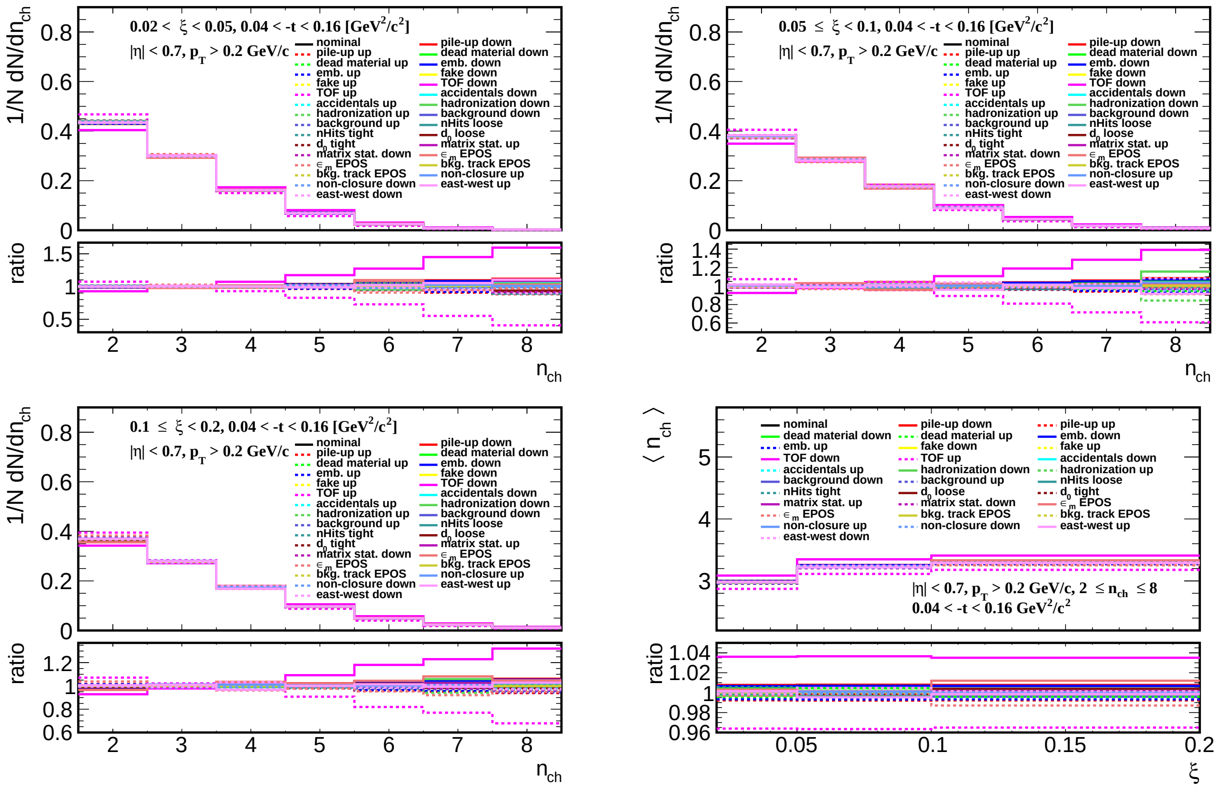

Figure 3.67: Components of the systematic uncertainties for the charged particle multiplicity in three ξ regions and for the mean charged particle multiplicity. The ratios to nominal distributions are shown in the bottom panels.

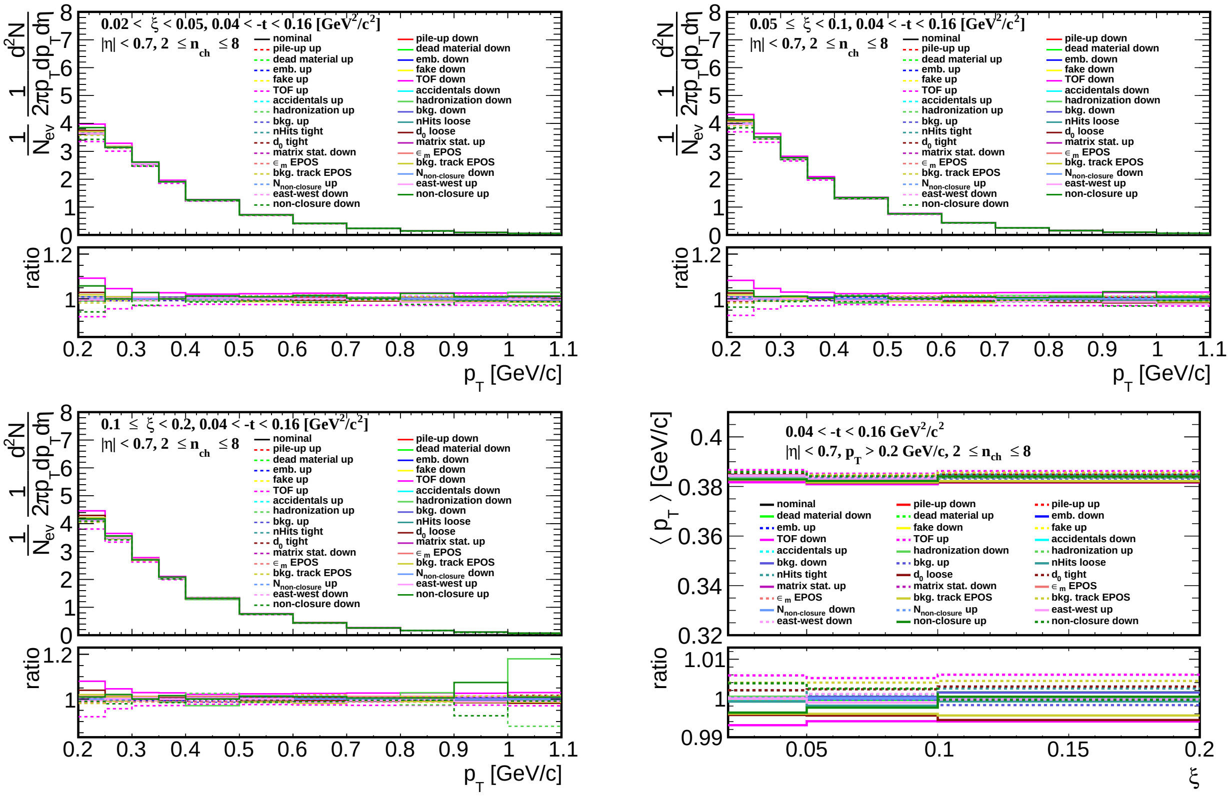

Figure 3.68: Components of the systematic uncertainties for p_{T} distributions in three ξ regions and for a mean p_{T} distribution. The ratios to nominal distributions are shown in the bottom panels.

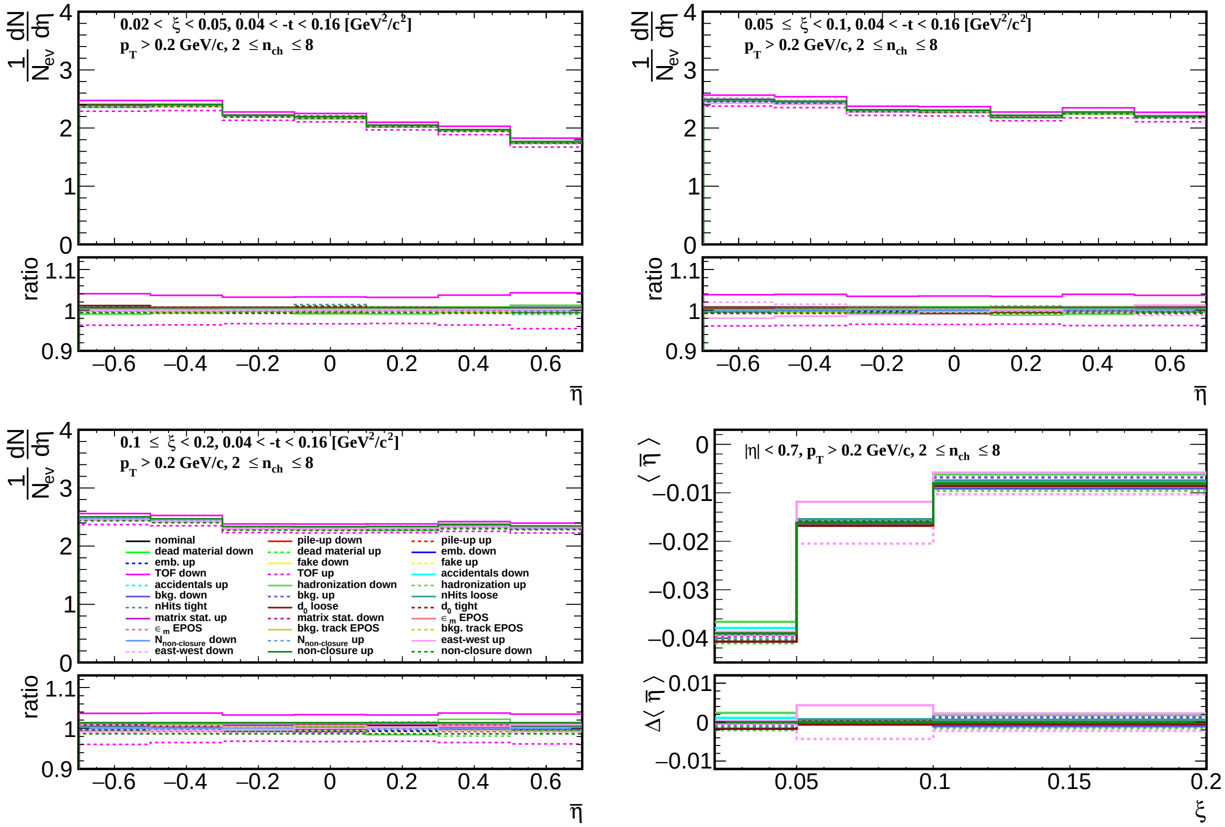

Figure 3.69: Components of the systematic uncertainties for $\bar{\eta}$ distributions in three ξ regions and for a mean $\bar{\eta}$ distribution. In case of $1/N_{\text{ev}}\ dN/d\bar{\eta}$, the ratios to nominal distributions are shown in the bottom panels. For $\langle\bar{\eta}\rangle$ distribution, a difference between modified and nominal distribution is shown.

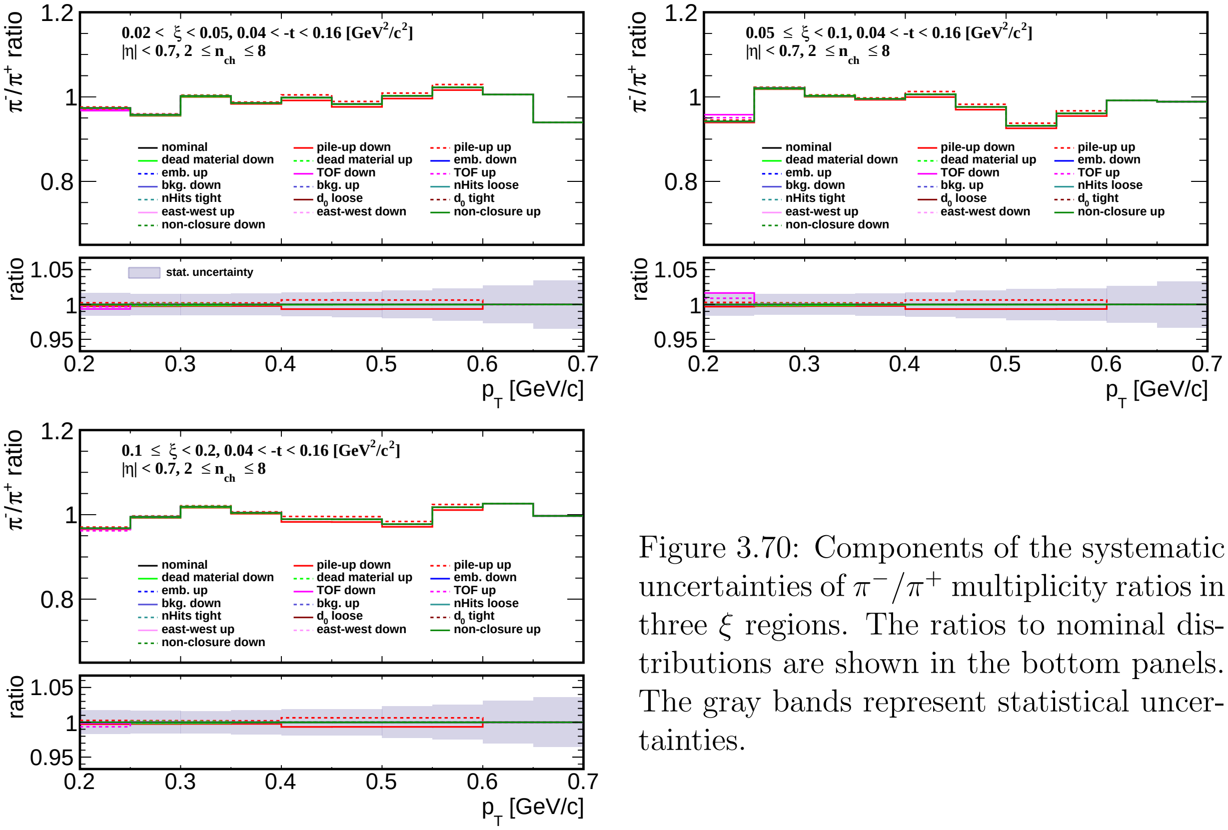

Figure 3.70: Components of the systematic uncertainties of π^-/π^+ multiplicity ratios in three ξ regions. The ratios to nominal distributions are shown in the bottom panels. The gray bands represent statistical uncertainties.

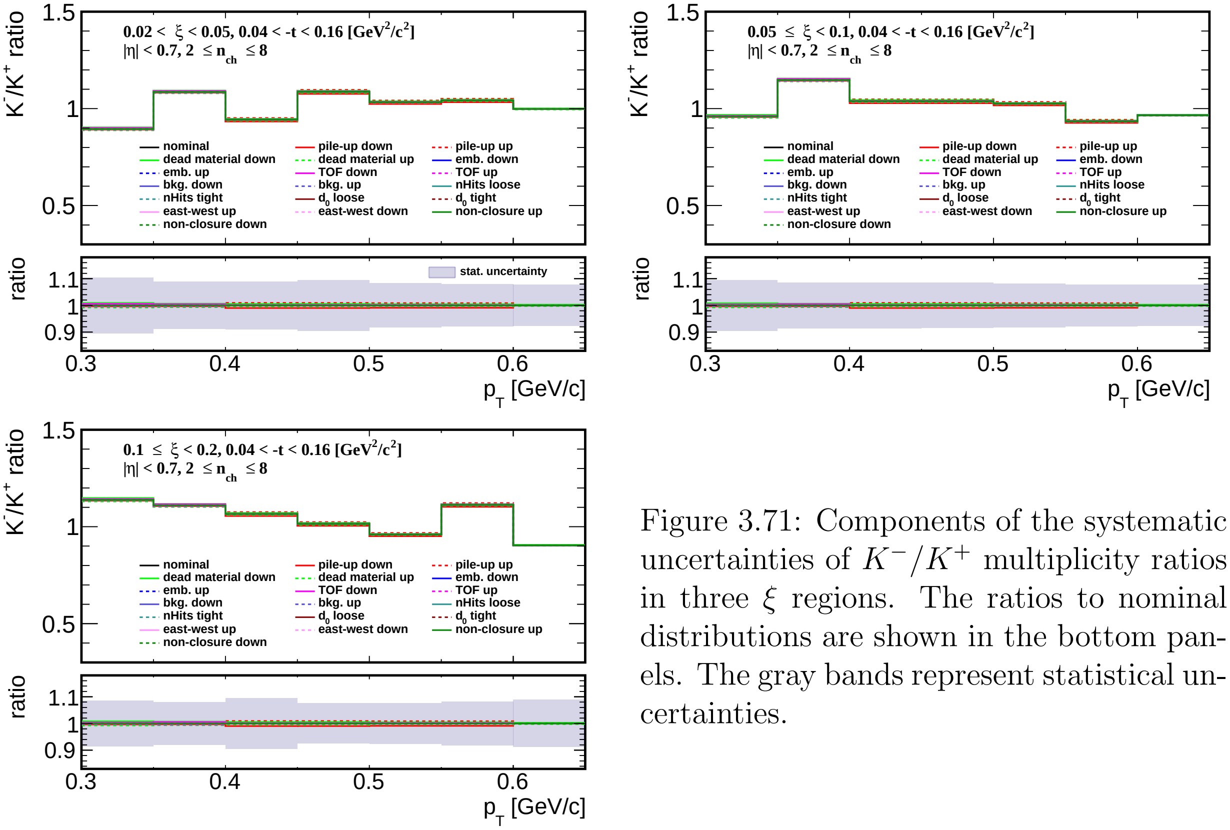

Figure 3.71: Components of the systematic uncertainties of K^-/K^+ multiplicity ratios in three ξ regions. The ratios to nominal distributions are shown in the bottom panels. The gray bands represent statistical uncertainties.

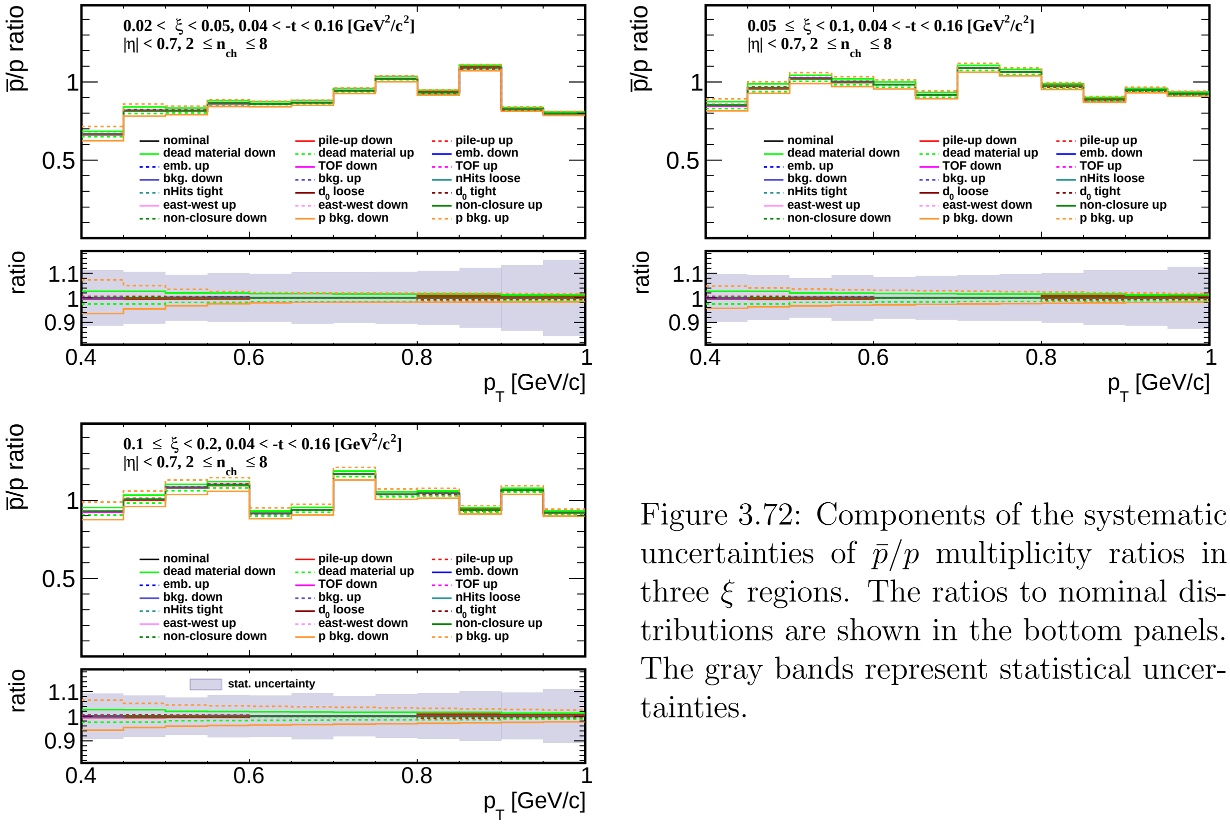

Figure 3.72: Components of the systematic uncertainties of $\bar{p}/p$ multiplicity ratios in three ξ regions. The ratios to nominal distributions are shown in the bottom panels. The gray bands represent statistical uncertainties.

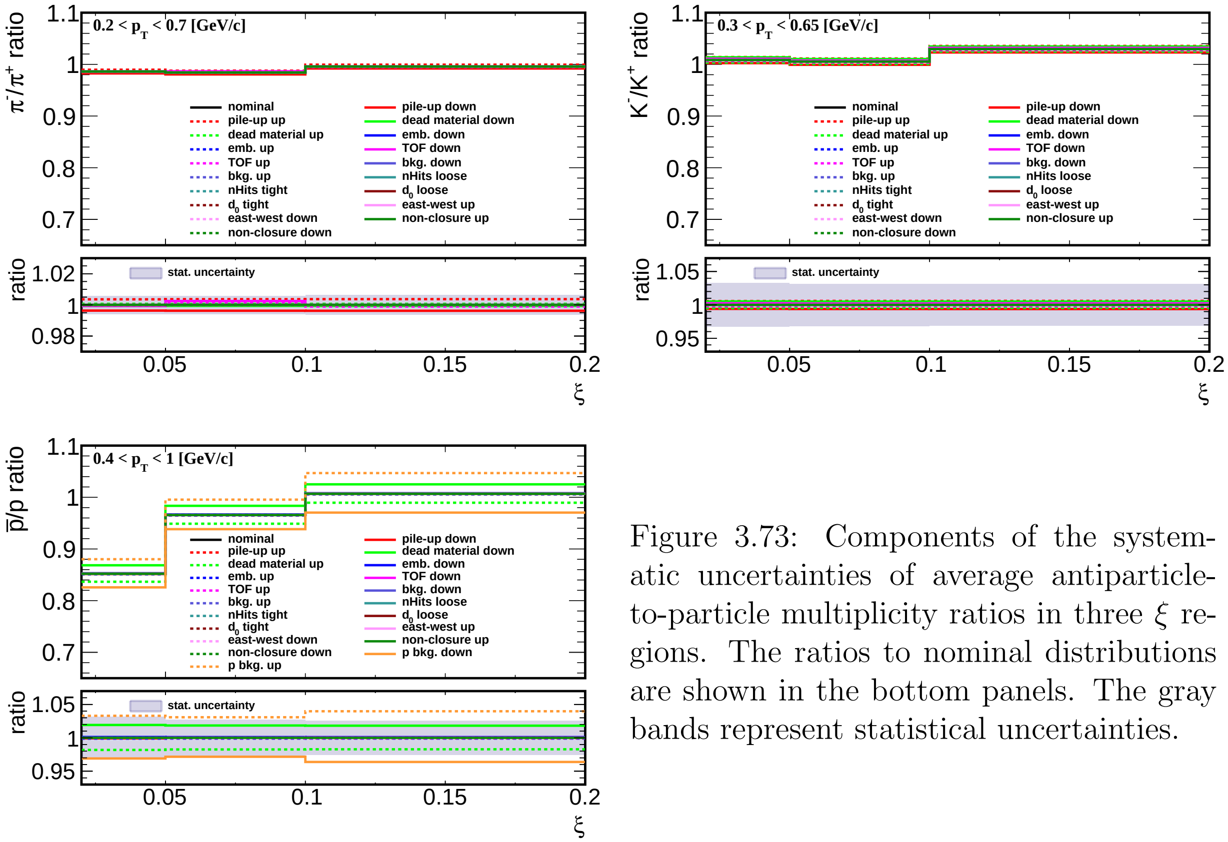

Figure 3.73: Components of the systematic uncertainties of average antiparticle-to-particle multiplicity ratios in three ξ regions. The ratios to nominal distributions are shown in the bottom panels. The gray bands represent statistical uncertainties.

3.11 Results

In the following section, the final-state charged particle distributions are compared with various SD MC predictions, i.e.

- PYTHIA 8 4C (SaS),
- PYTHIA 8 A2 (MBR),
- PYTHIA 8 A2 (MBR-tuned),
- HERWIG 7,
- EPOS LHC with combined two classes of processes: diffractive (EPOS SD) and non-diffractive (EPOS SD′),
- EPOS LHC SD′.

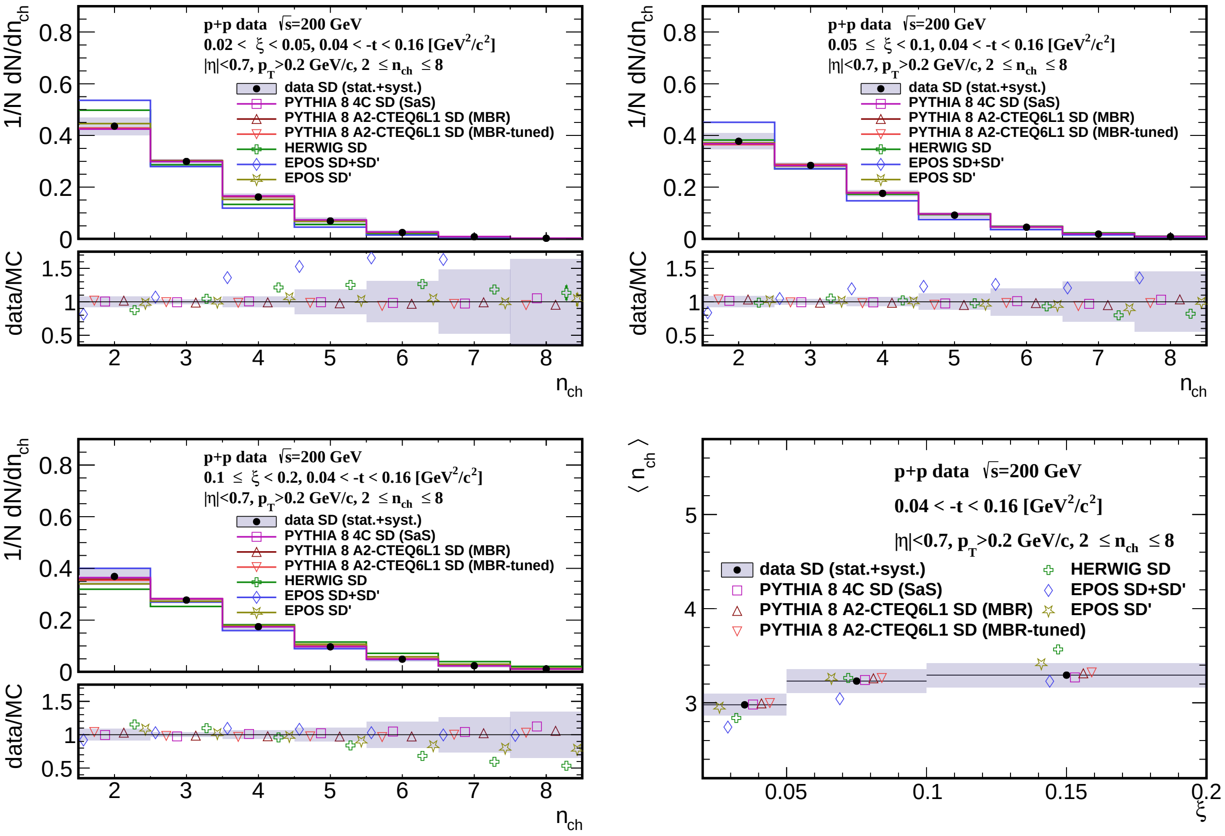

Figure 3.74: Primary charged-particle multiplicity shown separately for the three ranges of ξ: (top left) $0.02 < \xi < 0.05$, (top right) $0.05 < \xi < 0.1$, (bottom left) $0.1 < \xi < 0.2$ and (bottom right) the mean multiplicity $\langle n_{\mathrm{ch}} \rangle$ as a function of ξ. The ratio of data to the models' prediction is shown in the bottom panels.

In all figures, data are shown as solid points with error bars representing the statistical uncertainties. Gray boxes represent statistical and systematic uncertainties added in quadrature. Predictions from MC models are shown as colour histograms and markers. The lower panel in each figure shows the ratio of data to the models' predictions. All results are presented separately for three ranges of ξ: $0.02 < \xi < 0.05$, $0.05 < \xi < 0.1$, $0.1 < \xi < 0.2$.

Figure 3.74 shows primary charged-particle multiplicity separately for the three ranges of ξ and the mean multiplicity $\langle n_{\mathrm{ch}} \rangle$ as a function of ξ. Data follow the expected increase of $\langle n_{\mathrm{ch}} \rangle$ with ξ due to the larger diffractive masses probed by increasing ξ in SD process. The shapes of the measured distributions are reproduced reasonably well by all models except EPOS SD+SD′ and HERWIG SD which predicts smaller $\langle n_{\mathrm{ch}} \rangle$ for $0.02 < \xi < 0.1$ and $0.02 < \xi < 0.05$, respectively. HERWIG SD predicts too large $\langle n_{\mathrm{ch}} \rangle$ for $0.1 < \xi < 0.2$. Figure 3.75 shows primary charged-particle multiplicities as a function of p_{T} separately for the three ranges of ξ and the mean transverse momentum $\langle p_{\mathrm{T}} \rangle$ as a function of ξ.

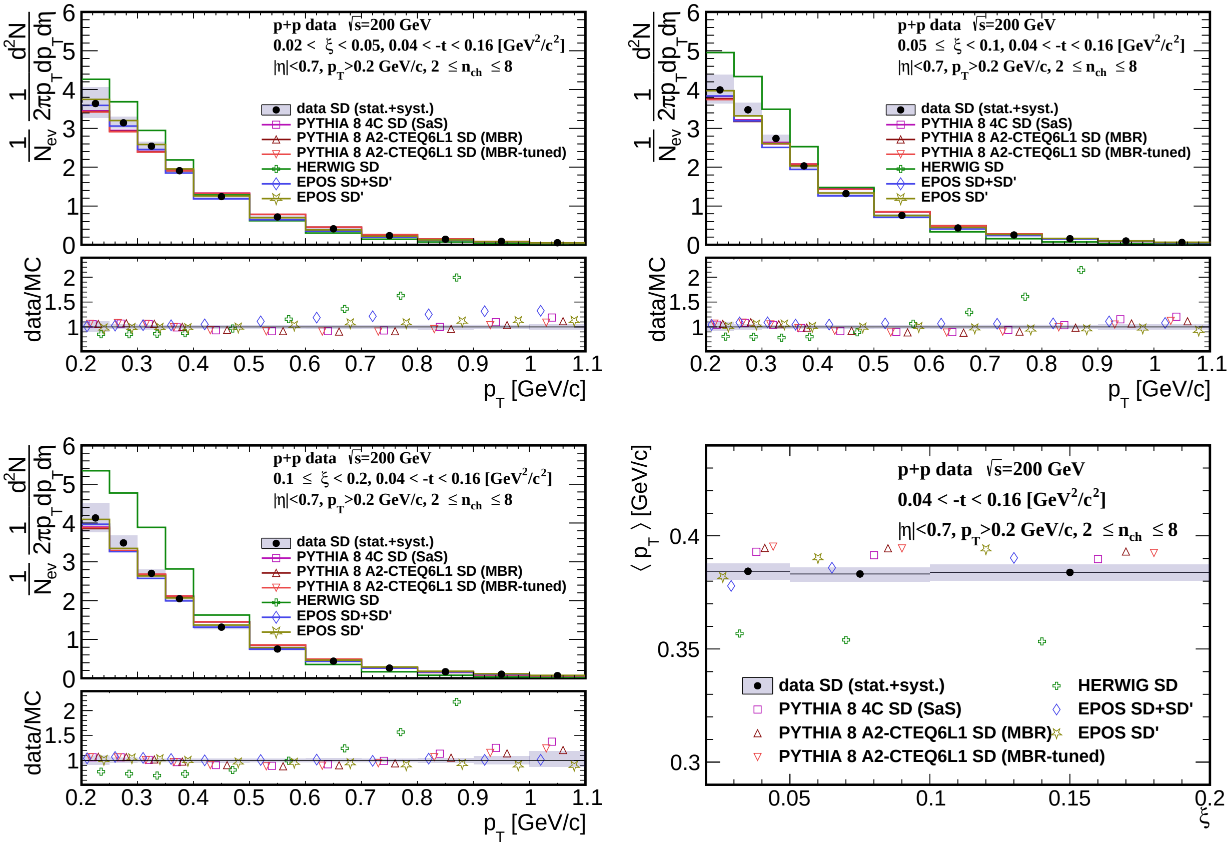

Figure 3.75: Primary charged-particle multiplicities as a function of p_{T} shown separately for the three ranges of ξ: (top left) $0.02 < \xi < 0.05$, (top right) $0.05 < \xi < 0.1$, (bottom left) $0.1 < \xi < 0.2$ and (bottom right) the mean transverse momentum $\langle p_{\mathrm{T}} \rangle$ as a function of ξ. The ratio of data to the models' prediction is shown in the bottom panels.

Data show that $\langle p_{\mathrm{T}} \rangle$ depends very weakly on ξ. Models describe data fairly well except HERWIG SD which predicts much steeper dependence of particle density with p_{T} in all three ξ ranges.

Figure 3.76 shows primary charged-particle multiplicity as a function of $\bar{\eta}$ (defined in Sec. 1.1.2) separately for the three ranges of ξ and the mean pseudorapidity $\langle \bar{\eta} \rangle$ as a function of ξ. Data show expected flattening of the $\bar{\eta}$ distribution with increasing ξ which reflects SD event-asymmetry and fact that the gap-edge at large ξ is outside $|\bar{\eta}| < 0.7$ region leading to more flat distribution of particle density as a function of $\bar{\eta}$. Models describe data fairly well except EPOS SD+SD′, which predicts less steep dependence of particle density with $\bar{\eta}$ for $0.02 < \xi < 0.1$, and HERWIG SD, which predicts steeper distribution for all three ξ ranges.

Figure 3.77 shows the ratio of production yields of π^-/π^+ as a function of p_{T} separately for the three ranges of ξ. Data in all three ξ ranges are consistent with equal amounts of π^+ and π^- with no significant p_{T} dependence. Models agree with data (except HERWIG)

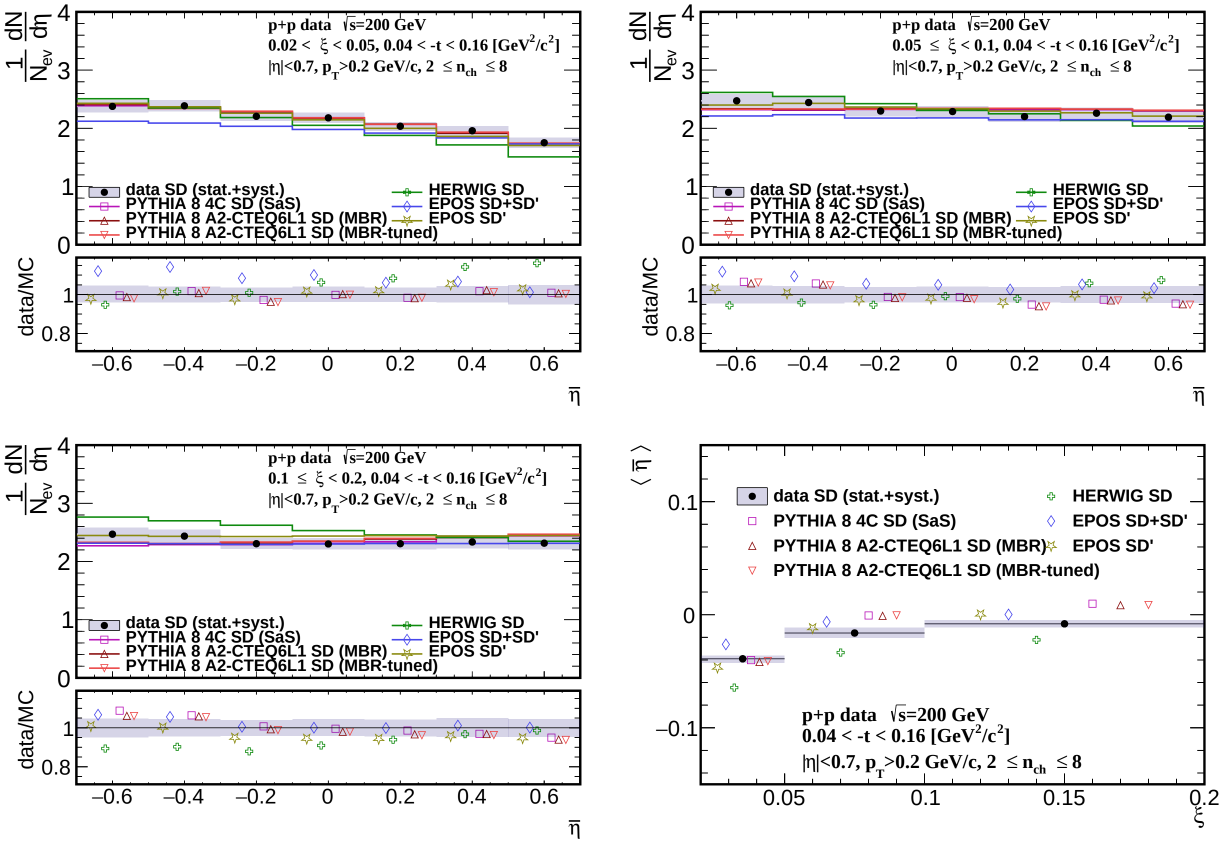

Figure 3.76: Primary charged-particle multiplicity as a function of $\bar{\eta}$ shown separately for the three ranges of ξ: (top left) $0.02 < \xi < 0.05$, (top right) $0.05 < \xi < 0.1$, (bottom left) $0.1 < \xi < 0.2$ and (bottom right) the mean pseudorapidity $\langle \bar{\eta} \rangle$ as a function of ξ. The ratio of data to the models' prediction is shown in the bottom panels.

predicting on average small deviation from unity by $\sim 2\%$ what is smaller than data uncertainties. HERWIG in first two ξ ranges predicts too large asymmetry between π^+ and π^-.

Figure 3.78 shows the ratio of production yields of K^-/K^+ as a function of p_{T} separately for the three ranges of ξ. Data in all three ξ ranges are consistent with equal amounts of K^+ and K^- with no p_{T} dependence. Models agree with data except HERWIG in the first ξ range predicting too large ratio of K^- to K^+.

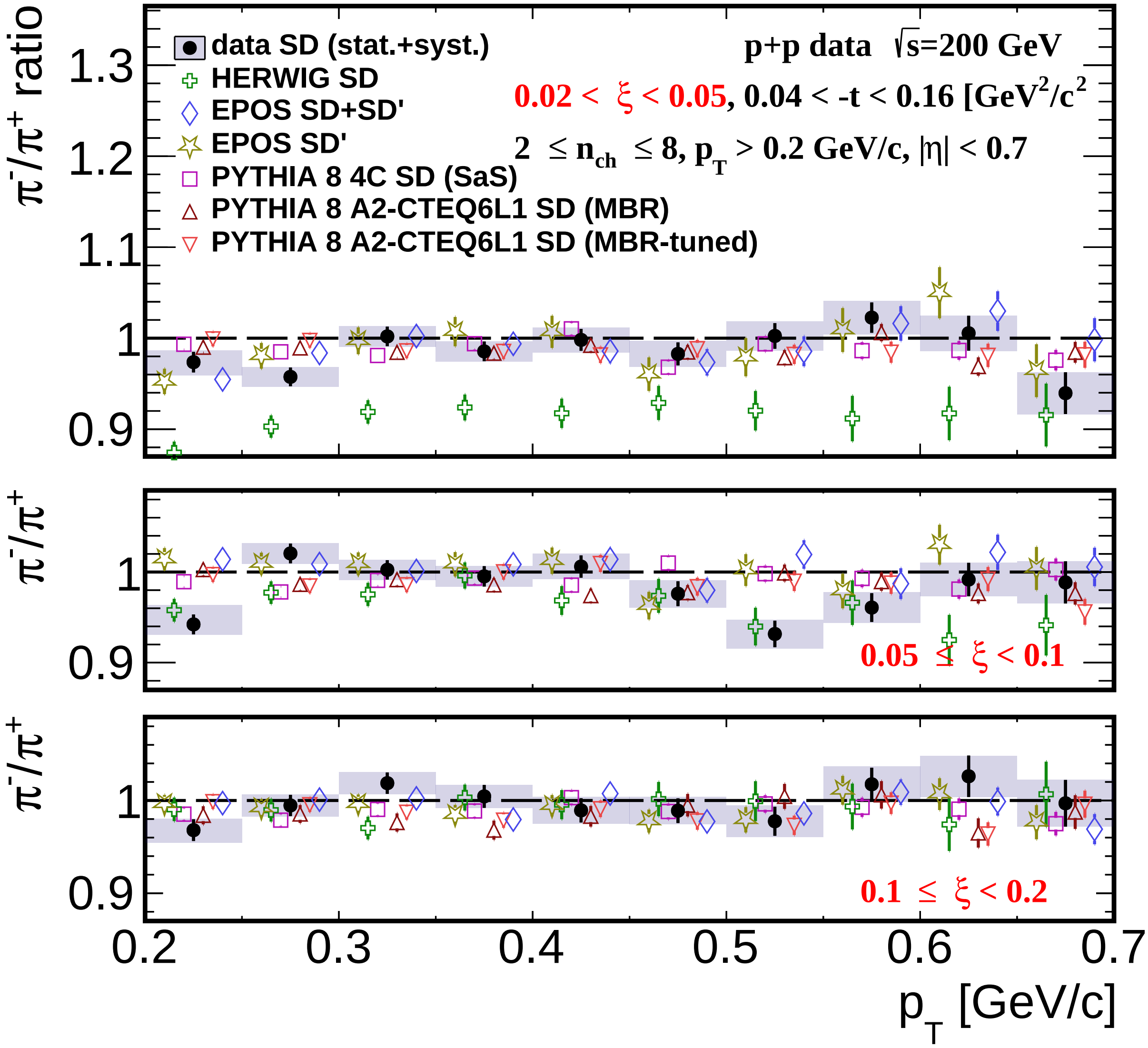

Figure 3.77: Ratio of production yields of π^-/π^+ as a function of p_{T} shown separately for the three ranges of ξ: (top) $0.02 < \xi < 0.05$, (middle) $0.05 < \xi < 0.1$, (bottom) $0.1 < \xi < 0.2$.

Figure 3.79 shows the ratio of production yields of $\bar{p}/p$ as a function of p_T separately for the three ranges of ξ. Data in the last two ξ ranges are consistent with equal amounts of p and $\bar{p}$ with no p_T dependence. However, in the first ξ range at $p_T < 0.7$ GeV/c data shows significant deviation from unity indicating a significant transfer of the baryon number from the forward to the central region. PYTHIA8, EPOS SD′ and EPOS SD+SD′ agree with data in the last two ξ ranges. In first ξ range PYTHIA8 and EPOS SD′ predict small

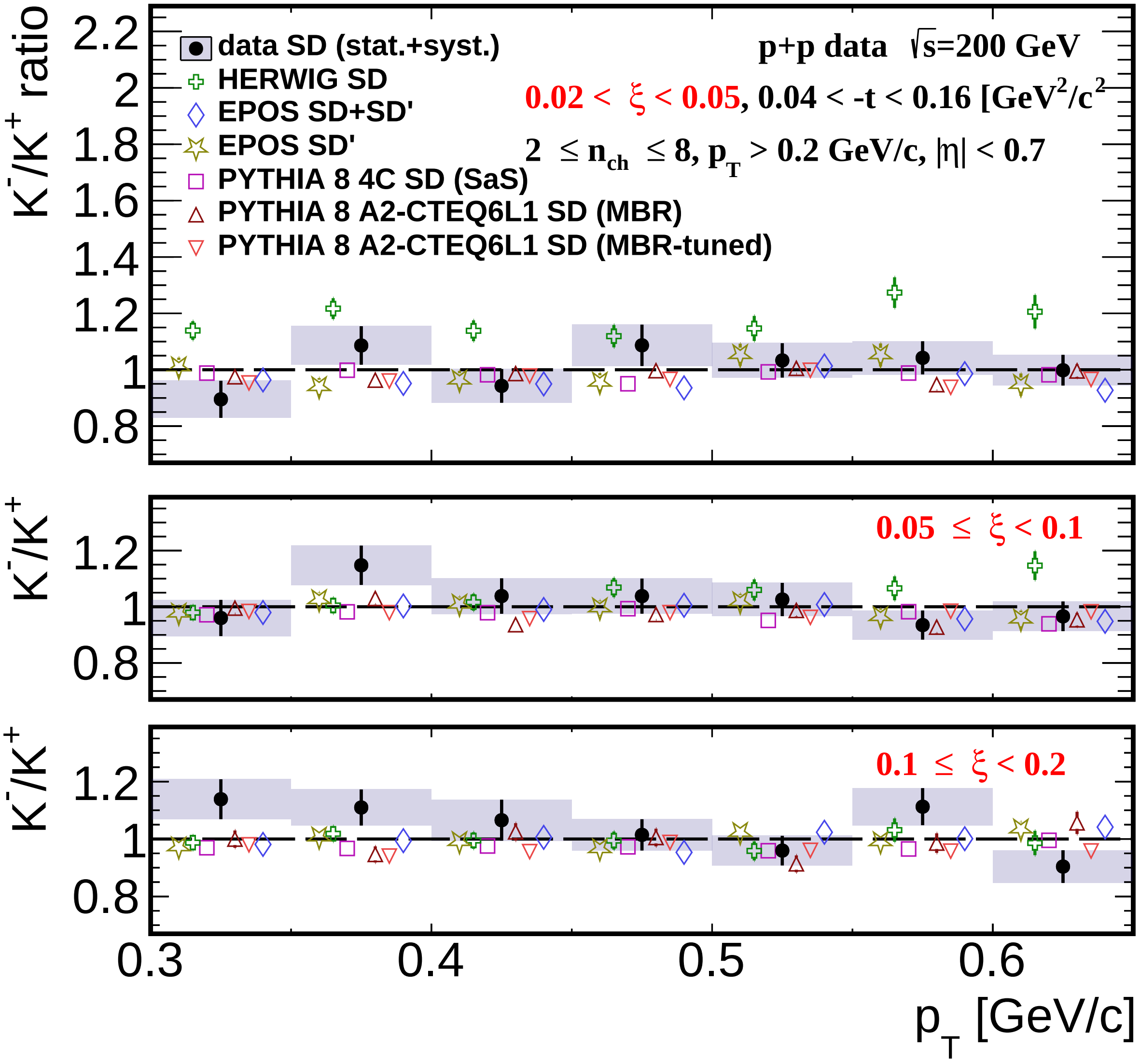

Figure 3.78: Ratio of production yields of K^-/K^+ as a function of p_T shown separately for the three ranges of ξ: (top) $0.02 < \xi < 0.05$, (middle) $0.05 < \xi < 0.1$, (bottom) $0.1 < \xi < 0.2$.

deviation from unity by ≈ 7% which is smaller than observed in data ($\bar{p}/p = 0.85 \pm 0.04$), whereas EPOS SD+SD′ predicts an asymmetry between $\bar{p}$ and p of ∼ 30% which is larger than observed in data except $p_{\mathrm{T}} < 0.5$ GeV/c. HERWIG predicts much larger baryon number transfer compared to data in first two ξ ranges and shows consistency with data in last ξ range.

Figure 3.80 shows mean ratio of production yields of π^-/π^+, K^-/K^+ and $\bar{p}/p$ as a function of ξ.

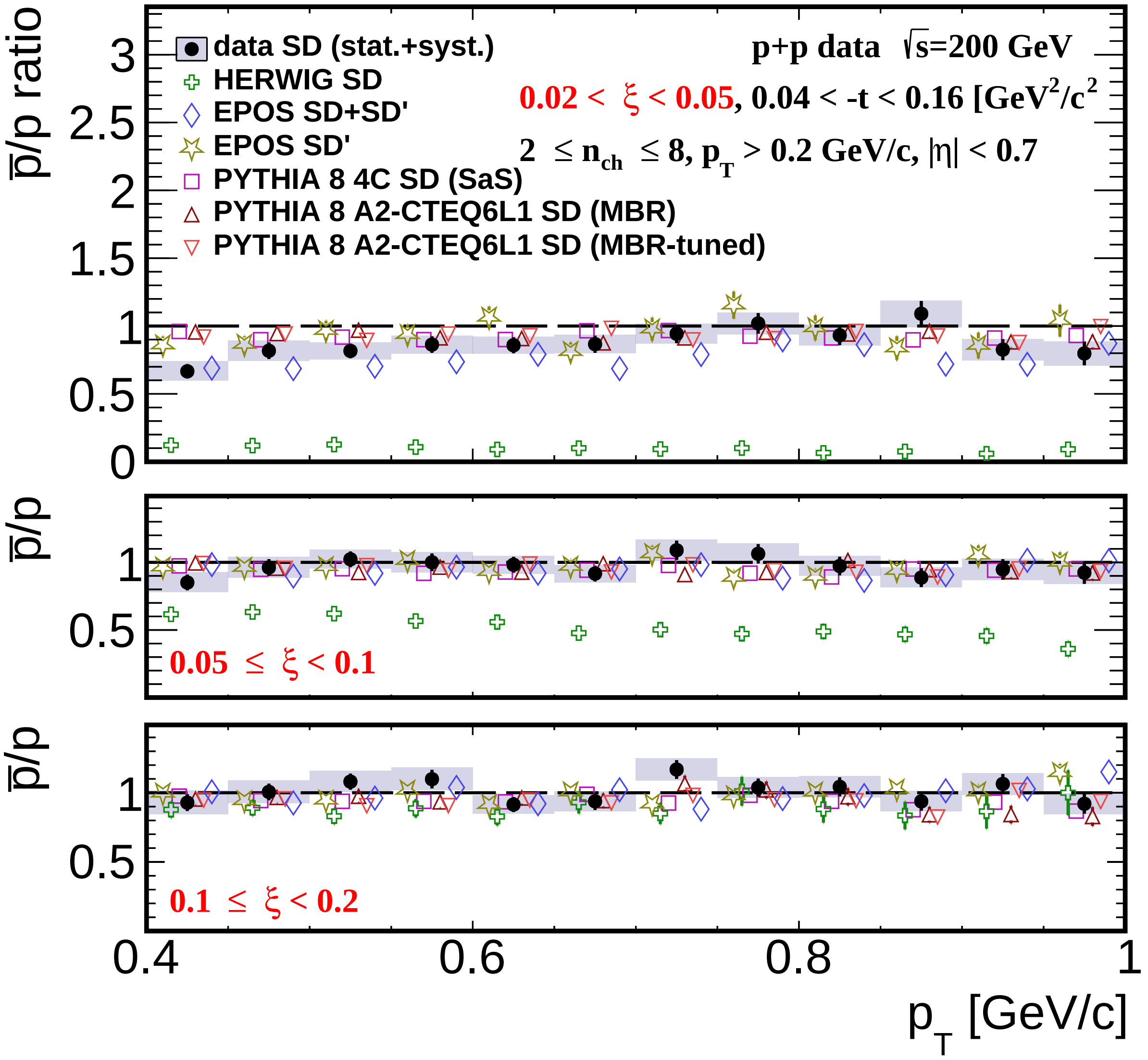

Figure 3.79: Ratio of production yields of $\bar{p}/p$ as a function of p_{T} shown separately for the three ranges of ξ: (top) $0.02 < \xi < 0.05$, (middle) $0.05 < \xi < 0.1$, (bottom) $0.1 < \xi < 0.2$.

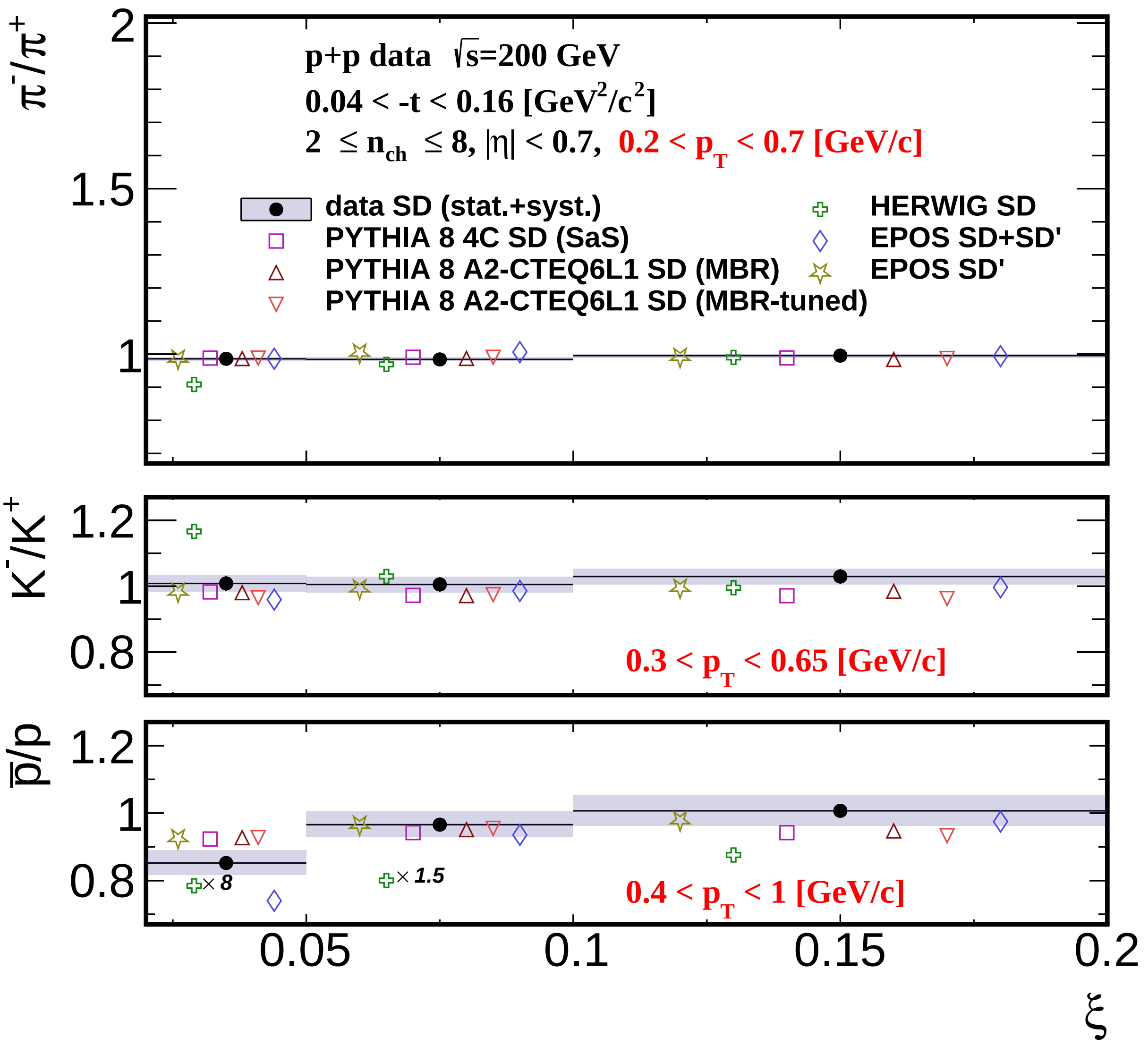

Figure 3.80: Ratio of production yields of π^-/π^+, K^-/K^+ and $\bar{p}/p$ as a function of ξ.

Summary

Above results are expected to provide an opportunity to perform further tunning of free parameters of the MC models. The measured distributions of charged-particle multiplicity and its dependence on p_T and $\bar{\eta}$, are well described by PYTHIA 8 models (MBR and MBR-tuned), except $\bar{\eta}$ at $\xi > 0.05$ for which PYTHIA 8 predicts flatter distribution than observed in the data. PYTHIA 8 shows asymmetry between $\bar{p}$ and p, which may indicate there is a baryon number transfer from the forward to the central region. However, it is smaller than measured in the data. The uncorrected ξ distributions are better described by PYTHIA 8 predictions without artificial suppression of diffractive cross sections at large ξ. This result may suggest that the default suppression of diffractive cross sections, implemented in MBR model, is too large in PYTHIA 8 and should be further tuned. The description of the ξ distribution can be also improved by changing the Pomeron intercept from $\epsilon = 0.104$ (MBR) to $\epsilon = 0$ (SaS).

Results indicate that the relative contribution of EPOS SD and SD′ may be further tuned. The measured distributions of charged-particle multiplicity and its densities as a function of $\bar{\eta}$ are well described by EPOS SD′, while EPOS SD+SD′ does not describe the data. The results suggests that the contribution of SD events is overestimated in EPOS. It is in agreement with the production ratios of $\bar{p}$ and p at $0.02 < \xi < 0.05$, for which EPOS SD′ predictions are approximately 2σ above the data (as PYTHIA 8), while EPOS SD+SD′ predictions are approximately 3σ below the data.

Significant differences are observed between the measured distributions and HERWIG model. HERWIG predicts smaller mean charged-particle multiplicity than observed in the data for $0.02 < \xi < 0.05$ and too large for $0.1 < \xi < 0.2$. The dependence of particle densities with p_{T} and $\bar{\eta}$ is too steep in this model. The production ratios of π^-/π^+ and K^-/K^+ for $0.02 < \xi < 0.05$ are underestimated and overestimated, respectively. HERWIG predicts much larger baryon number transfers compared to data for $\xi < 0.1$.

Chapter 4

ATLAS Data Analysis

4.1 Monte Carlo Samples

Several MC samples were used to correct the data for acceptance and detector effects. There are few steps in the simulation chain for the ATLAS experiment: event generation, detector simulation, digitalization, and reconstruction. All simulation steps are done under the ATLAS simulation infrastructure [226], which is integrated into the ATLAS simulation framework, ATHENA [227].

First, the MC event generation is done using multi-purpose generators. After that, the detector simulation is performed using GEANT4 package for all the particles generated in the central detectors acceptance. Finally, the central detector activity is processed through the reconstruction chain, which is the same for data and MC events.

Almost all of the MC samples, used in this thesis, were produced for analysis of charged particle distributions at $\sqrt{s} = 13$ TeV in MB events [21, 22]. Instead of the ALFA simulation, which was not included in the MC production, the ForwardTransportFast [199] tool was used to simulate the propagation of particles from the IP to the forward detectors. The x and y coordinates of the proton are smeared and used as the coordinates for tracks if the proton reaches the z-position of ALFA. This package uses the output of the MAD-X [221], called *twiss file*, which contains information about the propagation of protons through the LHC beam-line. Although, the MAD-X twiss files contain information on each element of the magnetic lattice (dipoles, quadrupoles, drift spaces, solenoids, kickers, etc.), the simulation of secondary interactions with beam-pipe is not included and full GEANT4 simulation of forward region is necessary for that purpose. The tool also contains

The DL model implemented in PYTHIA 8 and EPOS LHC were used as the nominal MC samples. The A3 tune of PYTHIA 8 was used, which is based on the NNPDF23LO PDFs [228]. In addition to these two models, the data were compared to:

- QGSJET-II,
- PYTHIA 8 with SaS parametrization of Pomeron flux and A2 tune (MSTW2008LO PDFs),

- PYTHIA 8 with Monash tune (NNPDF23LO PDFs) generated separately for three Pomeron flux models: SaS, DL and MBR.

In order to study the systematic uncertainty related to dead-material effect on track reconstruction efficiency, three additional PYTHIA 8 samples with SaS Pomeron flux model, A2 tune and modified geometry were generated:

- nominal geometry with 5% additional dead-material,
- nominal geometry with 10% additional IBL material,
- nominal geometry with 50% additional material in the Patch Panel 0 (PP0) region.

The summary of all MC samples, used in this analysis, is presented in Table 4.1.

Generator	Setting	PDFs	Model	#events	Geometry
PYTHIA 8	A3, DL	NNPDF23LO	SD	8M	nominal
PYTHIA 8	A3, DL	NNPDF23LO	CD	0.5M	nominal
PYTHIA 8	A3, DL	NNPDF23LO	DD	0.5M	nominal
PYTHIA 8	A3, DL	NNPDF23LO	ND	0.5M	nominal
PYTHIA 8	A2, SaS	MSTW2008LO	SD	5M	nominal
PYTHIA 8	A2, SaS	MSTW2008LO	DD	5M	nominal
PYTHIA 8	A2, SaS	MSTW2008LO	ND	20M	nominal
EPOS	LHC	n/a	inclusive	10M	nominal
EPOS	LHC	n/a	inclusive	2.4M	only true-level
PYTHIA 8	Monash, SaS	NNPDF23LO	SD	5M	only true-level
PYTHIA 8	Monash, DL	NNPDF23LO	SD	1M	only true-level
PYTHIA 8	Monash, MBR	NNPDF23LO	SD	1M	only true-level
PYTHIA 8	A3, DL	NNPDF23LO	SD	1M	only true-level
QGSJET-II	LHC	n/a	inclusive	72M	only true-level
PYTHIA 8	A2, SaS	MSTW2008LO	ND	5M	+5% dead-material
PYTHIA 8	A2, SaS	MSTW2008LO	ND	5M	+10% IBL material
PYTHIA 8	A2, SaS	MSTW2008LO	ND	5M	+50% PP0 material

Table 4.1: Details of the MC samples used in the analysis.

Figure 4.1 shows the distribution of $\log_{10}\xi$ generated with EPOS (SD and SD+SD$'$) and PYTHIA 8 A3 SD. EPOS predicts that the region of $\log_{10}\xi \gtrsim -3$ is dominated by SD$'$ events, while SD is only relevant for very small ξ ($\log_{10}\xi \lesssim -3$). The dependence of the cross section on ξ is much stronger in EPOS SD compared to PYTHIA 8 SD. EPOS SD+SD$'$ predicts an increase in the number of events in the region of $\log_{10}\xi \gtrsim -3$. Figure 4.2 shows the distribution of $|t - t_0|$ in three ranges of ξ: $10^{-5} < \xi < 0.035$, $0.035 < \xi < 0.08$ and $0.08 < \xi < 0.16$, where t_0 is the maximum kinematically allowed value of t. The t-slope changes with ξ in PYTHIA 8 and is ξ-independent, but different for SD and SD$'$ in EPOS. For $\xi > 0.035$, the distribution of $|t - t_0|$ is very similar for EPOS SD$'$ and PYTHIA 8, while much steeper for EPOS SD.

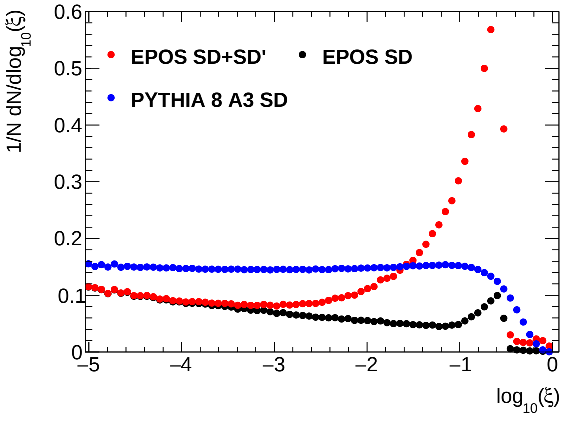

Figure 4.1: $\log_{10}\xi$ distribution for various MC generators.

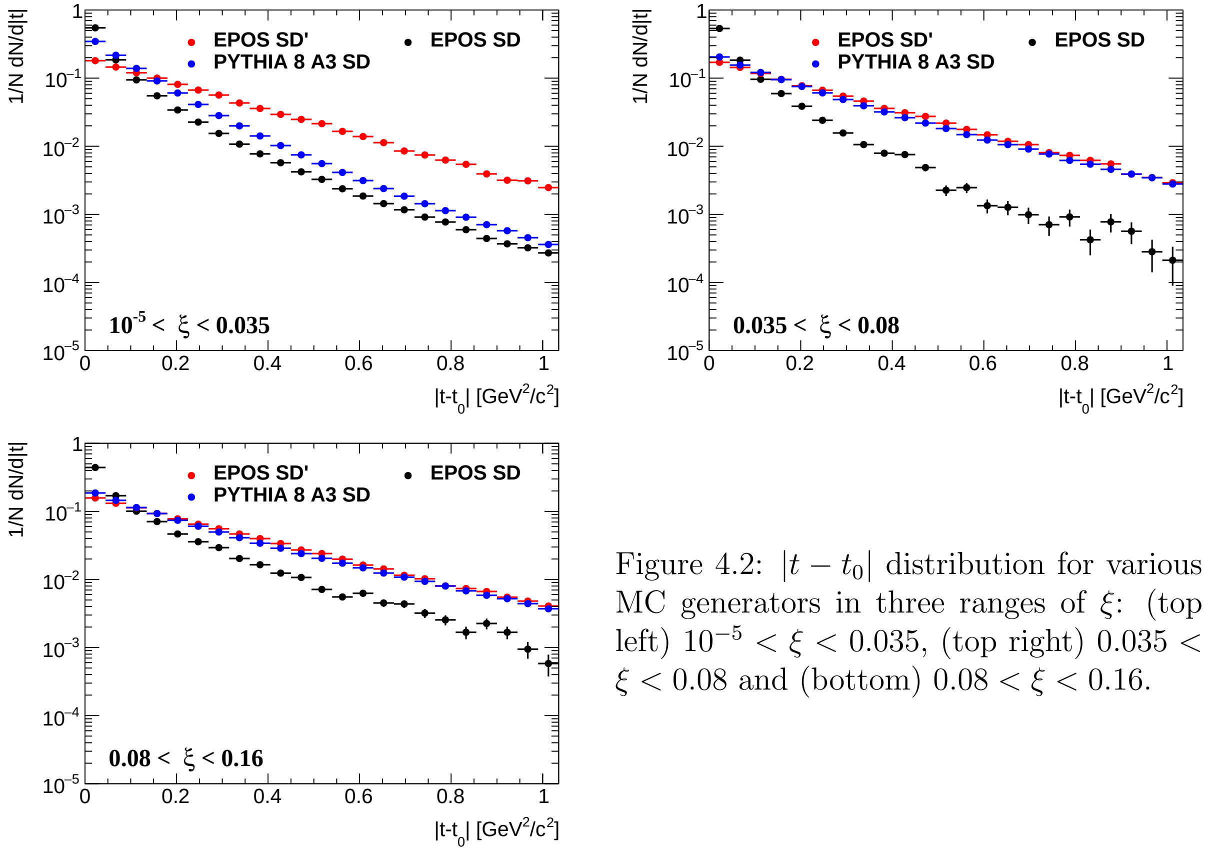

Figure 4.2: $|t - t_0|$ distribution for various MC generators in three ranges of ξ: (top left) $10^{-5} < \xi < 0.035$, (top right) $0.035 < \xi < 0.08$ and (bottom) $0.08 < \xi < 0.16$.

4.2 Data Sample and Signal Selection

Data analysed in this thesis were collected during special pp collisions at the LHC in October 2015. This special runs were characterized by $\beta^* = 90$ m and the centre-of-mass energy of $\sqrt{s} = 13$ TeV. There were 671 colliding bunches and a pile-up of about $\mu = 0.1$. The crossing angle was $\theta_c = 2 \times 50$ µrad. The 20M SD triggers were selected from a 729.96 nb^{-1} sample collected by the ATLAS experiment during nine special runs (LHC stores).

Online Selection

SD events were selected online using the HLT_noalg_L1ALFA_Diff_Phys trigger, where "noalg" implies that events seeded from L1ALFA diffractive streams passed through HLT without any additional selection except prescale, the "L1ALFA_Diff_Phys" suffix signifies that events were accepted by the L1 trigger, which required a hit in one of the ALFA trigger tiles, and for some streams also signals in other detectors. In this analysis, events triggered by L1_MBTS_1_A_ALFA_C or L1_MBTS_1_C_ALFA_A streams are used, which required at least one MBTS counter to have a signal above threshold on side A (C) in coincidence with a hit in the ALFA trigger tiles on side C (A). For convenience, this trigger conditions will be referred to as "SD trigger".

The accidental background was studied from events passing the following triggers:

- HLT_noalg_mb_L1MBTS_1 required at least one MBTS counter with a signal above threshold on L1 (referred to as "MBTS trigger" in the following). This trigger is not biased by ALFA and ID,
- HLT_mb_sptrk was a random trigger on L1, while it required space points in Pixel and SCT detectors at the HLT (referred to as "ID trigger" in the following). This trigger is not biased by ALFA and MBTS,
- HLT_noalg_L1ALFA_PhysAny required a hit in one of the ALFA trigger tiles (referred to as "ALFA trigger" in the following). This trigger is not biased by MBTS and ID.

Event Selection

Events were selected from colliding proton bunches where the SD trigger fired. To limit the amount of non-SD and accidental backgrounds, signals in the ALFA trigger detectors were required in exactly one of the four arms of ALFA and exactly one proton track had to be reconstructed in that arm. Proton track is the one created of a single track in the near ALFA station paired with a single track in the far ALFA station. Both tracks were required to have hits in at least six overlapping fibre layers in each U and V plane. When more than one such track was reconstructed in an individual station, the event was rejected from the analysis. Additional shorter tracks that are initiated by interactions within ALFA are acceptable. Further, the proton tracks were restricted in the x and y coordinates to be away from the edge of the beamline apertures. These cuts were slightly different for each ALFA station, but on average the x and y coordinates were required to be $6 \lesssim |y| \lesssim 19$ mm, $|x_{\text{near}}| \lesssim 10$ mm, $|x_{\text{far}}| \lesssim 15$ mm. Figure 4.3 shows the correlation pattern between the average x-position of a track between the near and far station, $\bar{x} = (x_{\text{near}} + x_{\text{far}})/2$ and the track local angle in (x, z) plane, $\theta_x = (x_{\text{far}} - x_{\text{near}})/|z_{\text{far}} - z_{\text{near}}|$, where x and z are track positions in the beam and ATLAS coordinate systems, respectively, "near" and "far" refers to ALFA near and far stations, respectively.

Additional structures, corresponding to tracks originating from beam-halo protons or showering in the stations, were observed in the data. Hence, the region accepted in

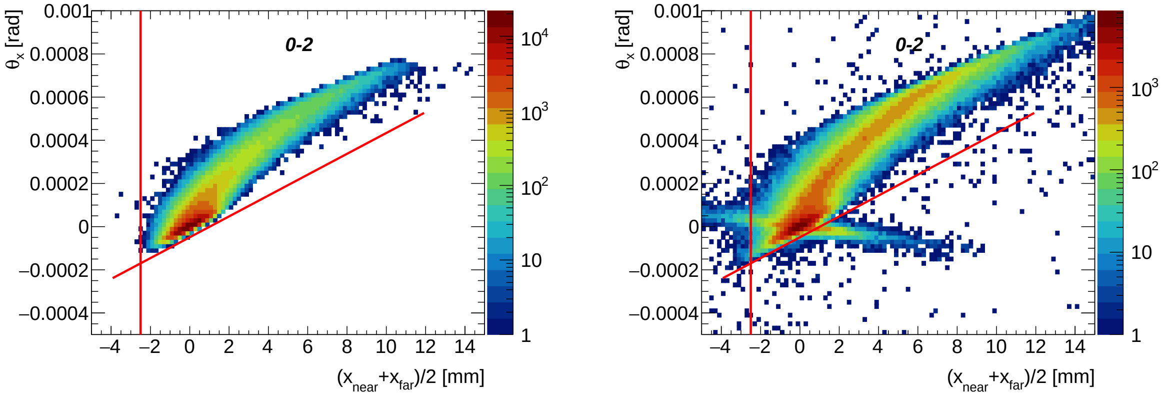

Figure 4.3: Correlation θ_x vs. $\bar{x}$ for single ALFA arm, 0-2, in (left) PYTHIA 8 A2 MSTW2008LO SD MC and (right) data. The correlation pattern, present in the MC sample, is formed by real SD proton tracks. Additional structures, present in the data, correspond to tracks originating from beam-halo protons or showering in the stations. Red lines indicate region accepted in the analysis.

the analysis was limited by:

$$\begin{aligned} &\bar{x} > -2.5 \text{ mm} \\ &\theta_x > \left(\bar{x} \cdot 4.8 \frac{\text{rad}}{\text{mm}} - 4.9 \text{ rad}\right) \cdot 10^{-5} \end{aligned} \tag{4.1}$$

The ALFA acceptance was defined as the probability that the true-level proton reached the z-position of ALFA, its smeared x and y positions were within the region accepted in the analysis, and θ_x vs. $\bar{x}$ cut was satisfied. The acceptance was calculated for each ALFA arm separately as a function of ξ and $|t|$ and is shown in Figs. 4.4 and 4.5. The region for which the acceptance in t is greater than 10% ranges from $0.02 < |t| < 1$ GeV^2/c^2 for the upper arms and depends on ξ for the lower arms: $0.02 < |t| < 1$ GeV^2/c^2 for $10^{-5} < \xi < 0.035$, $0.03 < |t| < 1$ GeV^2/c^2 for $0.035 < \xi < 0.08$ and $0.08 < |t| < 1$ GeV^2/c^2 for $0.08 < \xi < 0.16$. Thus, events were accepted only if the reconstructed values of $|t|$ for protons fell within these acceptance regions. Due to the crossing angle, the acceptance for protons with small $|t|$ and large ξ is higher in the upper stations.

The MBTS was used in the online trigger. Since the MBTS trigger efficiency is measured with respect to the events with MBTS offline signal, an offline signal in at least one MBTS counter on the opposite side of the IP to the ALFA-tagged proton was required. The MBTS offline thresholds on the measured charge in each tile were set to $e > 0.5$ pC for inner MBTS tiles and $e > 0.75$ pC for outer MBTS tiles.

The event selection criteria related to the central detector follow the ATLAS low-p_{T} MB analysis [22]. Events were required to have exactly one primary vertex with at least two primary tracks, $n_{\mathrm{sel}} \geq 2$, measured within an acceptance of the ID and satisfying the quality cuts listed in the next section. In order to suppress the background from more than one interaction per beam crossing, events were required to not contain a second vertex with four or more tracks.

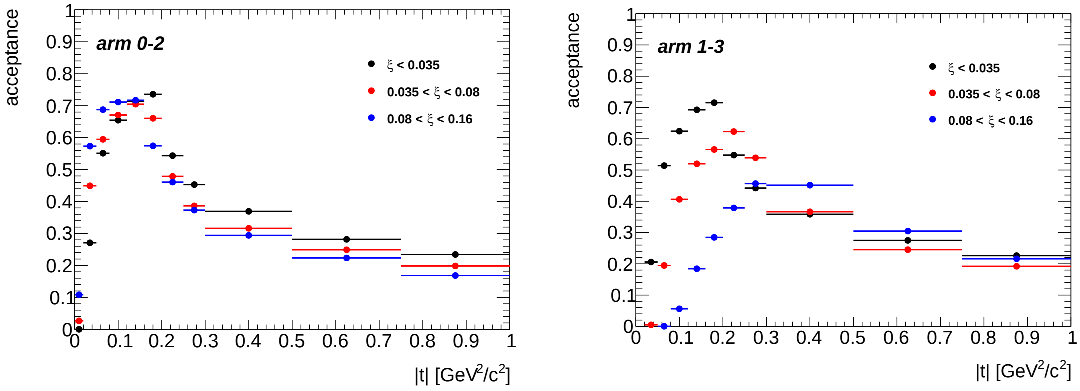

Figure 4.4: ALFA acceptance as a function of $|t|$ in three ranges of ξ, shown separately for ALFA arms (left) 0-2 and (right) 1-3.

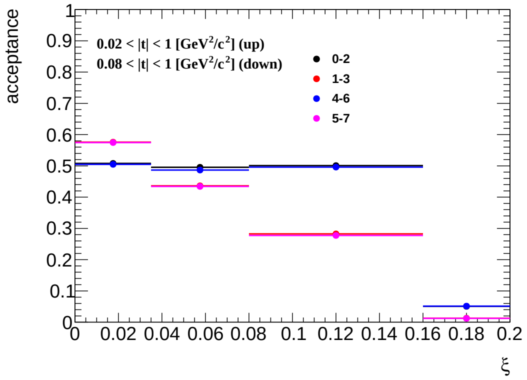

Figure 4.5: ALFA acceptance as a function of ξ, shown separately for each arm.

The requirements on the selected tracks followed the low-p_{T} MB analysis [22]:

- the track's transverse momentum p_{T} must be greater than 0.1 GeV/c,
- the track's absolute value of pseudorapidity $|\eta|$ must be smaller than 2.5,
- the number of Pixel hits must be at least equal to 1,
- if a hit is expected in Pixel IBL, then the one is required,
- the track must have at least 2, 4 or 6 SCT hits for $p_{\mathrm{T}} < 300$ MeV, $p_{\mathrm{T}} < 400$ MeV or $p_{\mathrm{T}} > 400$ MeV, respectively. Inactive layers, which are passed by tracks, are counted as hits,
- the transverse impact parameter with respect to the primary vertex d_0 must be less than 1.5 mm,
- $|z_0 \sin\theta|$ must be less than 1.5 mm, where z_0 is the longitudinal impact parameter with respect to the primary vertex, θ is the polar angle of the track,
- for tracks with $p_{\mathrm{T}} > 10$ GeV/c, the χ^2 fit probability must be greater than 0.01.

The d_0 and $|z_0 \sin\theta|$ cuts are used to select tracks that originate from the primary interaction vertex. The other track selection criteria are used to reject low quality tracks and to exclude the region (p_T, η) where the track reconstruction efficiency is small.

For the identified particle-antiparticle ratio analysis, where in addition to charged pions, also charged kaons and (anti)proton are measured, the p_T cut was increased to 0.3 GeV/c for all particles. This requirement followed the ATLAS recommendations described in [209].

Fractional Energy Loss of Forward Protons

The fractional energy loss of the forward-scattered proton was measured in two ways:

- from the proton kinematics in ALFA, referred as ξ^ALFA. The resolution/bias of ξ depends on the spatial resolution of ALFA and LHC optics,
- from the kinematic variables characterizing the diffractive system X [229, 230]:

  $$\xi^X = \frac{1}{\sqrt{s}} \sum_i p_\mathrm{T}^i e^{y^i} \tag{4.2}$$

  where $\sqrt{s}$ is the centre-of-mass energy, i runs over all particles in the diffractive system, p_T and y (assuming pion mass) are the transverse momentum and rapidity of the i-th particle, respectively. The ξ^X can be calculated from calorimeter clusters (will be referred as ξ^CAL) and ID tracks (will be referred as ξ^ID). The resolution/bias of ξ depends on the energy resolution of calorimeter clusters (ξ^CAL), limited geometrical acceptance, sensitivity to only charged particles (ξ^ID).

Figures 4.6 and 4.7 show the difference between the reconstructed and the true values of ξ using the information from ALFA, calorimeter system and ID. The reconstructed ξ^ALFA has best resolution and no bias only for $\xi^\mathrm{ALFA} \gtrsim 0.02$. At $\xi < 0.02$, ξ^CAL and ξ^ID are less biased than ξ^ALFA. There is an analogous measurement to the one presented in this thesis, in which at least one charge particle with $p_\mathrm{T} > 500$ MeV/c is required. The forward-scattered proton is measured in the range of $0.035 < \xi < 0.08$ using the AFP detector [231]. In case of a possible comparison of ALFA and AFP analyses, it is desirable that the range of ξ is the same in both. Therefore, the first ξ region of this analysis was limited to $\xi < 0.035$ and the second to $0.035 < \xi < 0.08$. Since migrations between three ξ bins are the smallest for ξ^ALFA, it was used in this analysis. ξ^CAL and ξ^ID were only used to analyse and limit the accidental background.

The comparison of the ξ^CAL vs. ξ^ALFA distributions obtained from data and PYTHIA 8 A3 simulation (shown in Fig. 4.8) allows to limit the region accepted in the analysis by:

$$\xi^\mathrm{CAL} < 0.02 + 0.75 \cdot \xi^\mathrm{ALFA} \tag{4.3}$$

in order to suppress the accidental and non-SD backgrounds but keep high efficiency for signal events.

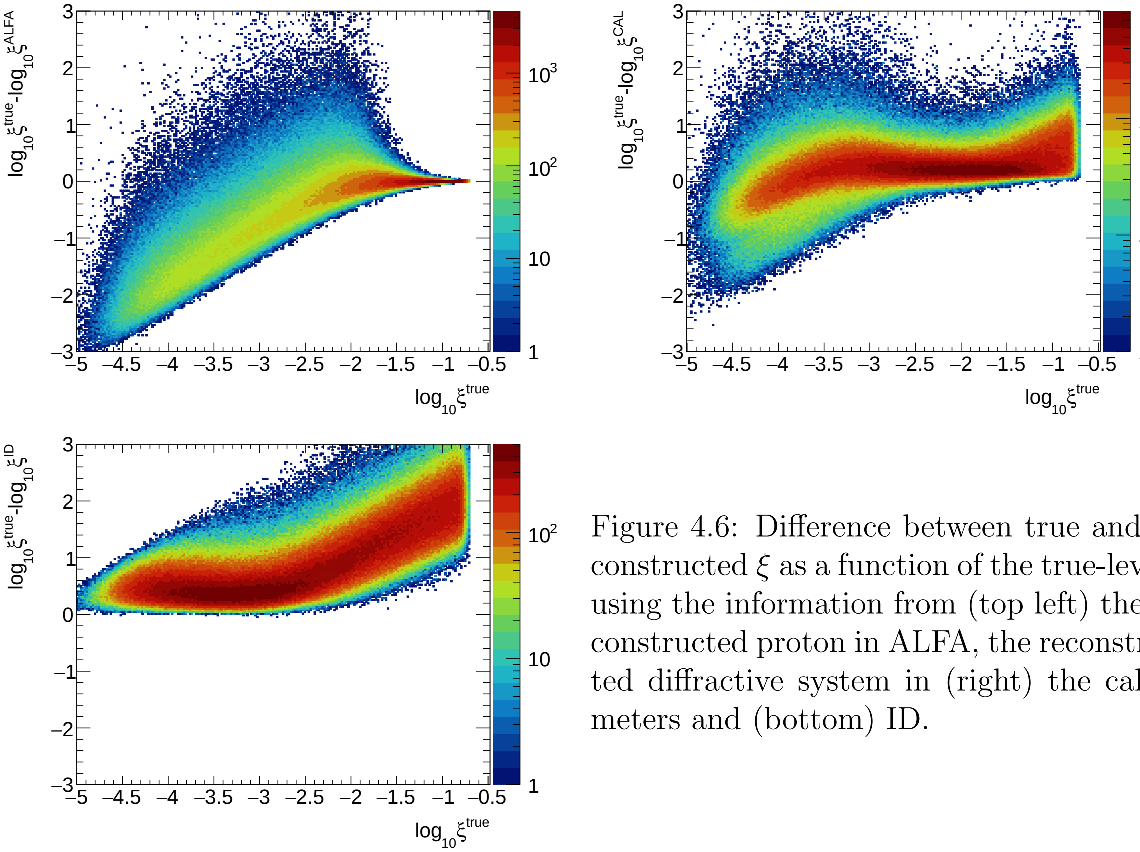

Figure 4.6: Difference between true and reconstructed ξ as a function of the true-level ξ using the information from (top left) the reconstructed proton in ALFA, the reconstructed diffractive system in (right) the calorimeters and (bottom) ID.

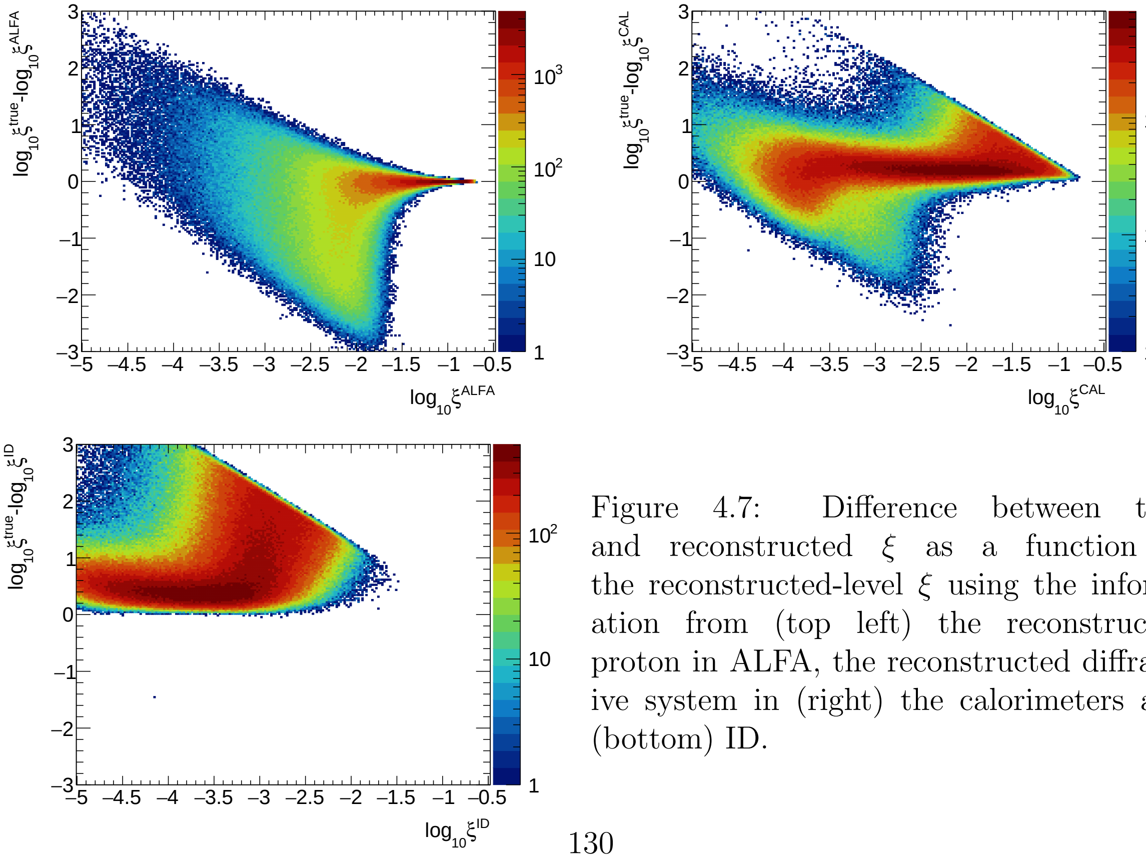

Figure 4.7: Difference between true and reconstructed ξ as a function of the reconstructed-level ξ using the information from (top left) the reconstructed proton in ALFA, the reconstructed diffractive system in (right) the calorimeters and (bottom) ID.

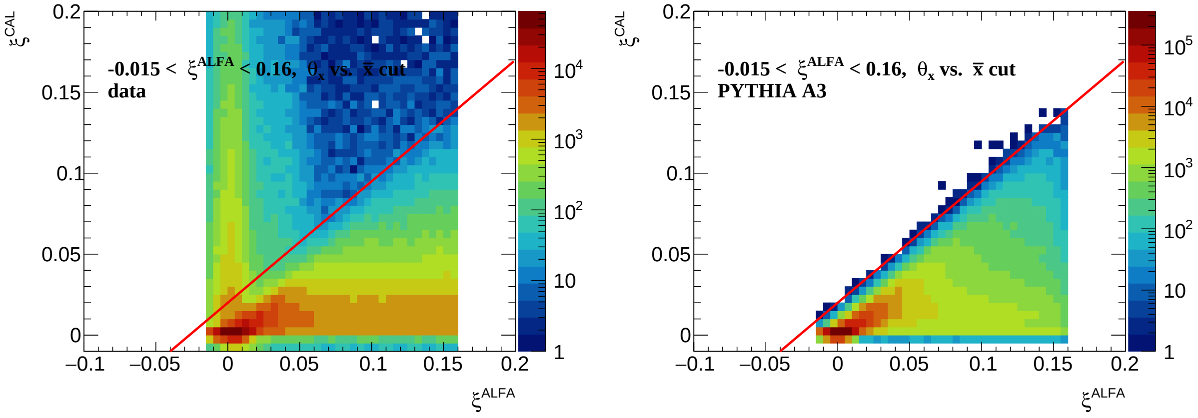

Figure 4.8: The $\xi^{\rm CAL}$ vs. $\xi^{\rm ALFA}$ distributions obtained from (left) data and (right) PYTHIA 8 A3 SD simulation. The red lines indicate the cuts applied to the ξ variables.

4.3 Fiducial Region of the Measurement

In this analysis, primary charged particles had to be contained within the kinematic range of $p_{\rm T} > 0.1$ GeV/c and $|\eta| < 2.5$. The results are corrected to the region of the total primary charged particles, $n_{\rm ch} \geq 2$. In identified charged antiparticle to particle ratios measurements, the lower transverse momentum limit was changed to 0.3 GeV/c. Identified particles were also required to be within the pseudorapidity window of $|\eta| < 0.5$.

The measurements were performed in a fiducial phase space of the forward-scattered protons of $0.02 < -t < 1.0$ GeV^2/c^2 and $10^{-5} < \xi < 0.16$. All measured observables are presented in three ξ regions: $10^{-5} < \xi < 0.035$, $0.035 < \xi < 0.08$ and $0.08 < \xi < 0.16$. The lower ξ cut was imposed by the requirement of $n_{\rm ch} \geq 2$, while the upper ξ cut was required since the region of larger ξ is at the edge of ALFA acceptance.

4.4 Background Contribution

The total background contribution to the charged-particle density can be divided into event-level and track-level backgrounds, i.e. accidental, non-SD (except EPOS SD′) and track backgrounds.

Accidental Background

The accidental background is defined as a process where in one proton-proton bunch crossing a single-side proton signal in ALFA is collected in an accidental coincidence with a signal in ID and MBTS. The contribution of such background was obtained for each ALFA arm separately with fully data-driven method, which uses MBTS, ID and ALFA triggers.

The accidental background contribution can be split into three types (other combinations are negligibly small) due to three detectors used in the analysis:

A [ALFA & veto(ID) & veto(MBTS)] in a coincidence with [veto(ALFA) + ID & MBTS]

B [ALFA & veto(ID) & MBTS] in a coincidence with [veto(ALFA) + ID & veto(MBTS)]

C [ALFA & veto(ID) & MBTS] in a coincidence with [veto(ALFA) + ID & MBTS]

All of the above expressions consists of two parts, each represented by different data samples and having the following signatures:

1. Exactly one reconstructed proton in ALFA as described in Sec. 4.2, no reconstructed primary vertices with $n_{\mathrm{sel}} \geq 4$ and signal (types B, C) or no offline signal (type A) above threshold in any MBTS counter on the opposite side of the IP. Events from these samples are required to have passed the ALFA trigger. The total number of such events for samples A, B, C will be referred to as $N^{\mathrm{A}}_{\mathrm{ALFA}}$ and $N^{\mathrm{B}}_{\mathrm{ALFA}} = N^{\mathrm{C}}_{\mathrm{ALFA}}$.
2. No hits in any ALFA trigger tiles, passed the event selection criteria related to the central detector (as described in Sec. 4.2) and signal (types A, C) or no signal (type B) above threshold in any MBTS counter on the opposite side of the IP. Events from these samples are required to have passed the MBTS or ID (without MBTS) trigger. Since there is no information about the forward-scattered proton in these samples, the analysis is done twice assuming that the forward-scattered proton is on side A or C. Such offline selection was designed to favour SD-like events without signal in ALFA in all contributions. The total number of such events for samples A, B, C will be referred to as $N^{\mathrm{A}}_{\mathrm{ID}} = N^{\mathrm{C}}_{\mathrm{ID}}$ and $N^{\mathrm{B}}_{\mathrm{ID}}$.

The fraction of accidental background coming from each type has to be added. The background enriched regions of the ξ^{ID} distributions were selected with the following cuts: $-0.015 < \xi^{\mathrm{ALFA}} < 0.01$, $\xi^{\mathrm{ID}} > 0.004$ and no ξ^{ALFA} vs. ξ^{CAL} cut. The value of $\xi^{\mathrm{ID}} > 0.004$ corresponds to $\xi^{\mathrm{true}} > 0.02$, for which the probability that $\xi^{\mathrm{ALFA}} < 0.01$ is very small. The sample was additionally enriched into accidental background by omitting the cut on the correlation between ξ^{CAL} vs. ξ^{ALFA}. In these regions, no signal is expected and almost all events originate from accidental background. The contribution of accidental background was fitted with the following parametrization:

$$b = \mathrm{A}' \left(b^{\mathrm{A}} + \mathrm{B}' b^{\mathrm{B}} + \mathrm{C}' b^{\mathrm{C}} \right) \tag{4.4}$$

where b is the accidental background contribution observed in ξ^{ID} distribution, b^{i} is a template of the accidental background coming from type $i = $ A, B, C and A$'$ is fit free parameter, while B$'$ and C$'$ parameters were constrained from data:

$$\mathrm{B}' = \frac{N^{\mathrm{B}}_{\mathrm{ALFA}}}{N^{\mathrm{A}}_{\mathrm{ALFA}}} \frac{\mathrm{PS}^{\mathrm{B}}_{\mathrm{ID}} N^{\mathrm{B}}_{\mathrm{ID}}}{\mathrm{PS}^{\mathrm{A}}_{\mathrm{ID}} N^{\mathrm{A}}_{\mathrm{ID}}} \tag{4.5}$$

$$\mathrm{C}' = \frac{N^{\mathrm{C}}_{\mathrm{ALFA}}}{N^{\mathrm{A}}_{\mathrm{ALFA}}} \frac{\mathrm{PS}^{\mathrm{C}}_{\mathrm{ID}} N^{\mathrm{C}}_{\mathrm{ID}}}{\mathrm{PS}^{\mathrm{A}}_{\mathrm{ID}} N^{\mathrm{A}}_{\mathrm{ID}}} \tag{4.6}$$

where $\mathrm{PS}_{\mathrm{ID}}^{\mathrm{A}} = \mathrm{PS}_{\mathrm{ID}}^{\mathrm{C}}$ and $\mathrm{PS}_{\mathrm{ID}}^{\mathrm{A}}$ are the trigger prescales that correspond to data samples from which the $N_{\mathrm{ID}}^{\mathrm{A}} = N_{\mathrm{ID}}^{\mathrm{C}}$ and $N_{\mathrm{ID}}^{\mathrm{B}}$ are calculated.

Figure 4.9 shows the ξ^{ID} distribution with fitted accidental background contribution. The fit was performed separately for each ALFA arm and ATLAS run separately. The exemplary results are presented for ALFA arm 0-2 and one of the ATLAS runs with the highest statistics. The ξ^{ALFA} and ξ^{CAL} distributions, shown in Fig. 4.10, were used as a cross-check of the procedure. The accidental background contribution was normalized to the number of events obtained from the ID fit. In the background enriched regions of ξ^{CAL} distribution, i.e. $\xi^{\mathrm{CAL}} > 0.02$, the normalized templates fairly well describe the data. The accidental background is overestimated (up to 20%) in some regions of $\xi^{\mathrm{ALFA}} < -0.02$. This can be due to the assumption that all events with $\xi^{\mathrm{ID}} > 0.04$ (or $\xi^{\mathrm{CAL}} > 0.02$) and $\xi^{\mathrm{ALFA}} < 0.01$ originate from the accidental background. Therefore, the change of the accidental background contribution by ±20% was taken as a systematic uncertainty.

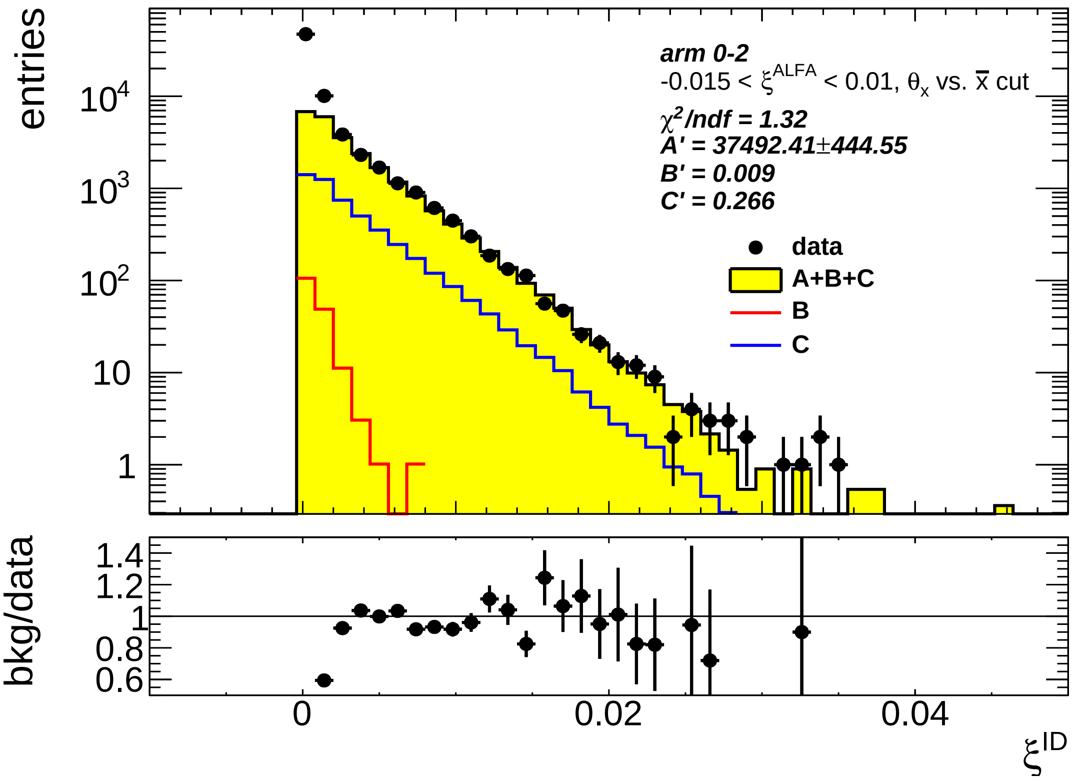

Figure 4.9: Uncorrected distributions of the reconstructed ξ^{ID} for events with proton reconstructed in 0-2 ALFA arm. Data is shown as black markers, whereas the fitted accidental background contribution is shown as yellow histogram. Colourful histograms represents the amount of accidental background of type B and C. The fit result is also shown. The ratio of accidental background and data is plotted in the bottom panel.

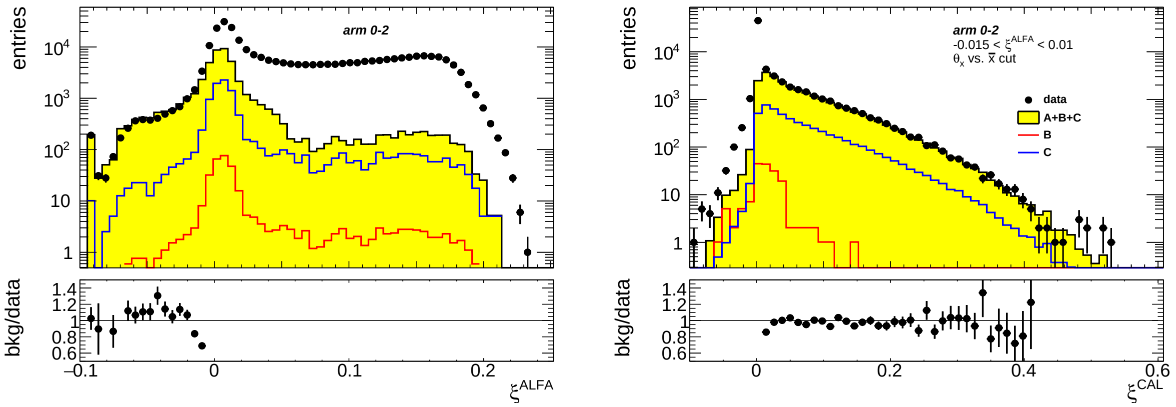

Figure 4.10: Uncorrected distributions of the reconstructed (left) ξ^{ALFA} and (right) ξ^{CAL} for events with proton reconstructed in 0-2 ALFA arm. Data is shown as black markers, whereas the fitted accidental background contribution is shown as yellow histogram. Colourful histograms represent the amount of accidental background of type B and C. The ratio of accidental background and data is shown in the bottom panel.

Non-SD Background

The background contribution having the SD signatures and originating from DD, ND and CD were obtained using the MC simulation. The simulation does not contain secondary interactions of forward-scattered particles with beam-pipe. Thus, only forward-scattered protons produced in the SD, CD, ND (for EPOS, SD′ is separated from the ND events) or DD events were propagated from the IP to the ALFA detectors. Therefore, fast simulation may not be reliable in the region of $\xi > 0.16$, in which an accurate modelling of beam-line apertures and secondary interactions with dead-material is necessary to reasonably describe the data. The reconstructed ALFA tracks that come from showering (not included in the simulation) are mostly rejected by θ_x vs. $\bar{x}$ and ξ^{CAL} vs. ξ^{ALFA} cuts since they do not originate from the IP and their distributions in ALFA are biased.

Figure 4.11 show the uncorrected ξ distribution in data compared to various MC models: PYTHIA 8 A3-NNPDF20LO (DL) and EPOS, where the MC distributions are split into SD, ND, DD and CD components. For EPOS, SD′ is separated from the ND events. The accidental background is also shown in the figures. Large-ξ protons, due to the beam-crossing angle, are more often reconstructed in the upper ALFA stations. Hence, there is an increase of events with ξ for these stations, starting from $\xi = 0.04$, with sharp drop caused by beam-pipe apertures around $\xi = 0.16$. PYTHIA 8 predictions do not agree with the data, especially large values of ξ in both, upper and lower, stations are not described. On the other hand, EPOS describes data better than PYTHIA 8 and reproduces the behaviour at large ξ. The main reason of good description by EPOS is SD′ contribution, which is not included in PYTHIA 8 by definition.

The CD contribution in EPOS, which was never tuned to describe any data, is about six times greater than in PYTHIA 8. The total CD cross section in PYTHIA 8 (DL) model, $\sigma_{\mathrm{CD}}^{\mathrm{tot}} = 1.279$ mb, is based on simple scaling assumption [101], and is about 1.6 times larger than in PYTHIA 8 (MBR), $\sigma_{\mathrm{CD}}^{\mathrm{tot}} = 0.816$ mb, where the latter was tuned to describe CDF data [222]. Due to differences between these two models, a CD-enriched control region was studied. It is similar to the signal selection (Sec. 4.2), but with a requirement of additional proton reconstructed in one ALFA arm on the opposite side of the IP. In addition, both protons are required to have $\xi^{\mathrm{ALFA}} > 0.02$ since negligible accidental background from elastic and beam-halo protons ($\xi^{\mathrm{ALFA}} < 0.01$) is expected in this region of ξ^{ALFA}. The normalization of the MC in the control region was kept to be the same as in the signal region. Figure 4.12 shows the uncorrected ξ data in the CD control region compared to PYTHIA 8 and EPOS expectations. Both the shape and the normalization of the measured distributions are poorly described by the MC simulations. In PYTHIA 8, the CD contribution is smaller than observed in the data by a factor of $2 - 3$ (even with the total CD cross section larger than that constrained by the CDF measurements). This is probably due to the fact that PYTHIA 8 does not describe ξ and $|t|$ distributions, as only

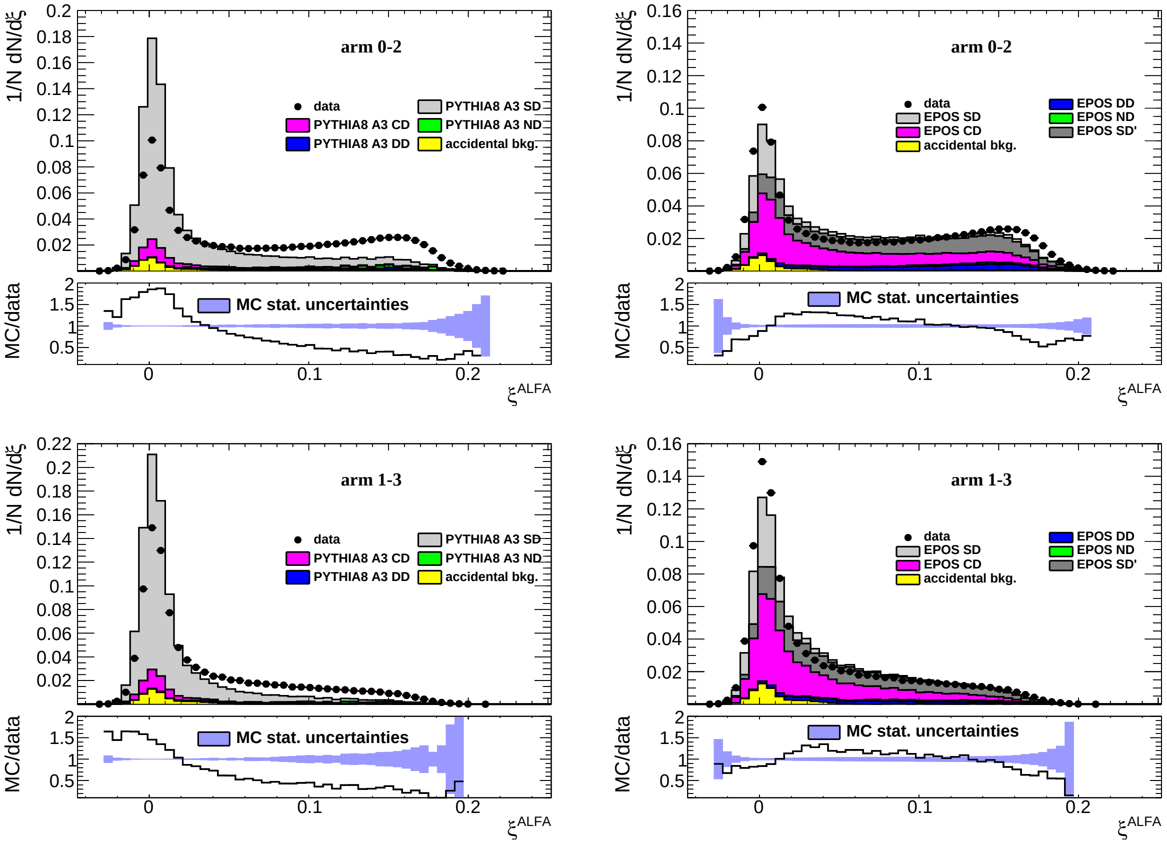

Figure 4.11: Uncorrected distributions of data compared to various MC models: (left) PYTHIA 8 A3-NNPDF20LO (DL) and (right) EPOS, as a function of ξ^{ALFA} for protons reconstructed in ALFA (top) $0 - 2$ and (bottom) $1 - 3$ stations. The ratio of the MC predictions and data is shown in the bottom panels.

a fraction of the full phase space can be measured in ALFA. In EPOS, the CD contribution is too large by a factor of $2-3$. The reason for this may be that the total CD cross section in EPOS is about 2 times larger than in PYTHIA 8. Therefore, a linear fit to the ratio of the MC and data was performed. This function was used to iteratively reweight the CD MC as a function of ξ^{true}. The comparison of ξ^{ALFA} distributions between data and the reweighted PYTHIA 8 and EPOS models in the CD control region is presented in Fig. 4.13. It is shown that these MC simulations provide a sufficient description of the data.

Figures 4.14 and 4.15 show the uncorrected ξ and $|t|$ data in the signal region compared to PYTHIA 8 and EPOS models, where the CD contribution was reweighted based on the CD control region. EPOS describes data better than PYTHIA 8, especially at $\xi^{\text{ALFA}} > 0.03$ where data/MC ratio is flat. Both MCs predict significant, but different, DD and ND background contributions at large ξ and $|t|$. Although the distributions for the lower and upper stations are different, the data/MC ratios are the same, thus, the conclusions are also the same.

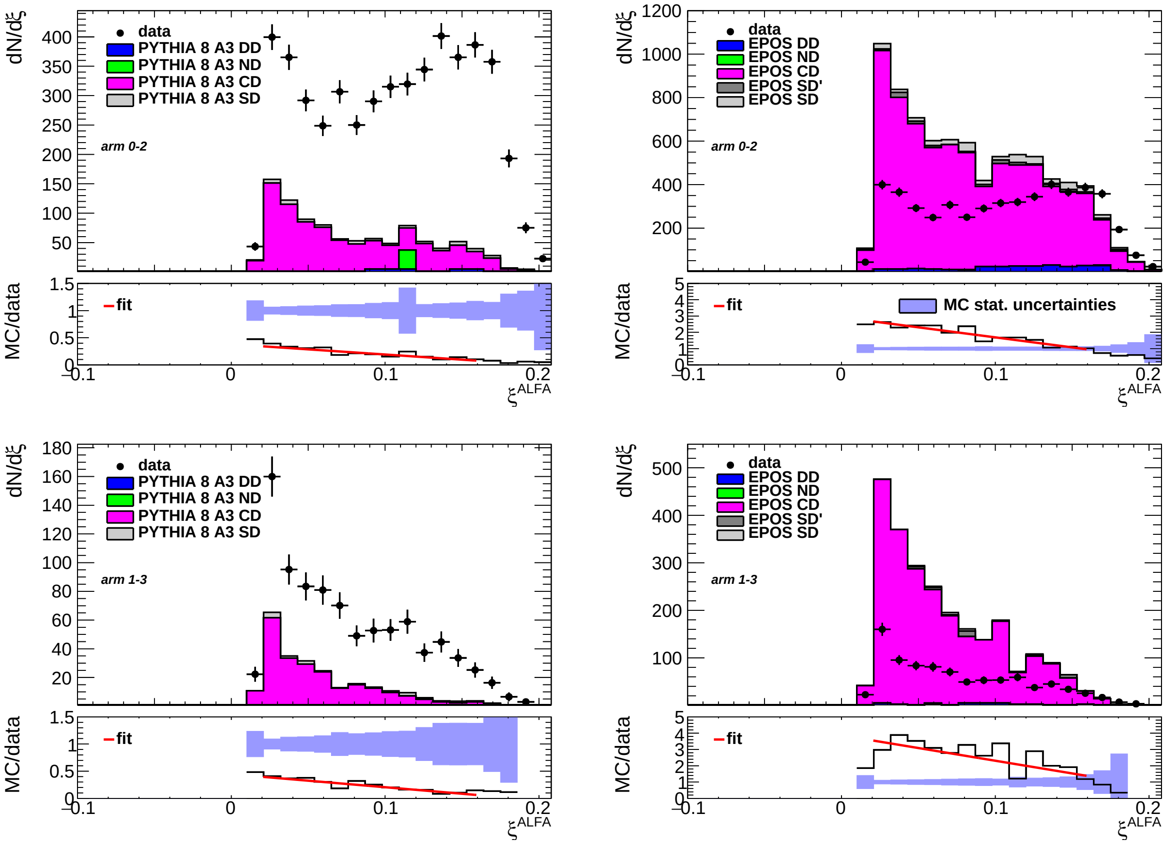

Figure 4.12: Uncorrected distributions of data in the CD control region compared to various MC models: (left) PYTHIA 8 A3-NNPDF20LO (DL) and (right) EPOS, as a function of ξ^{ALFA} for protons reconstructed in ALFA (top) $0-2$ and (bottom) $1-3$ stations. The ratio of the MC predictions and data, and a linear fit are shown in the bottom panels.

Figure 4.16 show the uncorrected distributions of variables used in the analysis: n_{sel}, p_{T} an $\bar{\eta}$. All distributions are poorly described by EPOS, whereas PYTHIA 8 reproduces them reasonably well, except low multiplicities, low p_{T} and $\bar{\eta}$ that is far away from the forward-scattered proton. The background contributions from DD and ND interactions are model-dependent and differ between these two MC models. For this reason, only CD background contributions were subtracted in the main analysis and the results were compared to MC predictions, which include all inelastic processes except CD. In addition, the analysis was repeated with DD and ND backgrounds subtracted. In both cases, the nominal background contribution was defined as a mean of PYTHIA 8 and EPOS (excluding SD′) predictions, whereas PYTHIA 8 and EPOS used separately specified an estimate of the systematic uncertainty.

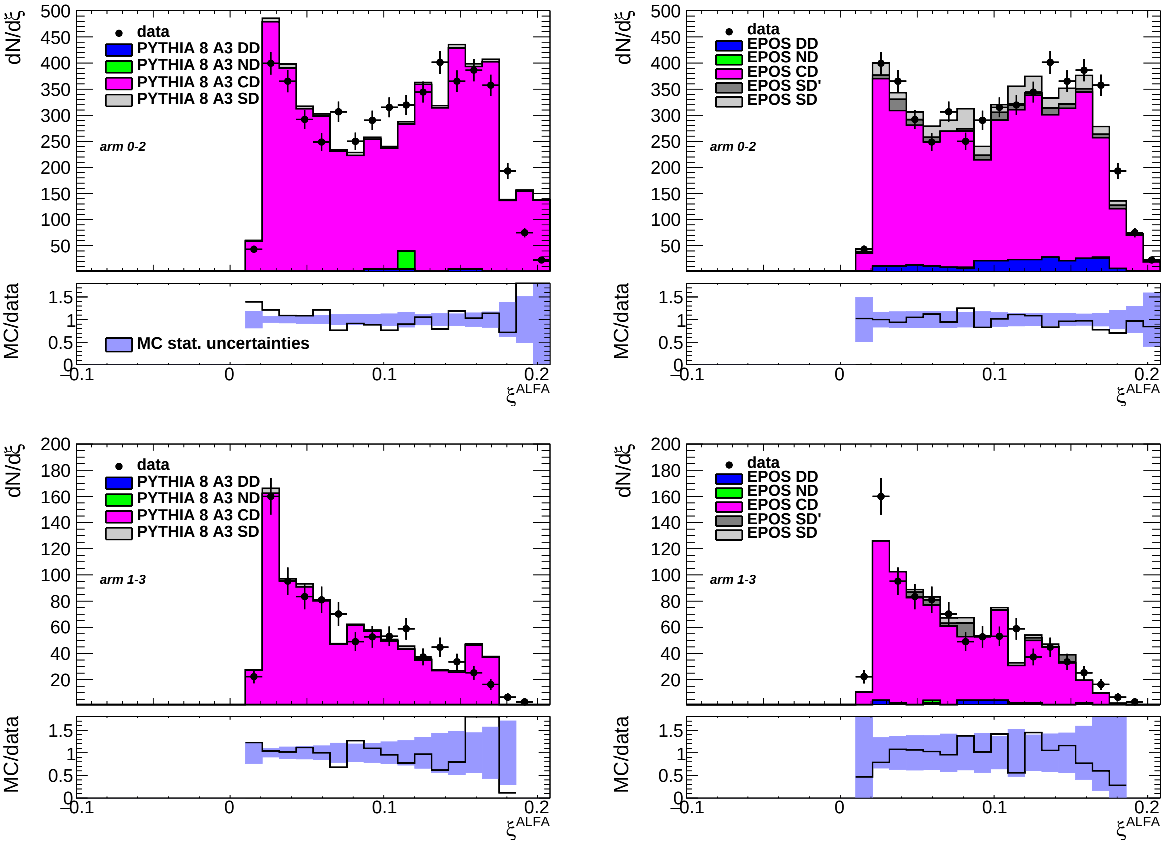

Figure 4.13: Uncorrected distributions of data in the CD control region compared to various MC models with reweighted CD contribution: (left) PYTHIA 8 A3-NNPDF20LO (DL) and (right) EPOS, as a function of ξ^{ALFA} for protons reconstructed in ALFA (top) $0-2$ and (bottom) $1-3$ stations. The ratio of the MC predictions and data are shown in the bottom panels.

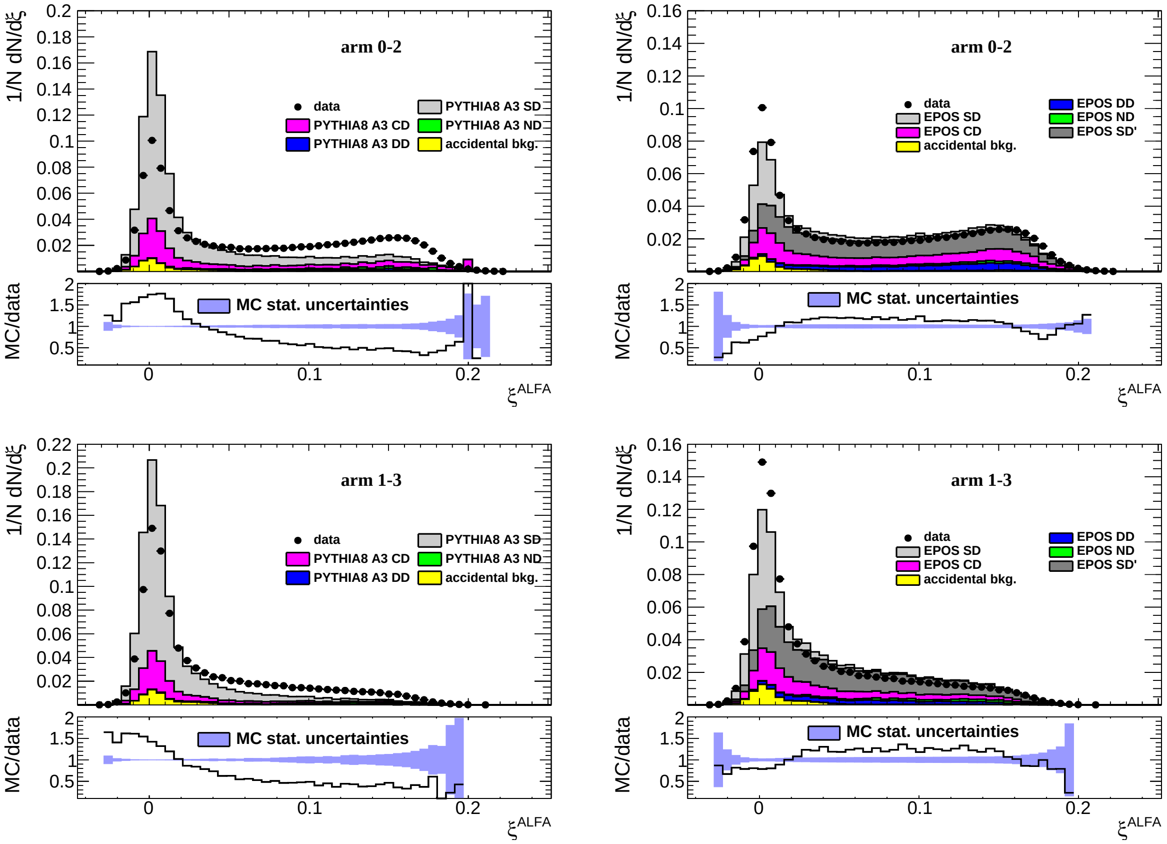

Figure 4.14: Uncorrected distributions of data compared to various MC models with reweighted CD contribution: (left) PYTHIA 8 A3-NNPDF20LO (DL), (right) EPOS, as a function of ξ for protons reconstructed in ALFA (top) $0-2$ and (bottom) $1-3$ stations. The ratio of MC predictions and data is shown in the bottom panels.

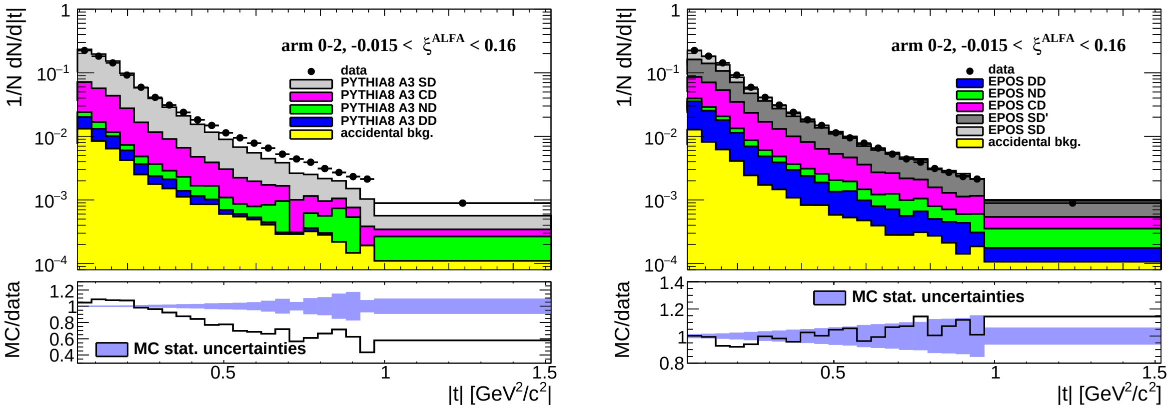

Figure 4.15: Uncorrected distributions of data compared to various MC models with reweighted CD contribution: (left) PYTHIA 8 A3-NNPDF20LO (DL) and (right) EPOS, as a function of $|t|$ for protons reconstructed in ALFA $0-2$ stations. The ratio of MC predictions and data is shown in the bottom panels.

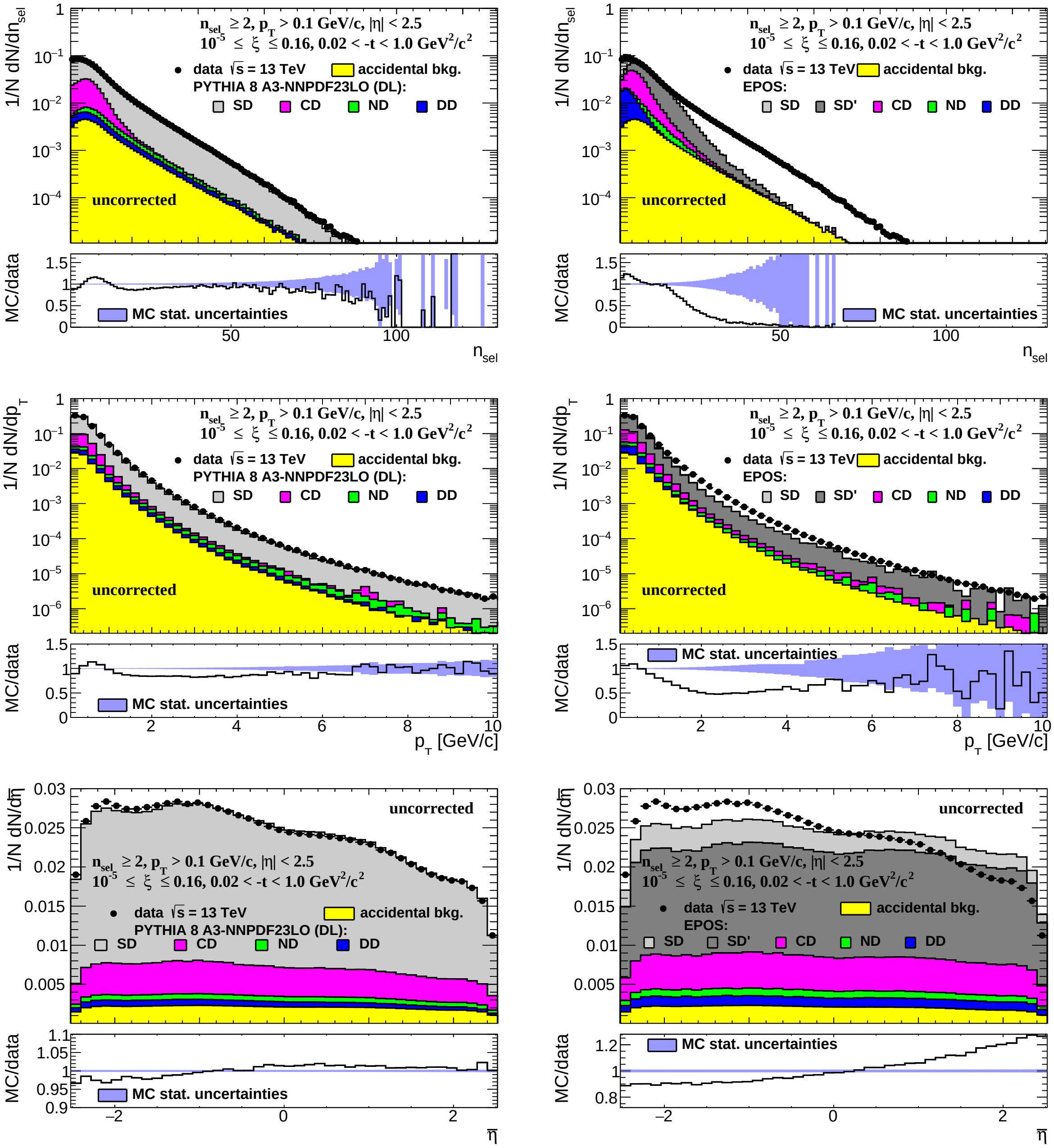

Figure 4.16: Uncorrected distributions of data compared to various MC models with re-weighted CD contribution: (left) PYTHIA 8 A3-NNPDF20LO (DL) and (right) EPOS, as a function of (top) n_{sel}, (middle) p_{T} and (bottom) $\bar{\eta}$. The ratio of MC predictions and data is shown in the bottom panels.

Background from Non-Primary Tracks

Some of the contributions of background tracks were estimated from simulation. The procedure of matching the reconstructed tracks to the true-level particles uses clusters, which are associated to a true-level particle and were used to form a track. The matching probability, P_{match} [232], which describes degree of matching between reconstructed track and true-level particle, is defined as follows:

$$P_{\mathrm{match}} = \frac{10 \cdot N_{\mathrm{Pixel}}^{\mathrm{particle}} + 5 \cdot N_{\mathrm{SCT}}^{\mathrm{particle}} + 1 \cdot N_{\mathrm{TRT}}^{\mathrm{particle}}}{10 \cdot N_{\mathrm{Pixel}} + 5 \cdot N_{\mathrm{SCT}} + 1 \cdot N_{\mathrm{TRT}}} \tag{4.7}$$

where $N_{\mathrm{Pixel}}^{\mathrm{particle}}$, $N_{\mathrm{SCT}}^{\mathrm{particle}}$ and $N_{\mathrm{TRT}}^{\mathrm{particle}}$ is the number of clusters which form a reconstructed track and are created by a true-level particle in the Pixel, SCT and TRT detectors, respectively, N_{Pixel}, N_{SCT} and N_{TRT} is the number of clusters which form a reconstructed track in the Pixel, SCT and TRT detectors, respectively. The reconstructed track is qualified as associated to a given true-level particle if $P_{\mathrm{match}} > 0.5$.

The background contribution from non-primary tracks includes particles originating from hadronic interactions with the detector dead-material, photon conversions and decays of long-lived particles. The amount of fake tracks (not associated to true-level particles) is very low, i.e. less than 0.1%. Figure 4.17 shows the contributions of background $f_{\mathrm{bkg}}\left(p_{\mathrm{T}}, \eta\right)$ and fake $f_{\mathrm{fake}}\left(p_{\mathrm{T}}, \eta\right)$ tracks predicted by PYTHIA 8 A2-MSTW2008LO (SaS) simulation.

The MC models do not necessarily predict the fraction of background tracks without any bias. Hence, the following procedure to estimate the contribution of non-primary tracks was used [21, 22].

Most of the reconstructed tracks, associated to non-primary particles, have large $|d_0|$ to the primary vertex. However, some of them, with small $|d_0|$, are included in the primary track sample. In order to correct for these background tracks, sample enriched in tracks associated to non-primary particles was used for background normalization. The standard

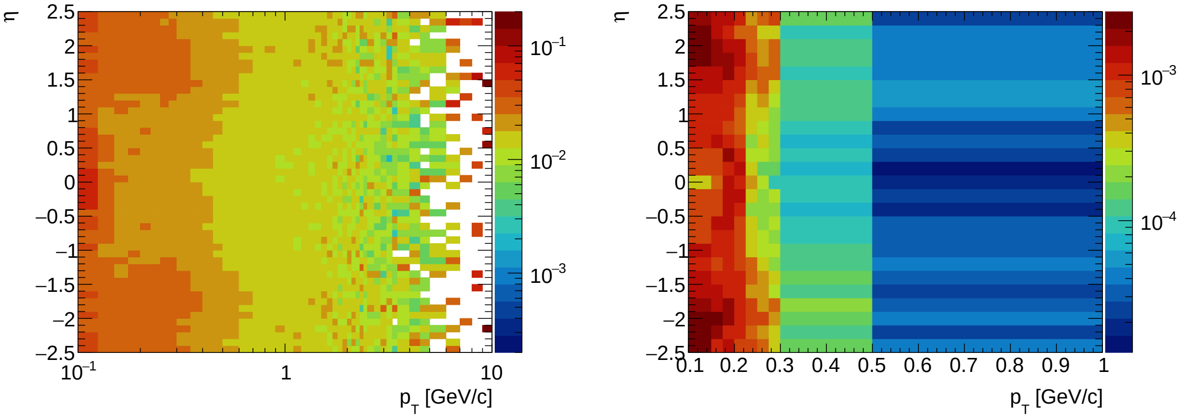

Figure 4.17: The contribution of (left) secondary, $f_{\mathrm{bkg}}\left(p_{\mathrm{T}}, \eta\right)$, and (right) fake, $f_{\mathrm{fake}}\left(p_{\mathrm{T}}, \eta\right)$, tracks estimated using PYTHIA 8 A2-MSTW2008LO (SaS) predictions

track selection was applied (as described in Sec. 4.2) but removing the transverse impact parameter (d_0) cut. The templates of reconstructed tracks corresponding to the charged particles were obtained from SD PYTHIA 8 A2-MSTW2008LO (SaS) sample. They were divided into those containing the primary and secondary tracks. The later consists of the electron, originating from photon conversions, and non-electron contribution, coming from decays and hadronic interactions. It was found that a single template for all sources of non-primary particles was sufficient for the procedure described below. Thus, the relative ratio of electron and non-electron secondaries predicted by the simulation was preserved.

First, the fake, predicted by PYTHIA 8, and accidental background contributions were subtracted from the d_0 distributions. Next, the templates of the d_0 in the PYTHIA 8 sample were fitted to the distributions in data in order to estimate the scaling factors, $f_{\mathrm{bkg}}^{\mathrm{scale}}(p_{\mathrm{T}})$, for non-primary track templates. Since the non-primary tracks dominate the tail of the d_0 distribution and the central part of the distribution is affected by the d_0 resolution, the fit was performed in the region $4.0 < |d_0| < 8.5$ mm. The upper bound of the fit was chosen

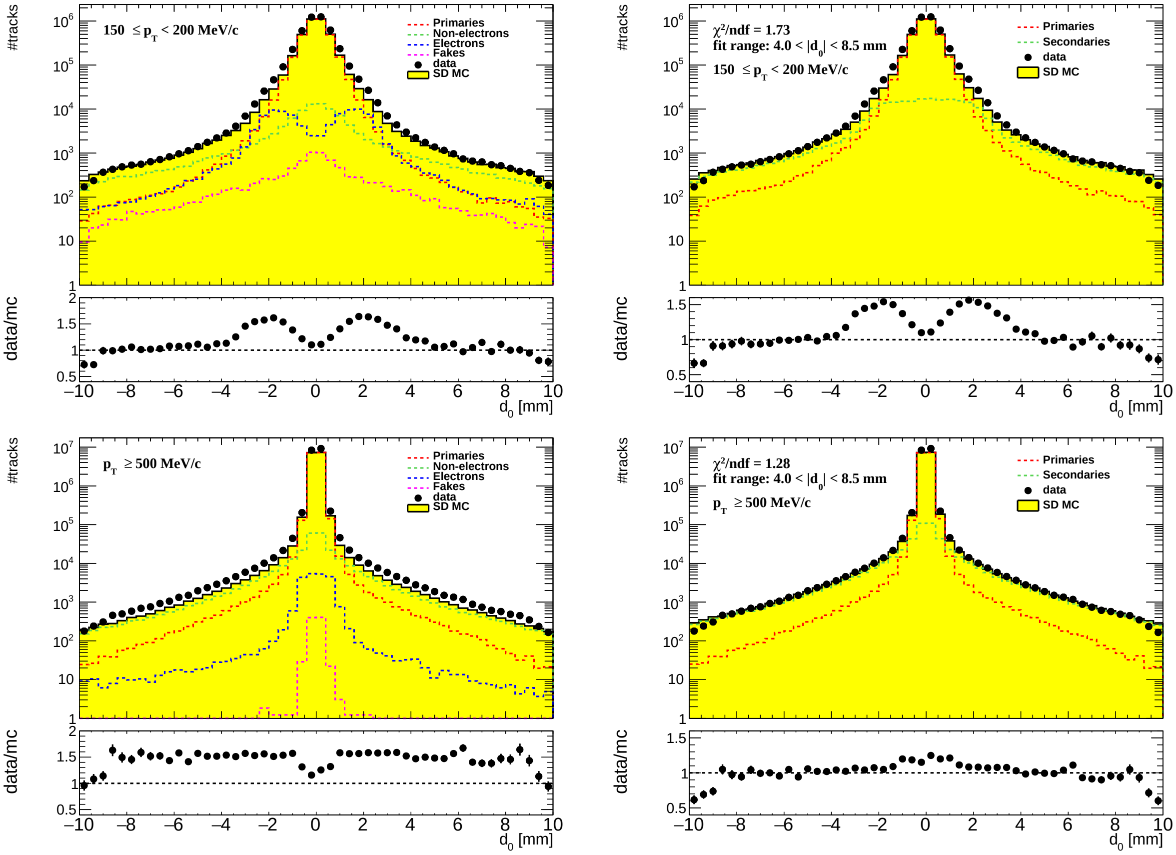

Figure 4.18: Comparison of the transverse impact parameter d_0 between data and PYTHIA 8 A2-MSTW2008LO (left) without and (right) with fitted scale factor applied to the non-primary track distributions. The ratio of data and MC predictions is shown in the bottom panels.

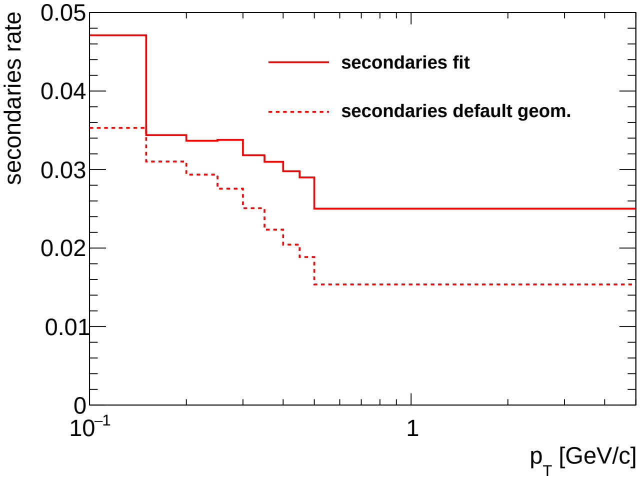

Figure 4.19: The fitted secondaries rate as a function of p_{T}. The secondaries rate without scaling factors applied is also shown.

to be insensitive to the $|d_0| < 10.0$ mm cut, which was used in the pattern recognition algorithm. The non-primary track contribution and the resolution of d_0 depend strongly on p_{T} of the reconstructed tracks. Hence, the fit was performed separately for various p_{T} bins, i.e. p_{T} bins of 50 MeV/c width between 100 MeV/c $< p_{\mathrm{T}} <$ 500 MeV/c, and one p_{T} bin for tracks with $p_{\mathrm{T}} >$ 500 MeV/c. As a result of this method, the non-primary track templates were multiplied by the fitted scaling factors. The fraction of the actual secondary track contribution in the signal region, $|d_0| < 1.5$ mm, was estimated from these scaled templates.

Figure 4.18 shows the comparison of d_0 between data and PYTHIA 8 for few exemplary p_{T} bins. The comparison for MC before fitting the non-primary track contribution is shown in the left column. The secondary track contribution was splitted into the categories of electrons and non-electrons. The fitted templates are shown in the right column. For each p_{T} bin the χ^2/ndf between the fitted template and the data was calculated within the regions given by $4.0 < |d_0| < 8.5$ mm. A large disagreement was observed in the central region of the d_0 distribution excluded from the fit ($|d_0| < 4.0$ mm). This may be due to different d_0 resolution in the data and simulation, caused by different options used in the vertex fit for data and MC: beam-spot was used as an additional parameter during the vertex reconstruction in the MC. However, this has almost no impact in the region of the distribution used for the fit.

Figure 4.19 shows the fitted secondaries rate as a function of p_{T}. The obtained secondaries rates in the data are about 1.5% higher than predicted by MC simulation.

Pion and Proton Background

The procedure to estimate the contribution of non-primary pions and protons was similar to the one used for charged particles without identification. However, due to the identification based on dE/dx and more restrictive pseudorapidity cut, $|\eta| < 0.5$, the analysis of the secondaries rate had to be repeated for identified $\pi^{\pm}$, p and $\bar{p}$. Since the contribution of secondary $K^{\pm}$ predicted by PYTHIA 8 was negligible, it was not studied. The d_0 templates

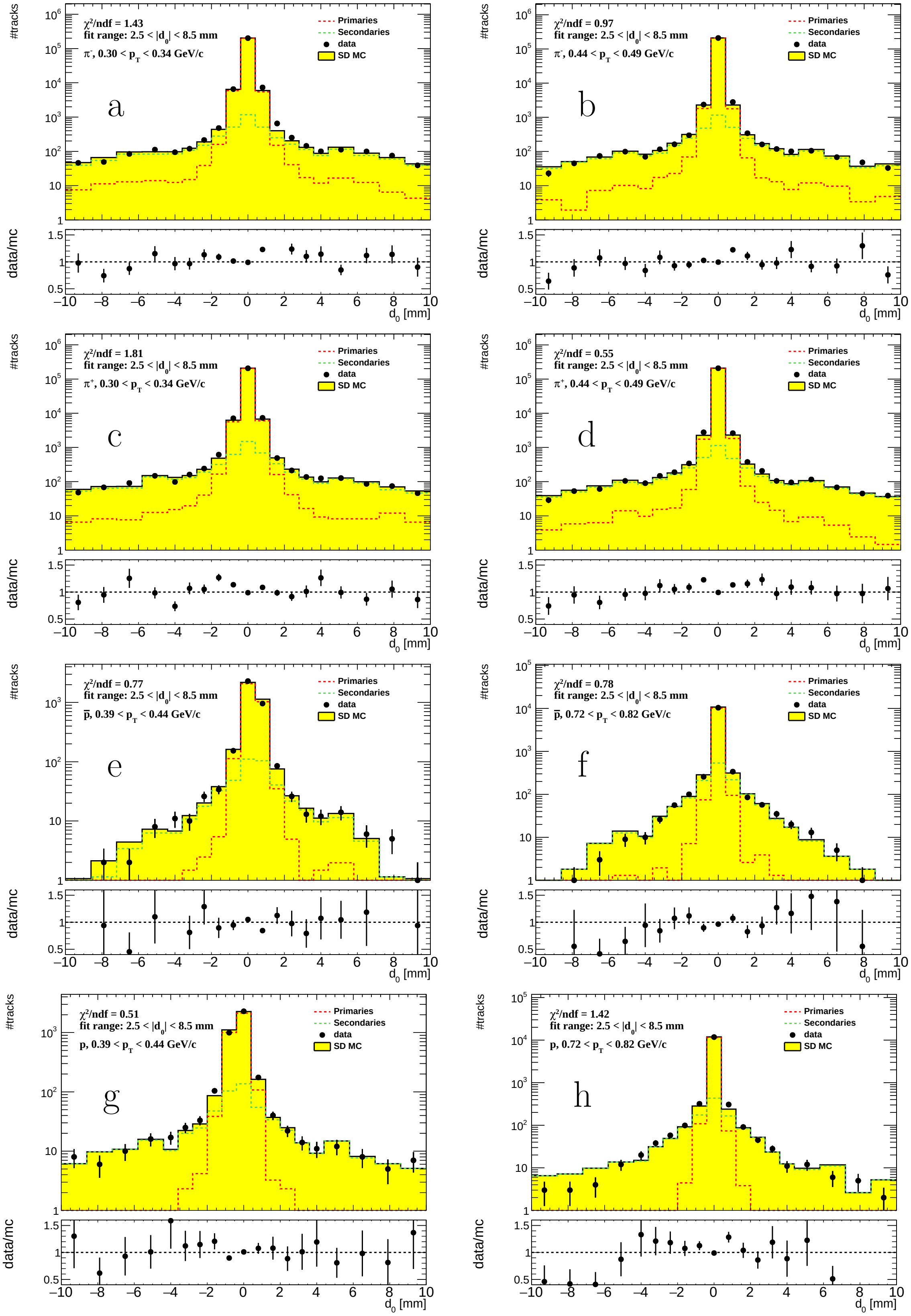

Figure 4.20: Comparison of the transverse impact parameter d_0 between data and PYTHIA 8 A2-MSTW2008LO with fitted scale factor applied to the non-primary track distributions for identified (a-b) π^-, (c-d) π^+, (e-f) $\bar{p}$ and (g-h) p in two sample p_T bins. The ratio of data and MC predictions is shown in the bottom panels.

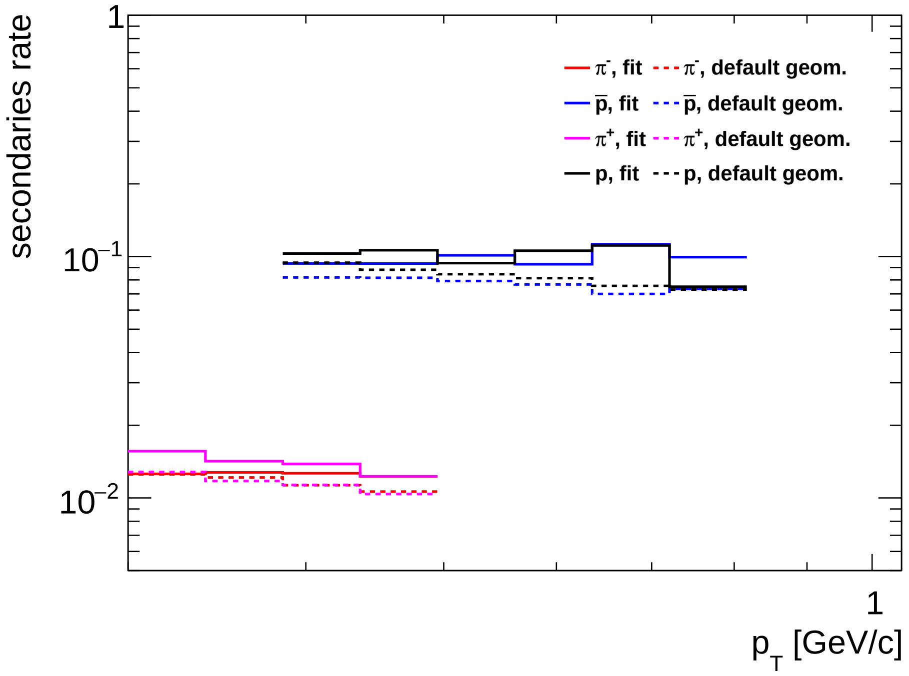

Figure 4.21: The secondaries rate as a function of p_{T} with and without scaling factors applied for identified $\pi^{\pm}$, p and $\bar{p}$.

were fitted in the p_{T} regions, where the separation in dE/dx between particles is satisfactory, i.e. $0.3 < p_{\mathrm{T}} < 0.49$ GeV/c for $\pi^{\pm}$ and $0.39 < p_{\mathrm{T}} < 0.82$ GeV/c for p, $\bar{p}$. The fit did not converge in the region $4.0 < |d_0| < 8.5$ mm for p and $\bar{p}$ since the d_0 distributions for these particles are narrower than for charged particles without identification. Therefore, the fit was performed in the region $2.5 < |d_0| < 8.5$ mm. For consistency, the same region was used for pions. The identified particles were selected through 1σ dE/dx cut[1]. The reconstructed tracks for MC templates were selected through the true-level information, i.e. by checking whether the true-level particle matched to the measured track is either a pion, or a proton. The fit was performed in the p_{T} bins that were used in the identification procedure.

Figure 4.20 show the sample comparisons of d_0 between data and PYTHIA 8 with fitted scaling factor applied to the non-primary track distributions for identified $\pi^{\pm}$ and $\bar{p}$, p. The fitted secondaries rate as a function of p_{T} for identified particles is shown in Fig. 4.21. The background for negative and positive pions varies between $1-2\%$, whereas the secondaries rate for protons and antiprotons is at the level of 10%. The d_0 distributions for protons and antiprotons are almost similar (no large asymmetry between p and $\bar{p}$ is observed). It is probably due to the fact that most of the secondary protons (antiprotons) originate from decays, what was confirmed by PYTHIA 8 predictions.

---

[1] The particle identification procedure via dE/dx was described in detail in Sec. 4.7.

4.5 Corrections

In this section, the trigger, track and vertex reconstruction efficiencies and the corresponding systematic uncertainties are described in detail.

Trigger Efficiency

The trigger efficiency of the ALFA detectors is approximately equal to 99.9% [233]. Hence, only the online signal of the MBTS counters needs to be studied. The efficiency of the main triggers used in the analysis, L1_MBTS_1_A(C)_ALFA_C(A), is measured in events selected by the L1_ALFA_ANY trigger. It is expressed as:

$$\epsilon_{\mathrm{trg}} = \frac{\text{number of events passing L1\_ALFA\_ANY and L1\_MBTS\_1\_A(C)\_ALFA\_C(A)}}{\text{number of events passing L1\_ALFA\_ANY}} \tag{4.8}$$

where L1_MBTS_1_A(C)_ALFA_C(A) is the trigger-before-prescale decision. Figure 4.22 shows the trigger efficiency as a function of n_{sel} and n_{MBTS}, where n_{MBTS} is the number of MBTS sectors with an offline signal above threshold on the opposite side of the IP to the ALFA-tagged proton. Since the MBTS trigger thresholds on the measured charge in each tile were on average (with some smearing) equal to 0.5 pC for inner MBTS tiles and 0.75 pC for outer MBTS tiles, the same values were used to define the MBTS offline thresholds. The trigger efficiency is approximately 86% for events with $n_{\mathrm{sel}} = 2$ and never reaches a plateau of 1. For the data analysed in this thesis, the space between proton bunches in the beams was 100 ns ($\mu \approx 0.1$). Therefore, some part of the signal (about 10%) in the MBTS tiles overlapped with the signal from previous collision(s) and the trigger was not 100% efficient. For the MB data, the bunch spacing was significantly larger, hence, the trigger efficiency is higher and varies between ≈ 96.5% for $n_{\mathrm{sel}} = 2$ and 99.3% for $n_{\mathrm{sel}} \geq 4$ [22].

There is no MBTS trigger simulation. Therefore, the trigger was emulated in the MC by the requirement of at least one MBTS tile with the measured charge above the cor-

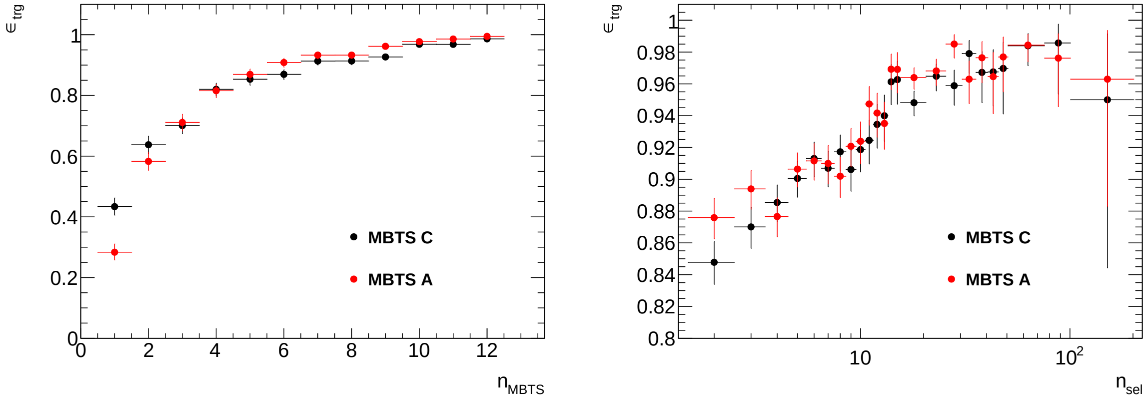

Figure 4.22: Trigger efficiency as a function of (left) n_{MBTS} and (right) n_{sel}.

responding online threshold in the data. The thresholds in the simulation were tuned to provide the same trigger efficiency as measured from the data, and are equal to 1.2 pC for inner MBTS tiles and 1.45 pC for outer MBTS tiles.

Systematic uncertainties on the trigger efficiency were assessed by varying the trigger MBTS thresholds in the simulation by ±0.3 pC. This values were chosen to cover the systematic uncertainties related to the smearing of the online MBTS thresholds in the data. However, the effect of this variation yields a negligible change in the measured distributions.

Track Reconstruction Efficiency

The track reconstruction efficiency, $\epsilon_{\mathrm{trk}}\left(p_{\mathrm{T}}, \eta\right)$, was defined as the probability that true-level primary particle was reconstructed as a track passing the selection criteria. The efficiency is expressed as:

$$\epsilon_{\mathrm{trk}}\left(p_{\mathrm{T}}, \eta\right) = \frac{N_{\mathrm{reco}}\left(p_{\mathrm{T}}, \eta\right)}{N_{\mathrm{gen}}\left(p_{\mathrm{T}}, \eta\right)} \tag{4.9}$$

where p_{T} and η are true quantities, $N_{\mathrm{reco}}\left(p_{\mathrm{T}}, \eta\right)$ is number of reconstructed tracks associated to a given true-level primary particle, $N_{\mathrm{gen}}\left(p_{\mathrm{T}}, \eta\right)$ is the number of true-level primary particles in a given $\left(p_{\mathrm{T}}, \eta\right)$ bin. Figure 4.23 shows the track reconstruction efficiency for charged primary particles as a function of p_{T} and η.

The track reconstruction efficiency, $\epsilon^{i}_{\mathrm{trk}}\left(p_{\mathrm{T}}\right)$, was also calculated separately for each identified particle type, where $i = \pi^{\pm}$, $K^{\pm}$, $\bar{p}$ and p. Such efficiency as a function of p_{T} is shown in Fig. 4.24.

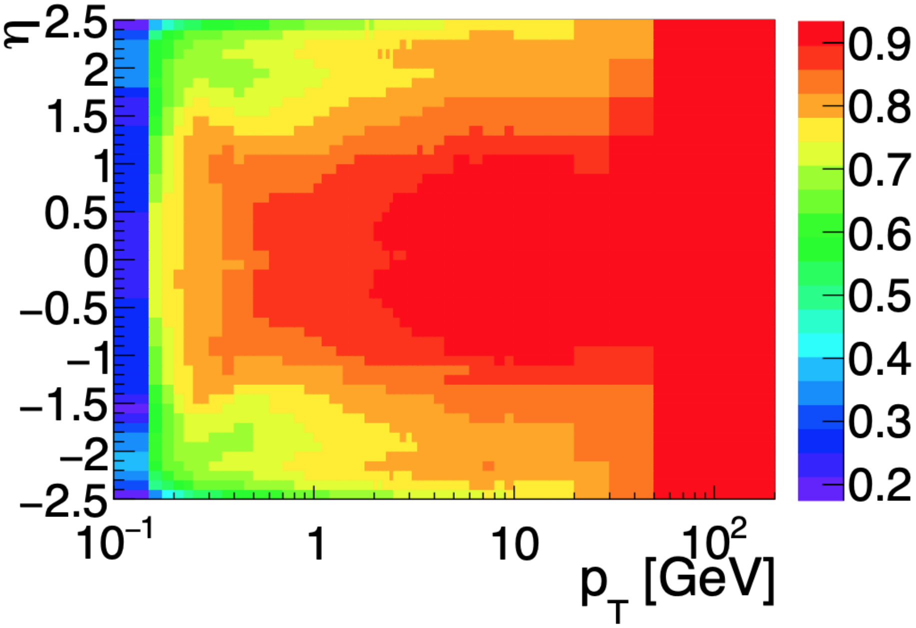

Figure 4.23: The track reconstruction efficiency as function of p_{T} and η. Figure taken from [232].

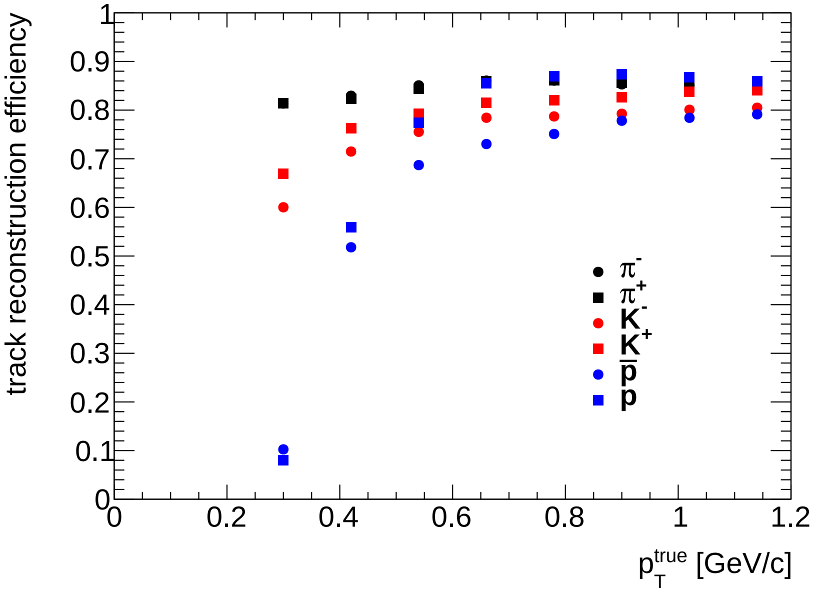

Figure 4.24: The track reconstruction efficiency as function of p_{T} for identified $\pi^{\pm}$, $K^{\pm}$, $\bar{p}$ and p, calculated from PYTHIA 8 A2-MSTW2008LO (SaS).

The track reconstruction efficiency and the systematic uncertainties related to it were calculated during the analysis of the MB data [21, 22, 232]. The following sources of systematic uncertainties are considered:

a) Amount of the Dead-Material

The proper description of the detector dead-material in the simulation is essential to correctly calculate the track reconstruction efficiency. The uncertainty on the amount of dead-material in ATLAS [22, 232, 234] is defined as the sum of the uncertainty on the ID material, which is about 5%, 10% uncertainty on the IBL material and 50% uncertainty on the material in the PP0 region. These uncertainties are based on studies [234], in which the rate of secondary vertices (originating from photon conversions and hadronic interactions) and the rate of tracks lost due to interactions in the PP0 region were compared between data and simulation. Figure 4.25 shows the relative systematic uncertainty on track reconstruction efficiency as a function of p_{T} and η due to the above components. Their sum leads to $1-10\%$ systematic uncertainty due to the description of dead-material in the simulation.

b) Probability Cut

Some of low-p_{T} charged particles are sometimes mismeasured as high-momentum tracks. These tracks mainly originate from particles interacting with the detector dead-material. To suppress fraction of such tracks, the χ^2 fit probability is required to be greater than

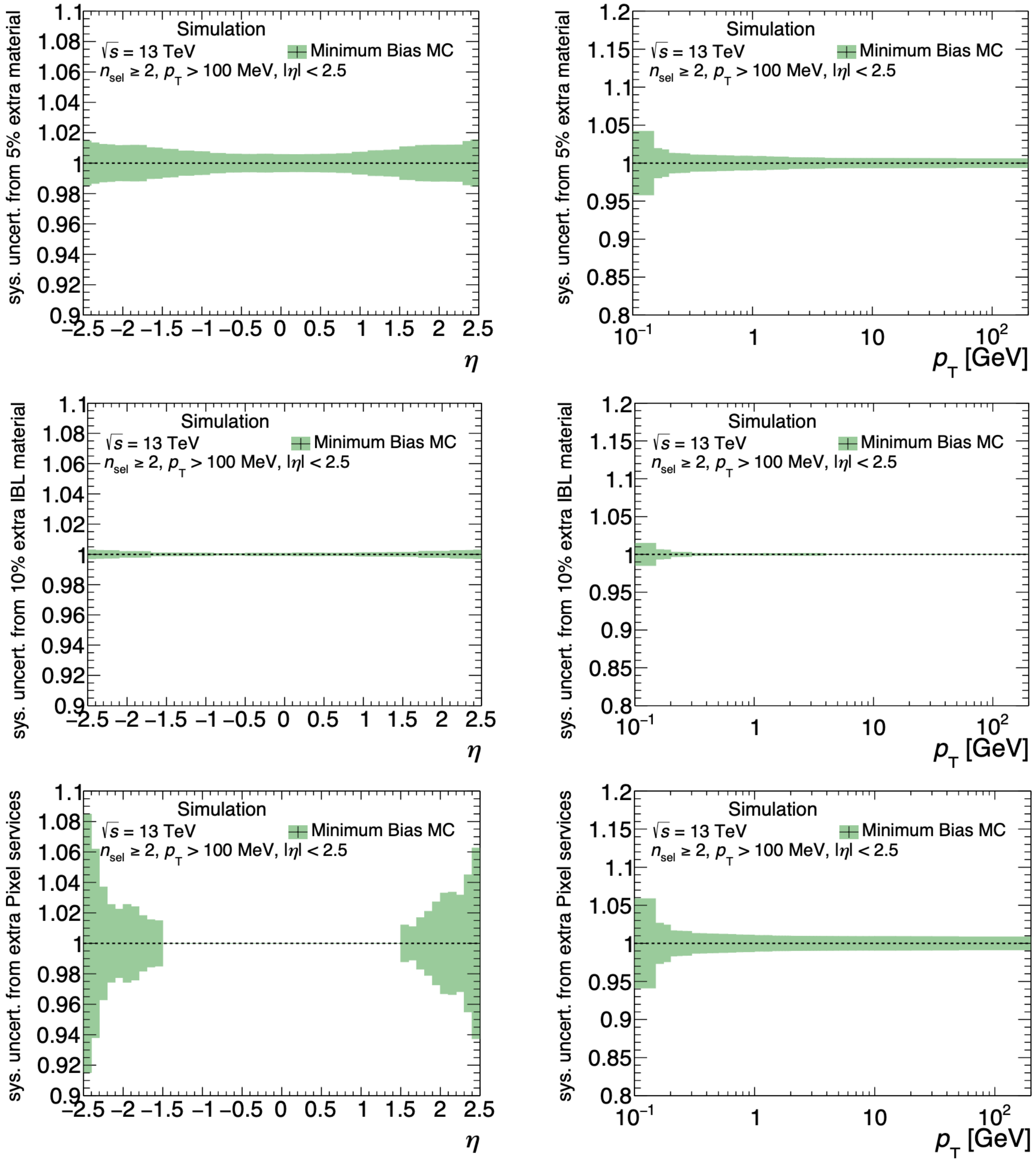

Figure 4.25: Systematic uncertainty on track reconstruction efficiency as a function of (left) η and (right) p_T due to additional material in the (top) ID, (middle) IBL and (bottom) PP0 region. Figure taken from [232].

0.01 for tracks with $p_{\mathrm{T}} > 10$ GeV/c. The systematic uncertainty due to the amount of mismeasured tracks was calculated by comparing the efficiencies of the χ^2 cut between data and simulation. The procedure used Pixel tracklets[2] and the topological clusters in the calorimeter system as a reference. The tracks were specified as mismeasured if the ratio of the track p_{T} to the tracklet (cluster) p_{T} was significantly larger than 1. The systematic uncertainty on the track reconstruction efficiency was estimated to be about 0.2% and 7% for particles with p_{T} at 10 and above 50 GeV/c, respectively [232].

c) Alignment (High-Momentum Tracks)

A small fraction of high-p_{T} tracks is affected by some biases due to the detector's misalignments, which can be divided into two categories: deformations that impact the track fit quality and deformations that introduce track parameter biases without changing the track fit quality (so called weak-modes) [232]. The former may be further divided into random misalignment of detector modules and temperature-dependent stave bowing of the IBL, while the latter consists of p_{T} dependent curvature (or sagitta) bias and smearing. The systematic uncertainties for the weak modes are based on Run-1 data [235, 236] since it was not possible to estimate them with limited amounts of data collected at the beginning of Run-2 [232]. Other systematic uncertainties were assessed by misaligning detector geometry in the simulation by the values obtained from cosmic ray data [237]. The systematic uncertainty related to the above four effects is negligible for tracks with $p_{\mathrm{T}} < 10$ GeV/c (majority of tracks used in this analysis), whereas above this value the dominant systematic effect is the random module misalignment (up to 10% for tracks with $p_{\mathrm{T}} = 100$ GeV/c).

Energy Loss Correction

A pion hypothesis is used during the track reconstruction procedure in order to correct the reconstructed momentum $p_{\mathrm{T}}^{\mathrm{meas}}$ for energy loss effects. The correction $p_{\mathrm{T}}^{\mathrm{meas}}$ to $p_{\mathrm{T}}^{\mathrm{true}}$ due to the rest biases for all particles but the pion, shown in Fig. 4.26, was determined from PYTHIA 8 A2-MSTW2008LO (SaS) MC as a function of p_{T}.

Vertex Reconstruction Efficiency

The vertex efficiency, ϵ_{vrt}, was calculated as a function of the number of selected tracks $n_{\mathrm{sel}}^{\text{no-z}}$, with all tracks passing the selection criteria described in Sec. 4.2 but the z_0 cut. In this analysis, it was required there is a primary vertex built from at least two reconstructed tracks and no secondary vertices with four or more tracks. Therefore, the vertex reconstruction efficiency was determined as the ratio of the number of good reconstructed events (reconstructed primary vertex with $n_{\mathrm{sel}} \geq 2$ and no secondary vertex with four or more tracks) to the number of input events. Figure 4.27 shows the vertex reconstruction efficiency calculated using no-pile-up PYTHIA 8 A2-MSTW2008LO (SaS) sample. Since the charged-particle multiplicity distributions does not depend on additional fake vertices,

---

[2] The Pixel tracklet is a track reconstructed only from Pixel hits

this MC sample (without pile-up) is sufficient for the studies of vertex reconstruction. The ϵ_{vrt} was measured to be ≈ 0.80 for events with $n_{\mathrm{sel}}^{\text{no-z}} = 2$, which is about 0.07 lower than for the MB analysis [22], and 1.0 at higher track multiplicities. The efficiency depends on the η and p_{T} distributions of tracks originating from the vertex, therefore, it is expected that ϵ_{vrt} depends on the process under study.

Correction to MBTS

The event selection imposed offline signal in at least one MBTS counter on the opposite side of the IP to the ALFA-tagged proton. Such offline MBTS efficiency, $\epsilon_{\mathrm{MBTS}}^{\mathrm{offline}}$, was obtained as a function of each measured quantity using PYTHIA 8 A3-NNPDF20LO (DL).

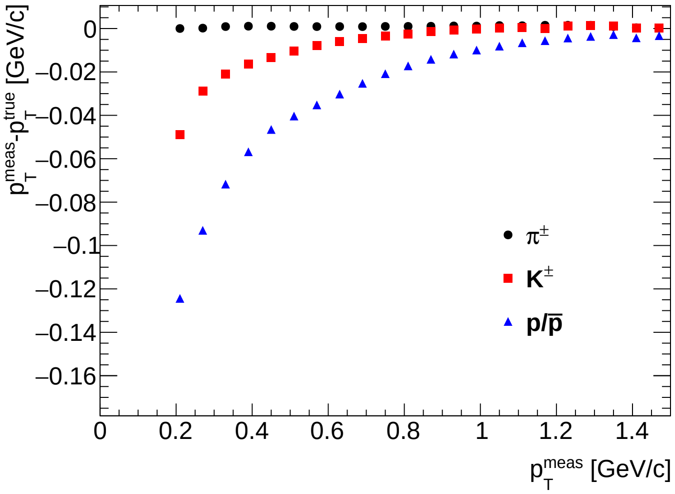

Figure 4.26: Energy loss correction $p_{\mathrm{T}}^{\mathrm{meas}} - p_{\mathrm{T}}^{\mathrm{true}}$ for identified $\pi^{\pm}$, $K^{\pm}$, $\bar{p}$ and p as a function of reconstructed transverse momentum $p_{\mathrm{T}}^{\mathrm{meas}}$ ($|\eta| < 0.5$).

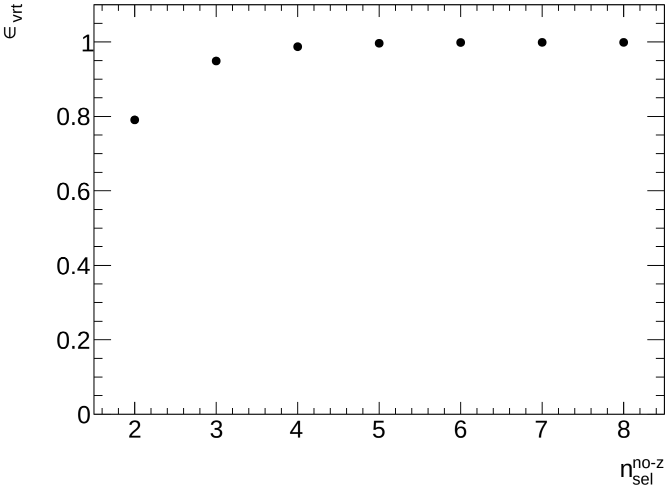

Figure 4.27: Vertex reconstruction efficiency as a function of $n_{\mathrm{sel}}^{\text{no-z}}$.

The efficiency was calculated for events within fiducial region as follows:

$$\epsilon_{\mathrm{MBTS}}^{\mathrm{offline}} = \frac{\text{number of MC events satisfying the offline MBTS selection criteria}}{\text{number of MC events}} \tag{4.10}$$

Figure 4.28 shows the offline MBTS efficiency, which was obtained from two MC models: PYTHIA 8 A3-NNPDF20LO (default) and EPOS. The $\epsilon_{\mathrm{MBTS}}^{\mathrm{offline}}$, obtained from PYTHIA 8 for $n_{\mathrm{ch}} = 2$, varies from about 90% for events with ξ within $0.035 - 0.16$ to about 99% for events with $10^{-5} < \xi < 0.035$. The efficiency reaches a plateau of 1 for larger multiplicities, $n_{\mathrm{ch}} > 10$, and all ranges of ξ. The efficiency is slightly below 1 for charged particles with $p_{\mathrm{T}} < 1.5$ GeV/c and $\bar{\eta} > -2.5$. Most of the charged particles are produced through the hadronization process, therefore, there is a correlation between their distributions in the central region of rapidity, the value of ξ and the offline MBTS signal that can be measured. A significant difference is observed between PYTHIA 8 A3-NNPDF20LO and EPOS predictions. Hence, the differences between these two models were used as a systematic uncertainty. The second systematic uncertainty was calculated using $\epsilon_{\mathrm{MBTS}}^{\mathrm{offline}} = 1$.

Since the offline MBTS efficiency depends on the charge-particle distributions, it also depends on the process under study. Therefore, the above study was repeated for only SD events and the results are shown in Fig. 4.29.

4.6 Migrations into and out of the Fiducial Region

In this section the corrections due to the migrations of tracks and forward-scattered proton into and out of the fiducial region are described.

Migrations of Tracks

The fraction of reconstructed tracks $f_{\mathrm{okr}}(p_{\mathrm{T}}, \eta)$, which migrate into the fiducial region ($p_{\mathrm{T}} > 0.1$ GeV/c and $|\eta| < 2.5$) and are associated to primary particles outside the kinematic range ($p_{\mathrm{T}} < 0.1$ GeV/c or $|\eta| > 2.5$), was estimated from MC in MB analysis [22]. The main residual migrations were observed at $|\eta| \approx 2.5$, where about 11% of reconstructed tracks were associated to a primary particle outside the fiducial region.

There are four contributions, which are added in quadrature and considered as a total systematic uncertainty on the track migration correction:

1. Difference between the $f_{\mathrm{okr}}(p_{\mathrm{T}}, \eta)$ corrections estimated from HERWIG and PYTHIA 8 Monash samples, which results in the systematic uncertainty of about 19% in p_{T} and 12% in η.

2. Difference between the $f_{\mathrm{okr}}(p_{\mathrm{T}}, \eta)$ corrections estimated from PYTHIA 8 ND samples with nominal geometry and with additional 5% ID material. This results in the systematic uncertainty of about 1% in p_{T} and 4% in η.

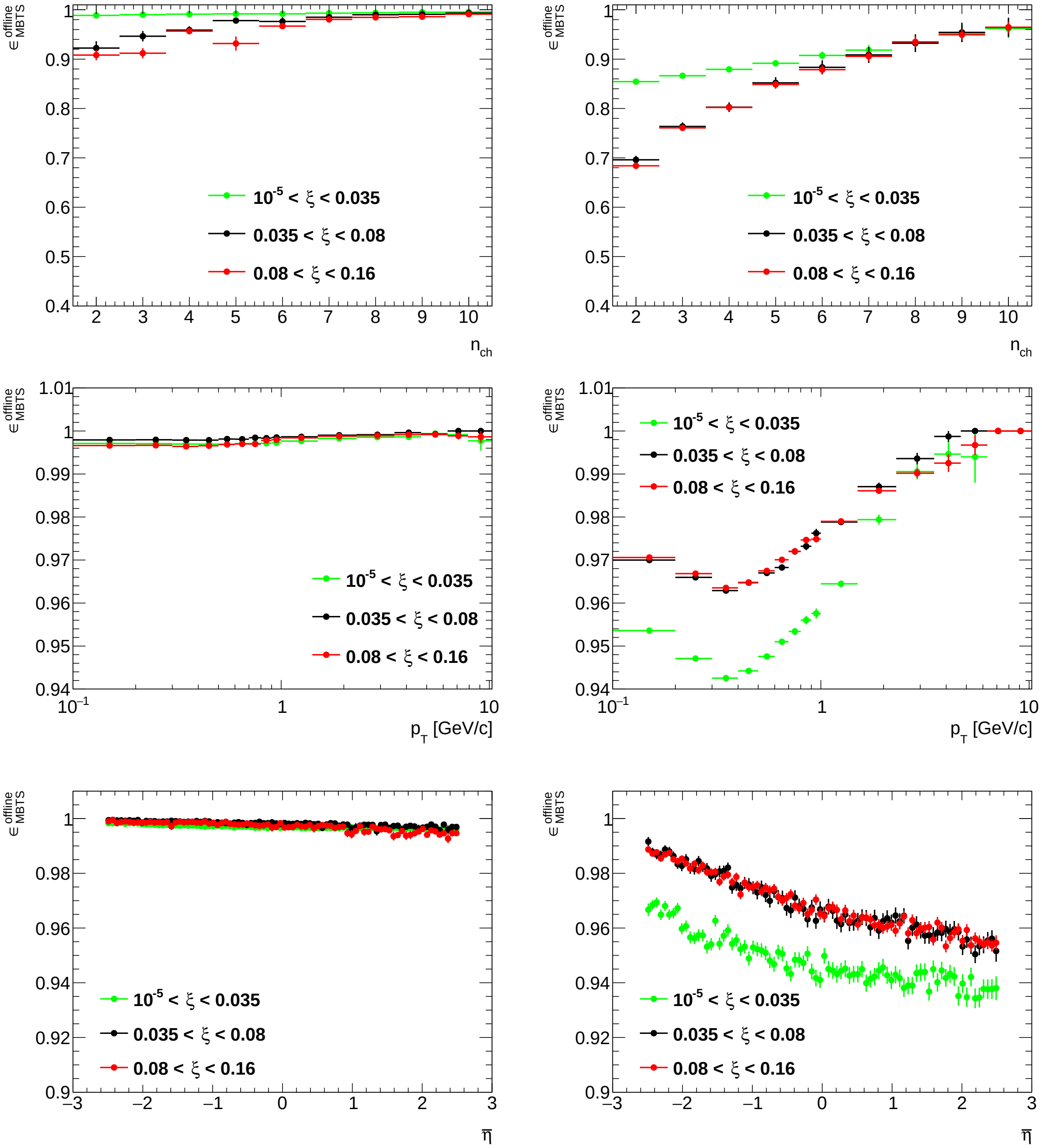

Figure 4.28: Offline MBTS efficiency calculated from (left) PYTHIA 8 A3-NNPDF20LO and (right) EPOS MC models, as a function of (top) n_{ch}, (middle) p_{T} and (bottom) $\bar{\eta}$ in three ranges of ξ.

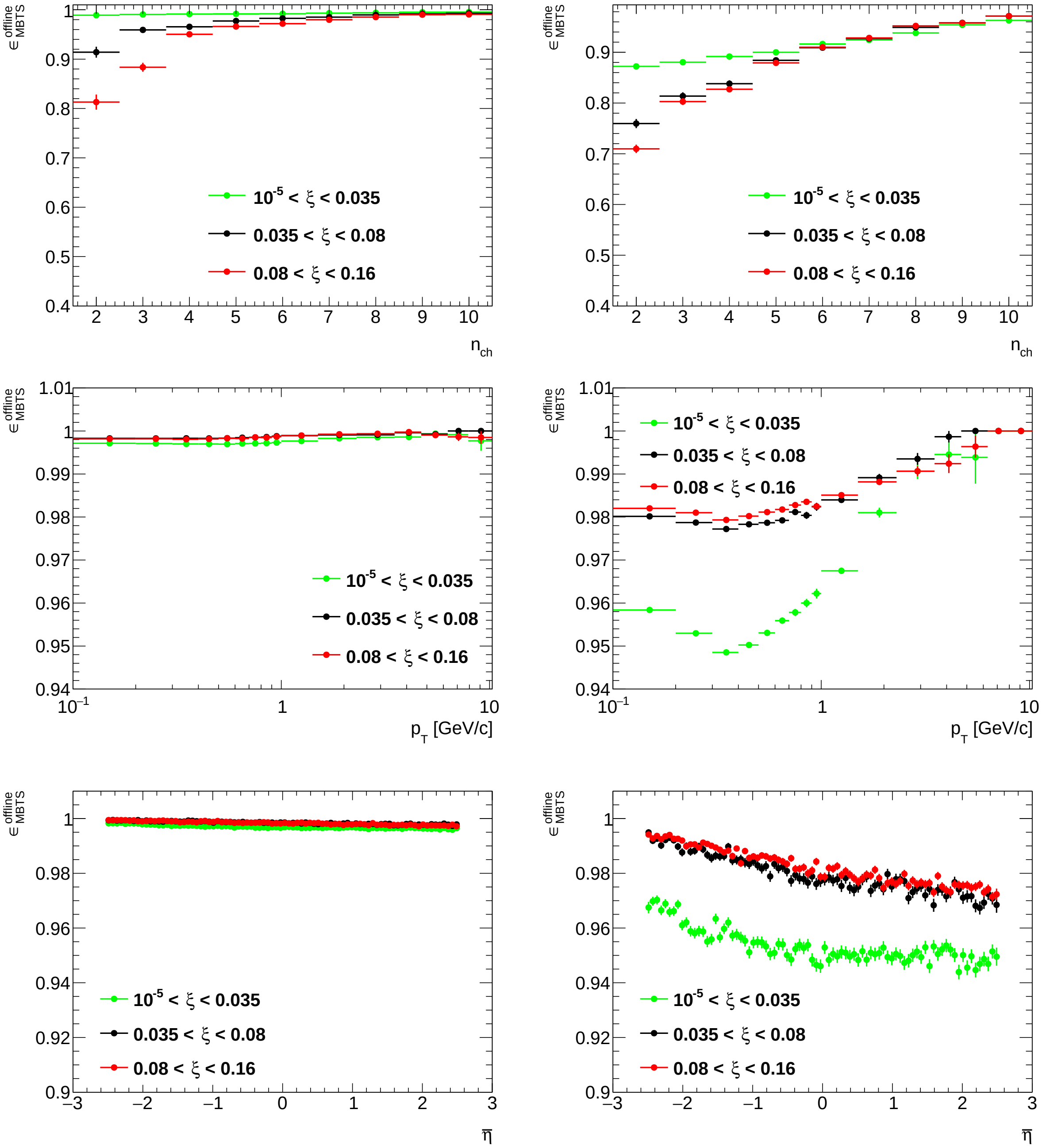

Figure 4.29: Offline MBTS efficiency calculated from (left) PYTHIA 8 A3-NNPDF20LO SD and (right) EPOS SD+SD′ MC models, as a function of (top) n_{ch}, (middle) p_{T} and (bottom) $\bar{\eta}$ in three ranges of ξ.

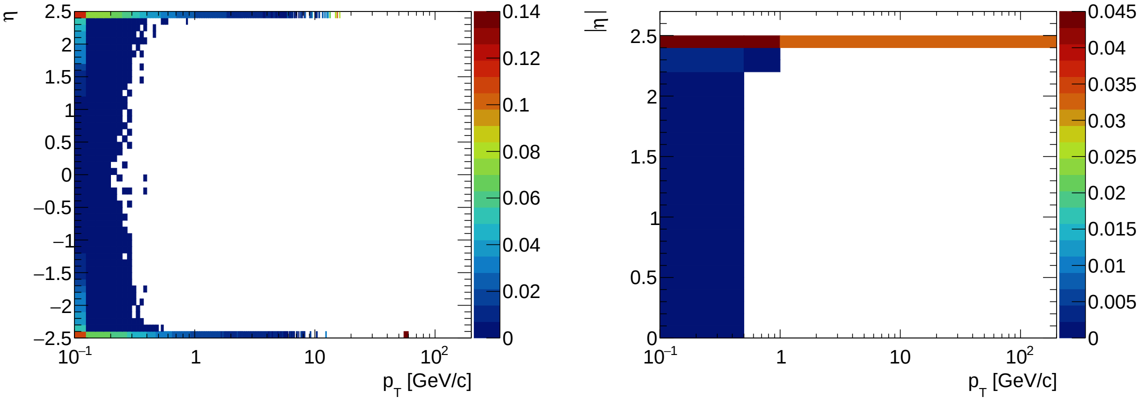

Figure 4.30: (left) Fraction of selected tracks migrating from outside of the kinematic range to the signal region as a function of p_{T} and η, and (right) the total systematic uncertainty on the $f_{\mathrm{okr}}\,(p_{\mathrm{T}},\eta)$ correction.

3. Difference between the $f_{\mathrm{okr}}\,(p_{\mathrm{T}},\eta)$ corrections estimated from PYTHIA 8 ND samples with nominal geometry and with additional 10% IBL material. This results in the systematic uncertainty of about 4% in p_{T} and 4% in η.

4. Difference between the $f_{\mathrm{okr}}\,(p_{\mathrm{T}},\eta)$ corrections estimated from PYTHIA 8 ND samples with nominal geometry and with additional $2 \times 10\%$ ID material in the high η region ($|\eta| > 2.2$). This results in the largest contribution to the total systematic uncertainty and equals to about 76% in p_{T} and 80% in η.

Both, the $f_{\mathrm{okr}}\,(p_{\mathrm{T}},\eta)$ correction and the total systematic uncertainty on the track migration corrections, are shown in Fig. 4.30.

The correction from the MB analysis (obtained from ND samples) was used. This is not strictly valid since it depends on the process under study and was calculated as a function of η instead of $\bar{\eta}$. This results in the non-closure of the corrected MC distributions for SD sample, which is observed at $|\bar{\eta}| \approx 2.5$ (Sec. 4.7). Therefore, any deviations from the closure tests were taken as a systematic uncertainty.

Migrations in ξ

The analysis was performed in three ranges of ξ. Thus, there are migrations into and out of these ξ regions. They mainly originate from the resolution of ξ, which is measured with the ALFA detectors. The corrections due to migrations into and out of ξ regions was defined as:

$$f_{\xi} = \frac{1 - f_{\xi}^{-}}{1 - f_{\xi}^{+}} \tag{4.11}$$

where f_{ξ}^{-} is the fraction of events for which the corresponding true-level ξ_{true}, is outside of the ξ region, and f_{ξ}^{+} is the fraction of events for which the corresponding reconstructed ξ_{reco} is outside of the ξ region.

The f_ξ was calculated for each measured variable separately. Figures 4.31 to 4.33 show the fraction of events f_ξ^- and f_ξ^+ as a function of n_{ch}, p_{T} and $\bar{\eta}$, calculated using PYTHIA 8 A3-NNPDF20LO inelastic sample. The largest migrations into and out of the ξ regions were observed at $0.035 < \xi < 0.08$, and at $10^{-5} < \xi < 0.035$, $n_{\mathrm{ch}} > 40$, where they are of the order of $6 - 8\%$. In the other ξ regions, f_ξ^- and f_ξ^+ are smaller than 2%. Moreover, the differences between f_ξ^- and f_ξ^+ are smaller than 2% in almost all bins. This study was repeated for the analysis of SD events (non-SD background subtracted distributions).

In order to calculate systematic uncertainties, the shape of f_ξ^- and f_ξ^+, normalized to unity, was taken from data, whereas the total normalization of migrations into and out of the fiducial region was calculated using MC. Corrections were defined as:

$$f_\xi = \frac{1 - f_\xi^{-,\,\mathrm{total}} \cdot f_\xi^{-,\,\mathrm{data}}}{1 - f_\xi^{+,\,\mathrm{total}} \cdot f_\xi^{+,\,\mathrm{data}}} \tag{4.12}$$

where $f_\xi^{-,\,\mathrm{total}}$ is the total fraction of events in the MC for which the corresponding ξ_{true}, is outside of the ξ region, $f_\xi^{+,\,\mathrm{total}}$ is the total fraction of events in the MC for which the corresponding ξ_{reco} is outside of the ξ region, $f_\xi^{-,\,\mathrm{data}}$ and $f_\xi^{+,\,\mathrm{data}}$ are the shapes of f_ξ^- and f_ξ^+, taken from the corresponding ξ bins in the data. In particular, $f_\xi^{+,\,\mathrm{data}}$ has the same shape as signal.

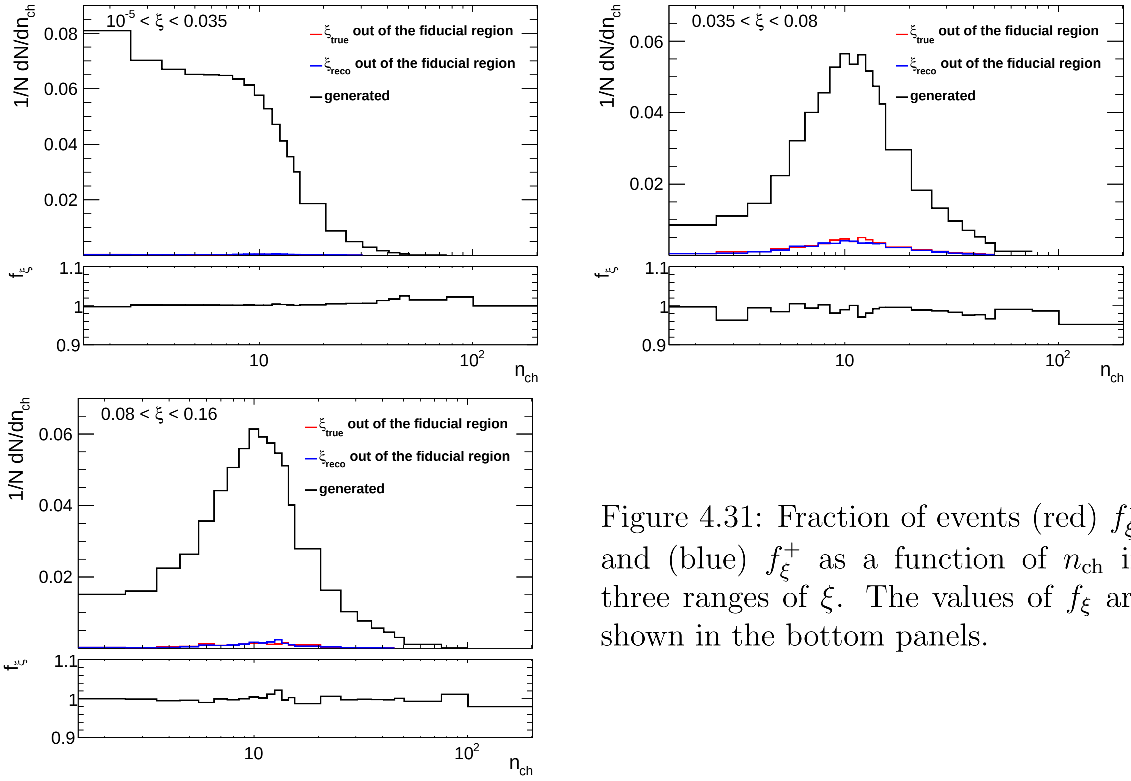

Figure 4.31: Fraction of events (red) f_ξ^- and (blue) f_ξ^+ as a function of n_{ch} in three ranges of ξ. The values of f_ξ are shown in the bottom panels.

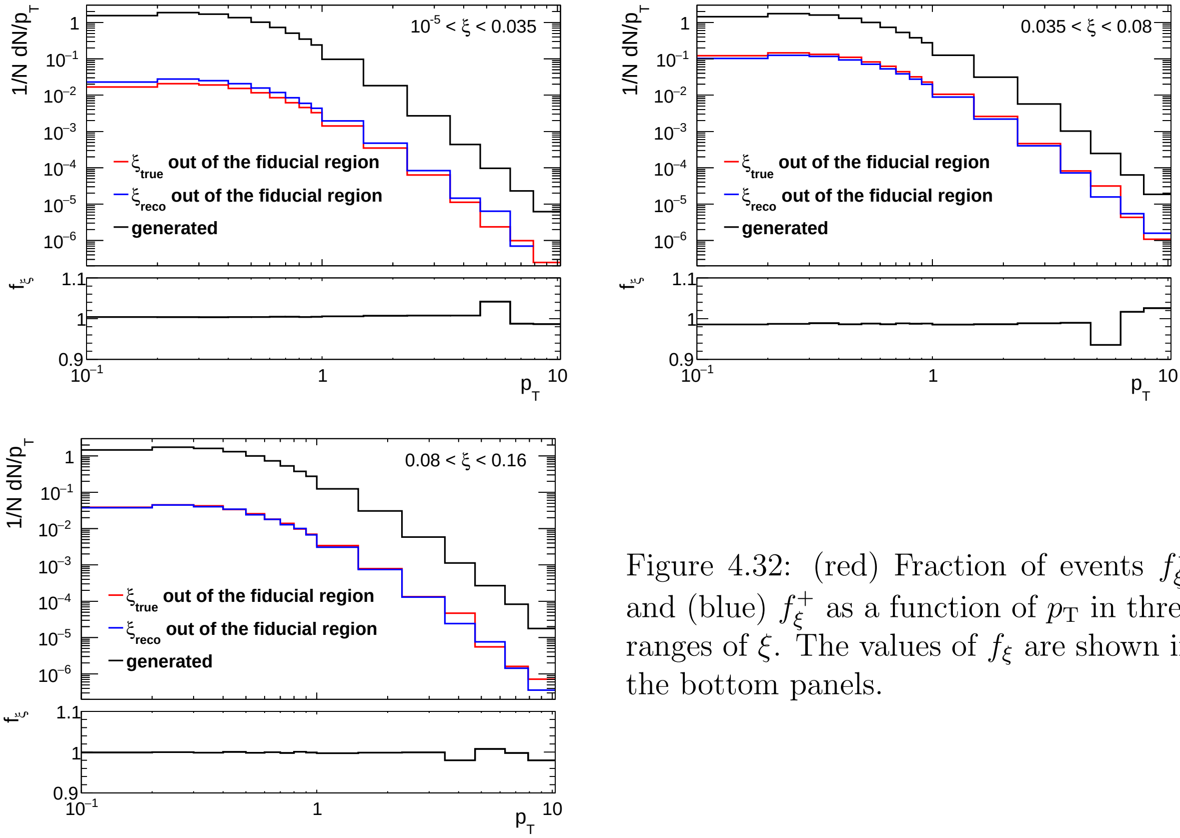

Figure 4.32: (red) Fraction of events f_ξ^- and (blue) f_ξ^+ as a function of p_T in three ranges of ξ. The values of f_ξ are shown in the bottom panels.

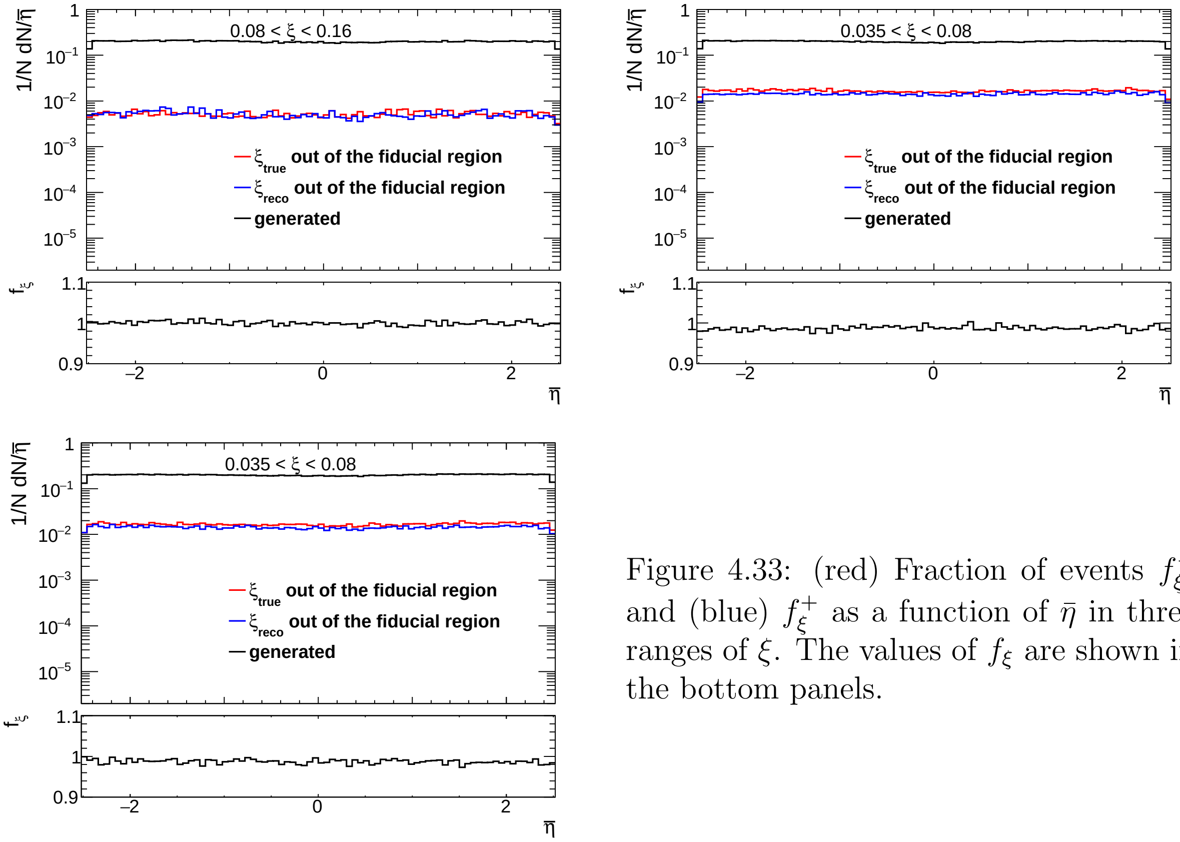

Figure 4.33: (red) Fraction of events f_ξ^- and (blue) f_ξ^+ as a function of $\bar{\eta}$ in three ranges of ξ. The values of f_ξ are shown in the bottom panels.

4.7 Event Corrections and Unfolding Procedure

In this section, the corrections applied to the measured distributions are described. First, the accidental, and non-SD (if applicable) backgrounds were subtracted from the uncorrected distributions, i.e. the inclusive distributions of charged particles and particle to antiparticle (pion, kaon, proton and their antiparticle) multiplicity ratios. Next, the data was corrected for detector inefficiencies by applying:

- event-by-event weights reflecting trigger and vertex reconstruction efficiencies:

  $$w_{\mathrm{ev}}\left(n_{\mathrm{sel}}^{\text{no-z}}, n_{\mathrm{MBTS}}\right) = \frac{1}{\epsilon_{\mathrm{vrt}}\left(n_{\mathrm{sel}}^{\text{no-z}}\right)} \cdot \frac{1}{\epsilon_{\mathrm{trg}}\left(n_{\mathrm{MBTS}}\right)} \tag{4.13}$$

  where $\epsilon_{\mathrm{trg}}\left(n_{\mathrm{MBTS}}\right)$ and $\epsilon_{\mathrm{vrt}}\left(n_{\mathrm{sel}}^{\text{no-z}}\right)$ are the trigger and the vertex reconstruction efficiencies, respectively.

- track-by-track weights related to the track reconstruction efficiency, track backgrounds from non-primary tracks and migrations of tracks into the fiducial region:

  $$w_{\mathrm{trk}}\left(p_{\mathrm{T}}, \eta\right) = \frac{1 - f_{\mathrm{bkg}}\left(p_{\mathrm{T}}, \eta\right) - f_{\mathrm{fake}}\left(p_{\mathrm{T}}, \eta\right) - f_{\mathrm{okr}}\left(p_{\mathrm{T}}, \eta\right)}{\epsilon_{\mathrm{trk}}\left(p_{\mathrm{T}}, \eta\right)} \tag{4.14}$$

  where $\epsilon_{\mathrm{trk}}\left(p_{\mathrm{T}}, \eta\right)$ is the track reconstruction efficiency, $f_{\mathrm{bkg}}\left(p_{\mathrm{T}}, \eta\right)$, $f_{\mathrm{fake}}\left(p_{\mathrm{T}}, \eta\right)$ and $f_{\mathrm{okr}}\left(p_{\mathrm{T}}, \eta\right)$ are the fractions of background, fake and outside of the kinematical range tracks, respectively.

- event-by-event (for n_{ch} distribution) or track-by-track (for p_{T} and $\bar{\eta}$ distributions) weights, f_{ξ}, due to migrations of events between three ξ regions.

Additionally, the obtained distributions were corrected for offline MBTS efficiency, $\epsilon_{\mathrm{MBTS}}^{\mathrm{offline}}$, using the following weight:

$$w_{\mathrm{MBTS}}^{\mathrm{offline}} = \frac{1}{\epsilon_{\mathrm{MBTS}}^{\mathrm{offline}}} \tag{4.15}$$

In the following sections the correction procedure for each of the measured distributions is presented separately. The uncorrected distributions in a wider range are shown in Fig. 4.16.

Apart from the measurements of charged particle distributions, the shapes of ξ and $|t|$ distributions were also obtained. The results were only corrected for MBTS trigger efficiency and ALFA acceptance (described in Sec. 4.2). Since this measurement was not considered as the main aim of this thesis, no systematics was obtained for these distributions.

Correction to dN/dn$_{\mathrm{sel}}$

After the subtraction of accidental and non-SD backgrounds (if applicable), and applying the $w_{\mathrm{ev}}\left(n_{\mathrm{sel}}^{\text{no-z}}, n_{\mathrm{MBTS}}\right)$ weights to the distribution of n_{sel}, the procedure based on

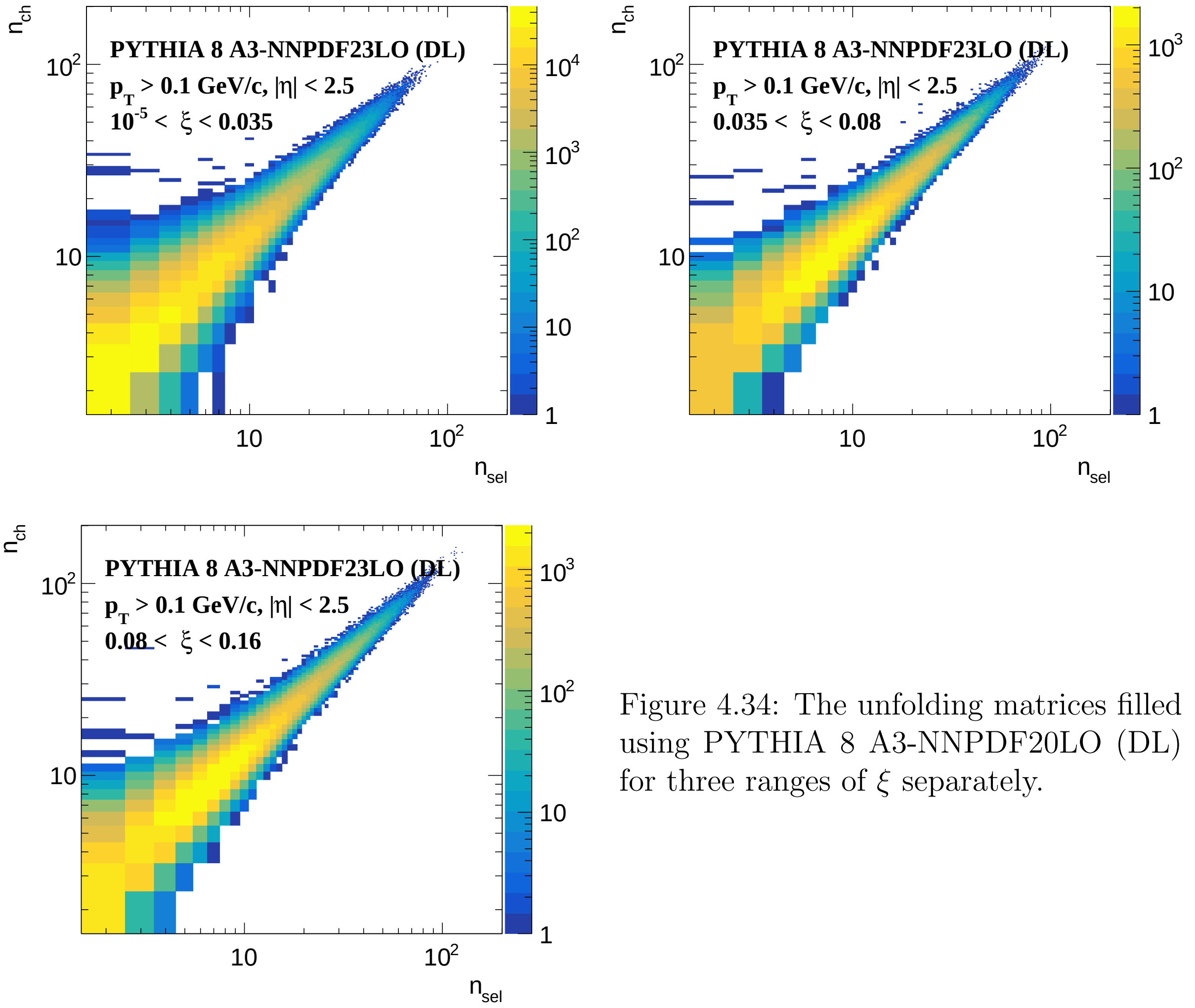

Figure 4.34: The unfolding matrices filled using PYTHIA 8 A3-NNPDF20LO (DL) for three ranges of ξ separately.

the Bayesian unfolding was used to express the multiplicity distribution in terms of the number of charged particles n_{ch}. Changes, in comparison to the STAR analysis (Sec. 3.9), are only needed to the $\epsilon_r\left(n_{\mathrm{ch}}\right)$ and $\epsilon_m\left(n_{\mathrm{ch}}\right)$ factors. The former was not necessary, since in this analysis there was no upper limit on n_{ch} in the fiducial region definition.

The applied correction for events, which are lost due to tracking inefficiencies, i.e. $n_{\mathrm{sel}} < 2$, but have $n_{\mathrm{ch}} \geq 2$, is given as follows [17]:

$$\epsilon_m\left(n_{\mathrm{ch}}\right) = 1 - \left(1 - \epsilon_{\mathrm{trk}}^m\right)^{n_{\mathrm{ch}}} - n_{\mathrm{ch}} \cdot \epsilon_{\mathrm{trk}}^m \cdot \left(1 - \epsilon_{\mathrm{trk}}^m\right)^{n_{\mathrm{ch}}-1} \tag{4.16}$$

where the $\epsilon_{\mathrm{trk}}^m$ is the mean track reconstruction efficiency in the first n_{sel} bin and is equal to about 0.71 in ATLAS.

The unfolding matrices $P\left(n_{\mathrm{ch}}|n_{\mathrm{sel}}\right)$ for each ξ region, which were obtained from PYTHIA 8 A3-NNPDF20LO (DL) and used in the first iteration of the unfolding procedure, are shown Fig. 4.34. The unfolding matrices for the analysis of only SD events were calculated separately.

The dN/dn_{ch} distribution, obtained after the unfolding procedure, was corrected for offline MBTS efficiency, through $w_{\mathrm{MBTS}}^{\mathrm{offline}}$ weights, and migrations of events between ξ ranges, through $f_{\xi}\left(n_{\mathrm{ch}}\right)$ weights. Since the unfolding matrices contain track reconstruction efficiencies, track backgrounds and migrations of tracks into the fiducial region, the weight $w_{\mathrm{trk}}\left(p_{\mathrm{T}}, \eta\right)$ was not used. The total number of events, $N_{\mathrm{ev}} = N$, was calculated as the integral of the unfolded n_{ch} distribution.

Correction to Pseudorapidity Distribution

First, the accidental and non-SD backgrounds (if applicable) were subtracted. Next, the tracks were corrected for detector effects by applying the $w_{\mathrm{ev}}\left(n_{\mathrm{sel}}^{\text{no-z}}, n_{\mathrm{MBTS}}\right)$, $w_{\mathrm{trk}}\left(\eta, p_{\mathrm{T}}\right)$, $w_{\mathrm{MBTS}}^{\mathrm{offline}}$ and $f_{\xi}\left(\bar{\eta}\right)$ weights. The unfolding procedure was unnecessary in this case because the η resolution is significantly smaller than bin widths. The corrected $\bar{\eta}$ distributions were normalized by the number of events N_{ev} in order to obtain the charged particle multiplicity distributions. In addition, the distributions were normalized to unity, hence, it was possible to compare only their shapes with the MC predictions. Moreover, the mean $\bar{\eta}$ in an event, $\langle\bar{\eta}\rangle$, was obtained from the measured distributions.

Correction to Transverse Momentum Distribution

After the subtraction of accidental and non-SD (if applicable) backgrounds, the tracks were corrected for detector effects by applying the $w_{\mathrm{ev}}\left(n_{\mathrm{sel}}^{\text{no-z}}, n_{\mathrm{MBTS}}\right)$ and $w_{\mathrm{trk}}\left(\eta, p_{\mathrm{T}}\right)$ weights. Then, the obtained distributions were used as an input to the Bayesian unfolding procedure, which was similar to the one used for the n_{ch} distribution. The unfolding matrices contain the relationship between the reconstructed track p_{T} and the p_{T} of primary particles. By this, the resolution and migration effects were included in the correction procedure. The distributions, obtained after the unfolding procedure, were further corrected for offline MBTS efficiency, through $w_{\mathrm{MBTS}}^{\mathrm{offline}}$ weights, and migrations of events between ξ ranges, through $f_{\xi}\left(p_{\mathrm{T}}\right)$ weights. Finally, the distributions were normalized either to the number of events, N_{ev}, or to the number of particles. In addition, the mean transverse momentum in an event, $\langle p_{\mathrm{T}}\rangle$, was obtained from the measured distributions.

Figure 4.35 shows the p_{T} unfolding matrices for three ranges of ξ, which were obtained from PYTHIA 8 A3-NNPDF20LO (DL). The unfolding matrices for the analysis of only SD events were calculated separately.

Correction to Mean Transverse Momentum Distribution

The $\langle p_{\mathrm{T}}\rangle$ vs. n_{ch} was defined by $\left(\sum_i p_{\mathrm{T}}(i)\right) / \left(\sum_i 1\right)$ as a function of n_{ch} [21, 22], where i runs over all particles within a given n_{ch} category. In the correction procedure, first the $\sum_i p_{\mathrm{T}}(i)$ and $\sum_i 1$ as a function of n_{sel} were corrected for the accidental and non-SD (if applicable) backgrounds. Then, the $w_{\mathrm{ev}}\left(n_{\mathrm{sel}}^{\text{no-z}}, n_{\mathrm{MBTS}}\right)$ and $w_{\mathrm{trk}}\left(p_{\mathrm{T}}, \eta\right)$ weights were applied to correct the number of selected tracks in the p_{T} and n_{sel} bin to the number of charged

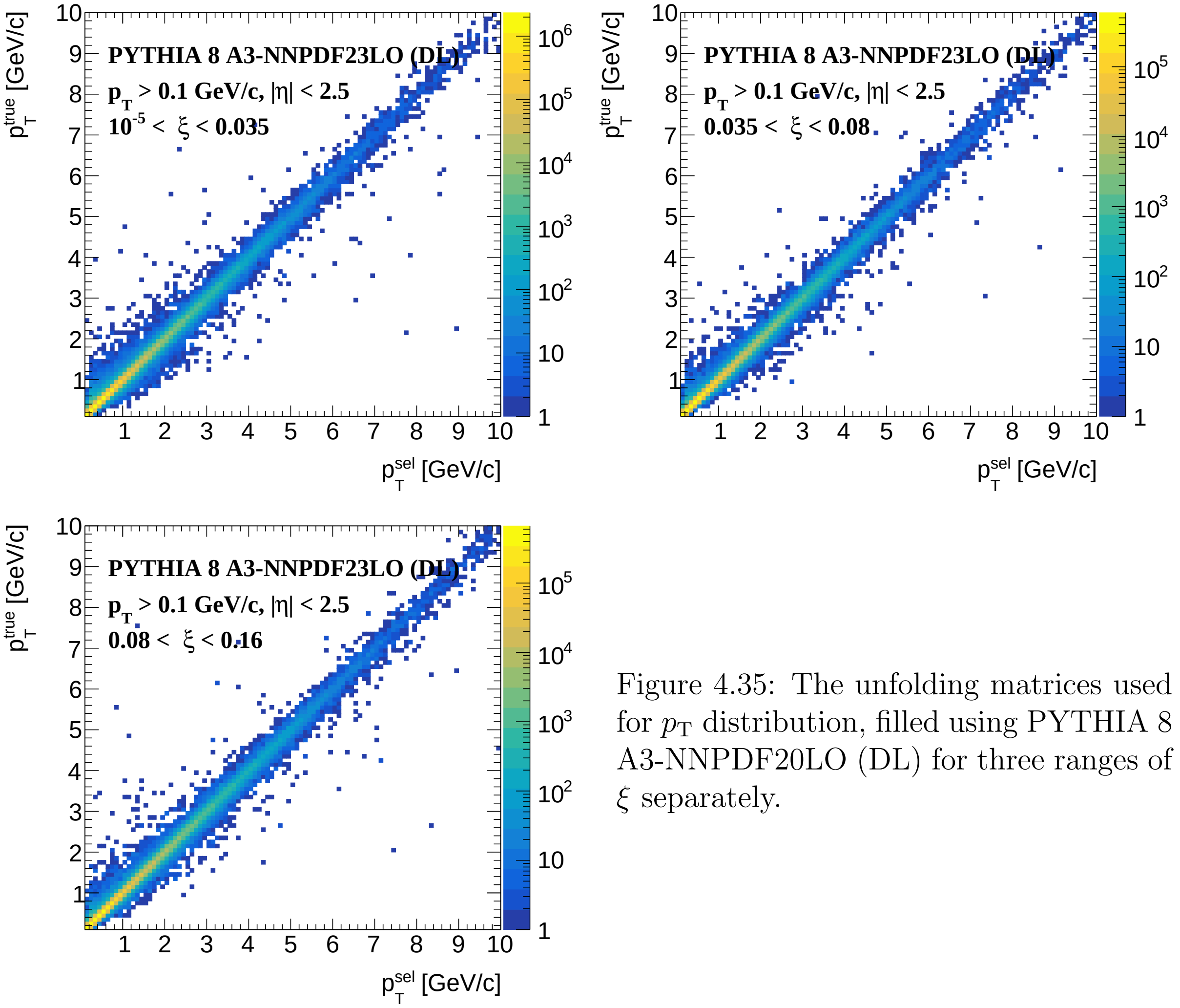

Figure 4.35: The unfolding matrices used for p_{T} distribution, filled using PYTHIA 8 A3-NNPDF20LO (DL) for three ranges of ξ separately.

particles in that bin. As a result the following distributions were obtained:

$$N^{n_{\mathrm{ch}}}\left(n_{\mathrm{sel}}\right) = N_{\mathrm{ev}} \int dp_{\mathrm{T}} \cdot P\left(n_{\mathrm{sel}}\right) \cdot \rho_{\mathrm{sel}}\left(p_{\mathrm{T}}|n_{\mathrm{sel}}\right) \cdot w_{ev}\left(n_{\mathrm{sel}}^{\text{no-z}}, n_{\mathrm{MBTS}}\right) \cdot w_{\mathrm{trk}}\left(p_{\mathrm{T}}, \eta\right) \cdot p_{\mathrm{T}} \quad (4.17)$$

$$D^{n_{\mathrm{ch}}}\left(n_{\mathrm{sel}}\right) = N_{\mathrm{ev}} \int dp_{\mathrm{T}} \cdot P\left(n_{\mathrm{sel}}\right) \cdot \rho_{\mathrm{sel}}\left(p_{\mathrm{T}}|n_{\mathrm{sel}}\right) \cdot w_{\mathrm{ev}}\left(n_{\mathrm{sel}}^{\text{no-z}}, n_{\mathrm{MBTS}}\right) \cdot w_{\mathrm{trk}}\left(p_{\mathrm{T}}, \eta\right) \quad (4.18)$$

where $N^{n_{\mathrm{ch}}}\left(n_{\mathrm{sel}}\right)$ and $D^{n_{\mathrm{ch}}}\left(n_{\mathrm{sel}}\right)$ are corrected distributions of $\sum_i p_{\mathrm{T}}\left(i\right)$ and $\sum_i 1$ as a function of n_{sel}, $\rho_{\mathrm{sel}}\left(p_{\mathrm{T}}|n_{\mathrm{sel}}\right)$ is the density of tracks (defined as the number of tracks per event per unit of p_{T} in a given n_{sel} bin), $P(n_{\mathrm{sel}})$ is the probability of observing n_{sel} tracks.

Using the unfolding matrices, determined in the final unfolding iteration of the n_{ch}

distributions (Sec. 4.7), the two above distributions were expressed as a function of n_{ch}:

$$N\left(n_{\mathrm{ch}}\right)=\int dp_{\mathrm{T}}\cdot\rho_{\mathrm{ch}}\left(p_{\mathrm{T}}|n_{\mathrm{ch}}\right)\cdot p_{\mathrm{T}} \tag{4.19}$$

$$D\left(n_{\mathrm{ch}}\right)=\int dp_{\mathrm{T}}\cdot\rho_{\mathrm{ch}}\left(p_{\mathrm{T}}|n_{\mathrm{ch}}\right) \tag{4.20}$$

$$\rho_{\mathrm{ch}}\left(p_{\mathrm{T}}|n_{\mathrm{ch}}\right)=\sum_{n_{\mathrm{sel}}=2}P\left(n_{\mathrm{sel}}\right)\cdot P\left(n_{\mathrm{ch}}|n_{\mathrm{sel}}\right)\cdot\rho_{\mathrm{ch}}\left(p_{\mathrm{T}}|n_{\mathrm{sel}}\right) \tag{4.21}$$

where $\rho_{\mathrm{ch}}\left(p_{\mathrm{T}}|n_{\mathrm{sel}}\right)$ is the number of charged particles per event per unit of p_{T} in a given n_{sel} bin, $P\left(n_{\mathrm{ch}}|n_{\mathrm{sel}}\right)$ is the probability of n_{ch} under condition of n_{sel}.

The distributions, obtained after the unfolding procedure, $N\left(n_{\mathrm{ch}}\right)$ and $D\left(n_{\mathrm{ch}}\right)$, were corrected for offline MBTS efficiency, through $w_{\mathrm{MBTS}}^{\mathrm{offline}}$ weights, and migrations of events between ξ ranges, through f_{ξ} weights.

Finally, the $\langle p_{\mathrm{T}}\rangle$ as a function of n_{ch} was calculated as a ratio of $N\left(n_{\mathrm{ch}}\right)$ and $D\left(n_{\mathrm{ch}}\right)$:

$$\langle p_{\mathrm{T}}\rangle\left(n_{\mathrm{ch}}\right)=\frac{N\left(n_{\mathrm{ch}}\right)}{D\left(n_{\mathrm{ch}}\right)}=\frac{\int dp_{\mathrm{T}}\cdot\rho_{\mathrm{ch}}\left(p_{\mathrm{T}}|n_{\mathrm{ch}}\right)\cdot p_{\mathrm{T}}}{\int dp_{\mathrm{T}}\cdot\rho_{\mathrm{ch}}\left(p_{\mathrm{T}}|n_{\mathrm{ch}}\right)} \tag{4.22}$$

In the above procedure there were two assumptions:

1. The correction weights, $w_{\mathrm{ev}}\left(n_{\mathrm{sel}}^{\text{no-z}},n_{\mathrm{MBTS}}\right)$ and $w_{\mathrm{trk}}\left(p_{\mathrm{T}},\eta\right)$, were used to transform the number of selected tracks in a given $\left(n_{\mathrm{sel}},p_{\mathrm{T}}\right)$ bin to the number of particles in the same bin:

   $$\rho_{\mathrm{ch}}\left(p_{\mathrm{T}}|n_{\mathrm{sel}}\right)=\rho_{\mathrm{sel}}\left(p_{\mathrm{T}}|n_{\mathrm{sel}}\right)\cdot w_{\mathrm{ev}}\left(n_{\mathrm{sel}}^{\text{no-z}},n_{\mathrm{MBTS}}\right)\cdot w_{\mathrm{trk}}\left(p_{\mathrm{T}},\eta\right) \tag{4.23}$$

   However, this procedure may not be valid because track reconstruction efficiency may slightly depend on the n_{sel}. The three-dimensional track reconstruction efficiencies, calculated as a function of p_{T}, η and n_{sel}, would be needed to check this assumption.

2. The p_{T} of the tracks was not expected to be changed when migrating from a given n_{sel} bin to the corresponding n_{ch} bin. The full two-dimensional unfolding of p_{T} and n_{ch} would be needed to check this assumption.

However, any deviations from the above assumptions were covered by the non-closure of the corrected MC distributions and were taken as a systematic uncertainty.

Closure Tests

In order to validate the correction procedures, closure tests were performed, i.e. full correction procedure was applied to the MC detector-level distributions and the results were directly compared to the true-level distributions. Figure 4.36 shows closure tests of multiplicity, transverse momentum, pseudorapidity and $\langle p_{\mathrm{T}}\rangle(n_{\mathrm{ch}})$ distributions for three ranges of ξ, separately. PYTHIA 8 A3-NNPDF20LO (DL) was used as an input. In order to compare corrected and true-level distributions, the statistical uncertainties of the true-level distributions were assumed to be 0. The difference between true-level and corrected distributions was taken as a systematic uncertainties.

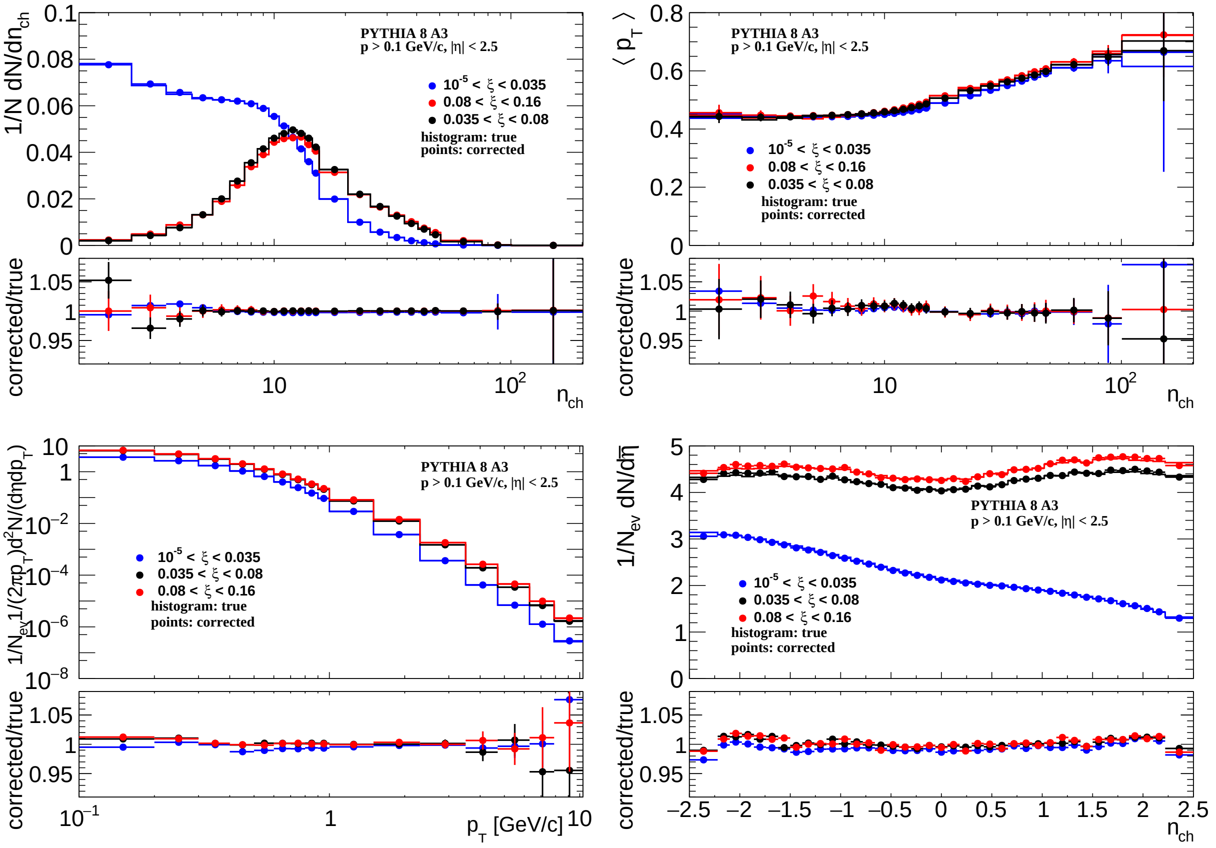

Figure 4.36: Closure tests of (top left) multiplicity, (top right) mean transverse momentum as a function of multiplicity, (bottom left) transverse momentum and (bottom right) pseudorapidity distributions for three ranges of ξ using PYTHIA 8 A3-NNPDF20LO (DL). The ratios of corrected to true-level distributions are shown in the bottom panels.

Particle Identification

In this section the particle identification via the dE/dx measured by the Pixel detector (including IBL) is described. The specific energy loss dE/dx is a function of the particle momentum magnitude. The dE/dx distribution within given p_T bin is additionally smeared because of the momentum variation with rapidity. Therefore, the analysis of identified particles was limited to a very narrow pseudorapidity region of $|\eta| < 0.5$, in which different particle species are well separated. This is important for this analysis due to generally poor dE/dx resolution of the ATLAS detector.

The procedure used for the particle identification follows the steps described in [209, 210]. The Bethe-Bloch inspired parametric function describing the MPV of the dE/dx as a function of $\beta\gamma$ is given by:

$$\mathrm{MPV}_{dE/dx}\left(\beta\gamma\right) = \frac{p_1}{\left(f\left(\beta\gamma\right)\right)^{p_3}} \ln\left(1 + \left(p_2\beta\gamma\right)^{p_5}\right) - p_4 \tag{4.24}$$

$$f\left(\beta\gamma\right)=\frac{\left(\beta\gamma\right)^{2}}{1+\left(\beta\gamma\right)^{2}} \tag{4.25}$$

where $\beta\gamma = p/m$, p is the momentum magnitude of the measured particle, i.e. pion, kaon or proton, m is its mass, $p_1 - p_5$ are free parameters that does not rely on any prior knowledge of the particle species.

The data sample of reconstructed tracks with $0.3 < p_{\mathrm{T}} < 1.0$ GeV/c was divided into 10 transverse momentum slices, which are equal in $\ln\left(p_{\mathrm{T}}\right)$. To extract the particle yield for a given particle type, the dE/dx distribution for each of the three input mass hypotheses (π, K, p) in each of the above transverse momentum slices was described by the ExpGausExp function [238] (consisting of the Gaussian core and exponential tails on both sides of the Gaussian). In the other ATLAS analyses [209, 210], a Crystal Ball function [239, 240] was used to model the dE/dx distribution in each $\ln\left(p_{\mathrm{T}}\right)$ bin. However, it was found during this analysis that better fit quality and stability is achieved with the ExpGausExp function. The ExpGausExp function is defined as:

$$f\left(m;k_L,k_H\right)=\begin{cases}\exp\left[\frac{k_L^2}{2}+k_L m\right], & \text{for } m\leq -k_L\\ \exp\left[-\frac{1}{2}m^2\right], & \text{for } -k_L< m\leq k_H\\ \exp\left[\frac{k_H^2}{2}-k_H m\right], & \text{for } k_H< m\end{cases} \tag{4.26}$$

$$m\left(\ln\left(dE/dx\right);\mathrm{MPV}_{dE/dx}\left(\beta\gamma\right),\sigma\right)=\left(\ln\left(dE/dx\right)-\ln\left(\mathrm{MPV}_{dE/dx}\left(\beta\gamma\right)\right)\right)/\sigma \tag{4.27}$$

where σ is the standard deviation of the Gaussian core, k_L and k_H are the decay constants of the exponentials on the low and high side tails.

All of the logarithmic p_{T} slices were fitted simultaneously with a sum of three ExpGausExp functions. The MPV of the dE/dx had to follow the parametrization given by Eq. (4.24) with the transverse momentum corrected for the energy loss effects (as described in Sec. 4.5). The relative fraction n_i^j of each particle, $i = \pi$, K, p, in each interval j of $\ln\left(p_{\mathrm{T}}\right)$, was left free in the fit. Hence there were $5+3+2\cdot 10$ free parameters in the fit, i.e. $p_1 - p_5$, σ, k_L, k_H and n_π^j, n_K^j in 10 $\ln\left(p_{\mathrm{T}}\right)$ slices (the fraction of (anti)protons was defined as $n_p^j = 1 - n_\pi^j - n_K^j$). The results depend slightly on the charge of analysed tracks and the number of hits used for dE/dx calculation (so-called good dE/dx hits). Hence, the fit was done separately for 6 cases: negative and positive tracks, having 2, 3 or more than 3 good dE/dx hits used for dE/dx calculation.

Figure 4.37 shows the distribution of dE/dx as a function of the rigidity $q \times p$, together with the fitted MPV of dE/dx for each particle species, for tracks having 3 good dE/dx hits (most of tracks has 3 hits used for the dE/dx calculation, what is shown in the distribution presented in the same figure).

Figures 4.38 and 4.39 show sample dE/dx fit (positive tracks with three good dE/dx hits) in a few $\ln\left(p_{\mathrm{T}}\right)$ slices, as well as the $\mathrm{MPV}_{dE/dx}\left(\beta\gamma\right)$ for pions, kaons and protons.

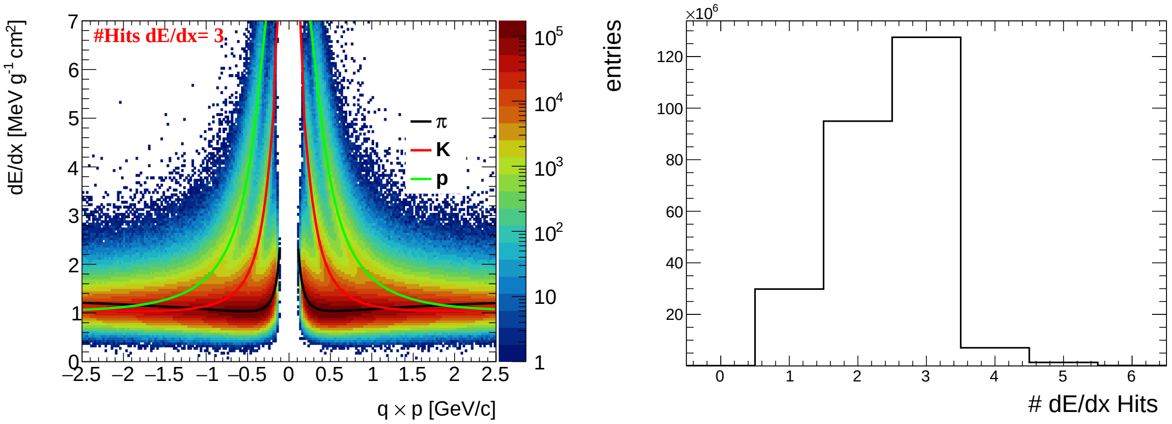

Figure 4.37: (left) Specific energy loss dE/dx as a function of rigidity $q \times p$ and (right) number of hits used in the dE/dx calculation for particles in $|\eta| < 0.5$. The fitted MPV of dE/dx for each particle species are also shown.

Antiparticle-to-Particle Ratios

The following steps were performed to correct an identified antiparticle to particle (pion, kaon, proton and their antiparticle) multiplicity ratios as a function of p_{T} (the ratios were averaged over three ranges of ξ due to the limited statistics):

- The raw particle yields were obtained through fits to the dE/dx distributions (described in Sec. 4.7), where the trigger and vertex reconstruction efficiencies were applied.
- The dE/dx fits were performed separately for tracks having 2, 3 or more than 3 good dE/dx hits. The results from these three fits were added up in this step.
- The p_{T} distributions for each particle species were shifted by the size of energy loss correction.
- The accidental backgrounds were not subtracted. It was assumed that they do not depend on the particle type.
- The particle p_{T} spectra were corrected for track reconstruction efficiencies. Also, the backgrounds from non-primary tracks were subtracted. Since fake track contribution is the same for particle and antiparticle, it was not subtracted. The ratio of particle to antiparticle corrections is shown in Fig. 4.40.
- Each antiparticle p_{T} distribution was divided by the corresponding particle p_{T} distribution in order to obtain fully corrected identified antiparticle to particle multiplicity ratios.

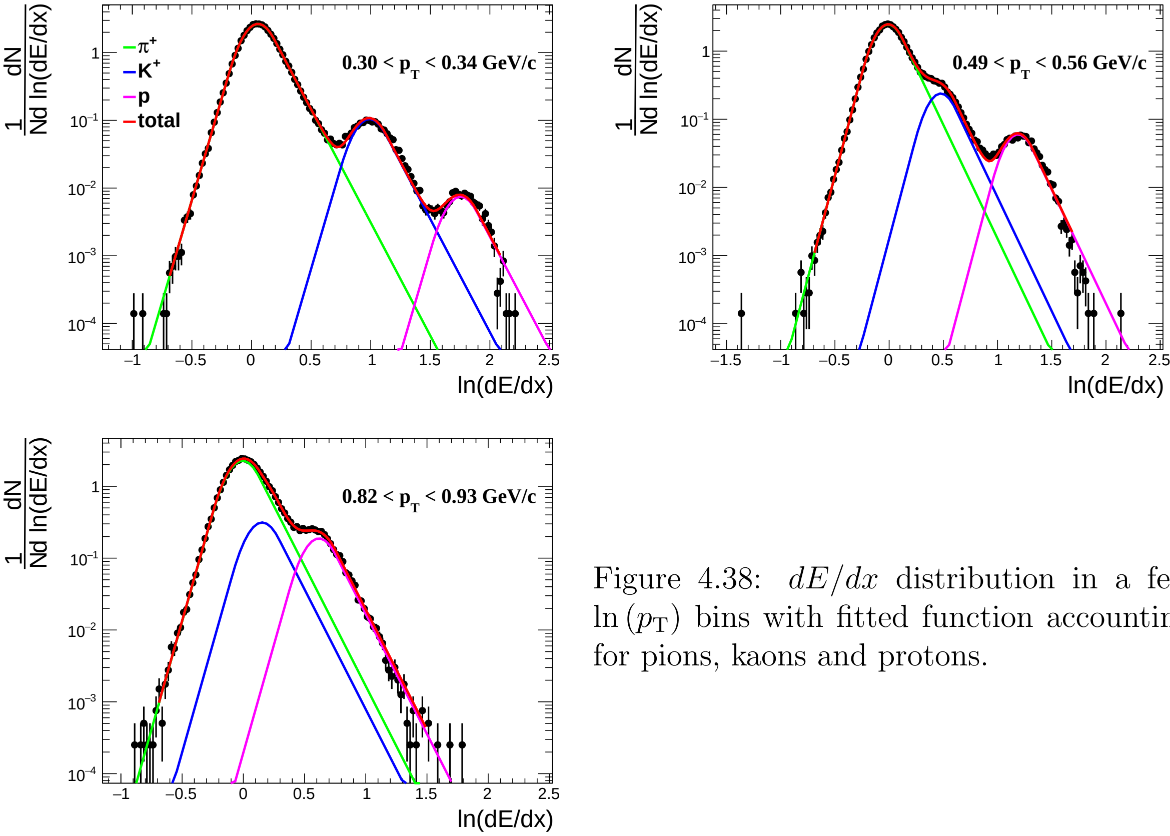

Figure 4.38: dE/dx distribution in a few $\ln(p_{\mathrm{T}})$ bins with fitted function accounting for pions, kaons and protons.

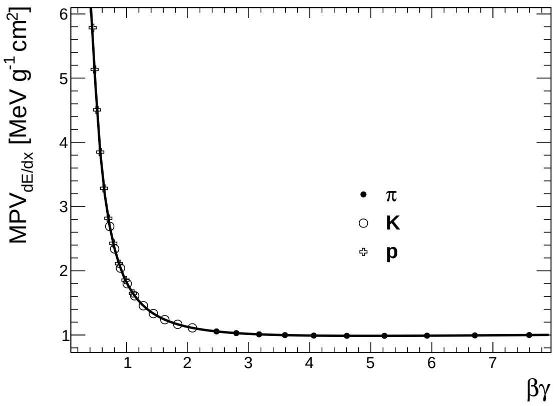

Figure 4.39: Fitted $\mathrm{MPV}_{dE/dx}(\beta\gamma)$ for π^+, K^+ and p, obtained from tracks with 3 good dE/dx hits.

4.8 Systematic Uncertainties

The systematics uncertainties were handled by modifying either the input distributions or the unfolding matrix. Next, the differences between standard and changed bins of the distributions were calculated.

Some of the systematic uncertainties on $1/N\ dN/dn_{\mathrm{ch}}$ due to the track reconstruction efficiency were propagated by using a random number from the uniform distribution. If this number is smaller than the absolute value of systematic uncertainty, then n_{sel} was increased or decreased, depending on the sign of systematic uncertainty. Events with $n_{\mathrm{sel}} = 0, 1$ do

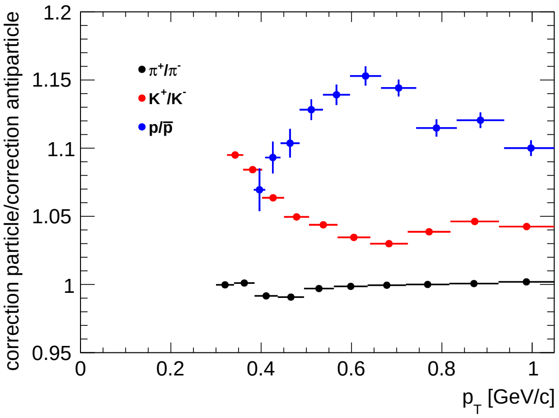

Figure 4.40: Ratio of particle to anti-particle corrections.

not pass the selection criteria, thus, the systematic uncertainty would be underestimated for low multiplicities without any symmetrization. Therefore, the systematic uncertainty for $n_{\mathrm{ch}} < 5$ due to the increase of the track reconstruction efficiency was symmetrized and taken also for the decrease of the track reconstruction efficiency, but with an opposite sign.

The following sources of systematic uncertainties were considered:

- the effect of modified unfolding matrix (using EPOS unfolding matrix, instead of the one obtained from PYTHIA 8 A3-NNPDF20LO (DL)),
- the effects related to the $f_{\mathrm{okr}}\,(p_T, \eta)$ correction (labelled as OSC, Sec. 4.6),
- the effect of the amount of dead-material on track reconstruction efficiency (Sec. 4.5),
- the effect of the badly measured low-p_{T} tracks (fit probability cut, $\chi^2 < 0.01$, for tracks with $p_{\mathrm{T}} > 10$ GeV/c) on the track reconstruction efficiency (Sec. 4.5),
- the effect of misalignments on the track reconstruction efficiency (high-p_{T} tracks, Sec. 4.5),
- accidental background contribution (Sec. 4.4),
- ND and DD background contributions (if applicable, Sec. 4.4),
- CD contribution (Sec. 4.4),
- variation of the offline MBTS threshold in MC (labelled as MBTS MC, Sec. 4.5),
- the effect of EPOS model on MBTS offline efficiency (Sec. 4.5),
- the effects related to ξ migrations (Sec. 4.6),
- non-closure (Sec. 4.7),
- the $1/N_{\mathrm{ev}}\; dN/d\bar{\eta}$ distribution was calculated separately for events in which forward-scattered proton is on one and the other side of the IP (A-C asymmetry).

All of the above contributions to the total systematic uncertainty were used in the analysis of charged particles without the identification. The distributions of antiparticle-to-particle multiplicity ratios contain only the systematic uncertainty due to the amount of dead material on tracking efficiencies. Other systematic uncertainties are the same for particle and its antiparticle, hence, they cancel out in the antiparticle-to-particle ratios.

Figures 4.41 to 4.44 show the breakdown of all different systematics for charged particle distributions without the identification. The dominant systematic uncertainty, which affects all distributions with $\xi > 0.035$ in the analysis of SD events, is due to the model-dependent subtraction of DD and ND backgrounds. The maximum values of this component vary up to $30 - 40\%$ for $n_{\mathrm{ch}} = 2$ and $0.035 < \xi < 0.16$. In case of the $\bar{\eta}$ distributions, this systematic uncertainty is larger for particles with positive $\bar{\eta}$.

In the main analysis, in which only CD background contributions were subtracted, the dominant systematic uncertainty for p_{T} and n_{ch} distributions is related to differences in MBTS offline efficiency obtained from PYTHIA 8 and EPOS models. It affects mainly high-p_{T} particles, where it is about 7.5% for $10^{-5} < \xi < 0.035$, and low charged particle multiplicities, where it varies up to 30% for $n_{\mathrm{ch}} = 2$ and $0.08 < \xi < 0.016$. In case of $\bar{\eta}$ distributions, the systematic uncertainty on modelling of the MBTS offline efficiency mainly refers to $\langle\bar{\eta}\rangle$, for which it is about $8 - 10\%$ for $0.035 < \xi < 0.16$. The subtraction of CD background introduces an uncertainty of about $5 - 10\%$ for n_{ch} distributions at $0.035 < \xi < 0.16$, and of about 5% for particles with $p_{\mathrm{T}} \lesssim 0.3$ GeV/c and $p_{\mathrm{T}} > 1$ GeV/c at $10^{-5} < \xi < 0.035$. Additionally, the A-C asymmetry in $\bar{\eta}$ distribution is small and affects mainly particles with $|\bar{\eta}| \approx 2.5$, for which it varies up to $2 - 3\%$. Moreover, the systematic uncertainty related to the accidental background contribution is large for all distributions at $10^{-5} < \xi < 0.035$, where it is about 4% for particles with large p_{T} and 10% for $n_{\mathrm{ch}} > 40$. The rest of the components have smaller contribution to the total systematic uncertainty. The largest of them are due to the simulation of dead material and migrations of tracks. The former affects mainly low-p_{T} and $|\bar{\eta}| > 1.5$ particles, where it is equal to about $2 - 3\%$. Migrations of tracks have an effect on charged particles produced at the edge of the fiducial region, where the systematic uncertainty is about 5% for particles with $|\bar{\eta}| \approx 2.5$. The use of a modified unfolding matrix introduces an uncertainty of about $5 - 10\%$ for n_{ch} distributions. The systematic uncertainty on non-closure for n_{ch}, p_{T}, $\bar{\eta}$ distributions is mostly at the level of $1 - 5\%$ which proves the consistency of the correction procedure. However, it reaches $3 - 4\%$ for $\langle p_{\mathrm{T}}\rangle(n_{\mathrm{ch}} = 2)$, mainly because the correction procedure depended upon additional assumptions (described in Sec. 4.7), which are not fulfilled for low charged-particle multiplicities, $n_{\mathrm{ch}} \lesssim 10$. This is one of the largest systematic uncertainties for $\langle p_{\mathrm{T}}\rangle(n_{\mathrm{ch}} \lesssim 10)$, therefore, the correction procedure should be improved in the future analyses. In addition, the systematic uncertainty on non-closure affects particles with $|\bar{\eta}| \approx 2.5$, for which it is about $1 - 3\%$. This uncertainty is due to the fact that the f_{okr} correction was obtained from ND sample (described in Sec. 4.6).

Figure 4.45 shows the systematic uncertainty on tracking efficiency due to the simulation of dead-material for the antiparticle-to-particle multiplicity ratio distributions. This source of systematic uncertainty is equal to about $1 - 2\%$ for $\bar{p}/p$ multiplicity ratio and smaller for other types of particles.

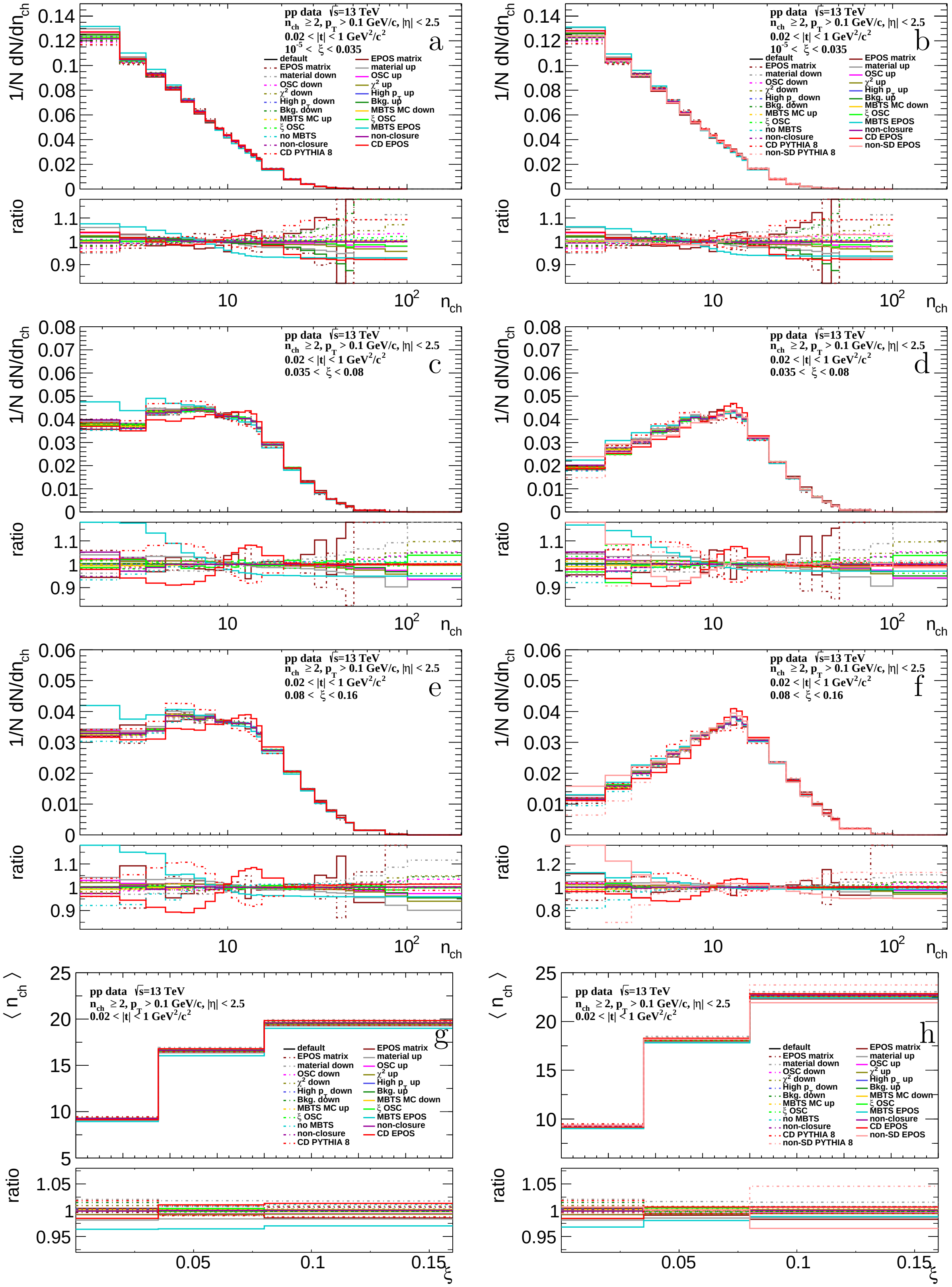

Figure 4.41: Components of the systematic uncertainties (a-f) for the charged particle multiplicity in three ξ regions and (g-h) for the mean charged particle multiplicity. (left) The CD and (right) CD+DD+ND background contributions were subtracted. The ratios to nominal distributions are shown in the bottom panels.

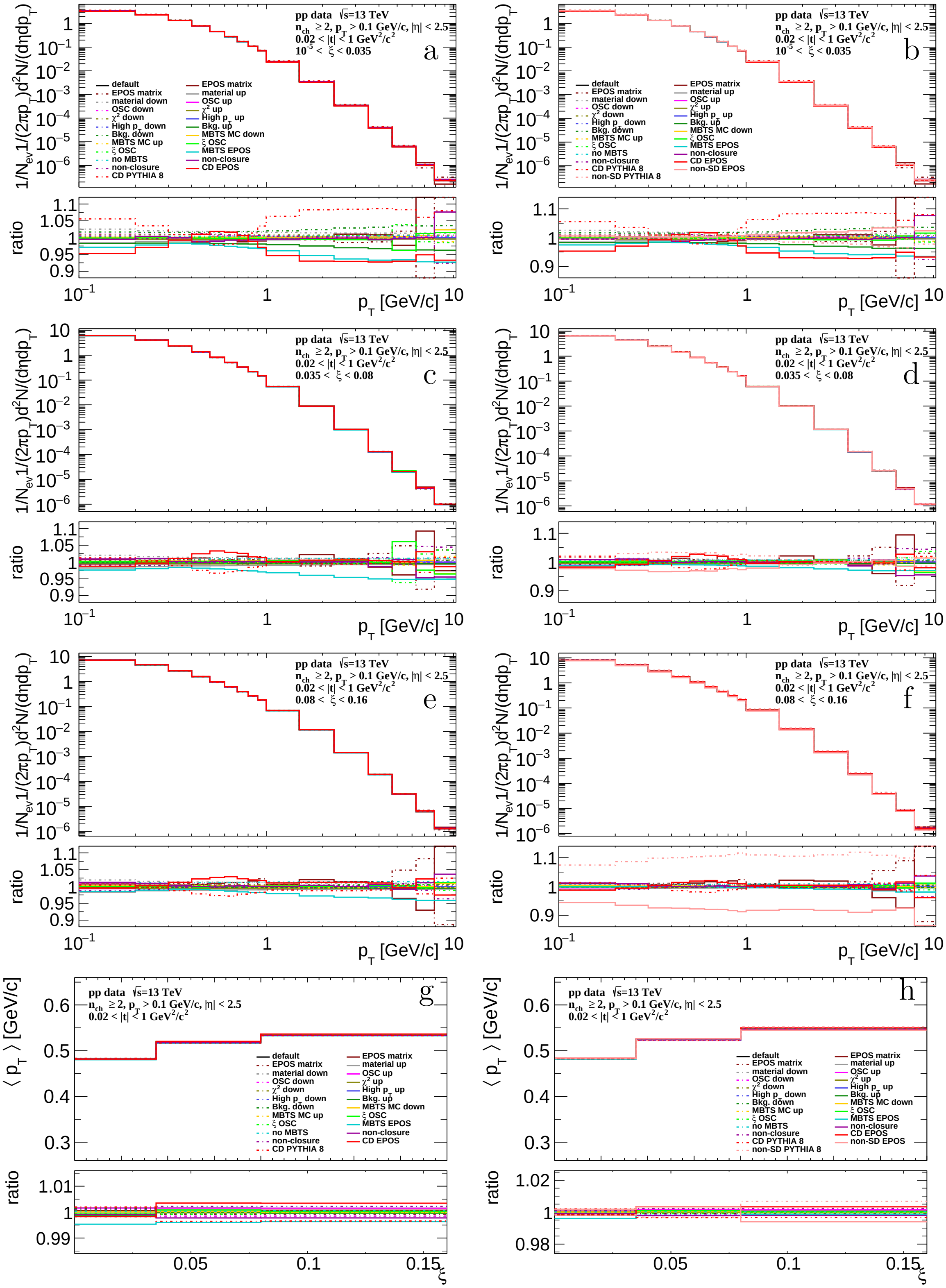

Figure 4.42: Components of the systematic uncertainties (a-f) for p_T distributions in three ξ regions and (g-h) for a mean p_T distribution. (left) The CD and (right) CD+DD+ND background contributions were subtracted. The ratios to nominal distributions are shown in the bottom panels.

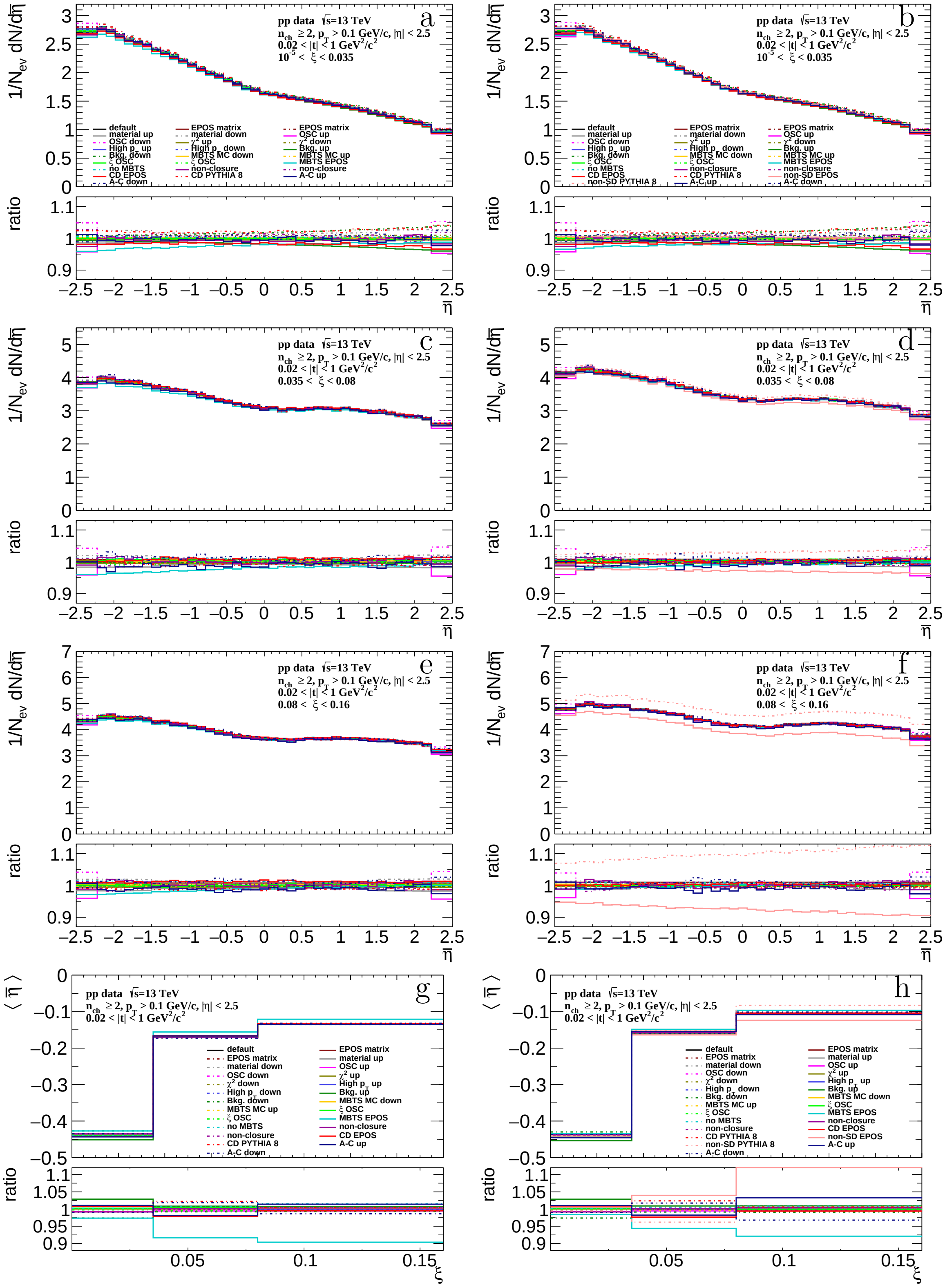

Figure 4.43: Components of the systematic uncertainties (a-f) for $\bar{\eta}$ distributions in three ξ regions and (g-h) for a mean $\bar{\eta}$ distribution. (left) The CD and (right) CD+DD+ND background contributions were subtracted. The ratios to nominal distributions are shown in the bottom panels.

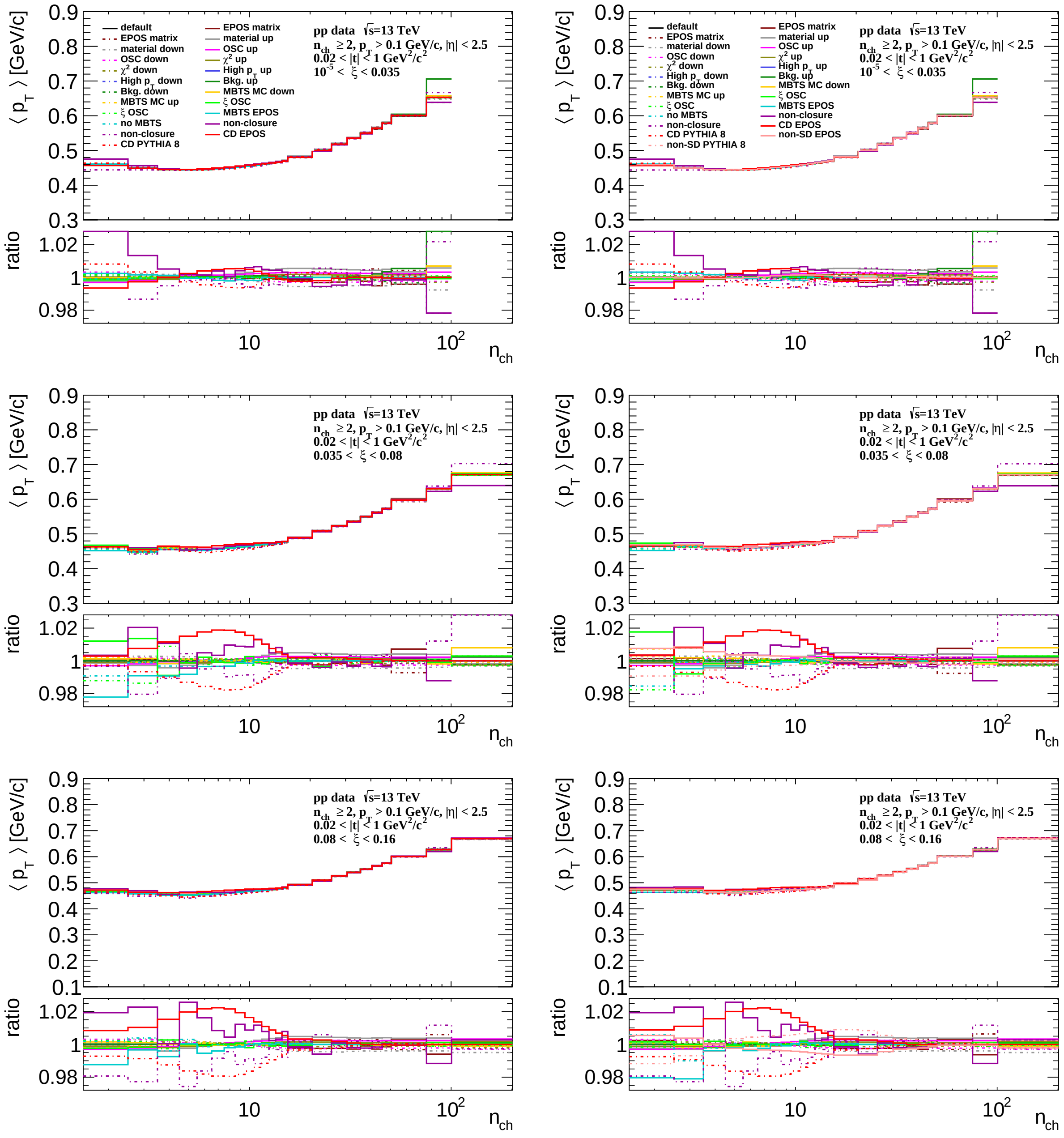

Figure 4.44: Components of the systematic uncertainties for $\langle p_{\mathrm{T}} \rangle$ vs. n_{ch} distributions in three ξ regions. (left) The CD and (right) CD+DD+ND background contributions were subtracted. The ratios to nominal distributions are shown in the bottom panels.

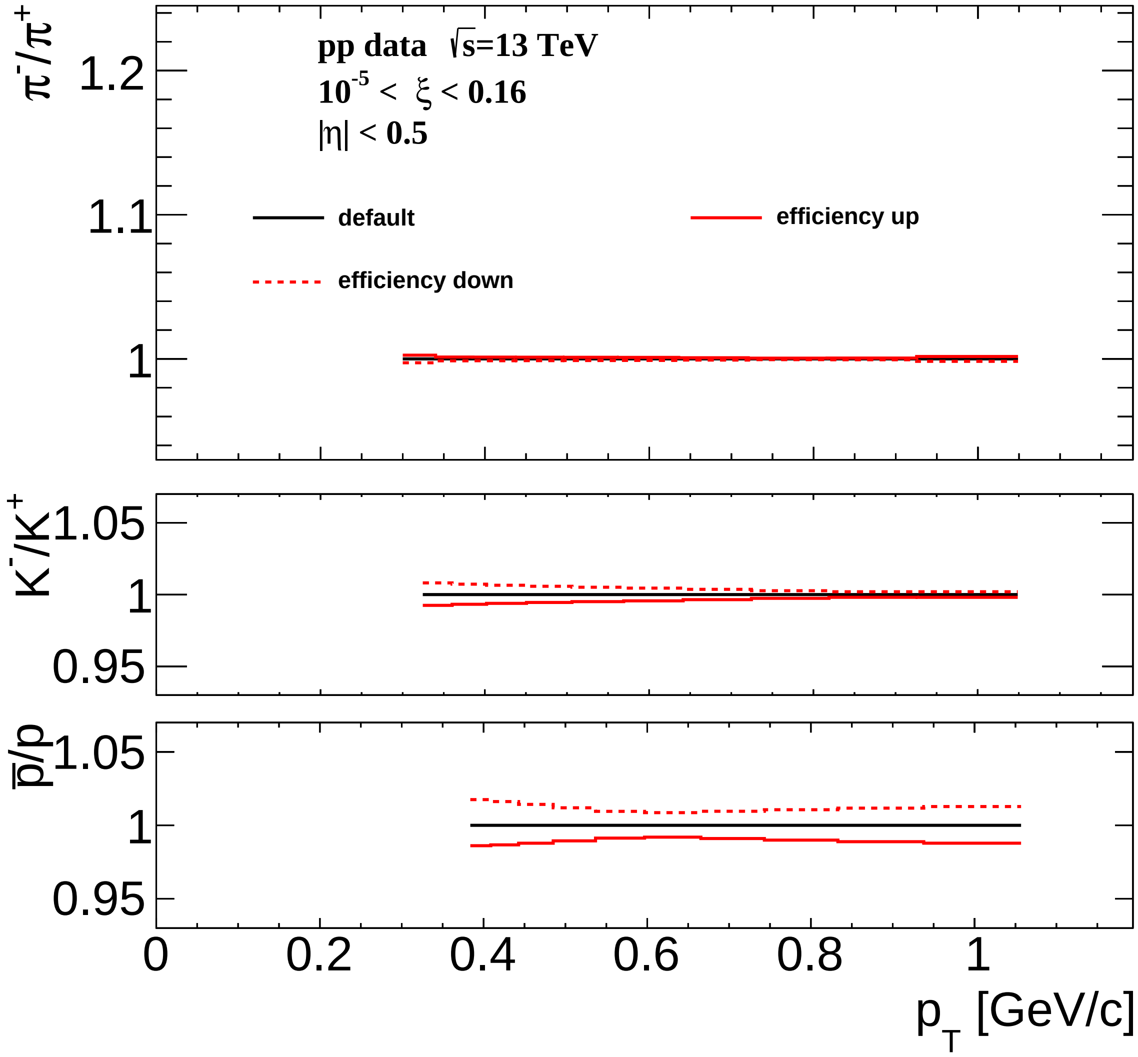

Figure 4.45: The systematic uncertainties on tracking efficiencies due to the simulation of dead-material for π^-/π^+, K^-/K^+ and $\bar{p}/p$ multiplicity ratios.

4.9 Results

In this section, the results on charged-particle distributions measurements with the ATLAS experiment are presented. The distributions, corrected for background and detector effects, are compared with several MC predictions, i.e.

- EPOS
- PYTHIA 8 A3-NNPDF23LO (DL)
- PYTHIA 8 A2-MSTW2008LO (SaS)
- PYTHIA 8 Monash-NNPDF23LO (SaS)
- PYTHIA 8 Monash-NNPDF23LO (DL)
- PYTHIA 8 Monash-NNPDF23LO (MBR)
- QGSJET

In all figures, data are shown as solid points with error bars representing the statistical uncertainties. Gray boxes represent statistical and systematic uncertainties added in quadrature, except the systematic uncertainties due to the DD+ND background subtraction, which are shown separately as yellow boxes. Predictions from MC models are shown as colour histograms. All results are presented separately for three ranges of ξ: $10^{-5} < \xi < 0.01$, $0.01 < \xi < 0.05$, $0.05 < \xi < 0.16$ and for events with CD, and with CD, DD and ND background subtracted. However, distributions for events, for which the DD and ND background was not subtracted, are dominated by SD.

Figure 4.46 shows primary charged-particle multiplicity separately for the three ranges of ξ. Data show expected increase of the $\langle n_{\text{ch}} \rangle$ with ξ due to the larger diffractive masses probed by increasing ξ in SD process. In the range of $0.035 < \xi < 0.16$, the $\langle n_{\text{ch}} \rangle$ is larger for events with DD and ND backgrounds subtracted since these backgrounds affect mainly low multiplicities. The shapes of the measured distributions are not reproduced by all models: PYTHIA 8 predict much larger $\langle n_{\text{ch}} \rangle$ in all three ξ ranges, whereas EPOS and QGSJET predict too small $\langle n_{\text{ch}} \rangle$ but better describe the data than PYTHIA 8 models for $10^{-5} < \xi < 0.08$ and $10^{-5} < \xi < 0.035$, respectively.

Figure 4.47 shows primary charged-particle multiplicities as a function of p_{T} separately for the three ranges of ξ. Shapes of the p_{T} distributions are shown in Fig. 4.49. Additionally, the low-p_{T} regions of the above distributions, $0.1 < p_{\text{T}} < 2.3$ GeV/c, are presented in Figs. 4.48 and 4.50. The lower panels show the ratio of models predictions to the data. No model gives a good description of the results in all p_{T} and ξ regions. In the main analysis, PYTHIA 8 A3-NNPDF23LO (DL) predicts less steep dependence of particle density with p_{T} in all three ξ ranges, underestimating the data in the low-p_{T} region and overestimating it in the high-p_{T} region. PYTHIA 8 A2-MSTW2008LO (SaS) and QGSJET predictions are above the data in all three ξ regions, except $p_{\text{T}} > 1.5$ GeV/c at $10^{-5} < \xi < 0.035$, where QGSJET reproduces the data reasonably. In the analysis of SD events, PYTHIA 8 models mostly overestimate the data, except high-p_{T} range at $10^{-5} < \xi < 0.035$, where PYTHIA 8 DL and MBR models describe the data. EPOS significantly underestimates particle density in both analyses, especially at $0.7 < p_{\text{T}} < 8$ GeV/c.

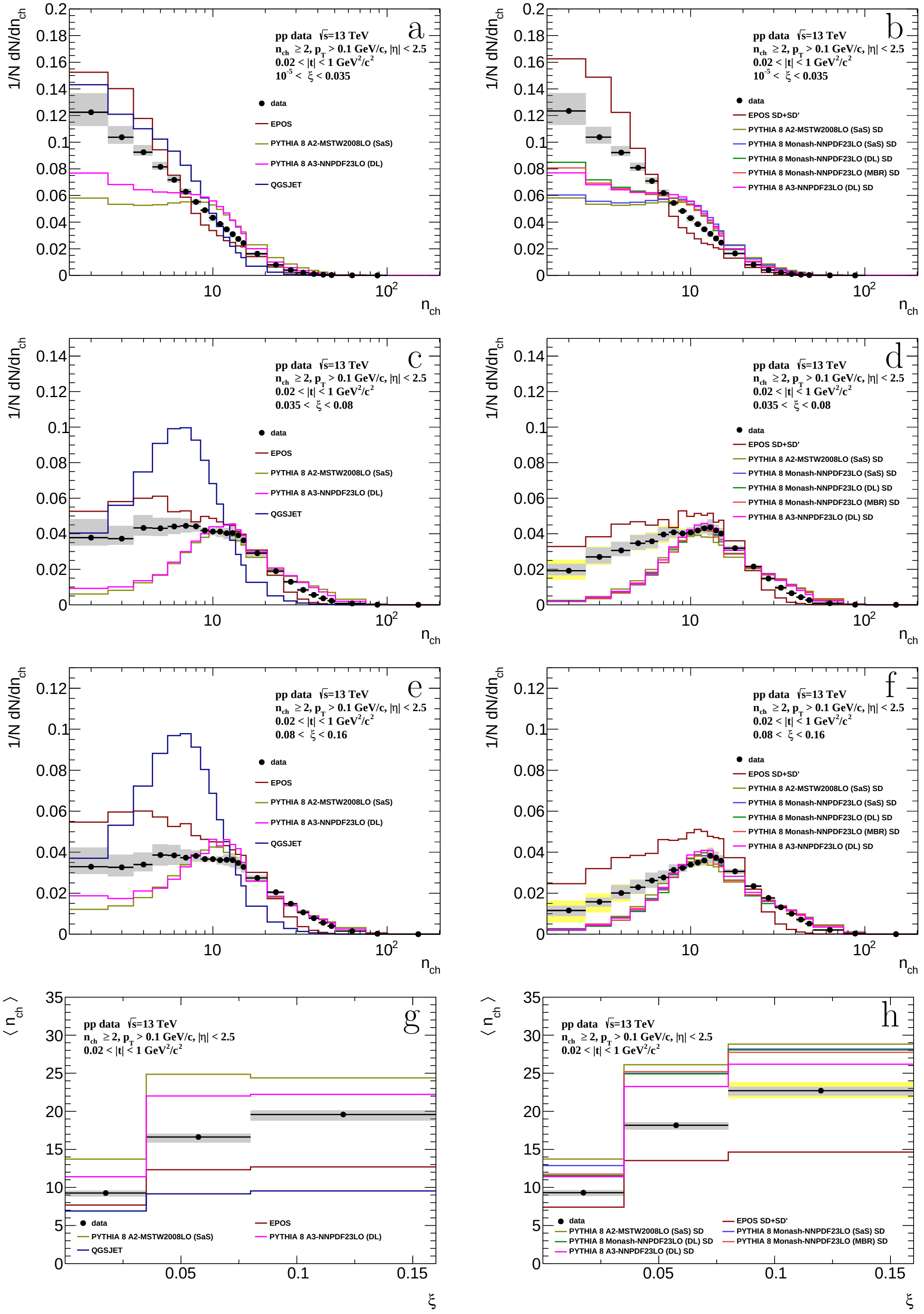

Figure 4.46: Primary charged-particle multiplicity shown separately for the three ranges of ξ: (a-b) $10^{-5} < \xi < 0.035$, (c-d) $0.035 < \xi < 0.08$, (e-f) $0.08 < \xi < 0.16$ and (g-h) the mean multiplicity $\langle n_{\rm ch} \rangle$ as a function of ξ for events with (left) CD, (right) and with CD, DD and ND backgrounds subtracted.

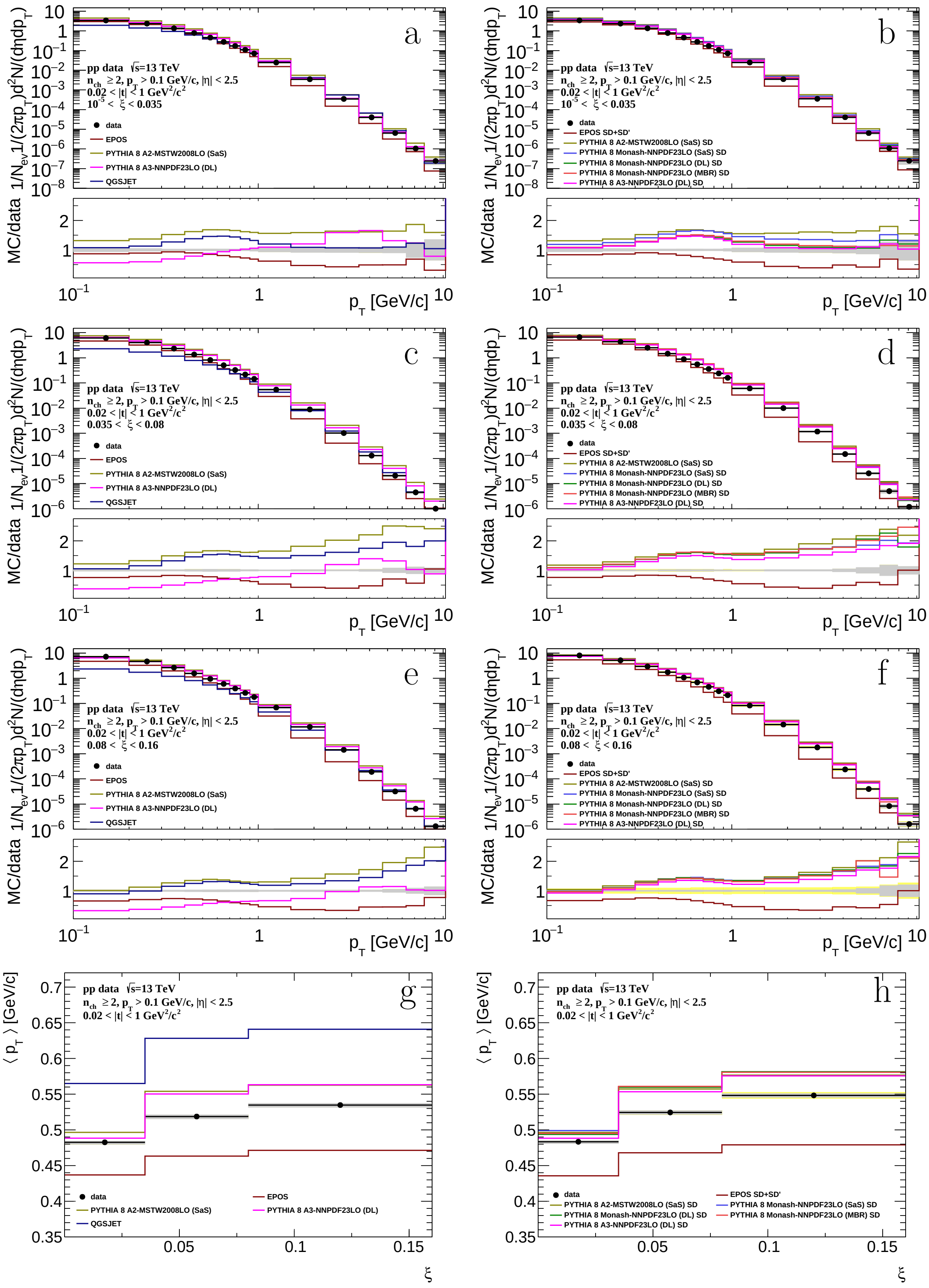

Figure 4.47: Primary charged-particle multiplicities as a function of p_T shown separately for the three ranges of ξ: (a-b) $10^{-5} < \xi < 0.035$, (c-d) $0.035 < \xi < 0.08$, (e-f) $0.08 < \xi < 0.16$ and (g-h) the mean transverse momentum $\langle p_T \rangle$ as a function of ξ for events with (left) CD, (right) and with CD, DD and ND backgrounds subtracted. The ratio of the models' prediction to data is shown in the bottom panels.

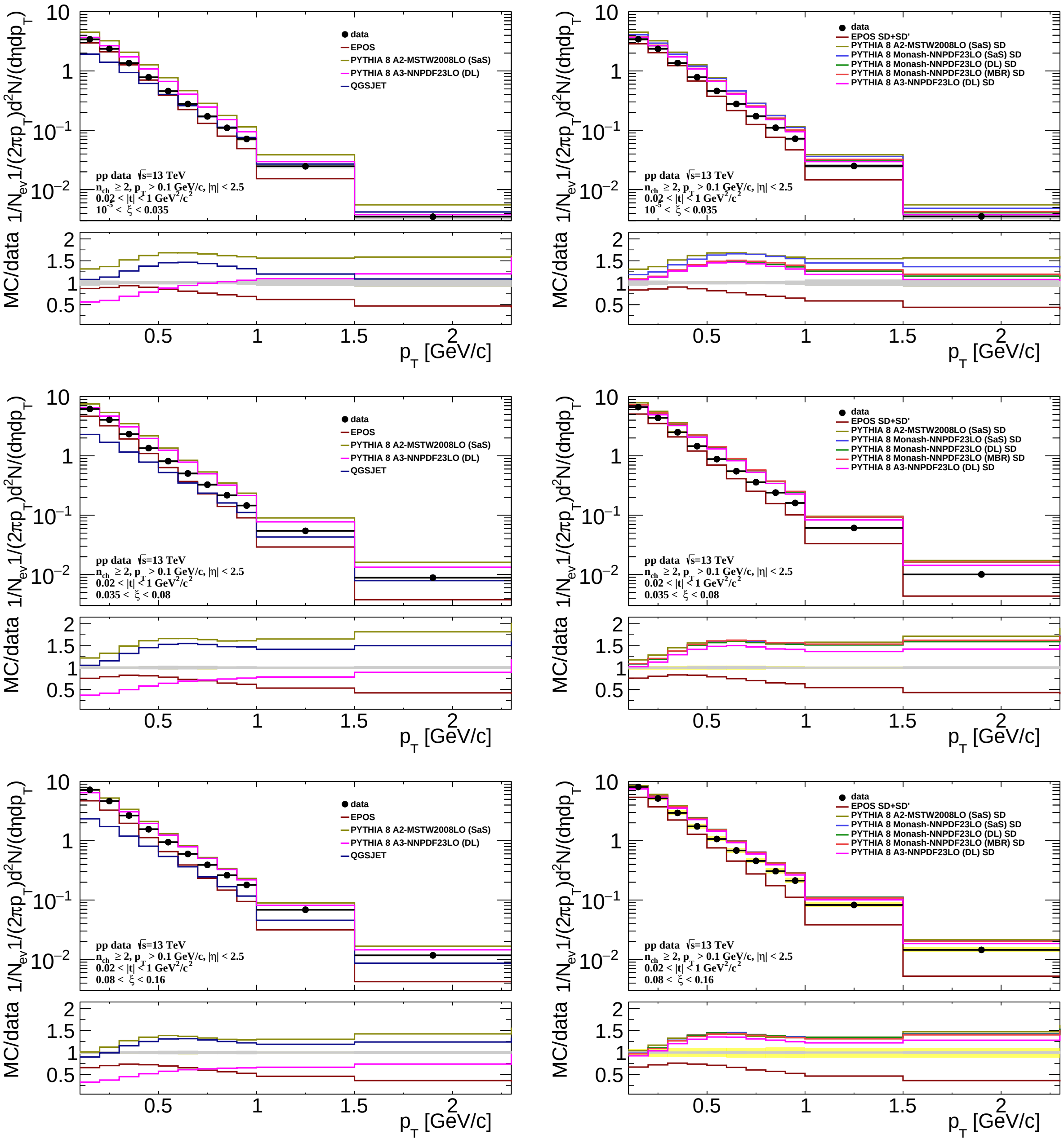

Figure 4.48: Primary charged-particle multiplicities as a function of p_{T} shown separately for the three ranges of ξ: (top) $10^{-5} < \xi < 0.035$, (middle) $0.035 < \xi < 0.08$, (e-f) $0.08 < \xi < 0.16$ and (bottom) for events with (left) CD, (right) and with CD, DD and ND backgrounds subtracted. Only the region of $0.1 < p_{\mathrm{T}} < 2.3$ GeV/c is shown. The ratio of the models' prediction to data is shown in the bottom panels.

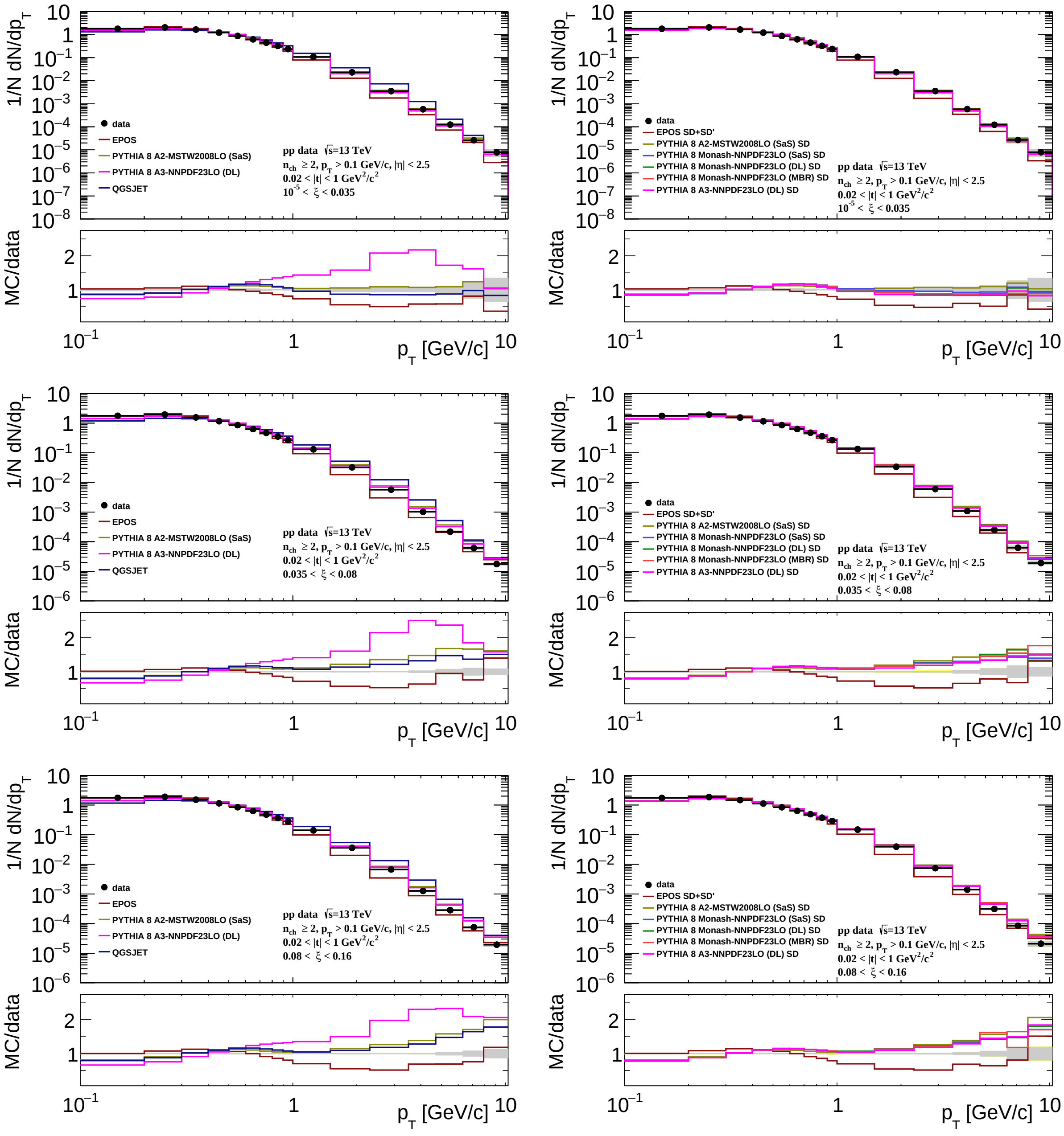

Figure 4.49: Shapes of primary charged-particle multiplicities as a function of p_{T} shown separately for the three ranges of ξ: (top) $10^{-5} < \xi < 0.035$, (middle) $0.035 < \xi < 0.08$, (bottom) $0.08 < \xi < 0.16$ for events with (left) CD, (right) and with CD, DD and ND backgrounds subtracted. The ratio of the models' prediction to data is shown in the bottom panels.

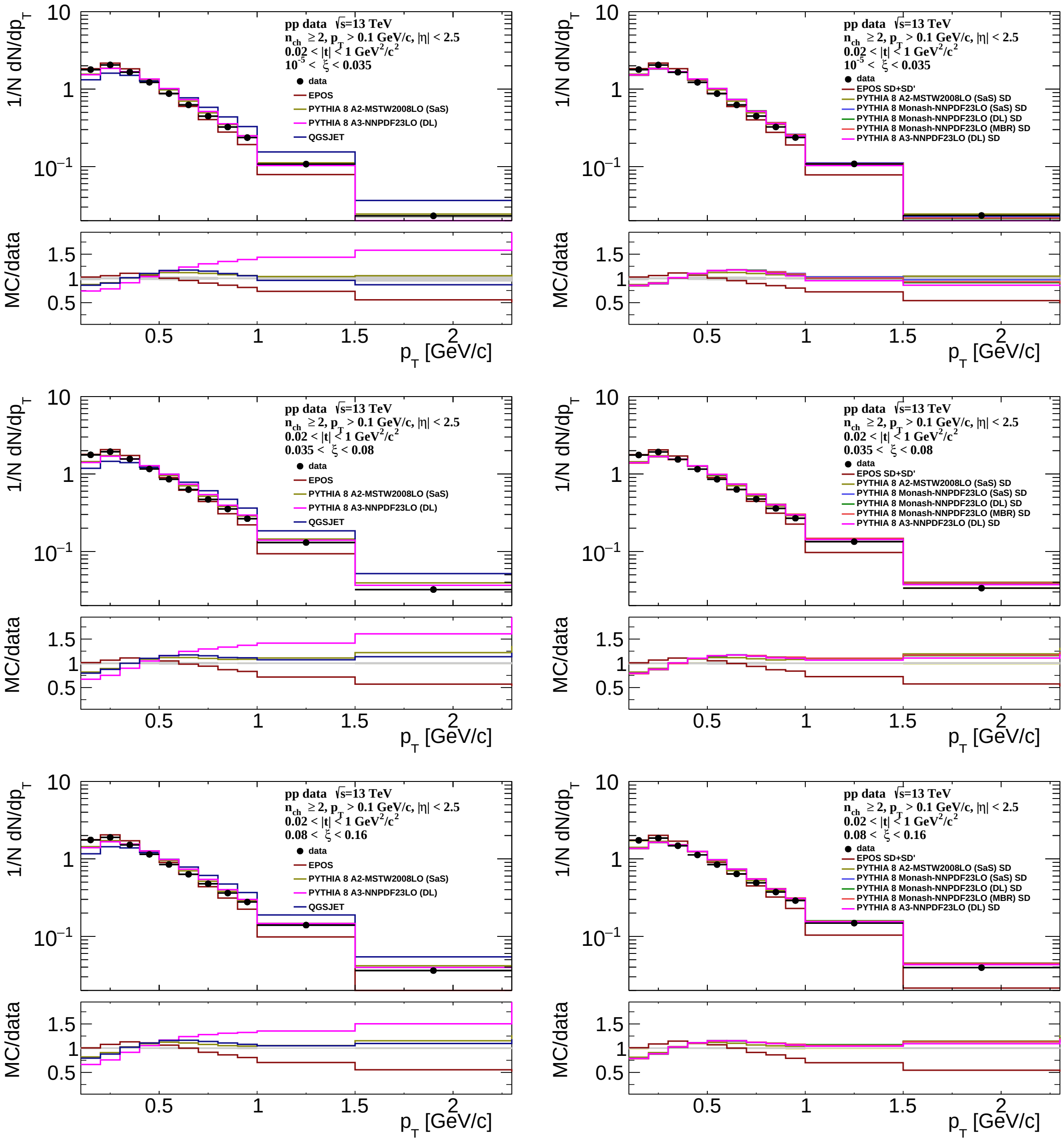

Figure 4.50: Shapes of primary charged-particle multiplicities as a function of p_{T} shown separately for the three ranges of ξ: (top) $10^{-5} < \xi < 0.035$, (middle) $0.035 < \xi < 0.08$, (bottom) $0.08 < \xi < 0.16$ for events with (left) CD, (right) and with CD, DD and ND backgrounds subtracted. Only the region of $0.1 < p_{\mathrm{T}} < 2.3$ GeV/c is shown. The ratio of the models' prediction to data is shown in the bottom panels.

Figure 4.51 shows primary charged-particle multiplicity as a function of $\bar{\eta}$ separately for the three ranges of ξ. Shapes of the $\bar{\eta}$ distributions are shown in Fig. 4.52. Data show expected flattening of the $\bar{\eta}$ distribution with increasing ξ which reflects SD event-asymmetry and fact that gap-edge at large ξ is outside $|\bar{\eta}| < 2.5$ region leading to more flat distribution of particle density as a function of $\bar{\eta}$. Models do not describe data. PYTHIA 8 significantly overestimates particle density in all ranges of ξ, whereas EPOS and QGSJET underestimate it. All MCs predict less steep dependence of particle density with $\bar{\eta}$ in the range of $10^{-5} < \xi < 0.035$, and flat distribution in two other ranges of ξ, $0.035 < \xi < 0.08$, $0.08 < \xi < 0.16$, for events with only CD background subtracted. For SD events, PYTHIA 8 predicts that particle density increases towards higher $\bar{\eta}$ in the range of $0.08 < \xi < 0.16$. The mean pseudorapidity $\langle\bar{\eta}\rangle$ is overestimated by all the other models.

Figure 4.53 shows mean transverse momentum versus the primary charged-particle multiplicity separately for the three ranges of ξ. Data show that the mean p_{T} rises with multiplicity for $n_{\mathrm{ch}} > 10$, although the rise becomes steeper as the multiplicity increases. In addition, $\langle p_{\mathrm{T}}\rangle$ depends very weakly on charged-particle multiplicity for $n_{\mathrm{ch}} \leq 10$. EPOS predicts smaller $\langle p_{\mathrm{T}}\rangle$, especially in the range of $10^{-5} < \xi < 0.035$ and $n_{\mathrm{ch}} < 30$. QGSJET provides significantly larger $\langle p_{\mathrm{T}}\rangle$ for $n_{\mathrm{ch}} < 40$ in all three ranges of ξ. PYTHIA 8 models give reasonably good description of data only in the range of $10^{-5} < \xi < 0.035$.

Figure 4.54 shows ratio of production yields of π^-/π^+, K^-/K^+ and $\bar{p}/p$ as a function of p_{T} for one range of ξ: $10^{-5} < \xi < 0.16$. Data are consistent with equal amounts of particle and antiparticles with no p_{T} dependence. Thus, transfer of the baryon number from the forward to the central region is not observed. All models are in agreement with data.

Figures 4.55 and 4.56 show the distributions of ξ and $|t|$ reconstructed from the scattered protons in ALFA. Both, data and MC, are normalized to the number of events. The distributions are compared to various MC models: PYTHIA 8 A3-NNPDF23LO (DL) and EPOS. PYTHIA 8 predicts much steeper dependence on ξ, as well as on $|t|$ in the range of $10^{-5} < \xi < 0.035$. These two results may suggest that PYTHIA 8 A3 default values of the Pomeron intercept, $\alpha(0) = 1.07$, and slope parameter, $B = 6.64\ \mathrm{c}^2/\mathrm{GeV}^2$, should be decreased in order to achieve a better description of data. EPOS describes data better than PYTHIA 8, however, it predicts significantly larger DD contribution and the distributions are dominated by SD′ events. In general, the contributions of ND secondary protons are small in both models. Similarly to PYTHIA 8, EPOS predicts much steeper dependence on $|t|$ in the range of $10^{-5} < \xi < 0.035$. It can be concluded from these results that the relative SD to SD′ ratio can be tuned in EPOS to achieve a better description of both ξ and $|t|$ distributions.

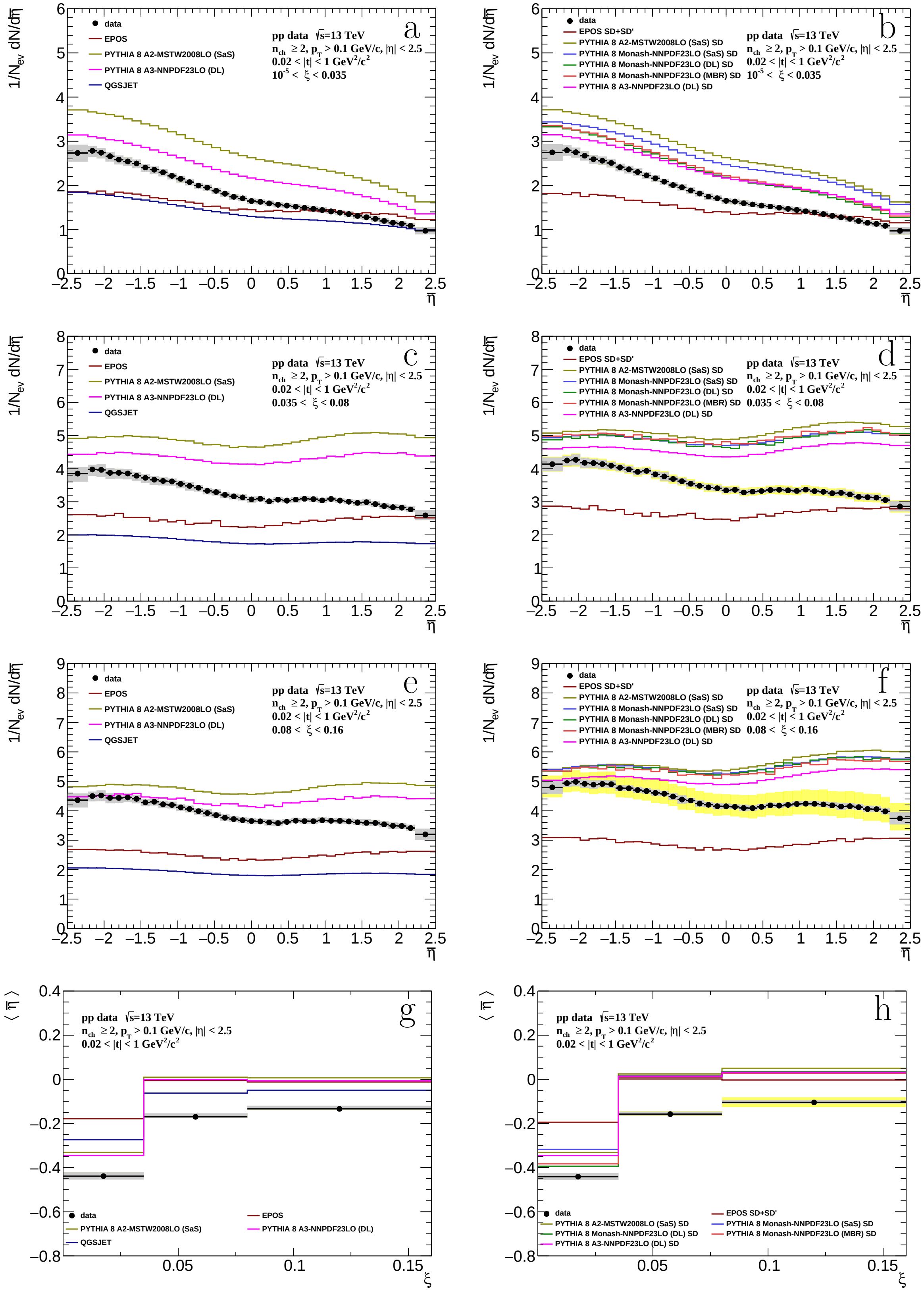

Figure 4.51: Primary charged-particle multiplicities as a function of $\bar{\eta}$ shown separately for the three ranges of ξ: (a-b) $10^{-5} < \xi < 0.035$, (c-d) $0.035 < \xi < 0.08$, (e-f) $0.08 < \xi < 0.16$ and (g-h) the mean pseudorapidity $\langle\bar{\eta}\rangle$ as a function of ξ for events with (left) CD, (right) and with CD, DD and ND backgrounds subtracted.

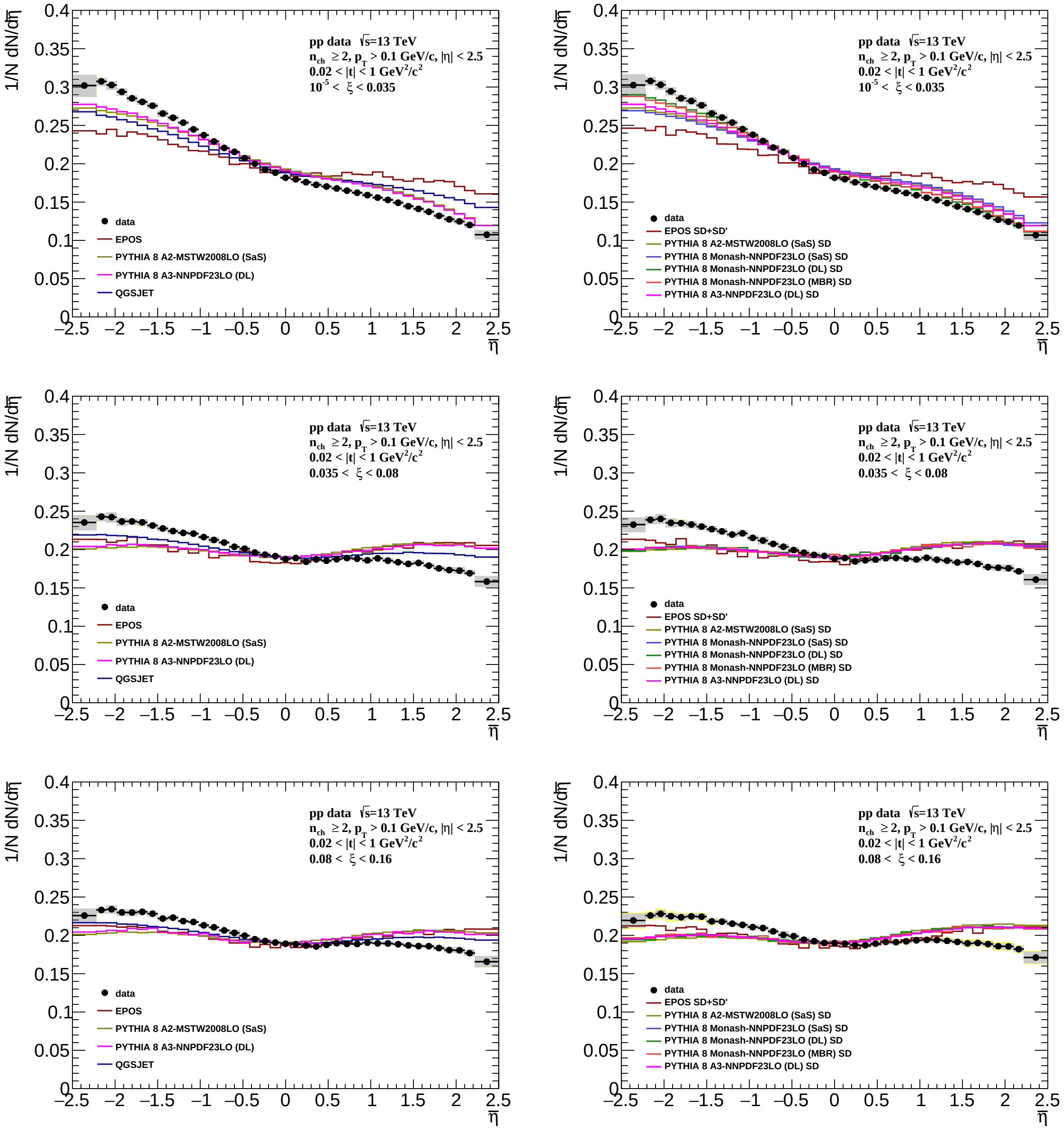

Figure 4.52: Shapes of primary charged-particle multiplicities as a function of $\bar{\eta}$ shown separately for the three ranges of ξ: (top) $10^{-5} < \xi < 0.035$, (middle) $0.035 < \xi < 0.08$, (bottom) $0.08 < \xi < 0.16$ for events with (left) CD, (right) and with CD, DD and ND backgrounds subtracted.

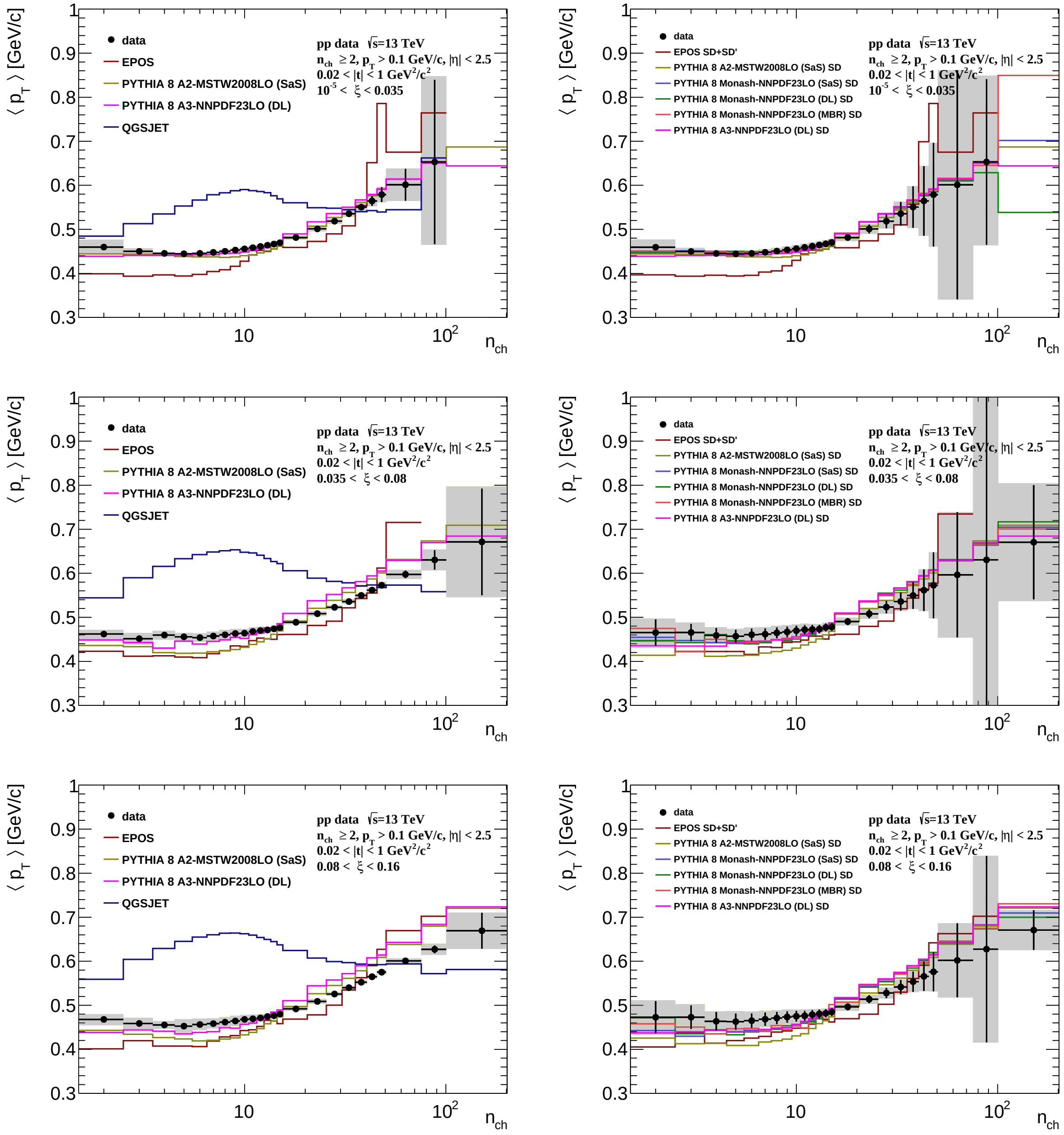

Figure 4.53: Mean transverse momentum $\langle p_{\rm T}\rangle$ as a function of $n_{\rm ch}$ shown separately for the three ranges of ξ: (top) $10^{-5} < \xi < 0.035$, (middle) $0.035 < \xi < 0.08$, (bottom) $0.08 < \xi < 0.16$ for events with (left) CD, (right) and with CD, DD and ND backgrounds subtracted.

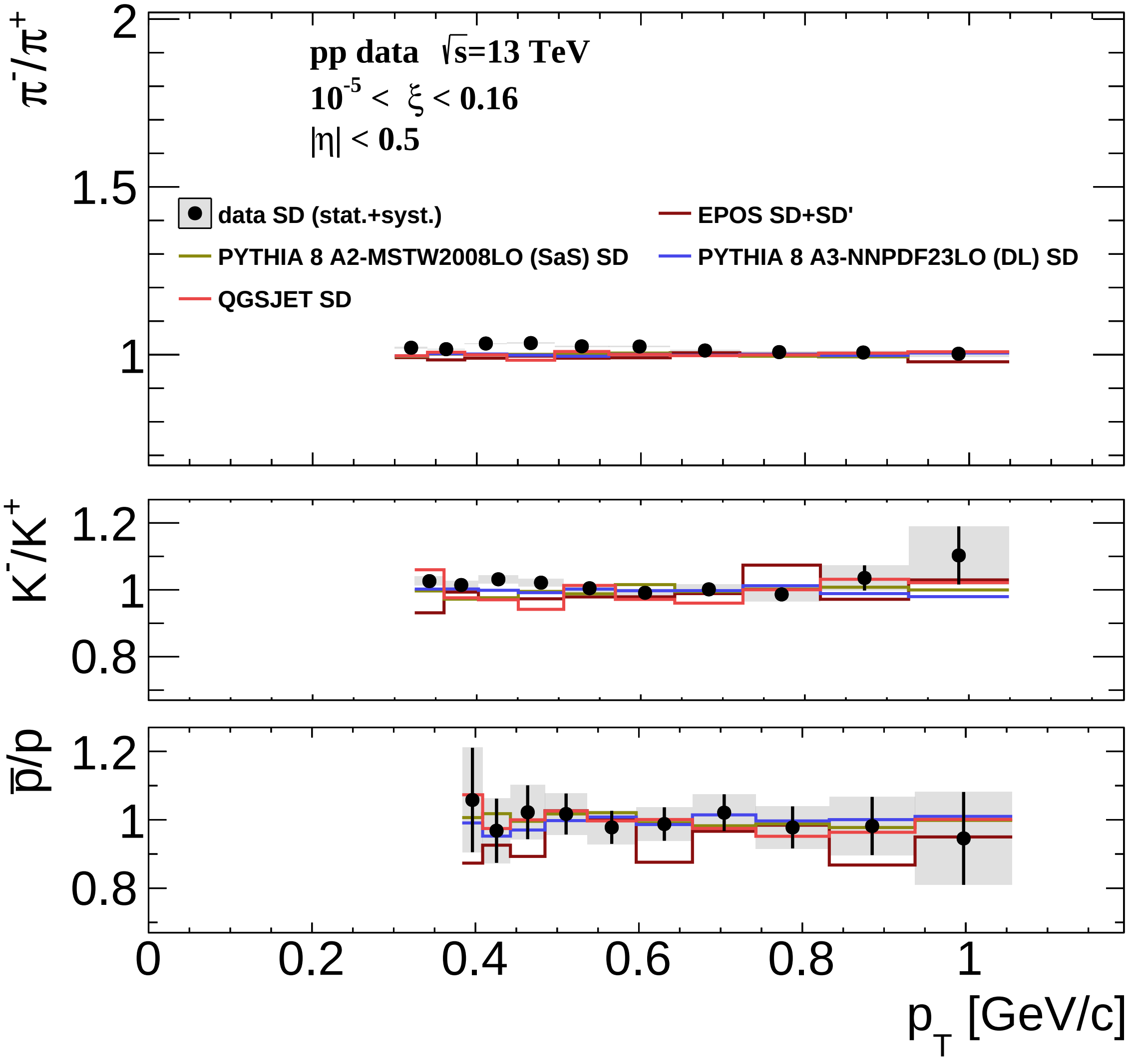

Figure 4.54: Ratio of production yields of $\pi^{/}\pi^+$, K^-/K^+ and $\bar{p}/p$ as a function of p_T.

Summary

The measured distributions of charged-particle multiplicity, its dependence on p_T and $\bar{\eta}$, and the mean transverse momentum as a function of charged-particle multiplicity, are not described by all MC models. PYTHIA 8 models predict much larger $\langle n_\mathrm{ch} \rangle$ than observed in the data, as well as overestimate almost all charged-particle densities. The $\langle p_\mathrm{T} \rangle (n_\mathrm{ch})$ distribution is reasonably described by PYTHIA 8, but only at $10^{-5} < \xi < 0.035$. The results on ξ and $|t|$ distributions indicate that the Pomeron intercept and slope parameter should be smaller than predicted by PYTHIA 8 A3-NNPDF23LO (DL).

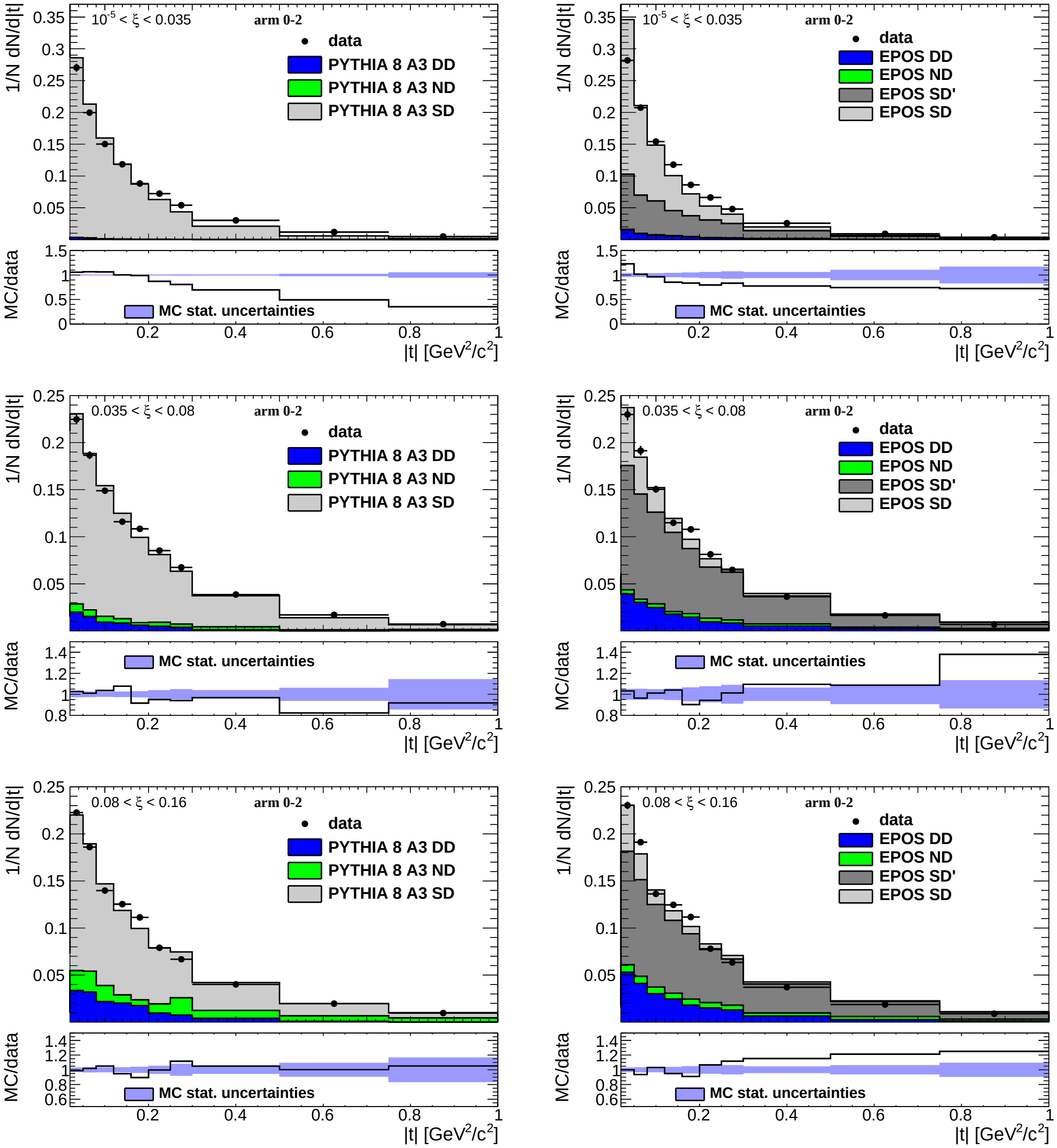

Figure 4.55: Mandelstam $|t|$ shown separately for the three ranges of ξ: (top) $10^{-5} < \xi < 0.035$, (middle) $0.035 < \xi < 0.08$, (bottom) $0.08 < \xi < 0.16$, and compared to various MC models: (left) PYTHIA 8 A3-NNPDF23LO (DL) and (right) EPOS. The ratio of the models' prediction to data is shown in the bottom panels.

EPOS shows smaller $\langle n_{\mathrm{ch}} \rangle$ than observed in the data, however, it better describes charged-particle multiplicity distributions at $10^{-5} < \xi < 0.08$ than PYTHIA 8 models. The measured distributions of charged-particle densities as a function of p_{T} and $\bar{\eta}$, as well

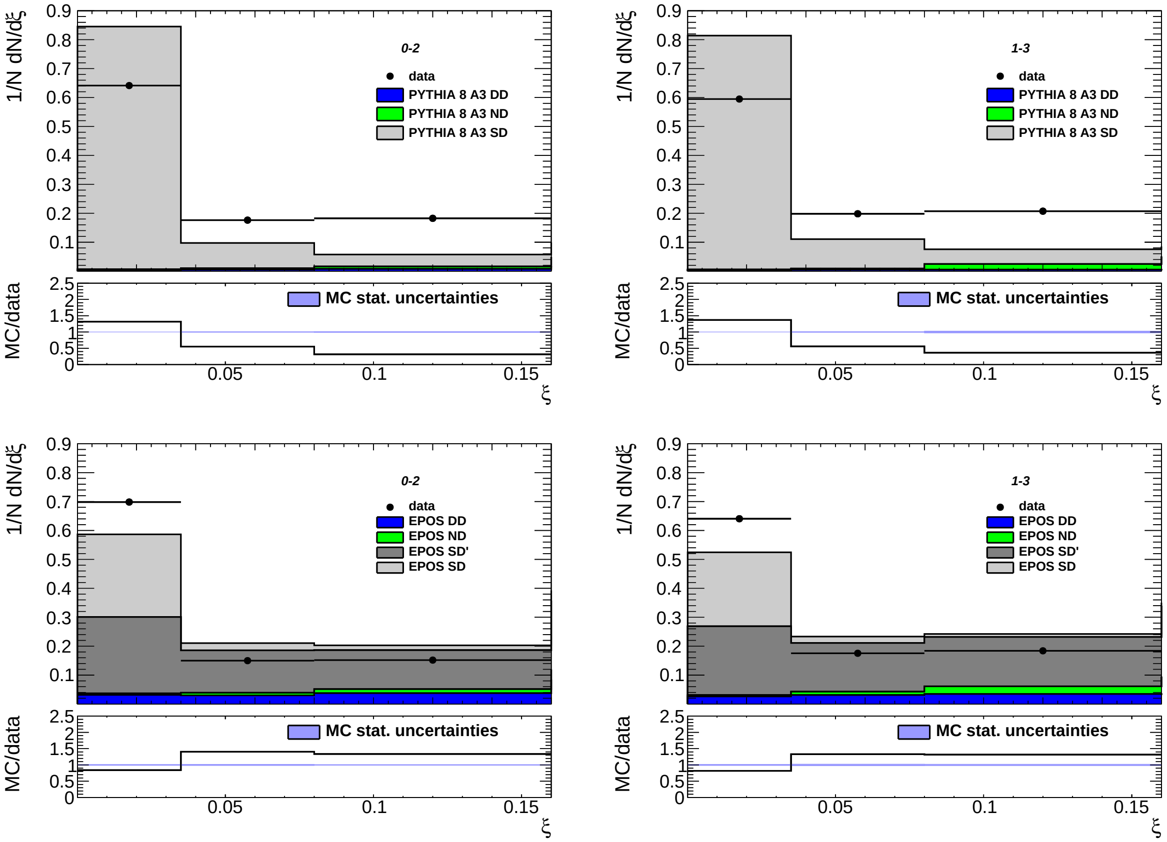

Figure 4.56: Fractional energy loss, ξ, reconstructed from the scattered protons in two separate ALFA arms: (left) $0-2$, (right) $1-3$, and compared to various MC models: (top) PYTHIA 8 A3-NNPDF23LO and (bottom) EPOS. The ratio of the models' prediction to data is shown in the bottom panels.

as $\langle p_{\mathrm{T}}\rangle(n_{\mathrm{ch}})$ for low-multiplicities, are underestimated in EPOS. The results on ξ and $|t|$ distributions suggest that the relative contribution of EPOS SD and SD$'$ may be further tuned.

Significant differences are observed between almost all measured distributions and QGSJET model. This model shows smaller $\langle n_{\mathrm{ch}}\rangle$ than observed in the data for all three ranges of ξ. However, its predictions on charged-particle multiplicities at $10^{-5} < \xi < 0.035$ better describe the data than PYTHIA 8. The dependence of particle densities with p_{T} and $\bar{\eta}$ is mostly not steep enough in this model. QGSJET shows significantly larger $\langle p_{\mathrm{T}}\rangle(n_{\mathrm{ch}})$ for $n_{\mathrm{ch}} < 40$ than observed in the data and predicted by other MC models.

Chapter 5

Comparison of Charged-Particle Densities at Central Rapidities

The measured charged-particle densities in pseudorapidity near $\eta \approx 0$ are compared to other experimental results from pp and $p\bar{p}$ collisions (shown in Fig. 5.1). Various event selections, based on the topology of the final state, allow to split the data samples into enhanced in non-SD (NSD) and SD events, whose sum forms the inelastic sample. For SD events, the midrapidity region is located at $\bar{\eta} = \eta^{\star} = -\ln(\sqrt{s}/M_X)$, instead of $\eta \approx 0$, and the proper energy scale is given by M_X instead of $\sqrt{s}$. The values of $\eta^{\star}$ and $\langle M_X \rangle$, calculated separately for STAR and ATLAS data, are presented in Tab. 5.1. For some ranges of ξ, the value of $\eta^{\star}$ is outside the fiducial region of the measurement. In the case of other experiments the pseudorapidity densities were obtained in the region of the total number of primary charged particles $n_{\mathrm{ch}} \geq 1$ (instead of $n_{\mathrm{ch}} \geq 2$ as in these analyses). Therefore, the results from STAR and ATLAS analyses were extrapolated to the above fiducial region using PYTHIA 8 A2 (MBR) SD and PYTHIA 8 A3 (DL) SD predictions, respectively. The uncertainties due to the corrections are not estimated.

The extrapolation procedure depends on whether the value of $\eta^{\star}$ is inside or outside the fiducial region of the measurement:

	ξ range	$\langle M_X \rangle$	$\eta^{\star}$	ρ_{M}	factor	ρ_{C}
STAR	$0.02 < \xi < 0.05$	37.53 GeV	-1.67	2.18 ± 0.08	0.80	1.74 ± 0.06
	$0.05 < \xi < 0.1$	53.52 GeV	-1.31	2.29 ± 0.09	0.84	1.92 ± 0.08
	$0.1 < \xi < 0.2$	72.71 GeV	-1.01	2.30 ± 0.10	0.83	1.91 ± 0.08
ATLAS	$10^{-5} < \xi < 0.035$	490 GeV	-3.28	1.65 ± 0.06	1.57	2.59 ± 0.09
	$0.035 < \xi < 0.08$	2990 GeV	-1.47	$4.03^{+0.13}_{-0.14}$	0.93	$3.75^{+0.12}_{-0.13}$
	$0.08 < \xi < 0.16$	4340 GeV	-1.09	$4.67^{+0.42}_{-0.32}$	0.84	$3.92^{+0.35}_{-0.27}$

Table 5.1: Values of $\langle M_X \rangle$, $\eta^{\star} = \ln(\sqrt{s}/M_X)$, ρ_{M}, ρ_{C} and the scale factor for STAR and ATLAS analyses.

- $\eta^\star$ is inside the fiducial region of the measurement:
  1. the ratio of particle density at $\bar{\eta} = \eta^\star$ in the region of $n_{\mathrm{ch}} \geq 1$ to that in the region of $n_{\mathrm{ch}} \geq 2$ was calculated using PYTHIA 8 predictions,
  2. this ratio was used to scale the measured particle density at $\bar{\eta} \approx \eta^\star$.
- $\eta^\star$ is outside the fiducial region of the measurement:
  1. the ratio of particle density at $\bar{\eta} = \eta^\star$ and $n_{\mathrm{ch}} \geq 1$ to that at $\bar{\eta} = 0$ and $n_{\mathrm{ch}} \geq 2$ was calculated using PYTHIA 8 predictions,
  2. differences in the slope of the pseudorapidity distribution in the region of $n_{\mathrm{ch}} \geq 2$ were observed between data and MC. Therefore, data and MC distributions were normalized to have the same particle density at $\bar{\eta} \approx 0$ and their ratio was fitted with a linear function,
  3. the correction from step #1, multiplied by the value of the above function at $\bar{\eta} = \eta^\star$, was used to scale the measured particle density at $\bar{\eta} \approx 0$.

The measured and corrected charged-particle densities near $\bar{\eta} = \eta^\star$, ρ_{M} and ρ_{C}, as well as the corresponding scale factors, are shown in Tab. 5.1.

Figure 5.1 presents the charged-particle densities near $\eta \approx 0$ as a function of $\sqrt{s}$ in inelastic pp and $p\bar{p}$ collisions. The SD results, calculated near $\bar{\eta} = \eta^\star$ at $\sqrt{s}$ (M_X), are also shown. The measured pseudorapidity densities in diffractive interactions rise with M_X and does not follow the trend of the NSD events at large $\sqrt{s}$ (M_X).

The particle density at $\eta \approx 0$ should be described by a power-law dependence [28]:

$$\frac{1}{N_{\mathrm{ev}}} \frac{dN}{d\eta}\bigg|_{\eta \approx 0} \propto s^\delta \tag{5.1}$$

The same dependence is expected to be valid for SD events, but with $\bar{\eta} = \eta^\star$ and $M_X^{2\delta}$. Hence, the particle densities at $\bar{\eta} = \eta^\star$ in SD interactions were fitted with the above parametrization and a value of $\delta = 0.085 \pm 0.005$ was obtained. This value is smaller than the one calculated by CMS and TOTEM for the NSD event selection ($\delta \approx 0.12$) [28]. This may suggest that the above simple power-law scaling of charged-particle densities with the collision energy may be different for SD and NSD interactions.

The measured mean transverse momentum $\langle p_{\mathrm{T}} \rangle$ as a function of n_{ch} is of special interest since it depends on many parameters implemented in the MC models [244], e.g. those describing the MPI. Therefore, the distributions of $\langle p_{\mathrm{T}} \rangle(n_{\mathrm{ch}})$, measured using ATLAS data, were compared to the results of MB analysis [22] (shown in Fig. 5.2). Data show increase of $\langle p_{\mathrm{T}} \rangle$ with ξ for low charged-particle multiplicities. It is observed that the results for the region of $10^{-5} < \xi < 0.035$ are in agreement with MB data. This may suggest that the MB data sample, especially for low multiplicities, is dominated by diffractive events.

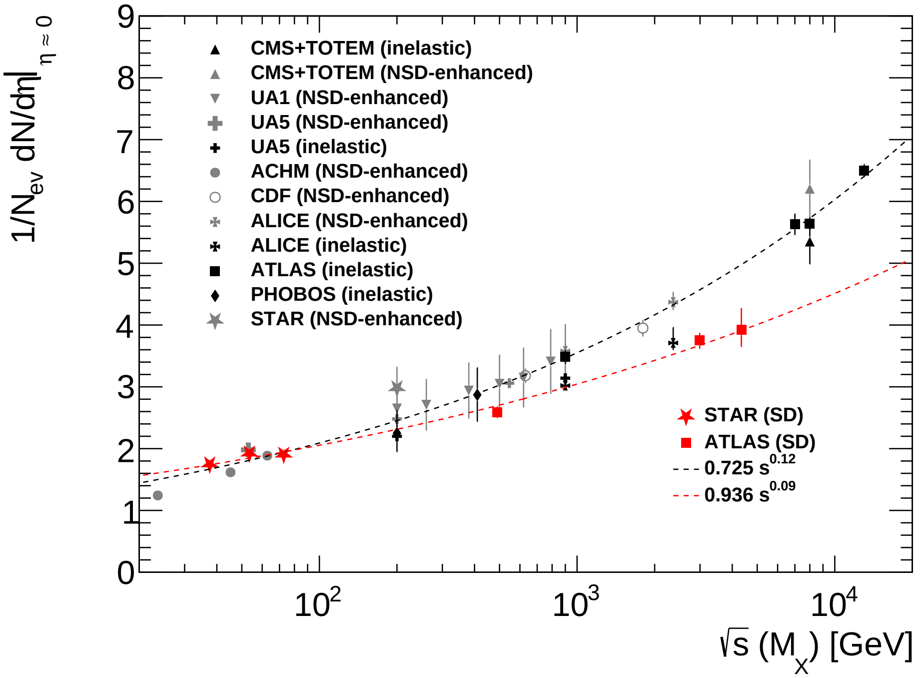

Figure 5.1: The evolution of $1/N_{\mathrm{ev}}\ dN/d\eta$ at $\eta \approx 0$ as a function of $\sqrt{s}$ in inelastic pp and $p\bar{p}$ collisions [6, 7, 10, 17, 22, 23, 25, 28, 241–243]. The SD results were calculated near $\bar{\eta} \approx \eta^{\star}$ at $\sqrt{s}$ (M_X). The dashed lines represent power-law fits to the NSD-enhanced [28] and SD data. The results from this thesis are shown in red.

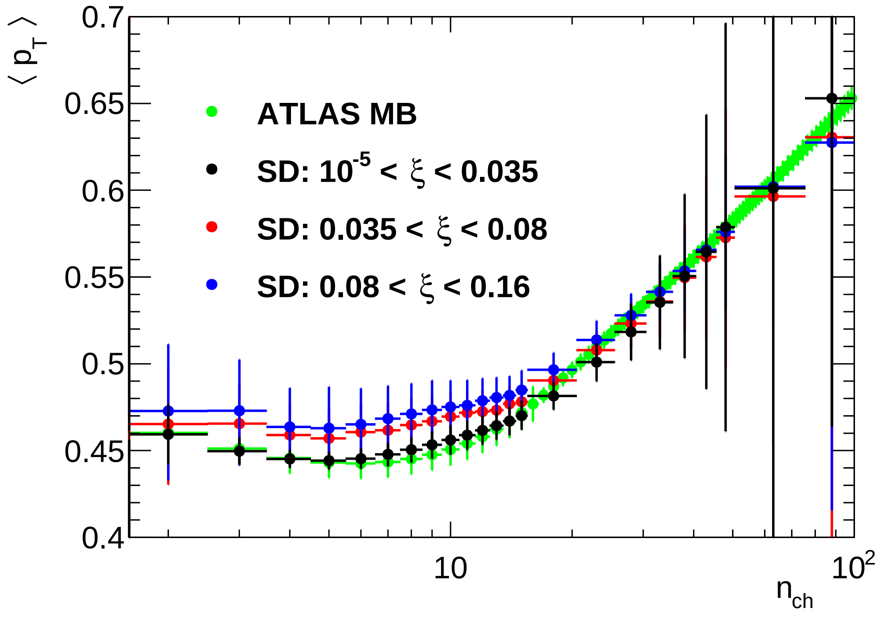

Figure 5.2: Mean transverse momentum $\langle p_{\mathrm{T}} \rangle$ as a function of n_{ch} in SD events compared to ATLAS MB data [22]. The SD results are shown separately for the three ranges of ξ. Error bars represent statistical and systematic uncertainties added in quadrature.

Chapter 6

Summary and Conclusions

In this thesis, measurements of charged-particle distributions with single forward-scattered proton tagging are presented. The analyses use the data from proton-proton collisions at centre-of-mass energies of $\sqrt{s}$ = 200 GeV and $\sqrt{s}$ = 13 TeV collected by the STAR experiment at RHIC and the ATLAS experiment at the LHC, respectively. The data correspond to integrated luminosities of 16 nb^{-1} at $\sqrt{s}$ = 200 GeV, and 723 nb^{-1} at $\sqrt{s}$ = 13 TeV. Data are corrected for detector effects using data-driven and simulation-based methods.

The results are compared to the predictions of several phenomenological models, developed and implemented in MC generators, namely EPOS, QGSJET, HERWIG and different tunes of PYTHIA 8.

Significant differences are observed between the distributions of ξ, measured using STAR data, and MC model predictions. Amongst the models considered, EPOS and PYTHIA 8 (MBR) without artificial suppression of diffractive cross sections at large ξ provide the best description of the data.

Charged-particle multiplicity and its dependence on the pseudorapidity and the transverse momentum, measured using STAR data, are well described by PYTHIA8 and EPOS SD$'$ models. EPOS SD+SD$'$ and HERWIG do not describe the data.

π^-/π^+ and K^-/K^+ production ratios, obtained with the STAR detector, are close to unity and consistent with most of model predictions except for HERWIG. $\bar{p}/p$ production ratio shows a significant deviation from unity in the $0.02 < \xi < 0.05$ range indicating a non-negligible transfer of the baryon number from the forward to the central region. Equal amount of protons and antiprotons are observed in the $\xi > 0.05$ range. PYTHIA8, EPOS SD+SD$'$ and EPOS SD$'$ agree with data for $\xi > 0.05$. For $0.02 < \xi < 0.05$ PYTHIA 8 and EPOS SD$'$ predict small deviations from unity (0.93) which is however higher than observed in data (0.85 ± 0.04). EPOS SD+SD$'$ predicts an asymmetry between $\bar{p}$ and p of $\sim 30\%$ at $0.02 < \xi < 0.05$. HERWIG predicts much larger baryon number transfers compared to data for $\xi < 0.1$ and shows consistency with data for $\xi > 0.1$.

The shapes of ξ and $|t|$ distributions, measured using ATLAS data, are not described by both PYTHIA 8 and EPOS models. PYTHIA 8 predicts much steeper dependence on ξ, as well as on $|t|$ in the range of $10^{-5} < \xi < 0.035$. EPOS describes data better, however, it is dominated by SD$'$ events.

Charged-particle distributions, measured using ATLAS data, are not well described by all models. The mean charged-particle multiplicity is overestimated in all PYTHIA 8 models, and underestimated in QGSJET and EPOS. None of the models considered is able to describe the transverse momentum and the pseudorapidity distributions in the entire range of measurement. The mean transverse momentum as a function of charged-particle multiplicity agrees reasonably with PYTHIA 8 only at $10^{-5} < \xi < 0.035$. Amongst the models, the largest discrepancies are observed for QGSJET.

π^-/π^+, K^-/K^+ and $\bar{p}/p$ production ratios, obtained with the ATLAS detector, are close to unity and consistent with all of model predictions. The results indicate there is no significant baryon number transfer from the forward to the central region.

Both measurements are compared with different NSD-enhanced results at various centre-of-mass energies. In order to obtain charged-particle densities at $\eta \approx 0$, an extrapolation based on PYTHIA 8 predictions is performed. The results indicate that the simple scaling of charged-particle densities with the collision energy may be different for SD and NSD interactions.

The charged-particle densities obtained in this thesis have the unique potential to probe the particle production at two significantly different centre-of-mass energies. Studies presented in this thesis are expected to provide an opportunity to perform further tunning of free parameters of the phenomenological models. Distributions of ξ and $|t|$ can significantly contribute to the description of the Pomeron intercept and slope parameter in PYTHIA 8 diffractive models, as well as the relative SD to SD$'$ ratio in EPOS.

Acknowledgements

First and foremost, I would like to express my gratitude to my supervisors: Prof. Mariusz Przybycień and Dr. Leszek Adamczyk, for their guidance and attention throughout my whole PhD studies.

I would also like to thank all the people I had pleasure to meet and work with at BNL and CERN.

Last but not least, I would like to thank my fiancée and friends, and above all, my parents for their encouragement throughout the years.

This work was partly supported by the National Science Centre of Poland under grants UMO-2015/19/B/ST2/00989 and UMO-2015/18/M/ST2/00162.

Acronyms

AGS	Alternating Gradient Synchrotron
AFP	ATLAS Forward Proton
ALFA	Absolute Luminosity For ATLAS
ATLAS	A Toroidal LHC Apparatus
BBC	Beam Beam Counter
BCID	Bunch Crossing Identifier
BEMC	Barrel Electromagnetic Calorimeter
BNL	Brookhaven National Laboratory
CD	Central Diffraction
CEP	Central Exclusive Production
CERN	European Laboratory for Particle Physics
CR	Colour Reconnection
DAQ	Data Acquisition System
DD	Double Diffraction
DIS	Deep Inelastic Scattering
DL	Donnachie and Landshoff
DPDFs	Diffractive Parton Distribution Functions
EBIS	Electron Beam Ion Source
FCAL	Forward Calorimeters
FSR	Final State Radiation

HCAL	Hadronic Calorimeter
HEC	Hadronic End-Cap
ECR	Electron Cyclotron Resonance
EM	Electromagnetic
HFT	Heavy Flavor Tracker
HLT	High Level Trigger
IBL	Insertable B-Layer
ID	Inner Detector
IP	Interaction Point
ISR	Initial State Radiation
L1	Level-1
LAr	liquid argon
LEIR	Low-Energy Ion Ring
LEP	Large Electron Positron Collider
LHC	Large Hadron Collider
LION	Laser Ion Source
MAPMT	Multi Anode Photomultiplier Tube
MB	Minimum Bias
MBR	Minimum Bias Rockefeller
MBTS	Minimum Bias Trigger Scintillator
MPV	Most Probable Value
MC	Monte Carlo
MD	Main Detector
MPI	Multiple Parton Interactions
MRPC	Multi-gap Resistive Plate Chambers
MWPC	Multi Wire Proportional Chambers

ND	Non-Diffractive
OD	Overlap Detector
OPPIS	Optically Pumped Polarized Ion Source
PDFs	Parton Distribution Functions
PP0	Patch Panel 0
PP	Patch Panel
PS	Proton Synchrotron
PSB	Proton Synchrotron Booster
QCD	Quantum Chromodynamics
QED	Quantum Electrodynamics
QGP	Quark Gluon Plasma
QFT	Quantum Field Theory
RFQ	Radio Frequency Quadrupole
RHIC	Relativistic Heavy Ion Collider
ROI	Regions-of-Interest
RP	Roman Pot
SaS	Schuler and Sjöstrand
SCT	Semiconductor Tracker
SD	Single Diffraction
SM	Standard Model
SMD	Shower Maximum Detector
SPS	Super Proton Synchrotron
SSD	Silicon Strip Detectors
STAR	Solenoidal Tracker at RHIC
TDAQ	Trigger and Data Acquisition
TOF	Time of Flight

TPC	Time Projection Chamber
TRT	Transition Radiation Tracker
UE	Underlying Events
VPD	Vertex Position Detector
ZB	Zerobias
ZDC	Zero Degree Calorimeter

Bibliography

[1] ABCDHW Collaboration, A. Breakstone et al., *Charged Multiplicity Distribution in pp Interactions at ISR Energies*, Phys. Rev. **D30** (1984) 528.

[2] UA1 Collaboration, G. Arnison et al., *Transverse Momentum Spectra for Charged Particles at the CERN Proton anti-Proton Collider*, Phys. Lett. **118B** (1982) 167.

[3] UA5 Collaboration, G. J. Alner et al., *UA5: A general study of proton-antiproton physics at $\sqrt{s}$ = 546-GeV*, Phys. Rept. **154** (1987) 247.

[4] UA5 Collaboration, R. E. Ansorge et al., *Charged Particle Multiplicity Distributions at 200-GeV and 900-GeV Center-Of-Mass Energy*, Z. Phys. **C43** (1989) 357.

[5] CDF Collaboration, F. Abe et al., *Transverse Momentum Distributions of Charged Particles Produced in $\bar{p}p$ Interactions at $\sqrt{s} = 630$ GeV and 1800 GeV*, Phys. Rev. Lett. **61** (1988) 1819.

[6] UA1 Collaboration, C. Albajar et al., *A Study of the General Characteristics of $p\bar{p}$ Collisions at $\sqrt{s}$ = 0.2-TeV to 0.9-TeV*, Nucl. Phys. **B335** (1990) 261.

[7] CDF Collaboration, F. Abe et al., *Pseudorapidity distributions of charged particles produced in $\bar{p}p$ interactions at $\sqrt{s} = 630$ GeV and 1800 GeV*, Phys. Rev. **D41** (1990) 2330.

[8] E735 Collaboration, T. Alexopoulos et al., *Multiplicity dependence of transverse momentum spectra of centrally produced hadrons in pp collisions at 0.3, 0.54, 0.9, and 1.8 TeV center of mass energy*, Physics Letters B **336** (1994) 599.

[9] CDF Collaboration, T. Aaltonen et al., *Measurement of Particle Production and Inclusive Differential Cross Sections in $p\bar{p}$ Collisions at $\sqrt{s} = 1.96$-TeV*, Phys. Rev. **D79** (2009) 112005, `arXiv:0904.1098 [hep-ex]`, [Erratum: Phys. Rev. D82 (2010) 119903].

[10] PHOBOS Collaboration, B. Alver et al., *Phobos results on charged particle multiplicity and pseudorapidity distributions in Au+Au, Cu+Cu, d+Au, and p+p collisions at ultra-relativistic energies*, Phys. Rev. **C83** (2011) 024913, `arXiv:1011.1940 [nucl-ex]`.

[11] ALICE Collaboration, K. Aamodt et al., *First proton-proton collisions at the LHC as observed with the ALICE detector: Measurement of the charged particle pseudorapidity density at* $\sqrt{s} = 900$ *GeV*, Eur. Phys. J. **C65** (2010) 111, `arXiv:0911.5430 [hep-ex]`.

[12] CMS Collaboration, V. Khachatryan et al., *Transverse Momentum and Pseudorapidity Distributions of Charged Hadrons in pp Collisions at* $\sqrt{s} = 0.9$ *and 2.36 TeV*, JHEP **02** (2010) 41, `arXiv:1002.0621 [hep-ex]`.

[13] ATLAS Collaboration, G. Aad et al., *Charged-particle multiplicities in pp interactions at* $\sqrt{s} = 900$ *GeV measured with the ATLAS detector at the LHC*, Phys. Lett. **B688** (2010) 21, `arXiv:1003.3124 [hep-ex]`.

[14] ALICE Collaboration, K. Aamodt et al., *Charged-particle multiplicity measurement in proton-proton collisions at* $\sqrt{s} = 7$ *TeV with ALICE at LHC*, Eur. Phys. J. **C68** (2010) 345, `arXiv:1004.3514 [hep-ex]`.

[15] CMS Collaboration, V. Khachatryan et al., *Transverse-momentum and pseudorapidity distributions of charged hadrons in pp collisions at* $\sqrt{s} = 7$ *TeV*, Phys. Rev. Lett. **105** (2010) 022002, `arXiv:1005.3299 [hep-ex]`.

[16] CMS Collaboration, V. Khachatryan et al., *Charged Particle Multiplicities in pp Interactions at* $\sqrt{s} = 0.9$*, 2.36, and 7 TeV*, JHEP **01** (2011) 79, `arXiv:1011.5531 [hep-ex]`.

[17] ATLAS Collaboration, G. Aad et al., *Charged-particle multiplicities in pp interactions measured with the ATLAS detector at the LHC*, New J. Phys. **13** (2011) 053033, `arXiv:1012.5104 [hep-ex]`.

[18] LHCb Collaboration, R. Aaij et al., *Measurement of charged particle multiplicities and densities in pp collisions at* $\sqrt{s} = 7$ *TeV in the forward region*, Eur. Phys. J. **C74** (2014) 2888, `arXiv:1402.4430 [hep-ex]`.

[19] CMS Collaboration, V. Khachatryan et al., *Pseudorapidity distribution of charged hadrons in proton-proton collisions at* $\sqrt{s}$ *= 13 TeV*, Phys. Lett. **B751** (2015) 143, `arXiv:1507.05915 [hep-ex]`.

[20] ALICE Collaboration, J. Adam et al., *Pseudorapidity and transverse-momentum distributions of charged particles in proton–proton collisions at* $\sqrt{s}$ *= 13 TeV*, Phys. Lett. **B753** (2016) 319, `arXiv:1509.08734 [nucl-ex]`.

[21] ATLAS Collaboration, G. Aad et al., *Charged-particle distributions in* $\sqrt{s}$ *= 13 TeV pp interactions measured with the ATLAS detector at the LHC*, Phys. Lett. **B758** (2016) 67, `arXiv:1602.01633 [hep-ex]`.

[22] ATLAS Collaboration, M. Aaboud et al., *Charged-particle distributions at low transverse momentum in $\sqrt{s} = 13$ TeV pp interactions measured with the ATLAS detector at the LHC*, Eur. Phys. J. **C76** (2016) 502, `arXiv:1606.01133 [hep-ex]`.

[23] ATLAS Collaboration, G. Aad et al., *Charged-particle distributions in pp interactions at $\sqrt{s} = 8$ TeV measured with the ATLAS detector*, Eur. Phys. J. **C76** (2016) 403, `arXiv:1603.02439 [hep-ex]`.

[24] ALICE Collaboration, K. Aamodt et al., *Midrapidity antiproton-to-proton ratio in pp collisions at $\sqrt{s} = 0.9$ and 7 TeV measured by the ALICE experiment*, Phys. Rev. Lett. **105** (2010) 072002, `arXiv:1006.5432 [hep-ex]`.

[25] STAR Collaboration, B. I. Abelev et al., *Systematic Measurements of Identified Particle Spectra in pp, d+Au and Au+Au Collisions from STAR*, Phys. Rev. **C79** (2009) 034909, `arXiv:0808.2041 [nucl-ex]`.

[26] UA4 Collaboration, D. Bernard et al., *Pseudorapidity Distribution of Charged Particles in Diffraction Dissociation Events at the CERN SPS Collider*, Phys. Lett. **B166** (1986) 459.

[27] UA5 Collaboration, R. E. Ansorge et al., *Diffraction Dissociation at the CERN Pulsed Collider at CM Energies of 900-GeV and 200-GeV*, Z. Phys. **C33** (1986) 175.

[28] CMS and TOTEM Collaborations, S. Chatrchyan, et al., *Measurement of pseudorapidity distributions of charged particles in proton-proton collisions at $\sqrt{s} = 8$ TeV by the CMS and TOTEM experiments*, Eur. Phys. J. **C74** (2014) 3053, `arXiv:1405.0722 [hep-ex]`.

[29] D. H. Perkins, *Introduction to high energy physics.* Cambridge University Press, Cambridge, UK, 1982.

[30] W. Cottingham and D. Greenwood, *An Introduction to the Standard Model of Particle Physics.* Cambridge University Press, Cambridge, UK, 2007.

[31] A. Bettini, *Introduction to elementary particle physics.* Cambridge University Press, Cambridge, UK, 2008.

[32] G. Altarelli, *The Standard model of particle physics*, CERN-PH-TH-2005-206 (2005), `arXiv:hep-ph/0510281`.

[33] P. Aurenche, *The Standard model of particle physics*, ENSLAPP-A-659-97 (1997), `arXiv:hep-ph/9712342`.

[34] ALEPH Collaboration, D. Decamp et al., *A Precise Determination of the Number of Families With Light Neutrinos and of the Z Boson Partial Widths*, Phys. Lett. **B235** (1990) 399.

[35] S. L. Glashow, *Partial Symmetries of Weak Interactions*, Nucl. Phys. **22** (1961) 579.

[36] A. Salam and J. C. Ward, *Electromagnetic and weak interactions*, Phys. Lett. **13** (1964) 168.

[37] S. Weinberg, *A Model of Leptons*, Phys. Rev. Lett. **19** (1967) 1264.

[38] P. W. Higgs, *Broken Symmetries and the Masses of Gauge Bosons*, Phys. Rev. Lett. **13** (1964) 508.

[39] F. Englert and R. Brout, *Broken Symmetry and the Mass of Gauge Vector Mesons*, Phys. Rev. Lett. **13** (1964) 321.

[40] F. Mandl and G. Shaw, *Quantum Field Theory.* Wiley, Chichester, UK, 1985.

[41] P. Skands, *Introduction to QCD*, CERN-PH-TH-2012-196 (2013), `arXiv:1207.2389 [hep-ph]`.

[42] Particle Data Group Collaboration, M. Tanabashi et al., *Review of Particle Physics*, Phys. Rev. **D98** (2018) 030001.

[43] R. K. Ellis, W. J. Stirling, and B. R. Webber, *QCD and collider physics*, Camb. Monogr. Part. Phys. Nucl. Phys. Cosmol. **8** (1996) 1.

[44] F. Wilczek, *QCD in extreme conditions*, IASSNS-HEP-99-92 (1999), `arXiv:hep-ph/0003183`.

[45] A. S. Kronfeld and C. Quigg, *Resource Letter: Quantum Chromodynamics*, Am. J. Phys. **78** (2010) 1081, `arXiv:1002.5032 [hep-ph]`.

[46] I. Hinchliffe and A. V. Manohar, *The QCD coupling constant*, Ann. Rev. Nucl. Part. Sci. **50** (2000) 643, `arXiv:hep-ph/0004186`.

[47] D. J. Gross and F. Wilczek, *Ultraviolet Behavior of Nonabelian Gauge Theories*, Phys. Rev. Lett. **30** (1973) 1343.

[48] H. D. Politzer, *Reliable Perturbative Results for Strong Interactions?*, Phys. Rev. Lett. **30** (1973) 1346.

[49] B. Povh et al., *Particles and Nuclei: an introduction to the physical concepts; 6th ed.,* Springer, Berlin, 2008.

[50] R. P. Feynman, *Very high-energy collisions of hadrons*, Phys. Rev. Lett. **23** (1969) 1415.

[51] G. Watt, *MSTW PDFs and impact of PDFs on cross sections at Tevatron and LHC*, Nucl. Phys. Proc. Suppl. **222-224** (2012) 61, `arXiv:1201.1295 [hep-ph]`.

[52] H.-L. Lai and others., *New parton distributions for collider physics*, Phys. Rev. **D82** (2010) 074024, `arXiv:1007.2241 [hep-ph]`.

[53] P. Jimenez-Delgado and E. Reya, *Dynamical NNLO parton distributions*, Phys. Rev. **D79** (2009) 074023, `arXiv:0810.4274 [hep-ph]`.

[54] H1 and ZEUS Collaborations, F. D. Aaron, et al., *Combined Measurement and QCD Analysis of the Inclusive e+- p Scattering Cross Sections at HERA*, JHEP **01** (2010) 109, `arXiv:0911.0884 [hep-ex]`.

[55] V. N. Gribov and L. N. Lipatov, *Deep inelastic ep scattering in perturbation theory*, Sov. J. Nucl. Phys. **15** (1972) 438.

[56] G. Altarelli and G. Parisi, *Asymptotic Freedom in Parton Language*, Nucl. Phys. **B126** (1977) 298.

[57] Y. L. Dokshitzer, *Calculation of the Structure Functions for Deep Inelastic Scattering and e+ e- Annihilation by Perturbation Theory in Quantum Chromodynamics.*, Sov. Phys. JETP **46** (1977) 641.

[58] J. C. Collins, D. E. Soper, and G. F. Sterman, *Factorization of Hard Processes in QCD*, Adv. Ser. Direct. High Energy Phys. **5** (1989) 1, `arXiv:hep-ph/0409313`.

[59] J. Campbell, J. Huston, and F. Krauss, *The Black Book of Quantum Chromodynamics.* Oxford University Press, 2017.

[60] J. Kretzschmar, *Standard Model physics at the LHC*, (2018), `https://cds.cern.ch/record/2644360`.

[61] B. Andersson, G. Gustafson, G. Ingelman, and T. Sjöstrand, *Parton Fragmentation and String Dynamics*, Phys. Rept. **97** (1983) 31.

[62] B. Andersson, *The Lund model*, Camb. Monogr. Part. Phys. Nucl. Phys. Cosmol. **7** (1997) 1.

[63] A. Buckley et al., *General-purpose event generators for LHC physics*, Phys. Rept. **504** (2011) 145, `arXiv:1101.2599 [hep-ph]`.

[64] B. Andersson, G. Gustafson, and T. Sjöstrand, *A Model for Baryon Production in Quark and Gluon Jets*, Nucl. Phys. **B197** (1982) 45.

[65] B. Andersson, G. Gustafson, and T. Sjöstrand, *Baryon Production in Jet Fragmentation and Υ Decay*, Phys. Scripta **32** (1985) 574.

[66] B. R. Webber, *A QCD Model for Jet Fragmentation Including Soft Gluon Interference*, Nucl. Phys. **B238** (1984) 492.

[67] P. Bartalini et al., *Multi-Parton Interactions at the LHC*, DESY-11-185 (2011), `arXiv:1111.0469 [hep-ph]`.

[68] T. Sjöstrand, *The Development of MPI Modeling in Pythia*, Adv. Ser. Direct. High Energy Phys. **29** (2018) 191, `arXiv:1706.02166 [hep-ph]`.

[69] R. Corke, *Multiple Interactions in Pythia 8*, in *Proceedings, 1st International Workshop on Multiple Partonic Interactions at the LHC (MPI08): Perugia, Italy, October 27-31, 2008*. `arXiv:0901.2852 [hep-ph]`.

[70] T. Sjöstrand, S. Mrenna, and P. Z. Skands, *PYTHIA 6.4 Physics and Manual*, JHEP **05** (2006) 026, `arXiv:hep-ph/0603175`.

[71] T. Sjöstrand, S. Mrenna, and P. Z. Skands, *A Brief Introduction to PYTHIA 8.1*, Comput. Phys. Commun. **178** (2008) 852, `arXiv:0710.3820 [hep-ph]`.

[72] ATLAS Collaboration, G. Aad et al., *Measurement of underlying event characteristics using charged particles in pp collisions at $\sqrt{s} = 900 GeV$ and 7 TeV with the ATLAS detector*, Phys. Rev. **D83** (2011) 112001, `arXiv:1012.0791 [hep-ex]`.

[73] T. Sjöstrand, *Status and developments of event generators*, PoS **LHCP2016** (2016) 007, `arXiv:1608.06425 [hep-ph]`.

[74] S. Donnachie et al., *Pomeron physics and QCD*, Camb. Monogr. Part. Phys. Nucl. Phys. Cosmol. **19** (2002) 1.

[75] V. Barone and E. Predazzi, *High-Energy Particle Diffraction*. Springer-Verlag, Berlin Heidelberg, 2002.

[76] Y. L. Dokshitzer, V. A. Khoze, A. H. Mueller, and S. I. Troian, *Basics of perturbative QCD*. Editions Frontieres, France, 1991.

[77] T. Regge, *Bound states, shadow states and Mandelstam representation*, Nuovo Cim. **18** (1960) 947.

[78] P. D. B. Collins, *An Introduction to Regge Theory and High-Energy Physics*. Cambridge Univ. Press, Cambridge, UK, 2009.

[79] T. Regge, *Introduction to complex orbital momenta*, Nuovo Cim. **14** (1959) 951.

[80] V. A. Petrov, *Nonlinear Regge Trajectories in Theory and Practice*, AIP Conf. Proc. **1105** (2009) 266, `arXiv:0812.0996 [hep-ph]`.

[81] G. F. Chew and S. C. Frautschi, *Regge Trajectories and the Principle of Maximum Strength for Strong Interactions*, Phys. Rev. Lett. **8** (1962) 41.

[82] V. N. Gribov, *The theory of complex angular momenta: Gribov lectures on theoretical physics*. Cambridge University Press, 2007.

[83] A. Donnachie and P. V. Landshoff, *Total cross-sections*, Phys. Lett. **B296** (1992) 227, `arXiv:hep-ph/9209205`.

[84] E. Levin, *An Introduction to pomerons*, (1998), `arXiv:hep-ph/9808486`.

[85] M. Froissart, *Asymptotic behavior and subtractions in the Mandelstam representation*, Phys. Rev. **123** (1961) 1053.

[86] A. Martin, *Extension of the axiomatic analyticity domain of scattering amplitudes by unitarity. 1.*, Nuovo Cim. **A42** (1965) 930.

[87] I. I. Pomeranchuk, *Equality of the nucleon and antinucleon total interaction cross section at high energies*, Zh. Eksp. Teor. Fiz. **34** (1958) 725.

[88] STAR Collaboration, J. Adam et al., *Results on Total and Elastic Cross Sections in Proton-Proton Collisions at* $\sqrt{s} = 200\ GeV$, (2020), `arXiv:2003.12136 [hep-ex]`.

[89] A. H. Mueller, *O(2,1) Analysis of Single Particle Spectra at High-energy*, Phys. Rev. **D2** (1970) 2963.

[90] W. Kittel and E. A. De Wolf, *Soft multihadron dynamics*. World Scientific, Hackensack, USA, 2005.

[91] A. B. Kaidalov, *Diffractive Production Mechanisms*, Phys. Rept. **50** (1979) 157.

[92] O. V. Kancheli, *Inelastic Differential Cross Sections at High energies and Duality*, JETP Lett. **11** (1970) 267.

[93] B. Z. Kopeliovich, I. K. Potashnikova, and I. Schmidt, *Diffraction in QCD*, Braz. J. Phys. **37** (2007) 473, `arXiv:hep-ph/0604097`.

[94] G. Ingelman and P. E. Schlein, *Jet Structure in High Mass Diffractive Scattering*, Phys. Lett. **152B** (1985) 256.

[95] ZEUS Collaboration, S. Chekanov et al., *Deep inelastic scattering with leading protons or large rapidity gaps at HERA*, Nucl. Phys. **B816** (2009) 1, `arXiv:0812.2003 [hep-ex]`.

[96] UA8 Collaboration, R. Bonino et al., *Evidence for Transverse Jets in High Mass Diffraction*, Phys. Lett. **B211** (1988) 239.

[97] UA8 Collaboration, A. Brandt et al., *Cross-section measurements of hard diffraction at the SPS collider*, Phys. Lett. **B421** (1998) 395, `arXiv:hep-ex/9709015`.

[98] H1 Collaboration, A. Aktas et al., *Measurement and QCD analysis of the diffractive deep-inelastic scattering cross-section at HERA*, Eur. Phys. J. **C48** (2006) 715, `arXiv:hep-ex/0606004`.

[99] H1 Collaboration, A. Aktas et al., *Dijet Cross Sections and Parton Densities in Diffractive DIS at HERA*, JHEP **10** (2007) 042, `arXiv:0708.3217 [hep-ex]`.

[100] G. A. Schuler and T. Sjöstrand, *Hadronic diffractive cross-sections and the rise of the total cross-section*, Phys. Rev. **D49** (1994) 2257.

[101] T. Sjöstrand et al., *An Introduction to PYTHIA 8.2*, Comput. Phys. Commun. **191** (2015) 159, `arXiv:1410.3012 [hep-ph]`.

[102] A. Donnachie and P. Landshoff, *Hard diffraction: Production of high p_T jets, W or Z, and Drell-Yan pairs*, Nuclear Physics B **303** (1988) 634.

[103] A. Donnachie and P. V. Landshoff, *Elastic Scattering and Diffraction Dissociation*, Nucl. Phys. **B244** (1984) 322.

[104] A. Donnachie and P. V. Landshoff, *Diffractive Deep Inelastic Lepton Scattering*, Phys. Lett. **B191** (1987) 309.

[105] R. Ciesielski and K. Goulianos, *MBR Monte Carlo Simulation in PYTHIA8*, PoS **ICHEP2012** (2013) 301, `arXiv:1205.1446 [hep-ph]`.

[106] K. A. Goulianos, *Hadronic diffraction: Where do we stand?*, Frascati Phys. Ser. **34** (2004) 251, `arXiv:hep-ph/0407035`.

[107] K. A. Goulianos, *Diffraction in QCD*, in *Proceedings, Corfu Summer Institute on Elementary Particle Physics (Corfu 2001): Corfu, Greece, August 31-September, 2001*. `arXiv:hep-ph/0203141`.

[108] R. J. M. Covolan, J. Montanha, and K. A. Goulianos, *A New determination of the soft pomeron intercept*, Phys. Lett. **B389** (1996) 176.

[109] K. Goulianos, *Diffraction, Saturation and pp Cross Sections at the LHC*, (2011), `arXiv:1105.4916 [hep-ph]`.

[110] A. Capella et al., *Dual parton model*, Phys. Rept. **236** (1994) 225.

[111] G. C. Rossi and G. Veneziano, *A Possible Description of Baryon Dynamics in Dual and Gauge Theories*, Nucl. Phys. **B123** (1977) 507.

[112] X. Artru, *String Model with Baryons: Topology, Classical Motion*, Nucl. Phys. **B85** (1975) 442.

[113] G. H. Arakelyan, C. Merino, C. Pajares, and Yu. M. Shabelski, *Midrapidity production of secondaries in pp collisions at RHIC and LHC energies in the quark-gluon string model*, Eur. Phys. J. **C54** (2008) 577, `arXiv:0709.3174 [hep-ph]`.

[114] B. Kopeliovich and B. Povh, *Baryon stopping at HERA: Evidence for gluonic mechanism*, Phys. Lett. **B446** (1999) 321, `arXiv:hep-ph/9810530`.

[115] B. Z. Kopeliovich and B. G. Zakharov, *Novel Mechanisms of Baryon Number Flow Over Large Rapidity Gap*, Z. Phys. **C43** (1989) 241.

[116] F. W. Bopp and Yu. M. Shabelski, *Baryon number transfer in high energy hp collisions*, Phys. Atom. Nucl. **68** (2005) 2093, `arXiv:hep-ph/0406158`.

[117] B. Kopeliovich and B. Povh, *Baryon asymmetry of the proton sea at low x*, Z. Phys. **C75** (1997) 693, `arXiv:hep-ph/9607486`.

[118] F. W. Bopp, *Baryon transport in dual models and the possibility of a backward peak in diffraction*, in *New trends in high-energy physics: Experiment, phenomenology, theory. Proceedings, International School-Conference, Crimea 2000, Yalta, Ukraine, May 27-June 4, 2000.* `arXiv:hep-ph/0007229`.

[119] P. Skands, S. Carrazza, and J. Rojo, *Tuning PYTHIA 8.1: the Monash 2013 Tune*, Eur. Phys. J. **C74** (2014) 3024, `arXiv:1404.5630 [hep-ph]`.

[120] ATLAS Collaboration, *Further ATLAS tunes of PYTHIA6 and Pythia 8*, ATL-PHYS-PUB-2011-014, ATL-COM-PHYS-2011-1507 (2011), `https://cds.cern.ch/record/1400677/`.

[121] ATLAS Collaboration, *A study of the Pythia 8 description of ATLAS minimum bias measurements with the Donnachie-Landshoff diffractive model*, ATL-PHYS-PUB-2016-017 (2016), `https://cds.cern.ch/record/2206965/`.

[122] A. D. Martin, W. J. Stirling, R. S. Thorne, and G. Watt, *Parton distributions for the LHC*, Eur. Phys. J. **C63** (2009) 189, `arXiv:0901.0002 [hep-ph]`.

[123] J. Pumplin et al., *New generation of parton distributions with uncertainties from global QCD analysis*, JHEP **07** (2002) 012, `arXiv:hep-ph/0201195`.

[124] K. Werner, *The hadronic interaction model EPOS*, Nucl. Phys. Proc. Suppl. **175-176** (2008) 81.

[125] T. Pierog et al., *Muon Production in Extended Air Shower Simulations*, Phys. Rev. Lett. **101** (2008) 171101, `arXiv:astro-ph/0611311`.

[126] K. Werner et al., *Evidence for hydrodynamic evolution in proton-proton scattering at 900 GeV*, Phys. Rev. **C83** (2011) 044915, `arXiv:1010.0400 [nucl-th]`.

[127] H. J. Drescher et al., *Parton based Gribov-Regge theory*, Phys. Rept. **350** (2001) 93, `arXiv:hep-ph/0007198`.

[128] J. Bellm et al., *Herwig 7.0/Herwig++ 3.0 release note*, Eur. Phys. J. **C76** (2016) 196, `arXiv:1512.01178 [hep-ph]`.

[129] M. Bahr et al., *Herwig++ Physics and Manual*, Eur. Phys. J. **C58** (2008) 639, `arXiv:0803.0883 [hep-ph]`.

[130] J. Bellm et al., *Herwig 7.1 Release Note*, (2017), `arXiv:1705.06919 [hep-ph]`.

[131] D. Amati, A. Stanghellini, and S. Fubini, *Theory of high-energy scattering and multiple production*, Nuovo Cim. **26** (1962) 896.

[132] S. Gieseke, F. Loshaj, and P. Kirchgaeßer, *Soft and diffractive scattering with the cluster model in Herwig*, Eur. Phys. J. **C77** (2017) 156, `arXiv:1612.04701 [hep-ph]`.

[133] S. Ostapchenko, *Monte Carlo treatment of hadronic interactions in enhanced Pomeron scheme: I. QGSJET-II model*, Phys. Rev. **D83** (2011) 014018, `arXiv:1010.1869 [hep-ph]`.

[134] S. Y. Lee, *Accelerator physics; 2nd ed.* World Scientific, Singapore, 2004.

[135] Y. Luo and W. Fischer, *Beam-beam observations in the RHIC*, in *Proceedings, ICFA Mini-Workshop on Beam-Beam Effects in Hadron Colliders (BB2013): CERN, Geneva, Switzerland, March 18-22 2013.* 2014. `arXiv:1410.5936 [physics.acc-ph]`.

[136] ATLAS Collaboration, *Pile-up subtraction and suppression for jets in ATLAS*, ATLAS-CONF-2013-083 (2013), `https://cds.cern.ch/record/1570994/`.

[137] H. Hahn et al., *The RHIC design overview*, Nucl. Instrum. Meth. **A499** (2003) 245.

[138] M. Harrison, S. G. Peggs, and T. Roser, *The RHIC accelerator*, Ann. Rev. Nucl. Part. Sci. **52** (2002) 425.

[139] W. Fischer, *Run Overview of the Relativistic Heavy Ion Collider*, `http://www.agsrhichome.bnl.gov/RHIC/Runs/`.

[140] M. Anerella et al., *The RHIC magnet system*, Nucl. Instrum. Meth. **A499** (2003) 280.

[141] I. Alekseev et al., *Polarized proton collider at RHIC*, Nucl. Instrum. Meth. **A499** (2003) 392.

[142] J. Alessi et al., *Electron Beam Ion Source Preinjector Project (EBIS) Conceptual Design Report*, BNL-73700-2005-IR-R1 (2005).

[143] A. Zelenski et al., *The RHIC polarized source upgrade*, J. Phys. Conf. Ser. **295** (2011) 012147.

[144] *Brookhaven National Laboratory*, `https://www.bnl.gov/`.

[145] E. Beebe et al., *Reliable operation of the Brookhaven EBIS for highly charged ion production for RHIC and NSRL*, AIP Conf. Proc. **1640** (2015) 5.

[146] PHOBOS Collaboration, B. Back et al., *The PHOBOS experiment at the RHIC collider*, Nucl. Phys. **A661** (1999) 690.

[147] BRAHMS Collaboration, M. Adamczyk et al., *The BRAHMS experiment at RHIC*, Nucl. Instrum. Meth. **A499** (2003) 437.

[148] PHENIX Collaboration, D. P. Morrison et al., *The PHENIX experiment at RHIC*, Nucl. Phys. **A638** (1998) 565, `arXiv:hep-ex/9804004`.

[149] sPHENIX Collaboration, S. Campbell, *sPHENIX: The next generation heavy ion detector at RHIC*, J. Phys. Conf. Ser. **832** (2017) 012012, `arXiv:1611.03003 [physics.ins-det]`.

[150] M. Connors, *Fulfilling the RHIC mission with sPHENIX*, J. Phys. Conf. Ser. **736** (2016) 012027.

[151] STAR Collaboration, L. Adamczyk et al., *Single Spin Asymmetry A_N in Polarized Proton-Proton Elastic Scattering at $\sqrt{s} = 200$ GeV*, Phys. Lett. **B719** (2013) 62, `arXiv:1206.1928 [nucl-ex]`.

[152] E. C. Aschenauer et al., *eRHIC Design Study: An Electron-Ion Collider at BNL*, (2014), `arXiv:1409.1633 [physics.acc-ph]`.

[153] STAR Collaboration, K. H. Ackermann et al., *STAR detector overview*, Nucl. Instrum. Meth. **A499** (2003) 624.

[154] M. Anderson et al., *The STAR Time Projection Chamber: A Unique tool for studying high multiplicity events at RHIC*, Nucl. Instrum. Meth. **A499** (2003) 659, `arXiv:nucl-ex/0301015`.

[155] STAR Collaboration, L. Kotchenda et al., *STAR TPC gas system*, Nucl. Instrum. Meth. **A499** (2003) 703.

[156] W. J. Llope, *The large-area time-of-flight upgrade for STAR*, Nucl. Instrum. Meth. **B241** (2005) 306.

[157] W. J. Llope et al., *The TOFp / pVPD time-of-flight system for STAR*, Nucl. Instrum. Meth. **A522** (2004) 252, `arXiv:nucl-ex/0308022`.

[158] F. Geurts et al., *Performance of the prototype MRPC detector for STAR*, Nucl. Instrum. Meth. **A533** (2004) 60.

[159] W. J. Llope et al., *The STAR Vertex Position Detector*, Nucl. Instrum. Meth. **A759** (2014) 23, `arXiv:1403.6855 [physics.ins-det]`.

[160] F. S. Bieser et al., *The STAR trigger*, Nucl. Instrum. Meth. **A499** (2003) 766.

[161] STAR Collaboration, C. Adler et al., *The STAR level-3 trigger system*, Nucl. Instrum. Meth. **A499** (2003) 778.

[162] Y.-F. Xu et al., *Physics performance of the STAR Zero Degree Calorimeter at relativistic heavy ion collider*, Nucl. Sci. Tech. **27** (2016) 126.

[163] STAR Collaboration, C. A. Whitten, *The beam-beam counter: A local polarimeter at STAR*, AIP Conf. Proc. **980** (2008) 390.

[164] E. G. Judd et al., *The evolution of the STAR Trigger System*, Nucl. Instrum. Meth. **A902** (2018) 228.

[165] STAR Collaboration, A. Rose, *STAR integrated tracker*, eConf **C0303241** (2003) THLT004, `arXiv:nucl-ex/0307015`.

[166] R. Reed et al., *Vertex finding in pile-up rich events for p+p and d+Au collisions at STAR*, J. Phys. Conf. Ser. **219** (2010) 032020.

[167] D. Smirnov et al., *Vertex Reconstruction at STAR: Overview and Performance Evaluation*, J. Phys. Conf. Ser. **898** (2017) 042058.

[168] G. Contin, *The STAR Heavy Flavor Tracker and Upgrade Plan*, Nuclear Physics **A956** (2016) 858.

[169] R. Sikora, *Measurement of the diffractive central exclusive production in the STAR experiment at RHIC and the ATLAS experiment at LHC.* PhD thesis, AGH UST, Kraków, 2020, (in preparation).

[170] O. Bruning, H. Burkhardt, and S. Myers, *The Large Hadron Collider*, Prog. Part. Nucl. Phys. **67** (2012) 705.

[171] L. Evans and P. Bryant, *LHC Machine*, JINST **3** (2008) S08001.

[172] *The CERN accelerator complex*, `https://cds.cern.ch/record/2197559`.

[173] K. Schindl, *LEP performance. Proceedings, 9th Workshop, Chamonix, France, January 26-29, 1999: The injector chain for the LHC.* 1999. CERN-PS-99-018-DI, `https://cds.cern.ch/record/384396/`.

[174] S. Gilardoni and D. Manglunki, *Fifty years of the CERN Proton Synchrotron*, CERN-2011-004 (2011), `https://cds.cern.ch/record/1359959/`.

[175] J. Lettry et al., *Overview of the Status and Developments on Primary Ion Sources at CERN*, Conf. Proc. **C110904** (2011) 3474.

[176] M. Benedikt et al., *LHC Design Report. 3. The LHC injector chain*, CERN-2004-003-V-3 (2004), `https://cds.cern.ch/record/823808/`.

[177] ATLAS Collaboration, G. Aad et al., *The ATLAS Experiment at the CERN Large Hadron Collider*, JINST **3** (2008) S08003.

[178] CMS Collaboration, S. Chatrchyan et al., *The CMS Experiment at the CERN LHC*, JINST **3** (2008) S08004.

[179] LHCb Collaboration, A. A. Alves, Jr. et al., *The LHCb Detector at the LHC*, JINST **3** (2008) S08005.

[180] ALICE Collaboration, K. Aamodt et al., *The ALICE experiment at the CERN LHC*, JINST **3** (2008) S08002.

[181] K. Potamianos, *The upgraded Pixel detector and the commissioning of the Inner Detector tracking of the ATLAS experiment for Run-2 at the Large Hadron Collider*, PoS **EPS-HEP2015** (2015) 261, `arXiv:1608.07850 [physics.ins-det]`.

[182] G. Aad et al., *ATLAS pixel detector electronics and sensors*, JINST **3** (2008) P07007.

[183] ATLAS Collaboration, M. Capeans et al., *ATLAS Insertable B-Layer Technical Design Report*, ATLAS-TDR-19 (2010), `https://cds.cern.ch/record/1291633/`.

[184] A. Abdesselam et al., *The integration and engineering of the ATLAS SemiConductor Tracker barrel*, JINST **3** (2008) P10006.

[185] E. Abat et al., *The ATLAS TRT barrel detector*, JINST **3** (2008) P02014.

[186] E. Abat et al., *The ATLAS TRT end-cap detectors*, JINST **3** (2008) P10003.

[187] ATLAS Collaboration, B. Aubert et al., *Construction, assembly and tests of the ATLAS electromagnetic barrel calorimeter*, Nucl. Instrum. Meth. **A558** (2006) 388.

[188] M. L. Andrieux et al., *Construction and test of the first two sectors of the ATLAS barrel liquid argon presampler*, Nucl. Instrum. Meth. **A479** (2002) 316.

[189] ATLAS Collaboration, M. Aleksa et al., *Construction, assembly and tests of the ATLAS electromagnetic end-cap calorimeters*, JINST **3** (2008) P06002.

[190] ATLAS Collaboration, *ATLAS tile calorimeter: Technical design report*, CERN-LHCC-96-42 (1996), `https://cds.cern.ch/record/331062/`.

[191] D. M. Gingrich et al., *Construction, assembly and testing of the ATLAS hadronic end-cap calorimeter*, JINST **2** (2007) P05005.

[192] A. Artamonov et al., *The ATLAS forward calorimeters*, JINST **3** (2008) P02010.

[193] A. Sidoti, *Minimum Bias Trigger Scintillators in ATLAS Run II*, JINST **9** (2014) C10020.

[194] S. Abdel Khalek et al., *The ALFA Roman Pot Detectors of ATLAS*, JINST **11** (2016) P11013, `arXiv:1609.00249 [physics.ins-det]`.

[195] P. Jenni et al., *ATLAS Forward Detectors for Measurement of Elastic Scattering and Luminosity*, ATLAS-TDR-18 (2008), `https://cds.cern.ch/record/1095847/`.

[196] ATLAS Collaboration, K. W. Janas, *The track-based alignment of the ALFA Roman Pot detectors of the ATLAS experiment*, PoS **LHCP2019** (2019) 060.

[197] ATLAS Collaboration, G. Aad et al., *Measurement of the total cross section from elastic scattering in pp collisions at $\sqrt{s} = 7$ TeV with the ATLAS detector*, Nucl. Phys. **B889** (2014) 486, `arXiv:1408.5778 [hep-ex]`.

[198] S. Jakobsen, *Commissioning of the Absolute Luminosity For ATLAS detector at the LHC*. PhD thesis, University of Copenhagen, 2014.

[199] A. P. Lind, *A Study of Diffractive Scattering with the ATLAS and ALFA Experiment*, Master's thesis, University of Copenhagen, 2017.

[200] L. Adamczyk et al., *Technical Design Report for the ATLAS Forward Proton Detector*, ATLAS-TDR-024 (2015), `https://cds.cern.ch/record/2017378/`.

[201] A. R. Martínez, *The Run-2 ATLAS Trigger System*, J. Phys. Conf. Ser. **762** (2016) 012003.

[202] ATLAS Collaboration, *ATLAS high-level trigger, data acquisition and controls: Technical design report*, CERN-LHCC-2003-022, ATLAS-TRD-016 (2003), `https://cds.cern.ch/record/616089/`.

[203] F. Akesson et al., *ATLAS tracking event data model*, ATL-SOFT-PUB-2006-004 (2006), `https://cds.cern.ch/record/973401/`.

[204] ATLAS Collaboration, M. Aaboud et al., *Performance of the ATLAS Track Reconstruction Algorithms in Dense Environments in LHC Run 2*, Eur. Phys. J. **C77** (2017) 673, `arXiv:1704.07983 [hep-ex]`.

[205] T. Cornelissen et al., *Concepts, Design and Implementation of the ATLAS New Tracking (NEWT)*, ATL-SOFT-PUB-2007-007, ATL-COM-SOFT-2007-002 (2007), `https://cds.cern.ch/record/1020106/`.

[206] T. Cornelissen et al., *The new ATLAS track reconstruction (NEWT)*, J. Phys. Conf. Ser. **119** (2008) 032014.

[207] R. Fruhwirth, *Application of Kalman filtering to track and vertex fitting*, Nucl. Instrum. Meth. **A262** (1987) 444.

[208] ATLAS Collaboration, G. Aad et al., *A neural network clustering algorithm for the ATLAS silicon pixel detector*, JINST **9** (2014) P09009, `arXiv:1406.7690 [hep-ex]`.

[209] ATLAS Collaboration, *dE/dx measurement in the ATLAS Pixel Detector and its use for particle identification*, ATLAS-CONF-2011-016 (2011), `https://cds.cern.ch/record/1336519/`.

[210] ATLAS Collaboration, M. Aaboud et al., *Search for metastable heavy charged particles with large ionization energy loss in pp collisions at $\sqrt{s} = 13$ TeV using the ATLAS experiment*, Phys. Rev. **D93** (2016) 112015, `arXiv:1604.04520 [hep-ex]`.

[211] ATLAS Collaboration, S. Boutle et al., *Primary vertex reconstruction at the ATLAS experiment*, J. Phys. Conf. Ser. **898** (2017) 042056.

[212] G. Piacquadio et al., *Primary vertex reconstruction in the ATLAS experiment at LHC*, J. Phys. Conf. Ser. **119** (2008) 032033.

[213] ATLAS Collaboration, G. Aad et al., *Topological cell clustering in the ATLAS calorimeters and its performance in LHC Run 1*, Eur. Phys. J. **C77** (2017) 490, `arXiv:1603.02934 [hep-ex]`.

[214] W. Lampl et al., *Calorimeter clustering algorithms: Description and performance*, ATL-LARG-PUB-2008-002 (2008), `https://cds.cern.ch/record/1099735/`.

[215] R. Brun et al., *GEANT3*, CERN-DD-EE-84-1 (1987), `https://cds.cern.ch/record/1119728/`.

[216] R. Sikora, *Elastic proton-proton scattering in the STAR experiment at RHIC*, Bachelor's thesis, AGH UST, Kraków, 2013.

[217] R. Sikora, *Study of elastic proton-proton scattering with the STAR detector at RHIC*, Master's thesis, AGH UST, Kraków, 2014.

[218] Ł. Fulek, *Transport of particles through RHIC magnet lattice*, Bachelor's thesis, AGH UST, Kraków, 2013, (in Polish).

[219] Ł. Fulek, *Study of single diffrative dissociation in proton-proton scattering with STAR detector at RHIC*, Master's thesis, AGH UST, Kraków, 2014, (in Polish).

[220] GEANT4 Collaboration, S. Agostinelli et al., *GEANT4: A Simulation toolkit*, Nucl. Instrum. Meth. **A506** (2003) 250.

[221] L. Deniau, H. Grote, G. Roy, and S. Frank, *The MAD-X Program (Methodical Accelerator Design Version 5.05.01 User's Reference Manual*, `http://mad.web.cern.ch/mad/`.

[222] CDF Collaboration, D. Acosta et al., *Inclusive double pomeron exchange at the Fermilab Tevatron $\bar{p}p$ collider*, Phys. Rev. Lett. **93** (2004) 141601, `arXiv:hep-ex/0311023`.

[223] C. O. Rasmussen and T. Sjöstrand, *Models for total, elastic and diffractive cross sections*, Eur. Phys. J. C **78** (2018) 461, `arXiv:1804.10373 [hep-ph]`.

[224] G. D'Agostini, *A Multidimensional unfolding method based on Bayes' theorem*, Nucl. Instrum. Meth. **A362** (1995) 487.

[225] H. Bichsel, *A method to improve tracking and particle identification in TPCs and silicon detectors*, Nucl. Instrum. Meth. **A562** (2006) 154.

[226] ATLAS Collaboration, G. Aad et al., *The ATLAS Simulation Infrastructure*, Eur. Phys. J. **C70** (2010) 823, `arXiv:1005.4568 [physics.ins-det]`.

[227] ATLAS Collaboration, G. Duckeck et al., *ATLAS computing: Technical design report*, ATLAS-TRD-017 (2005), `https://cds.cern.ch/record/837738/`.

[228] S. Carrazza, S. Forte, and J. Rojo, *Parton Distributions and Event Generators*, in *Proceedings, 43rd International Symposium on Multiparticle Dynamics (ISMD 13)*. 2013. `arXiv:1311.5887 [hep-ph]`.

[229] J. C. Collins, *Light cone variables, rapidity and all that*, (1997), `arXiv:hep-ph/9705393`.

[230] ATLAS Collaboration, G. Aad et al., *Dijet production in $\sqrt{s} = 7$ TeV pp collisions with large rapidity gaps at the ATLAS experiment*, Phys. Lett. **B754** (2016) 214, `arXiv:1511.00502 [hep-ex]`.

[231] S. Czekierda, *Hadronic final states in diffractive pp scattering at $\sqrt{s} = 13$ TeV using the ATLAS detector.* PhD thesis, The H. Niewodniczański Institute of Nuclear Physics, Polish Academy of Sciences, 2019.

[232] V. Cairo, *Charged-Particle Distributions and Material Measurements in $\sqrt{s} = 13$ TeV pp collisions with the ATLAS Inner Detector.* PhD thesis, University of Calabria, 2017, `https://cds.cern.ch/record/2291081/`.

[233] ATLAS Collaboration, M. Aaboud et al., *Measurement of the total cross section from elastic scattering in pp collisions at* $\sqrt{s} = 8$ *TeV with the ATLAS detector*, Phys. Lett. **B761** (2016) 158, `arXiv:1607.06605 [hep-ex]`.

[234] ATLAS Collaboration, *Studies of the ATLAS Inner Detector material using* $\sqrt{s}$ *=13 TeV pp collision data*, ATL-PHYS-PUB-2015-050 (2015), `http://cdsweb.cern.ch/record/2109010/`.

[235] ATLAS Collaboration, *Study of alignment-related systematic effects on the ATLAS Inner Detector tracking*, ATLAS-CONF-2012-141, (2012), `https://cds.cern.ch/record/1483518/`.

[236] ATLAS Collaboration, *Alignment of the ATLAS Inner Detector and its Performance in 2012*, ATLAS-CONF-2014-047, (2014), `https://cds.cern.ch/record/1741021/`.

[237] ATLAS Collaboration, *ATLAS Inner Detector Alignment Performance with February 2015 Cosmic Rays Data*, tech. rep. ATL-PHYS-PUB-2015-009, (2015), `https://cds.cern.ch/record/2008724/`.

[238] S. Das, *A simple alternative to the Crystal Ball function*, (2016), `arXiv:1603.08591 [hep-ex]`.

[239] M. Oreglia, *A Study of the Reactions* $\psi' \to \gamma\gamma\psi$. PhD thesis, SLAC, 1980.

[240] T. Skwarnicki, *A study of the radiative CASCADE transitions between the Upsilon-Prime and Upsilon resonances*. PhD thesis, Cracow, INP, 1986.

[241] UA5 Collaboration, G. J. Alner et al., *Scaling of Pseudorapidity Distributions at c.m. Energies Up to 0.9-TeV*, Z. Phys. **C33** (1986) 1.

[242] ACHM Collaboration, W. Thome et al., *Charged Particle Multiplicity Distributions in p p Collisions at ISR Energies*, Nucl. Phys. **B129** (1977) 365.

[243] ALICE Collaboration, K. Aamodt et al., *Charged-particle multiplicity measurement in proton-proton collisions at* $\sqrt{s} = 0.9$ *and 2.36 TeV with ALICE at LHC*, Eur. Phys. J. **C68** (2010) 89, `arXiv:1004.3034 [hep-ex]`.

[244] D. d'Enterria et al., *Constraints from the first LHC data on hadronic event generators for ultra-high energy cosmic-ray physics*, Astropart. Phys. **35** (2011) 98, `arXiv:1101.5596 [astro-ph.HE]`.